3 Dimensional Flow and Thermal Modelling of the Friction Stir Welding Process

Mr. Paul Colegrove

B. Eng (Hons), Adelaide, 1995

Department of Mechanical Engineering

The University of Adelaide

Submitted for the Degree of Master of Engineering Science, January 2001

CHAPTER 4

EXPERIMENTAL RESULTS FOR WELDING 12MM THICK 5083 ALUMINIUM ALLOY 115

CHAPTER 8

CHAPTER 9

Abstract

Friction Stir Welding (FSW) is a relatively new welding process, having being patented in 1991 by The Welding Institute, Cambridge. This process has great advantages in welding difficult to weld aluminium alloys. The process gives low post weld distortion, can weld thick sections in a single pass and produces welds with excellent mechanical properties. FSW uses a rotating tool to generate heat by mechanical work and friction. A key feature of the process is the localised deformation and material flow around the FSW tool.

Various authors have used analytical and numerical thermal models to predict the weld microstructure and residual stress and distortion. However these models have not yet been able to predict the conditions whereby a successful weld can be achieved. To fully understand the complete welding process flow modelling is required. Some preliminary flow models have been published, however the field is still largely in its infancy.

Therefore, this thesis presents:

- A thorough review of the thermal models that have been published to date.
- A brief investigation into the related field of friction welding.
- An investigation into the material properties that will be relevant to the process.
- A theory for describing how the material flows around the pin. This is an area that is not fully understood and is necessary to the development of a successful flow model of the process. The work reviews the current literature

in this area as well as presenting some new data to support the proposed theory.

- A theory for analysing the heat generated around the pin. This has been used in the thermal model described below.
- A basic thermal model of the process. This model is quasi-steady state and is solved using the finite element method. Features of this model are the inclusion of the tool and backing plate, and the inclusion of heat generation at the pin, which is particularly relevant to the welding of thick sections. This model has been validated for a weld with 12mm thick 5083 aluminium.
- The development of transient thermal models for thick plate aluminium. These models have shown how transient effects at the plate ends and the duration of the initial plunge have a drastic impact on the resulting thermal profile. 25mm thick 5083, 7150 and a 1000 series aluminium alloy have been used in this modelling work.
- The development of an automatic meshing program for use in a finite element model for solving the flow around the pin. Two finite element packages have been used to predict the flow of material around the pin. The model is isothermal and has not included the effect of any slip between the tool and the workpiece material. This model is able to show the amount of heat generated, and the pressure and flow of material around the pin.
- An investigation into the microstructure produced from a 5083 Friction Stir Weld. This microstructure demonstrated stick slip flow around the pin through analysing the 'so-called' pin retraction defect. The flow features observed in the weld were compared against the weld travel and rotational speeds to determine their likely cause.

- An investigation into the evidence for and against surface melting during Friction Stir Welding. While microstructural evidence indicates that surface melting does not occur, some temperature measurements suggest otherwise. A balanced review is presented. It is believed that more data is required for a definitive answer.

It is believed that the thesis lays the foundations for future thermal and flow modelling of the friction stir welding process.

Statement of Originality

This work contains no material which has been accepted for the award of any other degree or diploma in any university or other tertiary institution and, to the best of my knowledge and belief, contains no material previously published or written by another person, except where due reference has been made in the text.

I give consent to this copy of my thesis, when deposited in the University Library, being available for loan and photocopying.

Paul A. Colegrove, January 2001

Acknowledgments

This research has been undertaken with the support of the Co-operative Research Centre for Welded Structures.

The supervision of Dr. Mike Painter, Dr. Denny Graham and Dr. M. A. Wahab is gratefully acknowledged. The assistance of Dr. Tony Miller and Dr. Nick Stokes in providing guidance with the mathematical and modelling aspects of the project was greatly appreciated. I would like to thank Prakash Sabapathy for his assistance in computing relating issues and his friendship during the course of my research. I would also thank John Li, Alex Dunstone and Ryan Cottam for their friendship and lively discussion during my study.

Thanks especially to Rudolf Zettler for his assistance with the practical aspects of the project, without whom much of the work would not have been possible. Thanks too to Laurie Care, Graham Kelly, Silvio Dieso, Ian Linke, Jeremy Stewart, Ernie Murray and Peter Lloyd for their technical assistance with the project.

I would also like to thank Dr. Tom North and Dr. Gabe Bendzsak of the University of Toronto for their assistance and ideas on how best to approach the modelling aspects of the work.

Thanks also to my parents for their love and support over the last few years especially during the many challenges that I have faced. Finally I thank my God who loved me and gave me the ability to do this work.

Nomenclature

A = area

c_p = specific heat

f = fraction of heat which goes into the workpiece

f^* = volume of precipitate remaining in solution which can be used for strengthening by natural ageing.

f_o = volume fraction of precipitate of the material in the T6 condition

f_p = volume fraction of precipitate

F_r = friction force

h = convective heat transfer coefficient

h_p = thickness of plate.

HV_1 = hardness of the material for a particular amount of precipitate that has dissolved.

HV_{max} = maximum hardness in the T6 condition

HV_{min} = minimum hardness if all the precipitate is dissolved in the matrix.

$\boldsymbol{I}$ = identity matrix

k = thermal conductivity

$\boldsymbol{n}$ = 3 dimensional normal vector

N = normal force

n_1 = time exponent (<0.5)

p = pressure (uniform)

p_i = thread pitch

Q = power input / heat generation

Q_d = heat due to deformation

Q_f = heat due to friction generation

Q_l = heat due to linear deformation only

Q_p = heat generation at a point

Q_s = heat due to shearing only

r = particular radius

R = tool radius/shoulder radius/Contact Resistance

r_b = source radius

R_i = inner radii

R_o = outer radii

r_p = radius of pin

$\boldsymbol{S}$ = deviatoric stress tensor

T = temperature

t = time

t_1^* = maximum hold time for complete particle dissolution.

t_2^* = time taken to precipitate out a certain fraction of β' precitate.

T_o = Ambient Temperature

T_p = peak welding temperature

T_s = Solidus Temperature

$\boldsymbol{v}$ = 3 dimensional flow velocity vector.

V = Volume

v_{rel} = relative velocity

v_s = slip velocity

V_{weld} = travel speed

x = position in along x axis.

X_C = fraction of β' precipitate transformed.

y = position in along y axis.

z = position in along z axis.

α = thermal diffusivity

β = constant

γ = shear strain

ε = normal strain

θ = angle

θ_{weld} = angle of the incoming material to the position of the tool

λ = helix angle of thread

μ = viscosity / coefficient of friction

ξ = size of deformation region

ρ = density

σ = Normal linear stress

σ_y = yield strength

σ = 3 dimensional stress tensor

τ = shear strength of material

τ_i = source interaction time

Φ = proportionality constant.

ω = rotational speed

1 Introduction

Friction Stir Welding (FSW) is a process that was patented in 1991 by The Welding Institute [1].

A schematic diagram illustrating the process is shown in Figure 1-1. The key components of the friction stir welding tool are:

(a) The Shoulder.

This is the primary means for generating heat during the process which is produced through a combination of material deformation and frictional slip. The shoulder also prevents expulsion of the material and assists the movement of material around the tool.

(b) The Pin.

The pin's primary function is to deform the bulk material and its secondary function is to generate heat.

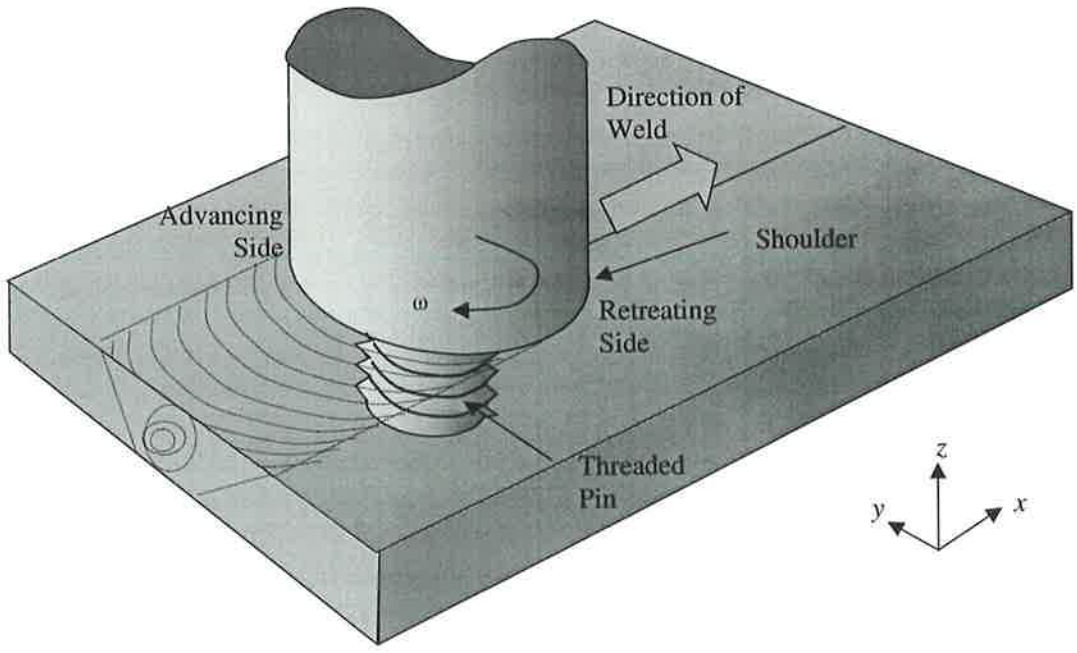

Figure 1-1 Schematic of the Friction Stir Weld

Usually the tool is inclined 2-3° toward the direction of travel, although some later tool designs allow the tool to be positioned normal to the surface. This angle is called the tilt angle.

The material is consolidated behind the tool and a solid joint is formed from the high temperatures, pressures and material deformation. A successful weld is produced when the correct tool design, and operating parameters are used for a given material. The main operating parameters of interest are the weld speed and tool rotational speed.

The aim of this work has been the numerical modelling of the FSW process. It is believed that a successful model of the process will:

- Assist in the development of process improvements, especially in the design of new tools.
- Enable the science behind the process to be better understood.
- Help optimise the process parameters.

In the past thermal models have been used to predict the microstructure occurring in a weld and the level of residual stress and distortion.

However, the focus of the present work has been the development of a flow model for the process. This is because it is believed that to predict whether or not a weld is possible an understanding of the flow is required in addition to the thermal conditions. Since it is not possible to jump straight into such a complex task, thermal models have been done with the aim of gaining a better understanding of the heat flows that occur during the process. Since the flow region is confined to a relatively small area around

the pin, these models will accurately predict the far field temperature characteristics. These will then be used as a basis for predicting the temperatures on the boundary to the much smaller flow model which will predict how the material flows around the pin. No microstructural modelling has been done as part of this thesis.

This thesis will form the basis for future work into the modelling of Friction Stir Welding.

2 Literature Review

An extensive amount of literature has been published over the years in the field of FSW, which has been encouraged by the FSW Symposiums hosted by TWI. Much of the work has focussed on microstructural analysis of the welds and the development of new applications, while modelling of the process and especially flow modelling is still largely in its infancy. This review covers the literature published to date, with the emphasis being on that work which is likely to have some impact on the flow/thermal modelling aspects of the process. Additional background information dealing with material properties and friction welding is also presented. Friction welding has many similar features to FSW, so literature in that area will contribute toward a good understanding of FSW.

2.1 Thermal Modelling of Friction Stir Welding

The first stage of modelling the friction stir welding process is thermal modelling. This has been done by various authors [2,3,4,5,6,7,8,9,10,11,12,13,14,15], with the aim of predicting the microstructure [4,9,10] and the likely distortion in the resulting friction stir weld.[2,3]. Please note that the work Dong et. al. [16] and Ulysse [17] while including thermal modelling are primarily based on the flow modelling aspects, so will therefore be included in section 2.6.

2.1.1 Heat Flow During the Friction Stir Welding Process

Before going into depth about the various modelling approaches it is worth going back to basics and examining the heat flows that will occur during FSW. A diagram describing this process is shown in Figure 2-1 from Russell and Shercliff [4,5 & 6].

There are three sources of heat generation identified, namely,

- Heat generated under the shoulder.
- Heat generated on the pin surface.
- Heat generated by shearing within the material.

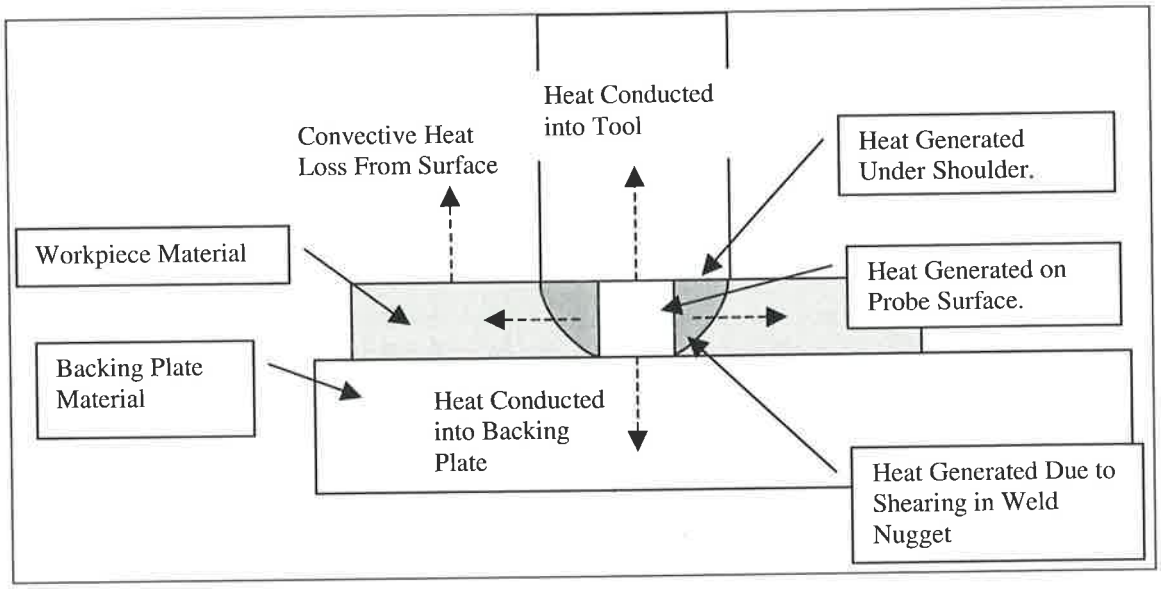

Figure 2-1 Heat Flows that Occur During Friction Stir Welding

It should be noted that the type of heat generated is dependent on the type of boundary condition that exists between the tool/material interface. If there is no slip between the tool and the material then all the heat generation will be within the material itself, so the surface heat generation terms are zero. If on the other hand there is slip then all three will be present. This is discussed in greater detail in section 3.2.

Please note that an extra term, the convective heat loss from the top of the plate has been added to the diagram. Including this in the model will improve the model's accuracy. Another factor that was not included in the model by Russel and Shercliff was the conductive heat loss through the clamping plates, which hold the material in position.

2.1.2 Calculating the Heat Source

All the authors [3,4,5,6,7,8,9,10,11,12,13,14,15], except for the flow modelling work discussed in section 2.6 have assumed that all the heat is generated at the shoulder, and have ignored the heat generated by the pin and that from shearing of the material in the weld nugget.

The heat generation is considered equivalent to the power consumed by the rotating tool and is estimated by calculating the power required to overcome friction or interfacial shear at the tool / material interface. For an incremental area dA at a radius r from the tool centre, the increment of heat generated can be expressed as follows,

(a) by assuming that the sliding resistance is due to friction.[8,9,10,14]

$$dq = \omega \mu p r dA \qquad \textbf{Eq. 2-1}$$

Usually the pressure p is assumed to be uniform. μ is also assumed constant, however in practice this is unlikely to be the case, for μ is likely to be dependent on pressure, slip velocity and temperature.

(b) by assuming interfacial shear takes place, dq_o can be determined by the following equation:[4,5,6]

$$dq = \omega \tau r dA \qquad \textbf{Eq. 2-2}$$

Where, τ is the shear strength of the material at an appropriate temperature and strain rate. The approach taken by Russell was derived from that used by Midling and Grong [48].

Integrating the chosen equation over the shoulder of the FSW tool gives an expression for the total heat generation rate as:

$$\dot{Q} = \tfrac{2}{3}\pi\mu p\omega(R_o^3 - R_i^3) = \tfrac{2}{3}\pi\tau\omega(R_o^3 - R_i^3) \qquad \textbf{Eq. 2-3}$$

Since R_i^3 is very small when compared with R_o^3 this term is usually set to zero.

In the two alternate approaches, one assumes that the heat input is dependent on the shear strength of the material [4,5,6] and the other on the coefficient of friction [8,9,10,14]. An alternative approach is to consider that both effects influence the flow of material around the friction stir welding tool. The material may flow or slip around the tool, however the speed at which it flows is limited by the shear strength of the material. An equilibrium condition is established between the force applied through friction and the shear resistance from the material. This effect together with the possibility of a stick/slip boundary condition is explained in greater detail in section 3.2.3.

To calculate the value of the heat input requires either known values of the normal force and coefficient of friction or known values of the shear strength. The values that have been used are:

- Russell and Shercliff [4] used a yield stress which was 5% of the room temperature value. (ie. 22MPa for 2014 T6).
- Gould et. al. [13,14] used a value of 2 for the coefficient of friction, which was often used in friction welding. The reason for using this high value was because Gould believed that bonding occurred between the FSW tool and the

workpiece material. There was no mention of the normal force used in the calculations.

- Midling and Rorvik [43] used a value of 0.2 for the coefficient of friction to calculate an approximate value of the heat input when investigated the effect of various parameters on the heat generated during a weld. To get an idea of the actual heat generated in the weld they measured the width of the heat affected zone (HAZ). Midling and Rorvik found that there was very little change in heat generation at the workpiece/tool interface (HAZ width) with varying tool load and rotational speed, once the workpiece material had plasticised. For example if the rotational speed was reduced, the cooling of the material resulted in an increase in the coefficient of friction and an increase in the heat input, which offset the original decrease in the heat input from the reduced speed of rotation. Therefore, Midling and Rorvik concluded that the coefficient of friction can vary between 0.2 to 0.33.

It appears that calculating the actual value of the heat input is exceedingly difficult to calculate because of the many variables involved. Because of these difficulties, Chao and Xinhai [2,3] used reverse engineering to find the total heat input from the resulting thermal profile. A similar approach was used in section 7.3.3 where the maximum temperature achieved during the weld was assumed, and the heat required to achieve this temperature calculated.

Another approach that has been used by Nguyen and Weckman [61] for modelling the friction welding of steel parts used the power input from the motor to calculate the heat input for the model. This was used because of the complexities in finding a suitable

relationship for the coefficient of friction, which would cover all welding circumstances. In addition, a constant temperature boundary condition at the welding interface was used once the average surface temperature exceeded a specified maximum temperature, T_{max}. This was to prevent the temperature of the metal exceeding the melting temperature.

In the above models only the heat generated by the tool shoulder is considered, however it must be remembered that another heat source exists, namely between the pin and the material. Russel and Shercliff [5] claimed that the amount of heat generated by the pin contact and the material shear is negligible compared to that generated by the shoulder contact. ie. They estimated that around 10-20W is produced by both the frictional contact and shear deformation of the material around the pin. This compares with the 1-2 kW which is produced at the shoulder – a ratio of 1:100. Presumably this data was obtained by welding the material with a tool which does not have a shoulder and comparing the result with a normal tool. Such a test was performed by McClure et. al. [12] who found that when welding 6.4mm thick 6061-T6 with a shoulder only, the peak temperature in the weld was 10°C (or 2.4%) less than that with a normal FSW tool.

2.1.3 The Heat Source Shape

Before investigating the shape of the heat source, it is worth investigating the heat flow timescales to determine the relative impact of various factors on the heat flow. These were presented in a paper by Russell and Shercliff [5] and have been summarised in Table 2-1.

Table 2-1

Time Constant	Definition	Equation	Value (Seconds)
t_1	Time for one tool rotation	$1/\omega$	0.1
t_2	Tool-workpiece interaction time	$2R/V_{weld}$	25
t_3	Time for heat conduction across one tool radius	R^2/k	1.8
t_4	Time for heat conduction through plate thickness	h_p^2/k	0.44

From this information it is clear that the heat will take much longer to travel across the tool radius (1.8 sec) than through the material. Therefore, the assumption that all the heat is generated at the shoulder is reasonable for the welding of thin materials.

Another conclusion that Russell and Shercliff [5] drew from the timescale data was that the heat generation underneath the tool shoulder could be assumed to be axisymmetric. The reasoning for this was the relatively short time for the tool to make one complete rotation resulting in any heat generation discrepancies being very quickly evened out by convective heat transfer underneath the tool shoulder. There are a couple of minor flaws to this line of reasoning, namely:

- This statement requires the validity of the assumption that there is zero relative velocity between the tool shoulder and the material underneath. ie. the material effectively sticks to the tool shoulder. In section 3.2.3, it is suggested that sliding contact may occur between the material and the tool.

In this case the amount of heat generation, will to some small degree be dependent on the normal force at the surface or the surface pressure. Most FSW are done with the tool inclined toward the direction of travel, which results in the pressure between the material and the tool on the front side being less than that occurring on the reverse side. Therefore, the heat which is generated behind the tool will be greater. A second, minor consequence of the sliding contact is that since the material no longer rotates with the tool, so t_1 is no longer representative of the time for material to flow around the tool.

- The statement that the uniform temperature around the tool surface results in the heat generation being uniform around the circumference is not strictly correct if the temperature in the bulk material varies in a radial direction. ie. Where the temperature in the bulk material is lower, the heat dissipation, and therefore the heat generation at that point is greater. Therefore, if we assume that the temperature is uniform in a radial direction at the surface the heat generation at the front of the tool will be greater than that behind.

Fortunately, these two effects will tend to offset each other. ie. One infers that there is greater heat generation in front of the tool and the other infers that there is greater behind. Secondly, both effects are likely to be relatively small and since coming up with another model would become exceedingly complex, the assumption of the axisymmetric heat is reasonable.

It is also worth considering asymmetry of the thermal profile between the advancing and retreating sides. It may be argued that due to the greater material deformation

occurring on the advancing side, the temperature in this region will also be slightly greater. However as mentioned previously, movement of the material will tend to even such effects out. Secondly, the surface speed of the tool is usually an order of 200 times greater than the traverse speed so any difference in the heat generation will be quite minimal. Finally, McClure et. al. [12] measured the difference between advancing and retreating sides and found the difference to be quite minimal.

Although all authors have used an axisymmetric heat source, there is some discrepancy in how this heat source has been applied to the model. In Russell and Shercliff [4] it was stated that the heat distribution is difficult to predict so it is applied as a line source at a single point. While this solution is obviously inaccurate directly underneath the tool, in the far field the difference will be small. This is the main area of interest as it provides the properties likely to be experienced in the HAZ, which has the lowest post-weld strength.

Gould and Feng [13] expanded on the concept of a line heat source and used a circular heat source around the periphery of the shoulder. This obviously resulted in a thermal profile where the greatest temperature was at the periphery of the shoulder.

Frigaard et al. [8] on the other hand used a radially distributed heat source. Since the model was based on the method of finite differences (See section 2.1.4.3), the applied heat source was not circular in shape, but had the square shape shown in Figure 2-2. Frigaard did not believe that this simplification led to a large error in the overall calculation. In any case it is more representative than the point line source used by Russell[4].

McClure et al.[11] and Chao and Xinhai [3] used a similar heat source to that used by Frigaard[8], except that it was circular and not square shaped. McClure based this assumption on the typical FSW macro-section which shows that:

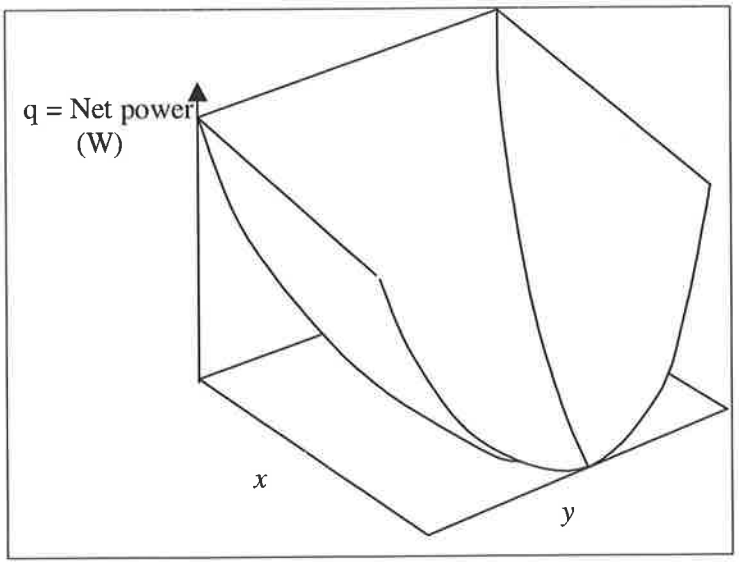

Figure 2-2 The Heat Source Used by Frigaard [8]

- The width of the HAZ approximates the width of the tool.
- The boundary of the HAZ and the base metal indicates that there is a thermal profile through the thickness of the weld.

Therefore, he concluded that the bulk of the heating for a thin material was at the shoulder, and secondly that the process must be analysed as a three dimensional system.

Note that all the authors [3,4,5,6,7,8,9,10,11,12,13,14,15] have used fairly thin plate thickness ie. 6.25mm Therefore, the effect of heat generation by the pin is fairly immaterial to the model. In

Figure 2-3 Heat Distribution, Anderson et. al. [7]

later modelling work by Russell in Anderson et.al.[7] heat generation was assumed to be uniform over the tool surface. This heat distribution profile is demonstrated in Figure 2-3.

Finally, since it is a related process it is worth examining some of the heat source shapes used in friction welding. In the thermal modelling work by Midling and Grong [48], a heat source which was linearly dependent on the radius was used.

While this is probably quite valid for the profile near the tool centre, this heat source will break down as one ventures further away. An alternative heat source that has been applied to friction welding is shown by Mitelea and Radu [46]. In this paper 3 different types of heat sources were investigated which are shown in Figure 2-4. It was found that the heat source B gave the best agreement with experimental results. Since the two processes are similar in many ways, this may in fact be a better heat source definition for friction stir welding.

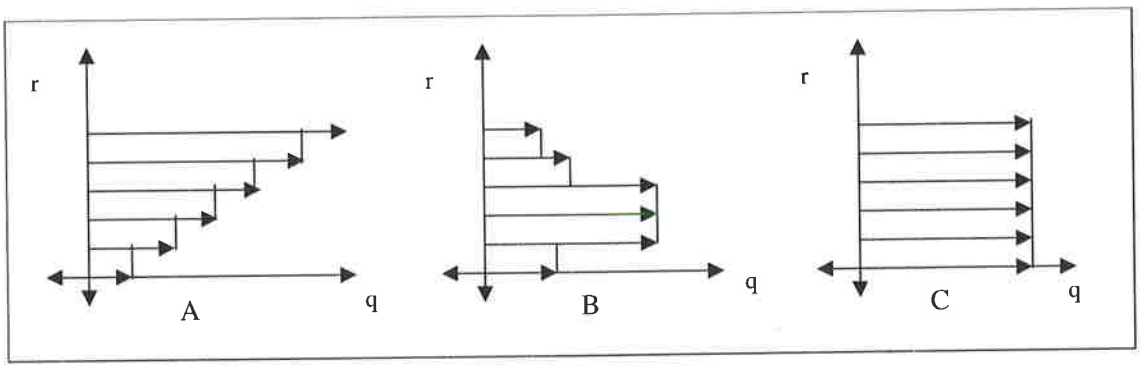

Figure 2-4 Heat Source Options for Friction Welding

2.1.4 Analysis Approaches

2.1.4.1 Distributed Circular Source Solution

In the paper by Russell and Shercliff [5], an initial estimate of the peak welding temperature was gained using the distributed circular source solution developed by Shercliff and Ashby [50] for laser welding. This gave the peak surface temperature, T_p from the following equation:

$$T_p - T_o = \frac{2Q}{\pi^{3/2} r_b^2 k}\sqrt{\alpha \tau_i} \qquad \textbf{Eq. 2-4}$$

This basic equation was then applied to friction stir welding, with a factor included for the heat loss through the FSW tool and an equation relating the heat generation to the yield strength of the material included. The final equation was:

$$\frac{T_p - T_o}{T_s - T_o} = \frac{2\sqrt{2} f}{3\sqrt{\pi}} \frac{\sigma_y \omega R^2}{k(T_s - T_o)} \sqrt{\frac{\alpha}{V_{weld} R}} \qquad \textbf{Eq. 2-5}$$

Note that f is approximately 0.83. It was found that the approximate value of the dimensionless temperature for a successful weld was:

$$\frac{T_p - T_o}{T_s - T_o} = 0.92 \qquad \textbf{Eq. 2-6}$$

Since $V_{weld}\ \alpha\ \sigma_y^2$, this suggests that the greater the yield strength, the greater the welding speed possible. Russell and Shercliff claimed that while this may be true, the higher yield strength materials also require a greater amount of plastic work to be done which limits the speed rather than the interface temperature.

Finally, tool breakage will also be more likely to occur with the higher strength alloys.

2.1.4.2 Analytical Solution Based on Rosenthal's Heat Conduction Equation

A slightly more complicated solution method is the analytical solution based on the Rosenthal heat conduction equation [51]. This has been used by Russell and Shercliff [4,5,6]. To model the effects of the position of the end of the plates the superposition of multiple point sources can be used.

McClure et al. [11] and Gould et. al. [13,14] also based their work on the Rosenthal heat conduction equation. However, unlike Russell and Shercliff it included a radially varying heat source. This resulted in the following equation for the temperature distribution at a radius r and angle θ.

$$T(r,\theta)-T_o=\frac{\mu p\omega}{k}\int_{R_i}^{R_o}\xi^2\left\{\int_{-\pi}^{\pi}\frac{e^{\left\{-\frac{V_{weld}}{2\alpha}\left[r\cos\theta-\xi\cos\gamma+\sqrt{\xi^2+r^2+z^2-2\xi r\cos(\gamma-\theta)}\right]\right\}}}{\sqrt{\xi^2+r^2+z^2-2\xi r\cos(\gamma-\theta)}}d\gamma\right\}d\xi \qquad \textbf{Eq. 2-7}$$

Note the definition of variables in Figure 2-5.

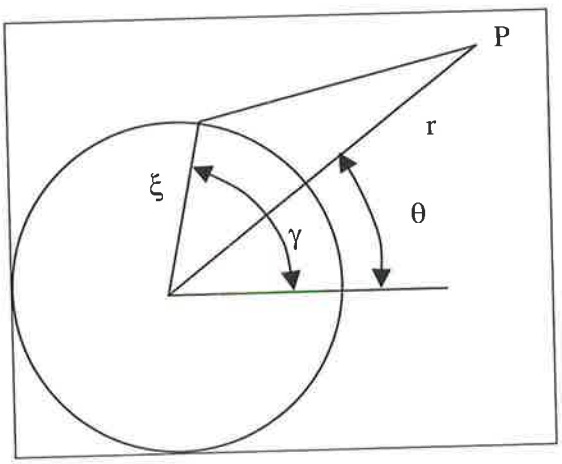

Figure 2-5 Parameter description for analytical solution

2.1.4.3 Finite Element/Difference/Volume Solutions

Several different methods have been used. Frigaard [8,9] implemented the finite difference procedure using MATLAB. In early work by Frigaard et. al. [8] the welding of thin plate aluminium was investigated so the thermal profile in the in z direction was negligible. Therefore, the

problem can be solved in 2 dimensions. In later work [9,10] the solution was extended to 3 dimensions.

In Anderson et. al. [7] FSW was modelled using the ABAQUS modelling package.

Chao and Xinhai [2,3] have used the finite element method in their modelling work. The model did not include the tool or backing plate in the model. Not including the tool will result in the heat input into the model being underestimated. Secondly, not including the backing plate in the model will result in a slightly inaccurate representation of the actual boundary condition on the bottom of the plate. This may be understood by considering that the heat lost at a point due to a convective loss as used by Chao and Xinhai will be:

$$\frac{Q}{A} = h(T_p - T_o) \qquad \textbf{Eq. 2-8}$$

Note that in this case T_p is the temperature of the bottom surface of the workpiece at a particular point. Therefore, the heat loss is proportional to the difference between surface temperature and ambient temperature

However, the actual case will be somewhat different and is one of conduction based on the following equation:

$$\frac{\dot{Q}}{A} = \frac{k(T_p - T_{bp})}{\Delta x} \qquad \textbf{Eq. 2-9}$$

Note that T_{bp} is the temperature of the backing plate at a distance Δx from the surface. In this case the temperature of the backing plate will rise as the material is welded. Therefore even if $k/\Delta x$ could be selected so that it approximated h, the heat loss would

still differ from that in equation 1-1, because T_{bp} raises as the backing plate heats up with the weld. Therefore the formulation in Chao and Xinhai will tend to over-predict the heat loss where the workpiece material temperature is high. ie. directly underneath the weld.

2.1.5 Evaluation of Solution Methods

The solution methods have been shown in order of increasingly complexity. The first two methods have the advantage that a solution can be found with very little effort required to set up the model. Secondly, they can be solved in a shorter time period. (Although finite element solutions can be found in a relatively short time.) However what advantages they have in solution time, they lack in flexibility, detail and accuracy. Including such effects as end effects, plate size, transient effects, and contact resistance between backing plate cannot be easily implemented with this method. Therefore the finite element/volume/difference methods are preferred for their inherent flexibility.

The trade-off between the different modelling approaches was discussed in Anderson et.al. [7] where the three methods were compared.

2.1.6 Transient Effects

Any friction stir weld undergoes the 4 stages illustrated in Figure 2-6.

Obviously, the material will not reach the welding temperature immediately. Frigaard et. al. [8] identified four transient stages in the welding process:

1. The stationary heating period.

   The material underneath the shoulder is heated to a sufficient temperature to allow the required plastic deformation during welding.

2. The transient heating period.

   This is the period between the start of translation and the pseudo steady state period.

3. The pseudo steady state period.

   The period during which the thermal field around the tool remains essentially constant.

4. The post steady state period.

   Heat is reflected from the end of the plate (or not conducted away) so that there is an additional build-up of heat around the tool shoulder, as the tool approaches the end of the joint.

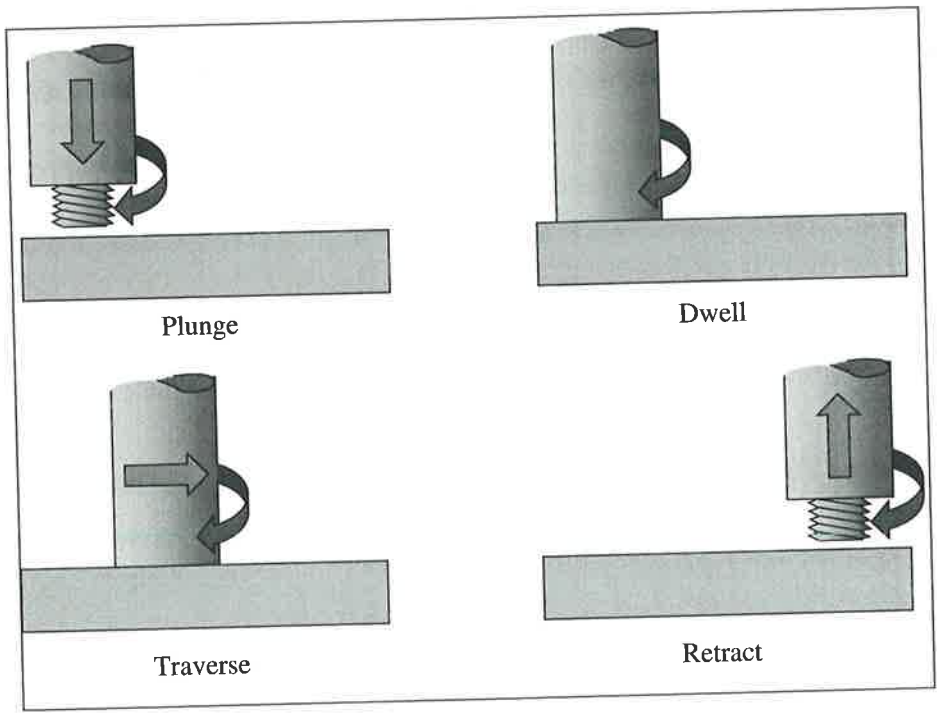

Figure 2-6 Sequence in a Friction Stir Weld

Frigaard stated that the transient effects play a significant role in FSW and should therefore be included in the heat flow analysis. He investigated the welding of 3mm plate and found that the pseudo steady state stage was reached after a welding distance of approximately 50mm.

Russell and Shercliff[5] were able to show experimentally that the steady state temperature was achieved after 150mm for thin aluminium plate. The thickness of the plate was not specified, although it seems likely that it was 6.25 mm as this was the thickness used in a subsequent paper [4]. It would seem reasonable to presume, that the distance required to achieve a steady state temperature profile will increase with increasing plate thickness. This is because the thicker material will have a greater capacity to conduct the heat away. Therefore the initial plunge and dwell sequence will tend to pre-heat the whole plate prior to welding, resulting in a large variation from the steady state condition. This has been demonstrated in section 8.

2.1.7 Limit to the Heat Generation

Both Frigaard et al. [10,55] and Russell and Shercliff [5] and Gould et. al. [14] have stated that eutectic melting imposes a natural limit to the heat generation that will occur during welding. This occurs when (for precipitation hardened alloys) there is insufficient time for the eutectic phase to fully dissolve in the matrix and it forms a liquid layer at the interface. This acts as a lubricant reducing the shear stress that can be applied to the material. Such an effect will not be applicable for solid solution strengthened alloys. In this case the onset of melting will occur at the solidus. Examples of such materials are the 1000, 3000 and 5000 series aluminium alloys.

2.1.8 Applications of Thermal Modelling

Obviously, thermal modelling needs to be extended from an academic exercise into something that has a real industrial use. Several applications have been suggested, which are described in the following sections:

2.1.8.1 Determining the Maximum Welding Speed

Russell and Shercliff [4] have alluded to this in one of their papers, however at this stage there has not been a paper published showing how it may be implemented. The concept is a relatively simple one and is demonstrated in Figure 2-7. Basically a temperature boundary is defined which may define the limit of the heat affected zone for example. If this boundary extends beyond the tool then an acceptable weld will be achieved, however if it is within the tool then achieving an acceptable weld will be difficult.

Chao and Xinhai [3] also investigated how thermal modelling could be used to optimise the process. However, they assumed that the heat input was independent of the welding

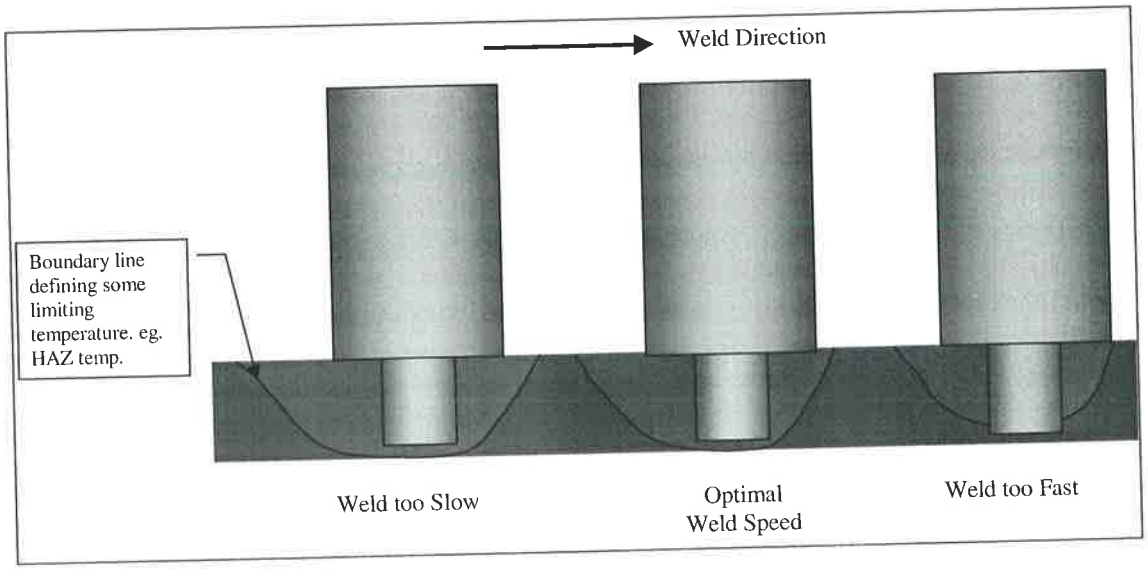

Figure 2-7 Thermal Modelling to Define the Maximum Welding Temperature [4]

speed and thickness of plate, provided the rotational speed remained constant. This author disagrees with this interpretation because it does not take into consideration how the temperature of the material affects the power required to make the weld. ie. The hotter the material, the softer it will become so heat generation will be reduced. This effect is demonstrated in the section on welding forces (section 3.4.7) and varying normal and rotational forces (section 3.4.6).

A similar approach was taken by Frigaard et.al. [8] who used the parameter q/vd to predict the temperature in front of the tool. Here q is the heat input, v is the velocity and d is the diameter of the heat source. Therefore the temperature in front of the weld is proportional to the heat input and inversely proportional to the weld speed. Frigaard then believed that there would be some cut-off temperature below which a sound weld could not be achieved. Like the method used by Chao et. al., this method does not consider how the weld temperature will effect the heat generation.

None of the authors were able to demonstrate a successful implementation of their methods. This author believes that it is impossible by the use of thermal modelling alone to predict the conditions whereby a successful weld will be achieved. This is the reason why the flow modelling is so necessary for a full understanding of FSW.

2.1.8.2 Predicting the Residual Stress and Distortion

In the papers by Chao and Xinhai [2,3], residual stress and distortion were predicted in the weld from the calculated temperature profile. They found that both residual stresses and distortion were considerably lower than the values found in fusion welding. This

obviously will be a great advantage to industrial processes where tight tolerances are required. The reasons for this good result are:

- The relatively low temperature of the process when compared with fusion welding.
- No additional molten material is added to the base material.
- The workpieces are clamped throughout the process, which assists in minimising the distortion after welding.

2.1.8.3 Microstructural Evolution

Although FSW has been applied to various materials, the main application continues to be aluminium and its alloys. Therefore this section will examine the microstructural evolution of these alloys, particularly those which are precipitation hardened.

Before describing the evolution of a typical microstructure, it is necessary to get an understanding of a typical microstructure and hardness plot across the weld. The typical microstructure is described later in section 3.4.1 and for the sake of conciseness will not be repeated here. A typical plot of the hardness across the weld is shown in Figure 2-8. The hardness is highest outside the HAZ, and decreases toward the centre of the weld till it reaches a minimum just outside the nugget region. (See section 3.4.1) Some strength is then regained in the central nugget region. The observed hardness is obviously related to the weld microstructure.

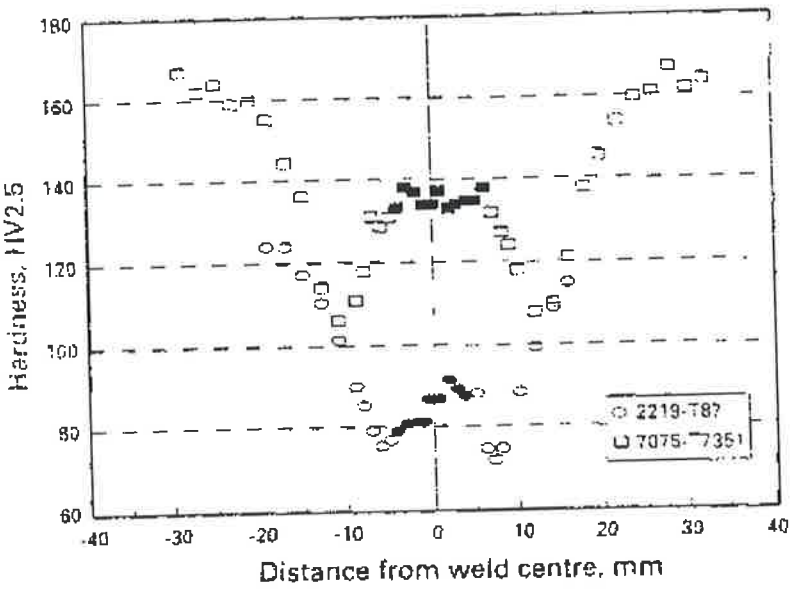

Figure 2-8 Hardness Traverse Across a Weld in 2219-T87 and 7075-T7531[76]

Threadgill and Leonard [76] gave a good summary of the microstructural evolution of age hardened alloys. In general, there are two mechanisms that cause the softening of the welded microstructure. These are:

- Over-aging of Precipitates. If the temperature in the weld remains below the temperature for dissolution then the precipitates that exist in the material will over-age and will lose their peak hardness condition.
- Dissolution of Precipitates. In this case the temperature of the weld exceeds the temperature required for dissolution of the precipitates. Subsequent natural ageing at room temperature will enable some the original strength to be regained via reprecipitation. See Leonard [36].

The degree to which each of the above processes occur will depend on the maximum temperature that occurs during the weld. In the HAZ for example only the former softening mechanism will occur, while in the nugget region both mechanisms are likely to be in action. The mechanism that predominates in the nugget is also alloy dependent. For example, when welding 7075 and 2014 it is found that both of the above mechanisms occur. However when welding 6061 and 6082 dissolution of precipitates predominates.

Finally, the reason why the hardness of the central nugget is higher than that of the adjacent Thermo-Mechanically Affected Zone (TMAZ) will be discussed. Threadgill and Leonard [76] stated that the observed peak in the hardness of the nugget was caused by the following three mechanisms:

- Decrease in the grain size due to recrystallisation
- Solid solution hardening.
- Breaking up of the constituent particles by the stirring action.

A more analytic approach to describing the microstructural evolution of precipitation hardened aluminium alloys was discussed by Grong [52]. Much of that work was based on a paper by Myhr and Grong [54]. This method predicts the loss in strength due to precipitate dissolution and does not consider the effect of precipitate over-aging.

There are 2 main phases identified for the fusion welding of precipitation hardened aluminium alloys which is also applicable to FSW. These are described for the 6000 series below:

1. Reversion.

   The β''(Mg_2Si) precipitates which strengthen the material are partly dissolved into solid solution due to the weld thermal cycle. The dimensionless strength parameter α_1 is given by:

$$\alpha_1 = \frac{HV_1 - HV_{\min}}{HV_{\max} - HV_{\min}} = {f_p}/{f_o} \approx 1 - \left[\int_0^t \frac{dt}{t_1^*}\right]^{n_1} \qquad \textbf{Eq. 2-10}$$

2. Natural Ageing.

   During cooling some of the solute recombines to form coarse, metastable β'(Mg_2Si) which do not contribute to strengthening of the material. However near the fusion boundary a large amount of the alloying elements will remain in the solid solution, enabling age hardening to occur at room temperature over the next 5-7 days. In this case the dimensionless strength parameter α_2 is given by:

$$\alpha_2 = {f^*}/{f_o} = \Phi\left[(1 - X_c)^{I_2} - \alpha_1\right]^2 \qquad \textbf{Eq. 2-11}$$

   Note that I_2 is given by:

$$I_2 = \left[\int_0^t \frac{dt}{t_2^*}\right] \qquad \textbf{Eq. 2-12}$$

   which is the kinetic strength with respect to the β' precipitation.

These two models may then be coupled together to produce a final plot of the hardness across the microstructure. This is demonstrated in Figure 2-9. Note that the point of lowest hardness occurs at the intersection point of the two models.

The microstructural evolution during friction welding and friction stir welding are very similar to fusion welding, except that they are complicated by the work hardening of the highly deformed region. In this case a third dimensionless strength parameter, α_3 is included which is equal to:

$$\alpha_3 = \Psi \qquad \textbf{Eq. 2-13}$$

where Ψ is a constant for the particular material under consideration.

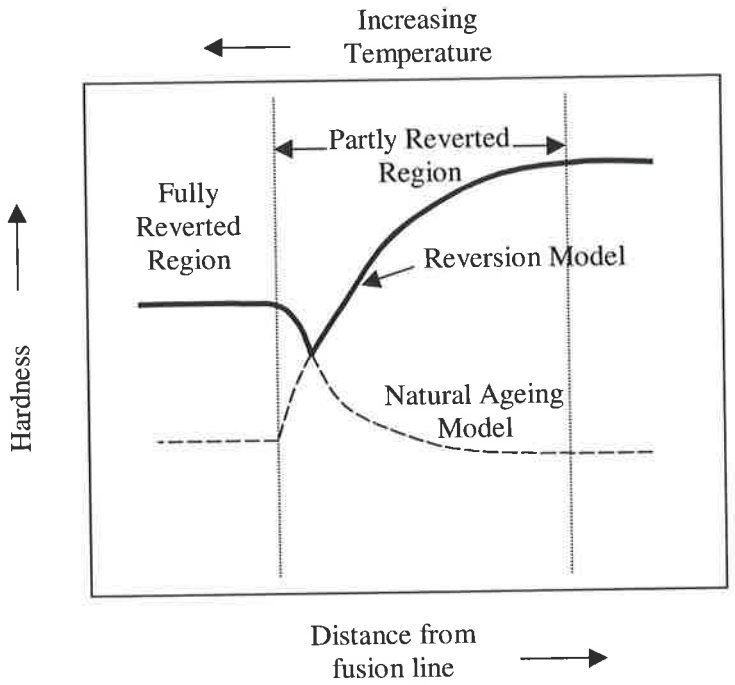

Figure 2-9 Coupling of Reversion and Natural Ageing

Although the effect of this is dependent on the temperature of the weld and the duration of the thermal cycle, the work hardening will often remove the minimum hardness as shown in Figure 2-10.

Both Russell and Shercliff [5] and Frigaard [9,10] have used this approach to predict the hardness of the as welded microstructure, however these predictions did not include the

work hardening aspects. Frigaard [10] found significant microstructural work hardening in some welds.

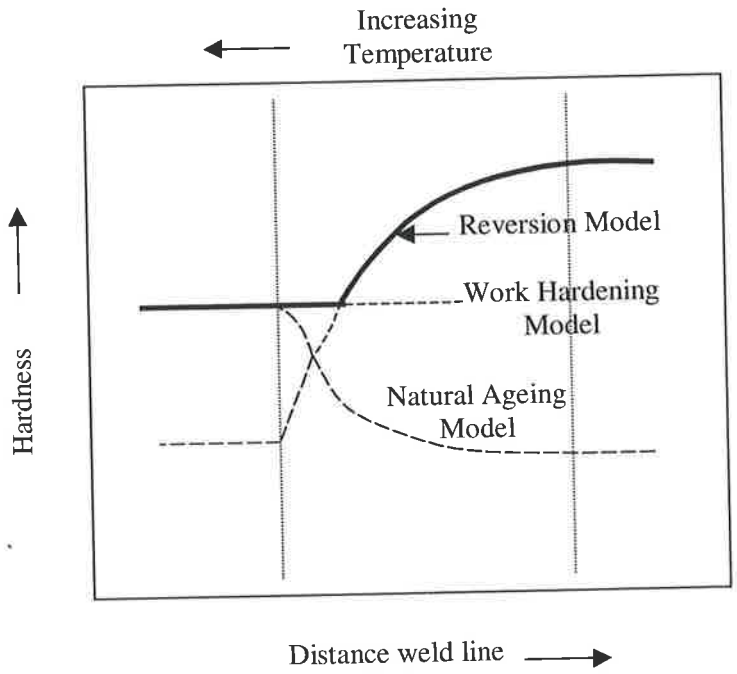

Figure 2-10 Coupling of Reversion and Natural Ageing

Note:

- Leonard [36] observed that welds in 7075-T651 did not reach full strength until 2 months of natural ageing after welding, while welds with 2014A-T651 alloy showed little variation from 5 days onwards. Therefore the ageing time required is very much material dependent.
- This theory explains the reason for the observed dip in hardness, which is observed at the edge of the HAZ in most FSW. See Leonard [36].
- One of the key advantages of FSW over traditional welding processes is that the maximum temperature achieved during welding is considerably less. From this discussion it can be seen that the lower temperature will result in

less of the precipitate dissolving into solution, resulting in a smaller drop-off in the observed strength.

- The above procedure is correct for a 6000 Series aluminium alloy. For a 2000 and 7000 series alloys slightly different equations are required and are demonstrated in Russell and Shercliff [4]and Frigaard et.al.[10].

Finally, it should be noted that the 5000 Series alloys derive their strength from solid solution hardening, and their properties are not affected to the same extent. See Reynolds [53] and Larsson et.al. [75].

2.1.8.4 Summary of Applications

Microstructure modelling appears to be the most successful application of thermal modelling to date. Predicting residual stress and distortion is not so important, because this is usually not an issue with FSW. Finally, predicting the conditions whereby a weld may be achieved is difficult because of the simplicity of the model and the complex changes in the material properties that occur at different welding temperatures.

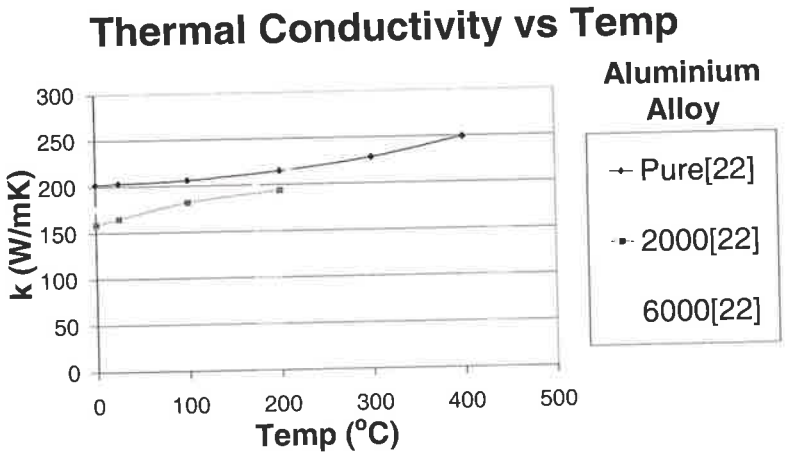

Figure 2-11 Thermal Conductivity of Aluminium Alloys from Holman [22]

2.2 Material Properties

This literature search has concentrated on the properties of aluminium alloys, as they tend to be the most common application of FSW. The literature search is by no means exhaustive, but should provide reasonable values for most of the key properties.

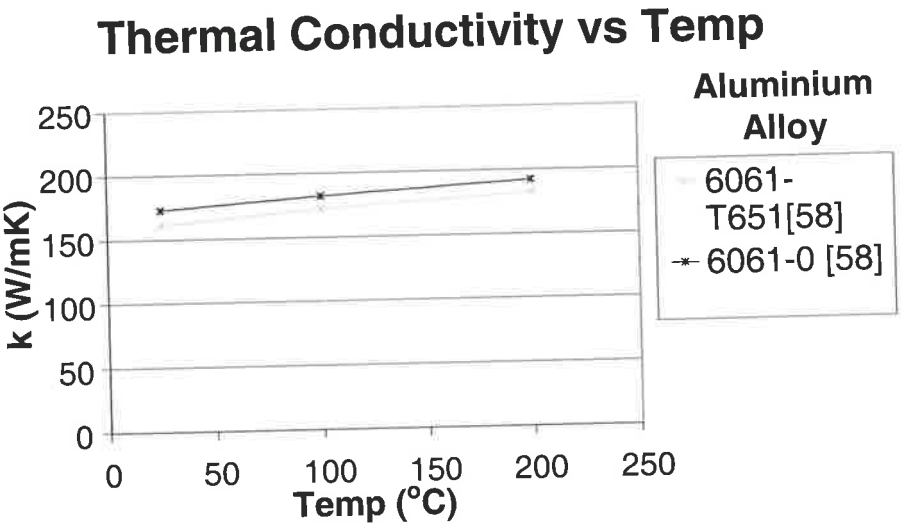

Figure 2-12 Thermal Conductivity of 6061 from Bogaard and Ho [58]

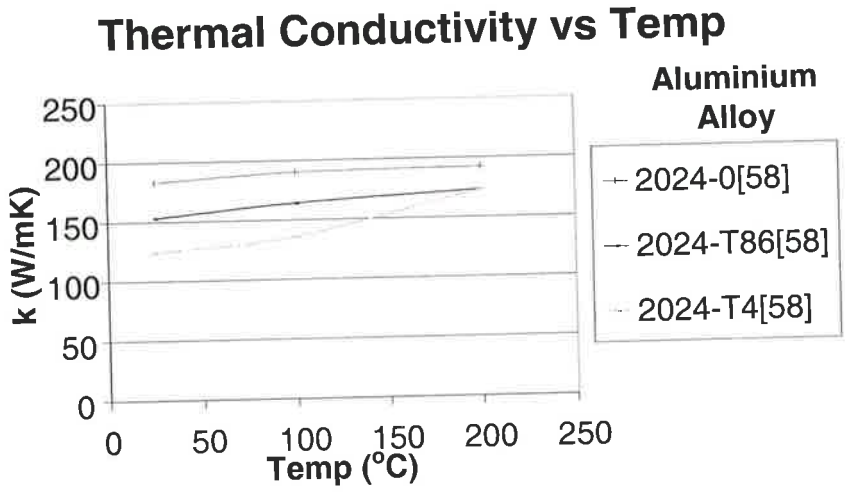

Figure 2-13 Thermal Conductivity of 2024 from Bogaard and Ho [58]

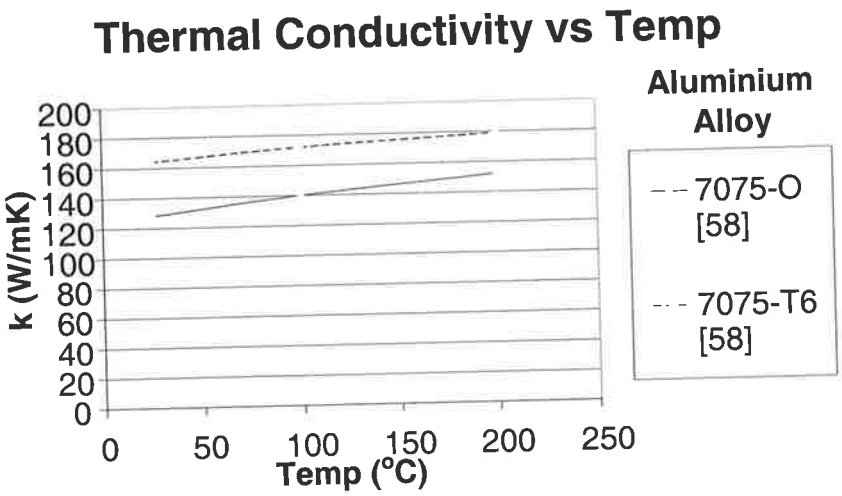

Figure 2-14 Thermal Conductivity of 7075 from Bogaard and Ho [58]

2.2.1 Thermal Conductivity

The main source of information on the thermal conductivity of aluminium alloys is the ASM handbook[59]. Unfortunately this source only quotes the thermal conductivities at room temperature. Therefore a factor is needed to take into account the temperature of the material.

Thermal conductivity is dependent not only on the type of aluminium alloy being considered, but the heat treatment to which this alloy has undergone. The effect of the heat treatment obviously diminishes at higher temperatures, where the material will anneal and the properties will tend toward the unheat treated state. In Holman [22], the thermal conductivities of various generic alloys are provided independent of heat treatment. See Figure 2-11. Bogaard and Ho [58] have provided a more in-depth analysis, which shows how the thermal conductivity varies with the initial heat

treatment. See Figure 2-12, Figure 2-13 and Figure 2-14. Finally the results in Bogaard and Ho also demonstrated that in most cases the thermal conductivity peaks at a temperature of around 200°C.

Because the thermal conductivity varies so little in the range of interest, an average value has been used which is independent of temperature. Even though the average temperature during welding is around 200°C. (See McClure et. al. [11]), it is believed that a good average temperature for calculating the thermal conductivity is 100°C, because the value at 200°C is usually a maximum. To find the conductivity at 100°C, the following ratio will be of interest:

$$\frac{k_{100}}{k_{25}}$$

where k_{100}, is the thermal conductivity at 100°C, and k_{25} is the thermal conductivity at 25°C. The values from the various sources are summarised in Table 2-2.

Table 2-2

Alloy	$\frac{k_{100}}{k_{25}}$	**Source**
Pure	1.01	[22]
2000	1.10	[22]
6000	1.06	[22]
6061-T651	1.07	[58]
6061-0	1.05	[58]
7039-T61	1.08	[58]

Alloy	$\frac{k_{100}}{k_{25}}$	Source
2024-0	1.04	[58]
2024-T86	1.07	[58]
2024-T4	1.10	[58]
7075-O	1.09	[58]
7075-T6	1.05	[58]

The average multiplier that is used throughout this work is 1.07. In any case the exact value is not critical to the overall result, as has been demonstrated in section 7.3.1.5.

2.2.2 Flow Strength of the Material/Viscosity

This data is one of the key inputs to any flow model and is also one of the most difficult to obtain. While stationary room temperature yield values are easily found, little data exists for the yield at high temperatures and strain rates. There is however a reasonable amount of literature published on general material characteristics and there is some data for pure aluminium.

2.2.2.1 Power Law Relationship

If temperature and work hardening effects in the material are ignored, the general form of the equation relating the yield strength to the strain rate is given by equation 5-1 in Hosford and Caddell [19]:

$$\sigma_y = C\bar{\dot{\varepsilon}}^m \qquad \textbf{Eq. 2-14}$$

where $\bar{\dot{\varepsilon}}$ is the effective strain rate defined by (Equation 6.227, Bathe [66]):

$$\bar{\dot{\varepsilon}} = \sqrt{\tfrac{2}{3}\dot{\varepsilon}\cdot\dot{\varepsilon}} \qquad \textbf{Eq. 2-15}$$

and $\dot{\varepsilon}$ is the strain rate tensor defined by:

$$\dot{\varepsilon} = \tfrac{1}{2}\left(v_{i,j} + v_{j,i}\right) \qquad \textbf{Eq. 2-16}$$

where v is the 3 dimensional flow velocity vector.

Often this is written in terms of an effective viscosity by: (NISA Manual p. 2.3-1 and 2.10-1 [67])

$$\tau_e = 2\mu\bar{\dot{\varepsilon}}$$

where:

$$\mu = \mu_0 \mathrm{I}^{m-1}$$

$$\mathrm{I} = \sqrt{3}\bar{\dot{\varepsilon}}$$

note that equating these two equations results in: (See Appendix A)

$$\mu_o = \frac{C}{2\sqrt{3}^{m-1}} \qquad \textbf{Eq. 2-18}$$

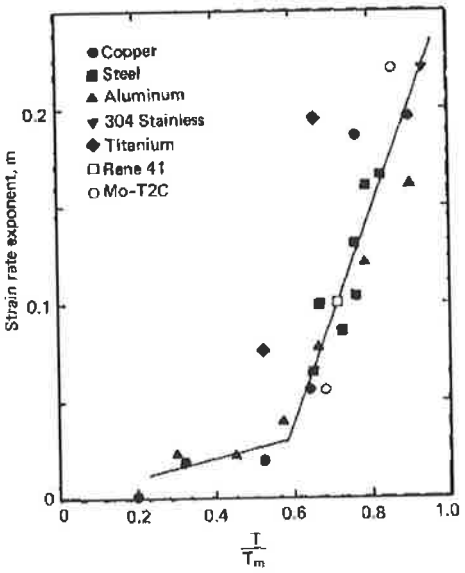

Figure 2-15 Value of the Strain Rate Exponent [19]

Hosford and Caddell [19] showed that for most materials, the value of m is dependent on the value of the temperature relative to the melting temperature. See Figure 2-15.

To get a feel for how the stress is related to the strain rate a graph of stress vs. strain rate is illustrated in Figure 2-16.

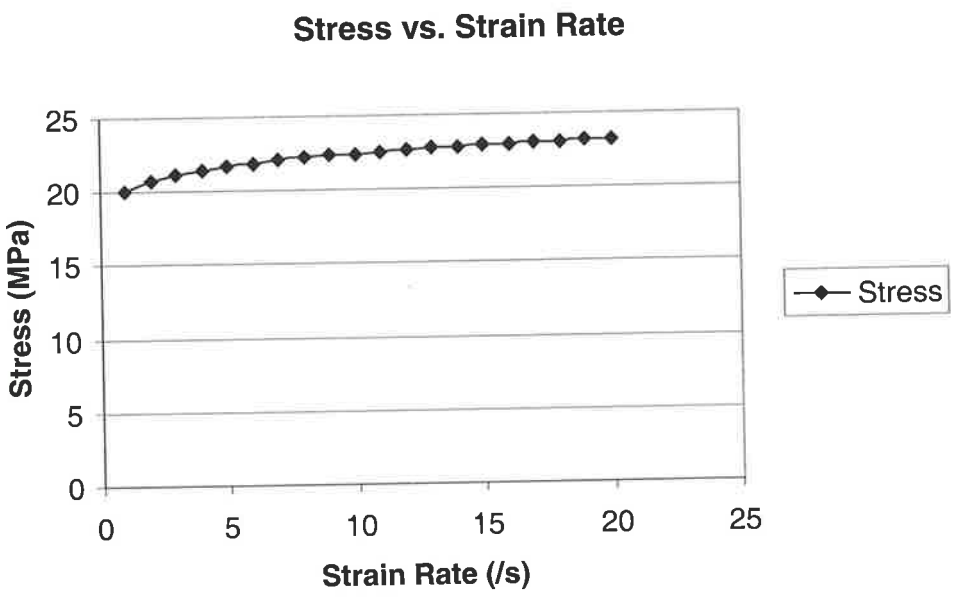

Figure 2-16 Stress vs. Strain Rate for C = 20 and m = 0.05 Power Law Relationship

Much of the modelling work that is done in this document has used 5083 aluminium alloy. Some data has been found on the FORGE2 Database [18] which is summarised in Table 2-3.

Table 2-3

Material	**Constitutive Relationship**
AlMg4.5Mn1.0 (5183)	$\sigma = 1660\varepsilon^{0.055}\exp(-0.00429T)\dot{\varepsilon}^{0.089}$
AlMg4.5	$\sigma = 2300\varepsilon^{0.055}\exp(-0.00429T)\dot{\varepsilon}^{0.089}$

The range of relevance for this data is:

$0.00<\varepsilon<0.45$

$1s^{-1} < \dot{\varepsilon} < 100s^{-1}$

$150 < T(^{o}C) < 600$

For 5083 which has a magnesium content between 4.0 and 4.9% the following relationship may be used:

$$\sigma = 2000\exp(-0.00429T)\dot{\varepsilon}^{0.089} \qquad \textbf{Eq. 2-19}$$

Note that as ε becomes large, $\varepsilon^{0.055}$ tends to 1.

There does however appear to be one glaring problem with this relationship. When a typical value of 370°C for the temperature are substituted:

$$\sigma = 409\dot{\varepsilon}^{0.089} \qquad \textbf{Eq. 2-20}$$

even if the units were to be changed to °K the value would be:

$$\sigma = 127\dot{\varepsilon}^{0.089} \qquad \textbf{Eq. 2-21}$$

Considering that the value of the yield strength of the material at this temperature (without strain-rate effects being included) is 29 MPa (Aluminium Handbook [59]), the above equation appears to be at least a factor of 10 out.

2.2.2.2 Sine-Hyperbolic Relationship

A more recent method for fitting stress vs. strain rate data is the sine-hyperbolic relation. This was used in the modelling work by Ulysse [17].

$$\sigma_e = \frac{1}{\alpha}\sinh^{-1}\left[\left(\frac{Z}{A}\right)^{\frac{1}{n}}\right] \qquad \textbf{Eq. 2-22}$$

where:

$Z = \dot{\varepsilon}\exp\left(\frac{Q}{RT}\right)$ = Zener-Holloman Parameter

α, Q, A, n are material constants.

R is the gas constant = 8.3213 J mol^{-1} K^{-1}.

T is the absolute temperature.

The value of these constants for pure aluminium from Sample and Lai[68] are:

α = 0.032238 MPa^{-1}.

n = 4.75.

$\ln(A) = 29.777 s^{-1}$

Q = 177244.3 $Jmol^{-1}$.

A plot of this curve at a temperature of 500°C is shown in Figure 2-17, which has much

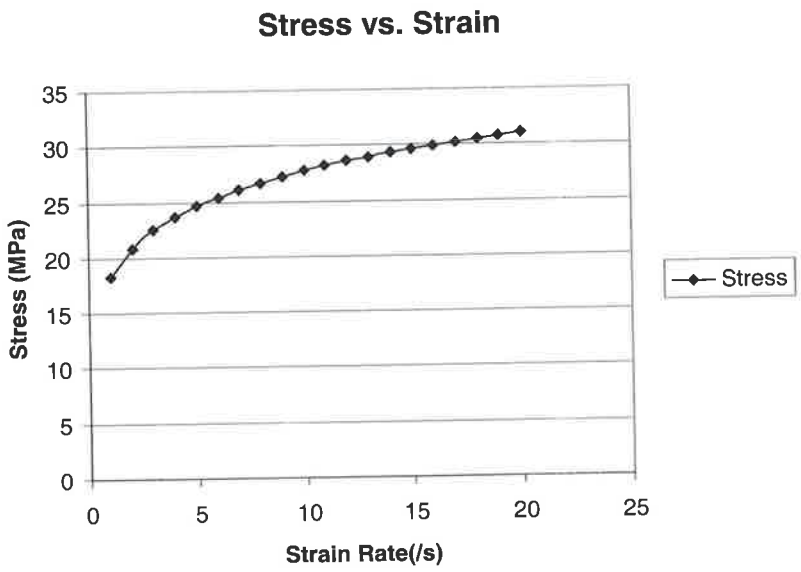

Figure 2-17 Stress vs. Strain Rate for Pure Aluminium for Sine-hyperbolic relationship.

the same form as the power law relationship.

2.2.2.3 Heuristic Model

In the friction welding work by Bendzsak and North [29,32], the material is modelled at an isothermal temperature with a heuristic material model being used.

$$\mu_a = \mu_o \exp(-B\tau_{r\theta})$$
$$\tau_{r\theta} = \mu_a \frac{dV_\theta}{dz} = 2\mu_a \dot{\varepsilon} \qquad \textbf{Eq. 2-23}$$

A graph of the resulting stress vs. strain rate curve is shown in for an aluminium base MMC-MMC material at 540°C is shown in Figure 2-18.

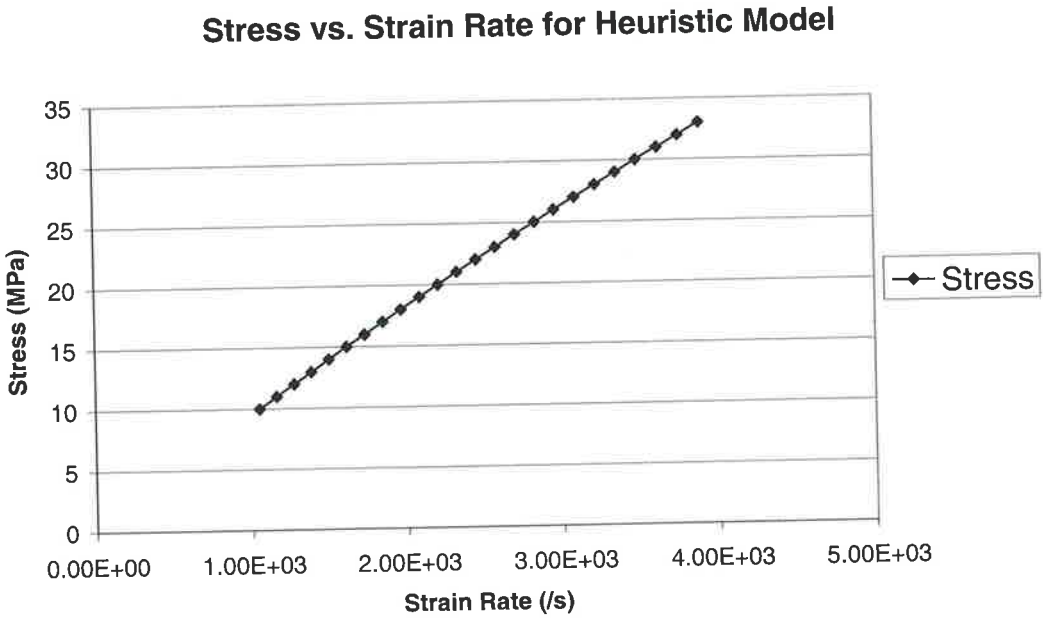

Figure 2-18 Stress vs. Strain Rate Curve for Aluminium Base MMC-MMC for the Heuristic Model Equation from Bendzsak and North [32].

Although the graph appears to give a reasonably linear relationship, the viscosity still reduces with increasing strain-rate. This reduction is obviously not as significant as that observed for the power law and sin-hyperbolic models in the previous sections.

2.2.2.4 Summary

From the above models it does not seem to really matter which model is used provided the data is accurate for the region of interest.

2.2.3 Methods for Determining the Flow Strength of the Material/Viscosity

2.2.3.1 Rotating Pin Plunge Tests

This method was used to find the effective material viscosity for FSW, and was proposed by North et. al. [28] and Smith et.al. [82]. In these papers, a technique was described where a rotating steel pin was inserted into a stationary aluminium plate and the required torque measured. The output from this experiment was used to find the effective viscosity of the material. The equipment used is described in Figure 2-19.

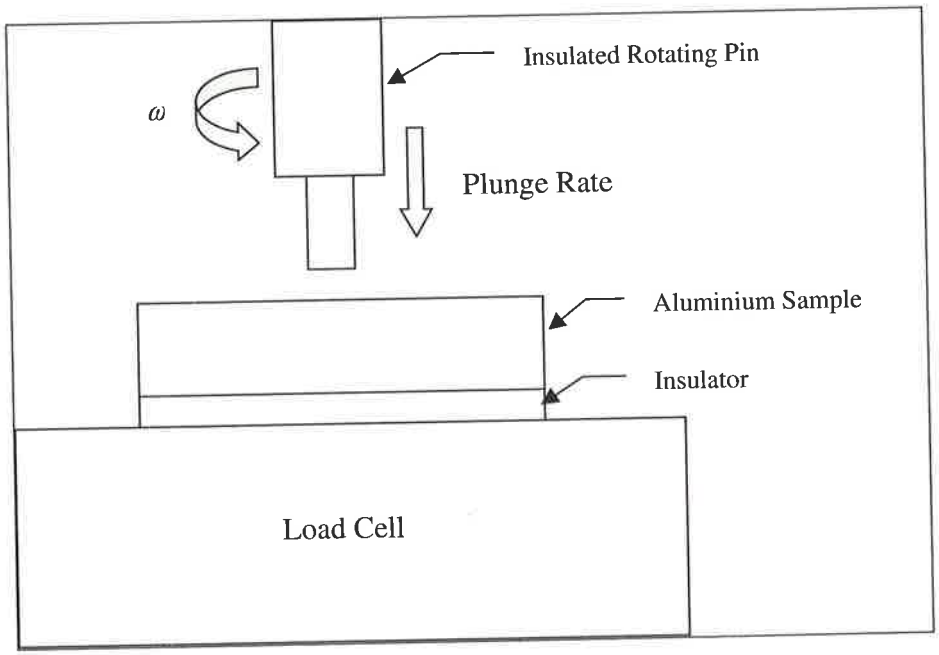

Figure 2-19 Experimental Set-up of North et. al. [28], Smith et. al. [82]

The main findings from this work were:

- The effective viscosity of the material reduced with increased angular speed as expected from all the previously described material models.
- The peak material temperature during this exercise was found to be the solidus temperature of the material being investigated. This could not be measured from thermocouples in the aluminium material since the material deformation tends to push them away from the interface. This data was obtained from thermocouple 0.2mm from the surface of the pin.
- North et. al. [28] drew a clear distinction between the plasticised or third body region and the undeformed bulk material. This region is analogous to the fully plasticised region in friction welding. See section 2.4.1. The size of this region was given by the following relationship:

$$\xi = \frac{\mu\beta\alpha\omega^2 R^2}{V_{weld} k(T_s - T_o)} \qquad \textbf{Eq. 2-24}$$

which was derived from an analytical solution to the heat conduction equation. The width of the deformation zone is defined as the minimum size required to enable the surface temperature of the tool to equal the solidus temperature. In Bendzsak and North [29,32] a similar approach was used to determine the size of the fully plasticised region for friction welding.

Some important things to note from these results are:

- A simple numerical model was used to confirm the heating values calculated from the calculated viscosity. The results correlated well.
- During this experiment there are in fact two shearing surfaces, one on the bottom of the pin and the other on its sides. As you go deeper and deeper downwards, the shearing surface around the cylinder will dominate. The

effect of the bottom shear surface has not been included in this analysis. (North[69])

- The viscosity found is an average one. Firstly there will be a temperature gradient across the deformed region. Secondly, it will include any slip which occurs at the material/tool interface.

While several assumptions have been made in the calculation of the effective viscosity, it is unclear whether this will effect the desired output. Therefore, the model needs to be validated. This is described in section 2.6.

2.2.3.2 Tension/Compression Testing

The traditional method for finding the stress vs. strain rate relationship is with a laboratory tension or compression test. The two methods for achieving this data are found in Hosford and Caddell [19] and are illustrated in Figure 2-20.

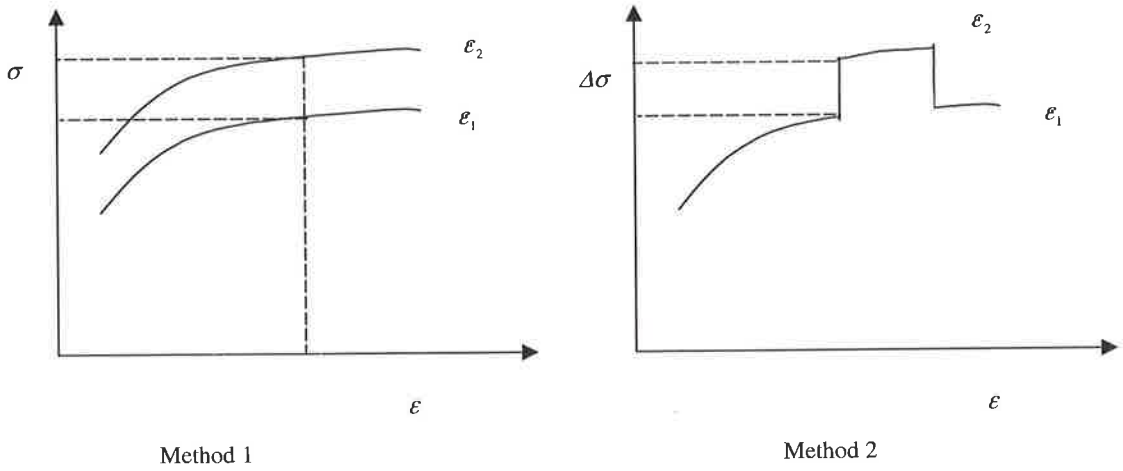

Figure 2-20 Flow Strength Determination by tension/compression testing

Obviously the graph is also strain dependent to a certain extent, however where the strain becomes large this effect flattens out. Seetharaman et. al. [70] published some

data for 7050 aluminium alloy, however the data was obtained for strain rates between 10^{-2} and 10^{-5}/s, which are not applicable to FSW. See section 3.4.9.

2.2.3.3 Summary of the Two Approaches

While the rotating pin test is obviously the easier of the two to perform, tests done by the compression/tension test approach will provide a better result, because the data is at a uniform temperature and will not include any slip which may occur at the interface. Finally, another method that could be investigated is hot torsion testing.

2.3 General Comments About Friction

One of the critical aspects to modelling FSW is understanding the interface between the two materials, namely steel and aluminium. Section 3.2.3 discusses the interface in FSW, while section 2.4.1 investigates the surface conditions that occur in friction welding. Before going into the details it is worth getting some background information on the coefficient of friction.

Under ideal conditions, the coefficient of friction μ is related to the normal force, N and the friction force F_r with the following relationship:

$$\mu = \frac{F_r}{N} \qquad \textbf{Eq. 2-25}$$

which is the well-known relationship for columbic friction. However this relationship usually only holds for low temperatures and pressures which are obviously not experienced in FSW.

The basic theory of solid friction states that there is never complete contact between two surfaces. This is because the surface is never perfectly smooth, but has asperities,

which protrude from the surface. Therefore the friction force is a result of the interaction between the asperities on the two surfaces. For a room temperature material the resulting coefficient of friction is a combination of: (See Larsen-Base[64])

$$\mu = \mu_{asp} + \mu_{plow} + \mu_{part} \qquad \textbf{Eq. 2-26}$$

where:

- μ_{asp} is the contribution from asperity deformation
- μ_{plow} is the contribution from the asperities on the harder material plowing through the softer material.
- μ_{part} is the contribution from the wear particles between the two surfaces.

In a paper on friction welding by Vill [60] a total of 9 factors were identified as effecting the coefficient of friction. Of these 9 factors a total of 5 seemed applicable to friction welding and therefore friction stir welding. These are:

1. Relative speed of motion of the friction surfaces.

   This is an interesting effect. Vill claimed that under some conditions the coefficient of friction increased with the slip velocity, while for others it decreased with slip velocity. The effect is dependent on such factors as the hardness of the two surfaces and the pressure.

2. The temperature of the friction surfaces.

   The temperature usually results in a reduction of the materials yield strength, therefore from the description of μ in Eq. 2-26, μ_{plow} is likely to be lower resulting in a reduced value of the μ. If the temperature is large enough surface melting can occur which produces a liquid layer at the surface which acts as a lubricant. This is discussed in greater detail in section 3.2.3.

3. The nature of the material and presence of surface films.
4. Magnitude of the normal pressure force.

   When the pressure becomes large the asperities on the surface flatten out, so that eventually there is complete contact between the two surfaces. In this case the coefficient of friction is the ratio of the shear strength to the normal yield stress in the material.

$$\mu = \frac{F}{N} = \frac{\tau}{\sigma} \qquad \textbf{Eq. 2-27}$$

   A plot of the normal force vs. the friction force for surfaces at a uniform temperature is shown in Figure 2-21 from Avitzur[65].

5. The rigidity and elasticity of the friction surfaces.

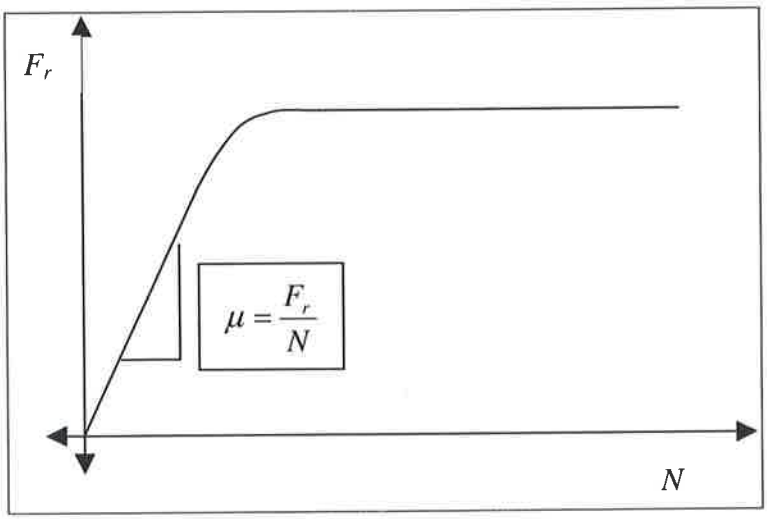

Figure 2-21 Friction force vs. normal force or surface pressure

Finally, Vill identified the state of pure friction, which occurs where two surfaces without absorbed films, or chemical compounds are brought into contact under high pressure. The result is the surfaces seize together. This kind of surface condition can be

formed under considerable plastic deformation where the brittle films are destroyed exposing the pure metal. It is this effect which enables friction welding and FSW to occur.

The different fiction scenarios are summarised in Friction-Heating Maps, a concept that was introduced by Kong and Ashby[30]. The generalised form of these maps, and the different boundary conditions that can occur is shown in Figure 2-22. The map shows a generalised plot of the regions that occur for various combinations of normal force (pressure) between the interfaces and slip velocity. It does not give any indication of

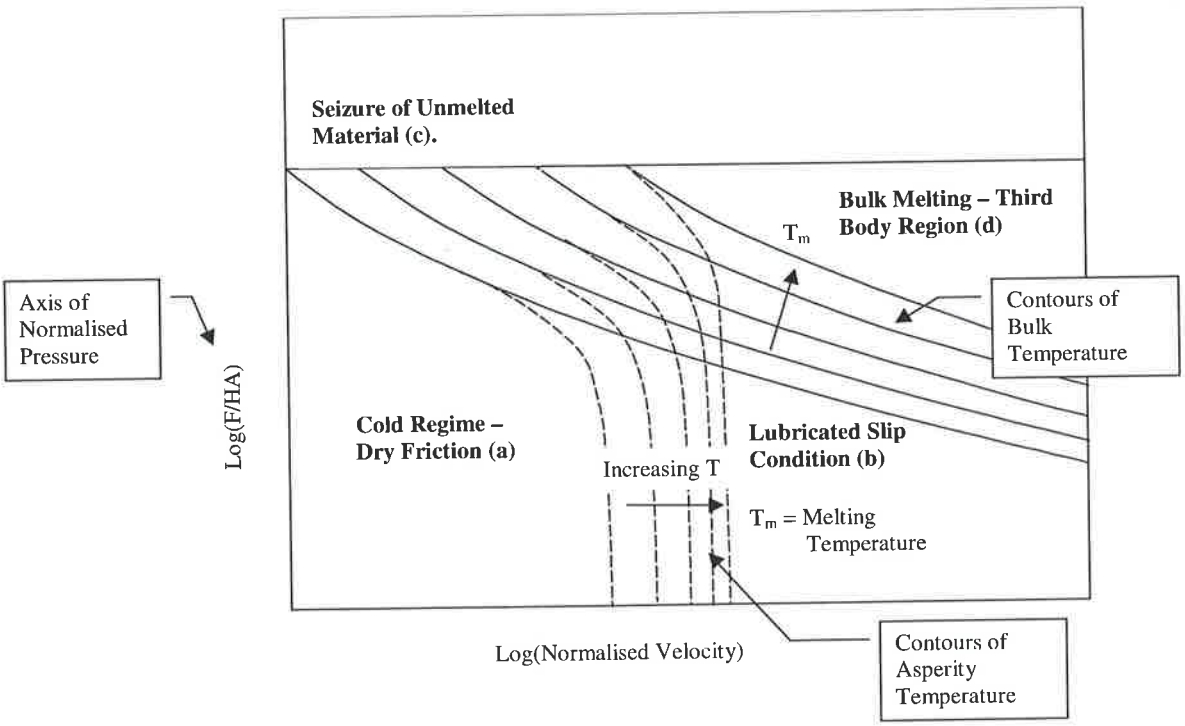

Figure 2-22 Friction Map Showing the Various Boundary Scenarios

the friction force. The map shows the region where it is possible to get asperity melting of the material at the surface, while the temperature of the bulk material can in fact remain quite cold.

Therefore obtaining a relationship to predict the coefficient of friction under all circumstances is a very difficult task.

2.4 Friction Welding

2.4.1 Process Characteristics

A good overview of friction welding process is provided in Vill [60]. A few interesting

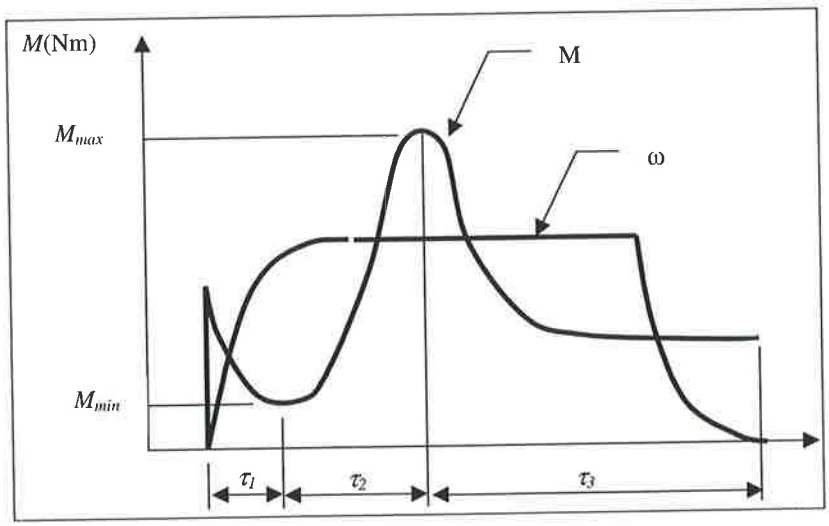

Figure 2-23 Typical curve of moment and speed variation during welding

results from this work are discussed below. Please note that Vill's work was for welding carbon steel to carbon steel:

1. The torque required to perform this process is far from being constant and exhibits the standard curve shown in Figure 2-23. There are three distinct periods. In the first stage τ_1, there is dry sliding contact between the two materials. The coefficient of friction (and torque) drops from the initial value of static friction (0.25) down to that for sliding contact (0.12). In the second stage the coefficient of friction rises as the contact changes from dry

friction to pure friction. ie. The surface oxides are swept away allowing perfect contact of the two metal surfaces resulting in seizure. This process is not instantaneous, but gradual. Centres of unit seizure are formed and are subsequently destroyed. This process tends to be unsteady resulting in an oscillation of the torque curve (not shown in Figure 2-23). The number of seizures gradually increases as more and more of the surface oxide is removed from the surface. Finally, in the last stage there is a reduction in observed torque due to:

- A reduction of the material strength.
- Liquid metal forming at the surface and acting as a lubricant.

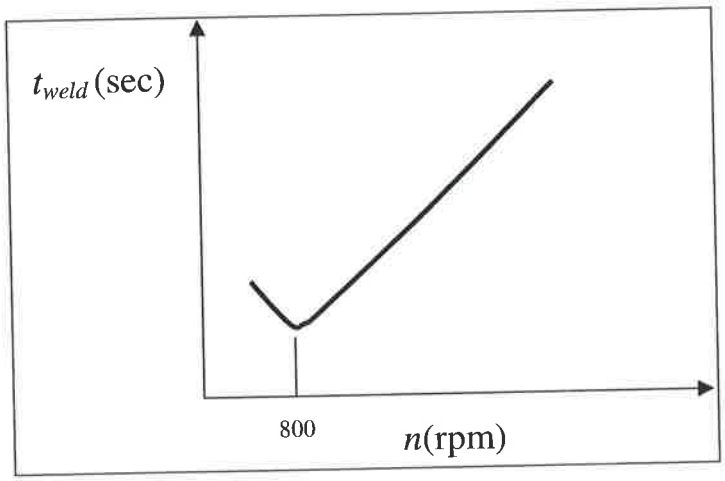

Figure 2-24 Variation of welding time on rotational

This results in a decrease in the observed torque to some stationary level.

2. Initially, one would expect that the heat liberated, while not necessarily being linearly dependent on the rotational speed would none the less show a gradual increase. This is not actually the case as is demonstrated by Figure 2-24, which shows the time to make a weld as a function of the rotational speed. The time reduces with increasing speed initially and then increases

from 800 rpm onwards. Vill proposed that the duration of the first two stages of the process were inversely proportional to the rotational speed, while the duration of the final phase was directly proportional to the rotational speed. Vill explained this characteristic by claiming that the apparent coefficient of friction is inversely proportional to the square of the rotational speed during the final stage. The duration of the weld was minimised when the sum of the three stages was minimised. Since FSW, is essentially friction welding operating at the second or third stage then these results suggest that the heat liberated may in fact increase with reduced rotational speed. Midling et. al. [43] found that the heat input for a FSW was almost independent of the rotational speed. A similar result was found by Reynolds and Lockwood [53]. This discrepancy may be attributed to the fact that steel on steel is being welded instead of steel to aluminium.

2.4.2 Regions in the Friction Welding Microstructure

Midling and Grong [48] identified 4 distinct regions in the weld microstructure of an

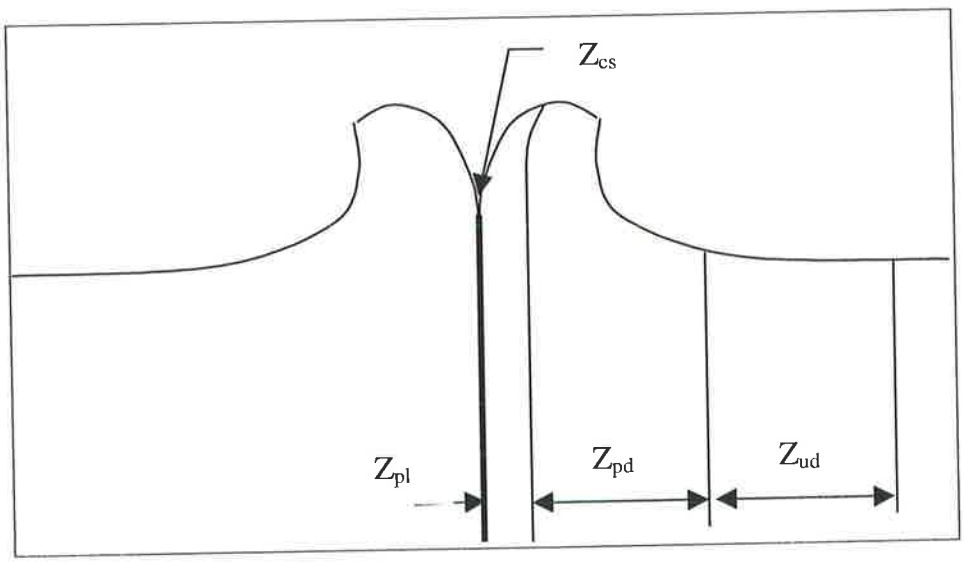

Figure 2-25 Regions in a friction weld

aluminium friction weld which are illustrated in Figure 2-25.

These are similar to the regions observed in a friction stir weld. See section 3.4.1. Briefly:

- The contact section. (Z_{cs}) Exhibits thixotropic behaviour due to eutectic melting at the surface. This may occur FSW, however its presence has not yet been observed in microstructures. See section 3.3.
- Fully plasticised region (Z_{pl}). High deformation occurs and temperature is sufficient for dynamic recrystallisation to occur. This is analogous to the dynamically recrystallised zone in the FSW.
- Partly deformed region (Z_{pd}). The degree of plastic deformation is controlled by the rates of axial and radial upsetting. This region does not exhibit dynamic recrystallisation or recovery. This region is analogous to the thermo-mechanically effected zone in FSW.
- Undeformed region (Z_{ud}). This exhibits reversion and reprecipitation as well as over-aging of constituent particles and is analogous to the heat-affected zone in FSW.

In the modelling paper by Bendzsak and North [32], only the fully plasticised region and partly deformed region are identified.

Finally some clear differences between friction welding and FSW should be noted:

- Obviously friction welding can only be applied to cylindrical parts and the entire joint is done in a single step. FSW is primarily used for butt joints and takes place gradually.
- In friction welding a large amount of flash is extruded from the plasticised region in making the joint. In friction stir welding most if not all of the original material becomes part of the resulting joint, except for a small amount of flash deposited on the top surface.
- In friction stir welding the bulk of the process is carried out under steady state or near steady state conditions. Friction welding on the other hand is largely transient in nature.

2.4.3 Modelling Friction Welding

While being far from an exhaustive investigation, a brief summary of the key papers is shown in the following sections.

2.4.3.1 Moal and Massoni [31]

This paper investigated the inertia welding of friction welded parts. The work shows an extensive description of the equations used including the finite element method used to solve the problem. Adaptive remeshing was required to take into account extrusion of material from the joint.

2.4.3.2 Bendzsak and North [29,32]

The finite volume method was used to predict the flow field found in the fully plasticised region only, and not the partly deformed region. A standard friction weld between two aluminium alloys was analysed [29,32] and one done between different

materials [32]. In the first paper [29] the problem was assumed to be isothermal, while the second [32] included temperature variation for the model of the dissimilar materials. In the first case, a heuristic viscosity relationship was used. See section 2.2.2.3. In the second paper, the weld between different materials demonstrated the concept of viscosity hysteresis which is discussed in section 3.5. The analysis did not taken into account the very thin molten layer which occurs at the interface. (See Midling and Grong [48]).

In the first paper [29] a first estimate of the flow was gained by solving the potential flow field. The full Navier-Stokes equations were then used to do the full analysis with the convective terms neglected [32] because of the very low Reynolds number involved. Additionally, the time dependent terms were also ignored [29]. A similar technique has been used in section 10.4 which describes how the flow equations can be set up for FSW.

2.4.3.3 Nguyen TC, Weckman DC [61]

Transient thermal modelling of friction welding was carried out, and used to predict the microstructure of 1045 steel. Measured power data was used to calculate the heat input for the model and a constant temperature boundary condition at the welding interface was invoked. This is discussed in section 2.1.3. Axial displacement was included in the model

2.4.3.4 Midling and Grong [48, 62]

In the first paper [48], analytical thermal modelling was used to predict the microstructure of aluminium alloys. No axial displacement was included in the model. Heat input was assumed to be constant and was based on the shear strength of the

material. Four main areas were identified in the weld which have been described previously in section 2.4.2. The existence eutectic melting at the interface was demonstrated. Finally, predictions of the strain rate were predicted from an analytical model.

In the second paper [62], evolution of the microstructure was predicted for both 6082 and one that was a composite Al-SiC. The technique used is described in section 2.1.8.3. Finally, the Zener-Holloman parameter was used to predict the maximum strain rate in a similar way to that described in section 3.4.9.

2.4.3.5 Mitelea and Radu [46]

Demonstrated thermal modelling of friction welding dissimilar materials. The paper demonstrated the use of different heat distributions which are discussed in section 2.1.3.

2.4.3.6 Comment on the Flow Modelling

One final comment should be made. Neither the flow modelling work by Midling and Grong [48, 62] or Bendzsak and North [29,32], modelled the contact section separately to the plasticised region. This is a little surprising considering the greatly reduced viscosity that is likely to occur in this region.

2.5 Description of the Flow

Before proceeding to investigate the flow models it is necessary to examine how exactly the material flows around the pin. This aspect of the work is covered later in section 3, because it includes both a review of current literature and experimental/modelling results.

2.6 Flow Modelling of Friction Stir Welding

Only 3 key papers have been published on the flow modelling of FSW. Their main features are summarised in the following sections

2.6.1 Dong et. al.[16]

This was the first paper to be published on the flow aspects of FSW. The model included heat generation at the surface due to slip and heat generation due to material deformation. The material deformation found in this modelling work was similar to that predicted by the single slip surface model. See section 3.2.2. It was found that friction based heating was more dominant in the upper part of the weld, while plastic work is more dominant toward the bottom. Tool threads were not included in the model.

2.6.2 Bendzsak et. al. [71]

This paper needs to be read in conjunction with the paper by North et. al. [28] describing how the material properties for FSW may be found. Because of the difficulty in predicting a value of the coefficient of friction, an alternative approach assumed that the material by and large sticks to the surface of the tool in a so called 'third body' region adjacent to the tool. This was based on the assumption that FSW essentially operates as friction welding in the 'third' stage. See section 2.4. Therefore, the process is modelled entirely as a fluid, so calculating the coefficient of friction is no longer necessary and the only material property required is the flow strength of the material/viscosity. While this modelling approach is obviously considerably simpler, there are some problems, which are discussed in greater detail in section 3.

The preliminary work modelled the material at a constant temperature with the viscosity being constant. The finite volume method was used to generate the solution.

The threads of the tool were included in the mesh, which enabled the complex flow around the rotating tool to be visualised. The mesh was divided into separate sub-regions, each having their own mesh. The regions near the tool surface obviously have a much finer mesh to allow an accurate prediction of the high material deformation. The preliminary model used 41 such sub-domains.

The above sub-domains are further divided into 2 separate inter-linked parts. They were:

- An Inclined Sliding Grid System.

  This included the tool threads and rotated with the rotating tool. This grid system was bounded by a tilted cylinder to simulate the effect of the inclined tool. Because the tool rotates, the mesh deforms with the rotation of the tool to take into account the inclination of the tool to the workpiece.

- A Fixed Frame Geometry.

  This was used for modelling the outer plate. Its frame of reference was the workpiece material.

Despite the simplifications made in the modelling approach, a good first estimate for the flow around the tool seemed to be gained from the model. Extrusion of the material around the pin was predicted lower down in the weld, while the material near the top surface obviously rotated with the tool. There was a transition region between these

two flow regimes. Various vortices are observed on the advancing side of the flow, which are consistent with observed microstructures and flaws that can occur in real welds. Finally, tracers were used in the model to help visualise the flow.

2.6.3 Ulysse [17]

This paper included both flow and thermal modelling of the FSW process and solved the problem using the FIDAP finite element solver. The basic equations governing the problem were presented and are discussed later in section 10.4.

The main features of the numerical model were:

- The backing plate has not been included in the finite element solution. To compensate for this an oversized plate thickness was used.
- The model was solved in steady state, with the tool being stationary and the material moving past it.
- The thread was not included in the model. Therefore the downward flow of material had to be simulated by specifying a downward flow of material against the pin.
- The sine-hyperbolic relationship was used to define the material properties which are discussed in section 2.2.2.2. A temperature dependent value of the thermal conductivity was also used. Since the author was an employee of Alcoa a major producer of aluminium, these material properties were likely to be more readily available.
- Some slip of material against the tool and the thread was included in the model, however no details were provided to describe how this was implemented.

- A gap is included in the model to simulate the two plates being separate prior to the material being welded. It is unclear why this is necessary.

The main output of the initial work was a prediction of the thermal history in the material. This was validated against experimental data. Generally the measured temperatures were considerably lower than the eutectic. The position of the thermocouples was not specified.

Predictions of forces on the tool and some limited particle tracking was also included from the flow modelling work. While the force measurements had not been experimentally validated they may be compared against the values found by Johnson and Horrex [63]. Please note that shear force used by Ulysse will be considered analogous to the tool torque used by Johnson and Horrex. Secondly, a comparison of the exact values will not be made because of the different materials and welding conditions used:

- Increasing the welding speed increased the value of the horizontal forces. While experimental evidence suggested that this was the case when increasing from low traverse speeds, at high speeds this was not the case. In fact it was more dependent on the rotational speed.
- In the modelling work the horizontal forces at lower rotational speed were lower. This contradicted the experimental results for 6082 aluminium.
- Modelling results indicated that the forces in the y direction are significantly greater than in the x. Experimental results indicated that they were approximately the same.

- When changing the translational velocity, only a small change was observed in the shear force on the material. Experimental results showed that this would be a reasonable result for 6082, however not 5083 where it is believed that significant material softening may occur at the surface. In this case torque increases quite significantly at higher travel speeds.
- Changing the translational speed increased the downward force on the pin. This is consistent with experimental observations.
- Increasing the rotational speed reduces both axial and shear forces. Experimental evidence suggested that while the shear force (or torque) may reduce for 5083, this was not the case for 6082. Finally the experimental evidence suggested that axial force increases with increased rotational speed for both materials.

This comparison gives some indication of the complexity of accurately modelling the FSW process for all welding conditions.

2.6.4 AeroMat 2000 Conference

Several papers were presented at the AeroMat 2000 Conference in Seattle, however only a brief abstract was provided in each case. Various methods of modelling the process have been investigated with not all examining the flow around the tool. A summary of the key papers are:

- Arbegast [78].

  A model has been developed which describes the process in terms of the preheat, initial deformation, extrusion, forging and post heat treat processing

zone. The model has examined the effect of process parameters and pin geometry.

- Lockwood WD, Reynolds AP [80].

  Strain measurements on welded samples were used to calibrate FEM models. The examination included the differentiation between tensile and compressive behaviour. The Bausinger effect was used to determine the level of residual stress in the weld. From this model the effect of weld parameters on the process has been determined. It is unclear from the abstract why the tensile and compressive behaviour in the weld is relevant. Modelling would suggest that the deformation around the tool is primarily via shear.

- Jones and Arbegast [79].

  A rather novel modelling approach has been used where a neural network model is used to predict the effect pin tool design, welding speed and rotational speed on the weld macrostructure defect formation and strength.

2.7 Applications

While applications of the technology have not been a major focus of the research effort, a few are worthy of mention to demonstrate the technology's value. These applications are found in Threadgill [45]:

- NASA/Lockeed Martin. Space shuttle external fuel tank.
- Boeing, Delta rocket fuel tanks, undercarriage doors, and cargo floor.
- Marine Aluminium, Norway. Various extrusions on ships.
- SAPA. Extrusions.

Another recent application is a machine produced by Crawford-Swift [47] for the in the welding of aircraft wings. This work is still only experimental.

This does not included the many applications which are currently under development. While obviously being far from a complete listing of all the process applications, it does give the reader a feel for some of the uses of the technology.

3 Theory for the Metal Flow

3.1 Introduction

It is ironic that one of the greatest topics of discussion in the field of FSW is 'How does the process work?' One knows that it is possible to get a good weld using a certain tool with certain operating parameters, but what are the mechanisms whereby the weld is produced? Also, why does one tool seemingly give better results than another, and some operating parameters work while others do not?

In an effort to answer some of these questions researchers have applied themselves to two tasks, namely:

(a) Visualising the flow around the FSW Tool.

(b) Modelling the process.

The two tasks are very much interrelated. One cannot produce a valid model unless they first have a good grasp of how the material flows around the tool and the boundary conditions that are likely to exist. Secondly modelling the process will allow one to see how the material has deformed to produce a certain weld and will hopefully give greater detail of the flow patterns that occur. Models almost inevitably contain physical parameters which have some degree of uncertainty. Therefore the model predictions must be validated.

This section proposes various flow models and then analyses flow visualisation and experimental data to assess their validity. The intention is to provide a map of the approach necessary to produce a valid Friction Stir Welding flow model.

3.2 Background and Flow Models

3.2.1 Terminology

Before starting, a brief comment needs to be made about the terminology convention used in this paper. The terminology conventions are shown in Figure 1-1.

3.2.2 Early Ideas

Nunes et. al.[15] and Stewart et. al. [69] have discussed the various process models for describing the flow around the pin during Friction Stir Welding. Three possible process models were suggested, namely:

1. Slip Model.

   The friction at the interface between the tool and the workpiece material generates the heat. The softened material flows around the pin and bonds on the trailing side due to the high temperatures and pressures. The process is similar to the process of extrusion and it appears that the predominant boundary condition is one of slip.

2. Fluid Model or Mixed Zone Model.

   In this model the principal region of slip is not the interface between the tool and the material, but rather within the material itself. ie. The metal acts like a fluid so there will be zero relative velocity between the tool and the workpiece material. Therefore, the metal in the plastic zone flows in a vortex pattern.

3. Single Slip Surface Model.

   A nugget of essentially stationary material is formed around the tool with all the deformation and therefore heating occurring on a slip plane between the tip of the pin and the edge of the shoulder. See Figure 3-1. As the pin moves through the workpiece material, the material is picked up from the front face and pulled around and deposited on the reverse side. Continuity requires that the slip zone be asymmetric in shape around the *y*-axis. ie. It will be wider on the retreating side to enable the material to be swept from the front to the back.

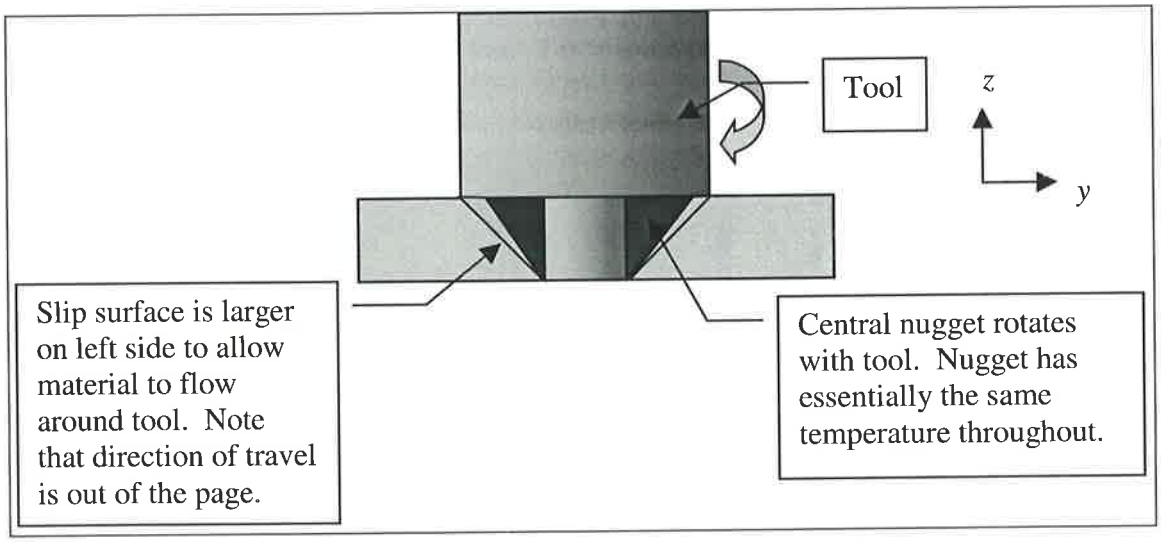

Figure 3-1 Single Slip Surface Model

Although some preliminary modelling work by Dong et. al. [16] indicated that this model was indeed valid, later experimental work by Colligan [26,27] (see section 3.4.4) and Reynolds[24,25] (see section 3.4.3) has largely discounted this as a valid process model. Therefore, for the sake of conciseness this model will only rate a brief mention in the subsequent work, with the emphasis being on the first two approaches and variants thereof.

3.2.3 Expanded Slip Theory

The difference between the slip and non-slip models basically comes down to the boundary condition that exists between the rotating tool and workpiece material. In an effort to more fully explain the flow that occurs in FSW the slip theory must be developed further. This section describes the basic concepts behind this theory.

3.2.3.1 The Possible Boundary Conditions

The boundary conditions that may occur between the steel and the aluminium are:

(a) The Dry Slip Boundary Condition.

This occurs where both the bulk material and the asperities at the surface are below the solidus temperature of the workpiece material. In this case one would expect there to be some correlation between the interface pressure and the friction force between the workpiece material and the tool. This may be described by the following equation:

$$\boldsymbol{\sigma}\cdot\boldsymbol{n}\cdot\frac{\boldsymbol{v}}{|\boldsymbol{v}|}=f(\boldsymbol{\sigma}\cdot\boldsymbol{n}\cdot\boldsymbol{n},T,\Delta v_s) \qquad \textbf{Eq. 3-1}$$

where:

$f(\boldsymbol{\sigma}\cdot\boldsymbol{n}\cdot\boldsymbol{n},T,\Delta v_s)$ is the function for the shear stress that can be supplied at the surface, $\boldsymbol{\sigma}\cdot\boldsymbol{n}\cdot\boldsymbol{n}$ is the pressure or shear stress normal to the surface, T is the temperature of the material and Δv_s is the slip velocity at the interface.

$\boldsymbol{\sigma}\cdot\boldsymbol{n}\cdot\frac{\boldsymbol{v}}{|\boldsymbol{v}|}$ is the shear stress normal to the surface.

(b) Lubricated Slip Condition.

There is obviously a limit to the amount of heat that can be applied to the material by method (a) before the temperature reaches the solidus temperature of the workpiece material and localised melting occurs. However it is important to note that the melting is limited to a very thin layer of workpiece material at the interface, so that the bulk material behind the surface is considerably cooler. This produces a lubricated film on the surface of the metal, which sticks to either surface and where intense shearing occurs. Depending on the thickness of this layer, there may also be some interaction between the asperities on either surface. A drastic reduction in the friction force from that observed in (a) is observed.

(c) Seizure.

If the friction force that can be supplied at the interface is such that:

$$\boldsymbol{\sigma}\cdot\boldsymbol{n}\cdot\frac{\boldsymbol{v}}{|\boldsymbol{v}|} < f(\boldsymbol{\sigma}\cdot\boldsymbol{n}\cdot\boldsymbol{n},T,0) \qquad \textbf{Eq. 3-2}$$

Sticking of the workpiece material to the tool will occur, so that the boundary condition at the interface is:

$$\boldsymbol{v} = \boldsymbol{v}_t \qquad \textbf{Eq. 3-3}$$

where $\boldsymbol{v}_t$ is the velocity of the tool. This of course is the standard definition of the boundary condition that is likely to occur in a typical fluid (no-slip) model.

These different scenarios are summarised in friction-Heating Maps, a concept that was introduced by Kong and Ashby[30] and is discussed in section 2.3.

Therefore it would appear that there are various boundary scenarios that may occur during friction stir welding. The reality may be that for a given weld a combination of the above scenarios may in fact occur. For example:

(a) Bottom of the Pin.

As demonstrated in section 4.2, the temperature around the bottom of the weld is much cooler than that around the top surface. The slip velocity is fairly low and the pressure is likely to be high due to the screwing action of the tool threads. Therefore, the temperature of the bulk material remains below the melting temperature, so that either seizure of the bulk material or dry slip between the interfaces is likely to occur.

(b) Periphery of Shoulder.

Around the periphery of the shoulder the slip velocity is high, however there is a large region of relatively cool material and heat diffusion will be high. Therefore, it is possible in some circumstances for the lubricated slip condition to exist.

The temperature and conditions that exist in a given region will of course be dependent on the welding parameters, material and the tool design used for a particular weld.

3.2.3.2 Stick Slip Flow

Another important point needs to be mentioned. Do we in fact have a constant boundary condition at a particular position in the weld? It may be possible for the boundary condition to vary over time. This type of boundary condition leads to the so called stick slip type of flow around the tool. There are two possible mechanisms by which this kind of flow may occur:

1. Surface Melting.

   Consider a condition where the bulk temperature of the material is below the solidus temperature and the material has in fact seized to the tool surface. In this case the intense shearing of the material will cause a large amount of heat generation. This in turn brings the surface to the solidus temperature, producing a liquid film at the surface. This reduces the friction force at the surface (coefficient of friction) causing the bulk material to slip. With the slip occurring at the interface, there will be less deformation within the material and therefore less heat generation. Therefore the material will cool, enabling it to once again stick to the tool surface. The reason why such a surface condition is transient in nature is that when the material sticks to the tool surface, too much heat is generated to maintain the material as a solid. Likewise, when the surface melts insufficient heat can be generated to maintain the molten surface layer so it will resolidify.

2. Centres of Unit Seizure.

   In a paper describing the characteristics of friction welding, Vill [60] found that in the third stage of friction welding, centres of unit seizure can occur when material oxides are scraped off the mating surfaces allowing a state of pure friction and hence seizure to occur. These centres are subsequently broken up due to the intense material deformation so slip once again occurs. This process could cause stick slip flow of material around the tool. It is not requisite on the solidus temperature being reached.

Either way the process may be unstable at a given point, resulting in material flow around the tool in layers rather than in a continuous flow. Part of the subsequent

evaluation of the models will involve an investigation into which if either of the above two mechanisms is likely to apply in a given weld.

3.2.3.3 Hot vs. Cold Welds

It is also necessary to distinguish between the type of flow that is likely to occur for a hot versus a cold weld. Initially one might think that at high temperatures the material would tend to stick on the pin and flow with it, while the low temperature weld would exhibit more slip because the material has a higher yield strength and will therefore be more difficult to flow around the tool.

However, it is proposed that the opposite is indeed the case. When the material is cold two things will occur:

- The deformation zone will be away from the tool threads because the material has in fact solidified in the threads.
- The material just outside the deformation zone remains fairly cool making it difficult to deform around the tool.

Both these factors lead to a process of extrusion illustrated by Figure 3-2.

Alternatively, when the material is at a higher temperature, two things will occur:

- Because the material is at a higher temperature surface melting may occur, lubricating the tool/material interface enabling the material to slip against the tool. Alternatively, if surface melting does not occur, the effect may be explained with reference to Figure 2-23 which describes the variation of torque with time for a friction weld. As can be seen from this diagram the maximum torque occurs when the material is at a critical temperature. Either above or below this temperature the torque that can be applied to the material is lower. Therefore, it is suggested that the cold weld operates at this critical temperature so the material will stick to the surface of the tool. The hot weld operates at a temperature where the torque that can be applied to the material is less because of the lower yield strength. Consequently the material effectively slides over the tool. Surface melting is not requisite on this occurring. Either way, the slip

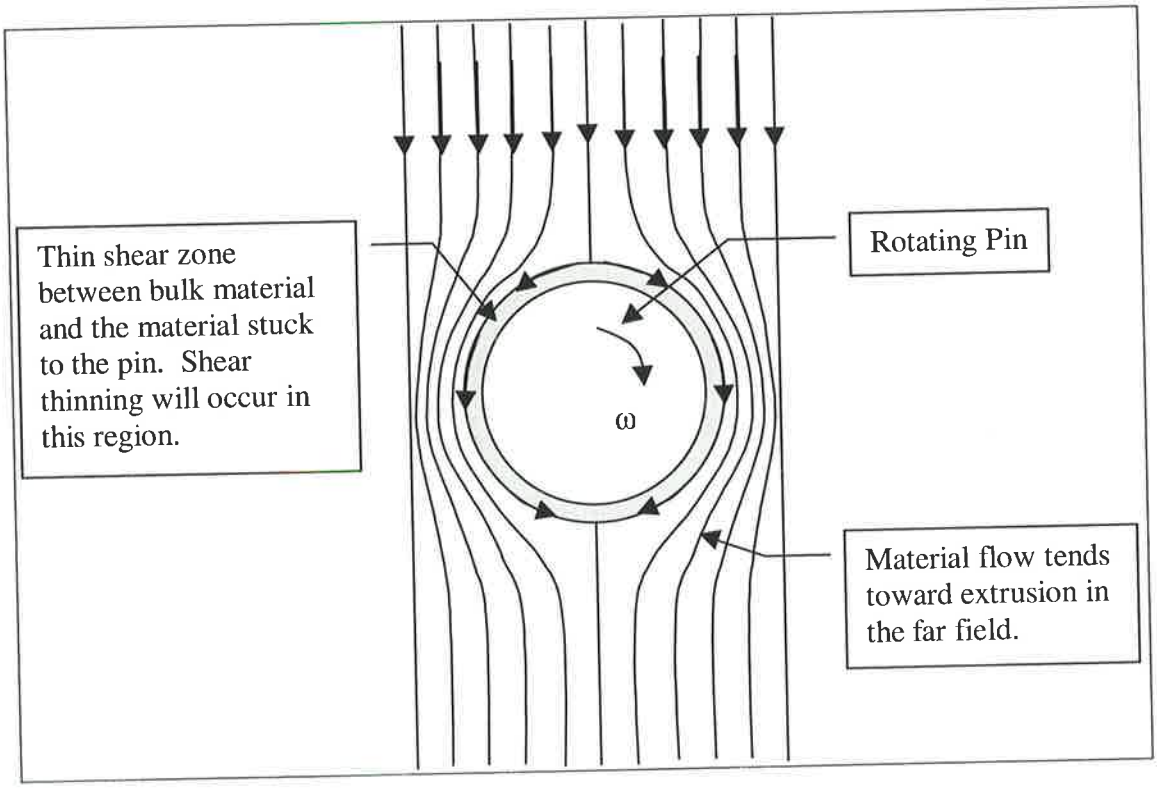

Figure 3-2 Flow of Material Around Pin for a Cold Weld

will start on the advancing side of the pin and will perhaps work its way around to the retreating side. This is because the material deformation is higher in this area and so also the heat generation promoting slip. Secondly, the resistance to flow will be greater in this area, which will also promote slip.

- Since the material is at a higher temperature it will have a lower viscosity and will therefore have a greater ability to flow around the tool.

These two factors lead to the flow pattern for the hot weld which is shown in Figure 3-3. Note the mixed zone behind the tool.

Therefore, the flow regimes for the two welds will be quite different. Why the material extrudes around the pin in one case and flows around it in another will become apparent from the following discussion:

Consider the flow around the pin (ignoring shoulder effects) in Figure 3-4 and Figure 3-5. It will be assumed that the size of the deformation region is the same for the left and right sides which is a reasonable assumption given that the central weld nugget is fairly symmetric about the axis of the weld. (See section 3.4.1) Secondly it will be assumed that the velocity of the periphery of the pin is large when compared with the velocity of the weld. For a typical weld this is usually greater than 200:1.

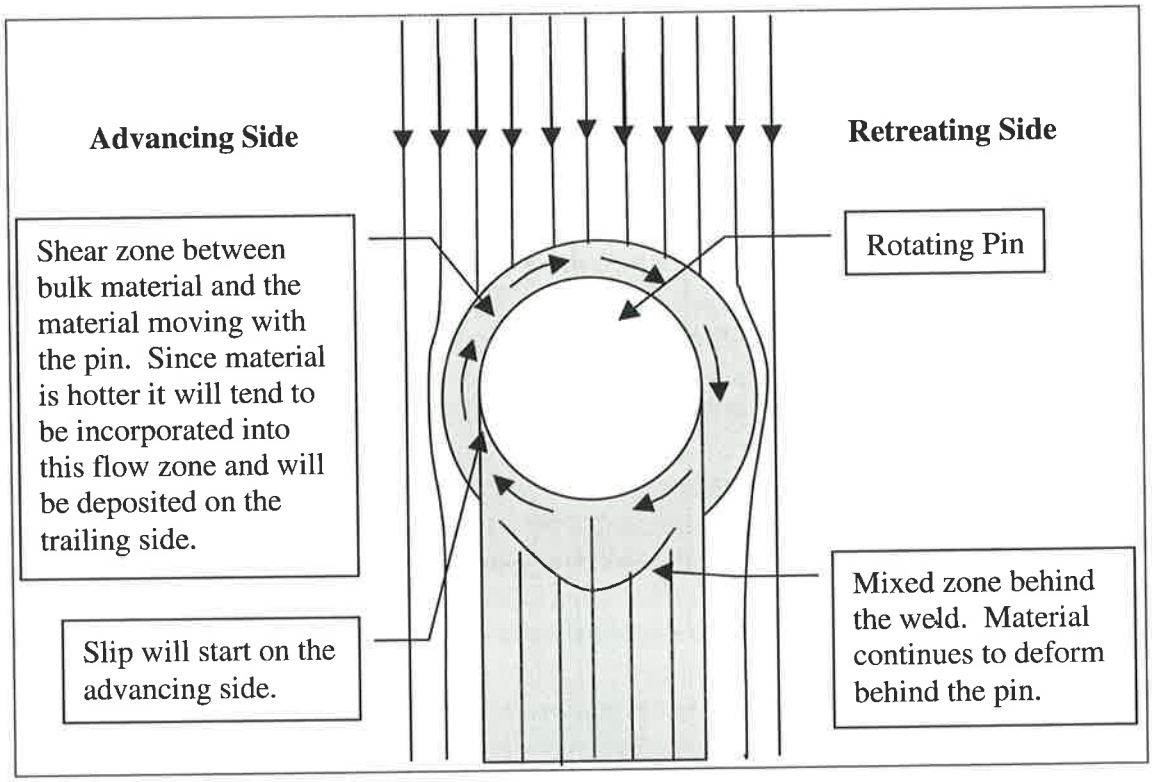

Figure 3-3 Flow of Material Around Pin for a Hot Weld

Firstly consider the no-slip weld. The velocities of the material at the surface of the tool and in the far field are indicated in Figure 3-4. The volume of material which flows around the right side of the weld will be given by:

$$\dot{Q}_r = wh\frac{(V_p + V_w)}{2} \approx wh\frac{V_p}{2} \qquad \textbf{Eq. 3-4}$$

Note:

- The assumption that $V_p >> V_w$ allows V_w to be ignored.
- h is the height in the z direction.
- Positive flow is in the direction of the material flow.

Similarly on the left side:

$$\dot{Q}_l = -wh\frac{(V_p - V_w)}{2} \approx -wh\frac{V_p}{2} \qquad \textbf{Eq. 3-5}$$

Therefore $\dot{Q}_r \approx -\dot{Q}_l$ so there is very little flow into or out of the deformation region, resulting in the material extruding around the tool.

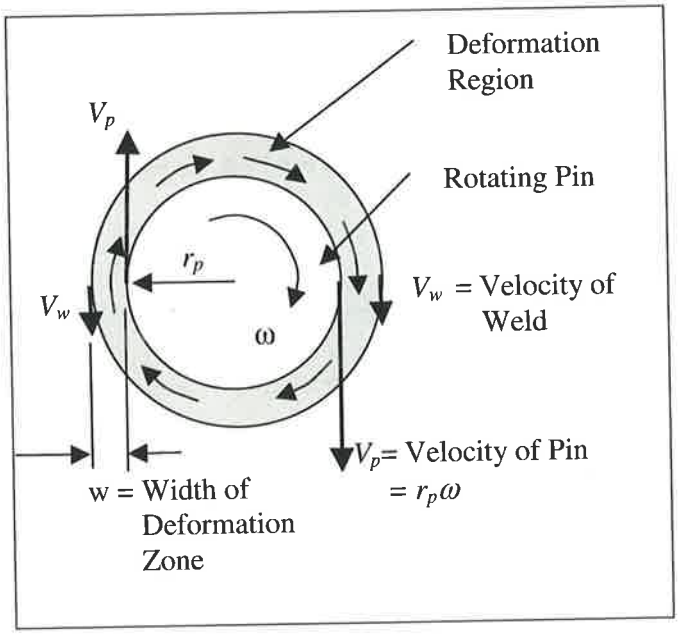

Figure 3-4 No-Slip Deformation Region

For the tool where slip is allowed to occur, it will be assumed that the material next to the tool flows with some velocity V_{mr} on the right side and that it approaches zero on the left side due to the incoming material flow. See Figure 3-5. Therefore the flow of material on the right side is given by:

$$\dot{Q}_r = wh\frac{(V_{mr} + V_w)}{2} \qquad \textbf{Eq. 3-6}$$

and on the left side by:

$$\dot{Q}_l = wh\frac{V_w}{2} \qquad \textbf{Eq. 3-7}$$

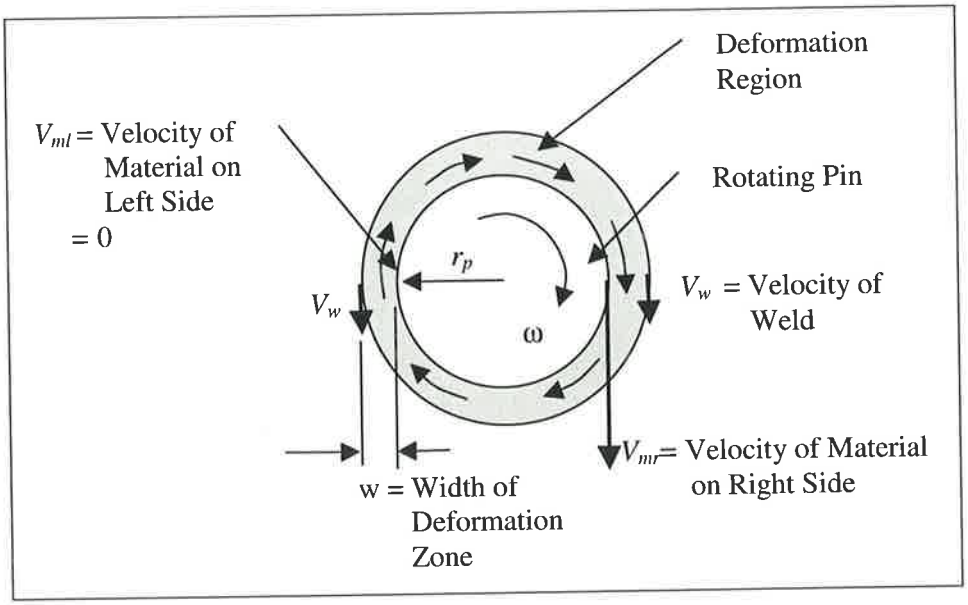

Figure 3-5 Slip Deformation Region

In this case the material flow around the right side is significantly greater than that on the left so the material flows around the pin in the deformation zone.

The above process models will now be evaluated against existing experimental data, to determine which boundary conditions are most likely to predominate in a given weld

3.3 Maximum Temperature that Occurs During Welding

To determine which of the proposed mechanisms is responsible for the stick slip behaviour observed in many friction stir welds, it is necessary to examine the maximum temperature that occurs during welding. There is currently some disagreement between researchers as to whether or not surface melting occurs during FSW.

It has been a common belief that the temperature achieved during welding does not exceed 0.8Tm [11,12], making melting impossible. However Frigaard et al. [10,55] and

Russell and Shercliff [5] stated that during FSW the peak interface temperature of the material would equal the melting temperature of the workpiece material. The mechanism by which this occurred was described in section 2.1.7. However these statements were made without any good supporting data for FSW and were based on observations found in similar metal forming operations. Examples of such observations are found in Midling and Grong [48] who analysed the friction welding of aluminium alloys, and Grong [49] who investigated the thermal processing of aluminium alloys in general.

The following sections describe the evidence both for and against surface melting in FSW.

3.3.1 Evidence for Surface Melting

The evidence supporting surface melting is:

1. Temperature Measurements.

   In a paper by Reynolds and Lockwood [53], the peak welding temperature was measured at a distance of 14mm from the weld centreline. While obviously not demonstrating temperatures near the eutectic because of the thermocouple's location they did find that 5083 and 6061-T6 alloys exhibited much higher welding temperatures than the higher strength 2000 and 7000 series aluminium alloys. Initially these results seem unusual as one would expect the higher strength alloys to generate more heat because of the higher torque to rotate the tool and would therefore have a higher welding temperature. However, the higher strength alloys also have a much

lower solidus or eutectic temperature, see Table 3-1. Therefore this limits the heat generation resulting in a much lower welding temperature.

Table 3-1

Material	**Solidus Temperature(°C) [59].**	**Insipient Melting Temperature (°C) [59].**	**Approximate Welding Temp (°C) [53].**
5083-0	574		420-440
6061	582		360-415
2219		543	315-370
2024		502	370-380
7050	524	488	325-390
7075	477	532	305-330

It should be stated that the above results are far from being a conclusive proof for the existence of surface melting. However they do suggest a limit to the maximum temperature that occurs during the weld based on the solidus temperature.

2. Rotating Pin Plunge Tests.

   North et. al. [28] found that while obtaining viscosity data for FSW 6061-T6 aluminium alloy (see section 2.2.3.1), the temperature of the pin reached the eutectic melting temperature. This was found by placing a thermocouple in the pin. One could argue that since FSW was not actually occurring, such measurements are irrelevant. However, it could also be argued that such a test will give a good indication of the conditions likely to occur in FSW.

3. Temperature Measurements from 12mm Thick 5083.

   Section 4 describes the temperature contours that are obtained from welding 12mm thick 5083 aluminium. The temperature measurements were from the workpiece material only. The results showed that the peak temperature in the material was 560°C, which was remarkably close to the solidus temperature of 574°C. Since the temperature was being obtained some distance from the tool surface, some form of surface melting may have occurred, especially in the hotter parts of the weld. There was no evidence for surface melting in the microstructure.

4. Temperature Measurements from 25mm Thick 5083.

   Section 9 describes the temperature contours that are obtained from welding 25mm thick 5083 aluminium. The temperature measurements from the workpiece material indicated that the maximum temperature of the material reached 574°C, which coincides with the solidus. This result did however contradict those from the thermocouples located in the spindle, which indicated that the maximum welding temperature reached 510°C. The reason for this discrepancy is unclear.

3.3.2 Evidence Against Surface Melting

The evidence against surface melting is described below:

1. Lack of Microstructural Evidence.

   If surface melting was occurring in FSW then it would seem reasonable to expect that some form of microstructural evidence in the form of dendrites at the tool surface or a triple point would have been published. No such papers have been found.

2. Temperature Measurements.

   McClure et. al. [12] found that while welding 6061-T6 alloy the temperature never exceeded 0.8Tm. Similarly Russell and Shercliff [4] found that the maximum temperature obtained when welding 2014 Aluminium was 460°C, around 50°C lower than the solidus temperature of 507°C.

3. Tool Thermocouple Measurements.

   As mentioned previously, section 9 describes an experiment where thermocouples were placed in the tool while welding 25mm thick 5083 aluminium. These thermocouples indicated that the maximum temperature at the tool surface never exceeded 510°C, well below the solidus temperature of 574°C.

3.3.3 Summary

From the evidence presented above the following conclusions can be made:

1. It may be possible for surface melting to occur in some circumstances, especially where the welding parameters are such that the weld temperature is high.
2. Perhaps in the vast majority of welds surface melting is unlikely to occur with the stick slip behaviour being a result of centres of unit seizure described by Vill [60].
3. The solidus temperature imposes some limit to the heat generation and therefore the maximum temperature that can be achieved in the weld.

3.4 Evaluating the Flow Models

Perhaps the best way of evaluating the various models is to look at the experimental evidence and see whether it is consistent with the results predicted by the models. The experimental evidence will be divided into two main areas:

- Flow Visualisation
- Experimental Data

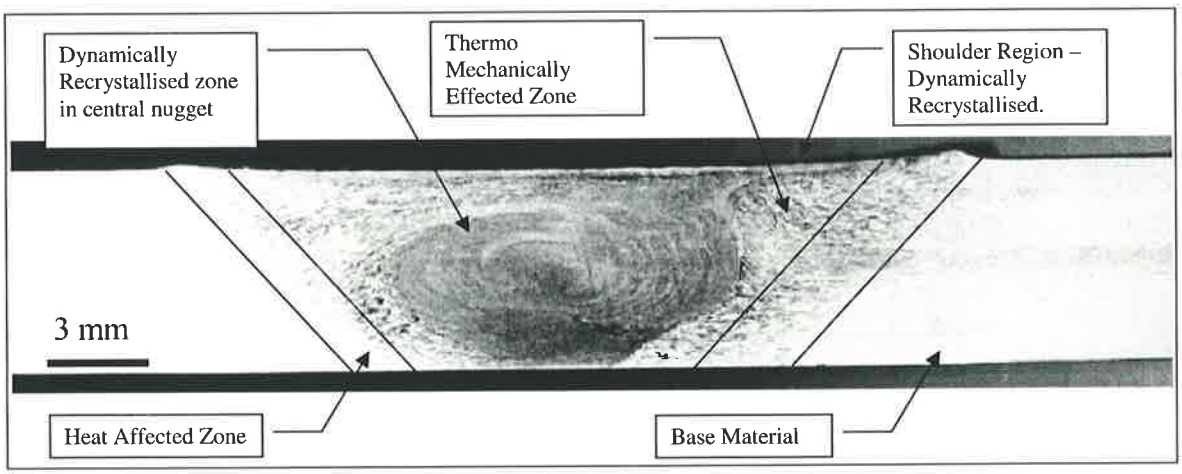

Figure 3-6 Standard FSW Microstructure at High Temperatures [36]

3.4.1 Flow Visualisation 1 - Typical Weld Bead Microstructure

A typical weld bead microstructure is shown in Figure 3-6 (Leonard [36]). Various authors (Mahony et. al. [33], Reynolds et. al. [24], Leonard [36] and Kinchen et. al. [34]) have labelled the regions in the microstructure. Note that distinguishing between the different regions, especially between thermo-mechanically affected and heat affected zones can be difficult. The following is a brief description of each:

1. Dynamically Recrystallised Zone.

   At low welding speeds where the temperature of the material is high, concentric rings can clearly be seen in the microstructure, while at high

welding speeds and therefore low temperatures, the swirling effect is much more difficult to distinguish and in some cases appears to not be present at all. (Figure 2 Reynolds et. al. [24] and Figure 4 Biallas et. al. [35]). The microstructure of a weld without a thread is similar to that from a high welding speed. See Dalle Donne et. al. [37]. Finally, Leonard made note of the fact that the dynamically recrystallised zone is not continuous, but exhibits layers of alternating coarser (≈6μm) and finer grains (≈5μm).

2. Thermo-Mechanically Affected Zone.

   This region, just outside of the dynamically recrystallised zone exhibits a much larger grain size indicating less deformation. The region exhibits lines of deformation, but there is none of the swirling effects shown in the dynamically recrystallised regions.

3. Heat Affected Zone.

   Here the thermal cycle has affected the properties of microstructure, however no deformation has occurred.

4. Parent Material.

   No deformation or heat effects.

These features are adequately explained by the process model described in section 3.2.3. When the welding temperature is high the flow features are described by Figure 3-3. The high temperature enables the material to flow around the screw thread. (See Figure 3-7) Once the material reaches the advancing side it experiences more resistance to flow, plus the deformation is higher and slip may occur. Therefore the material will flow down the threads of the tool. Once the material has been pushed down to the bottom of the weld it must work its way back to the retreating side and up to the surface

for continuity to hold. This whole process is assisted by the influence of the shoulder which generates a high velocity on the top surface and helps to rotate the material.

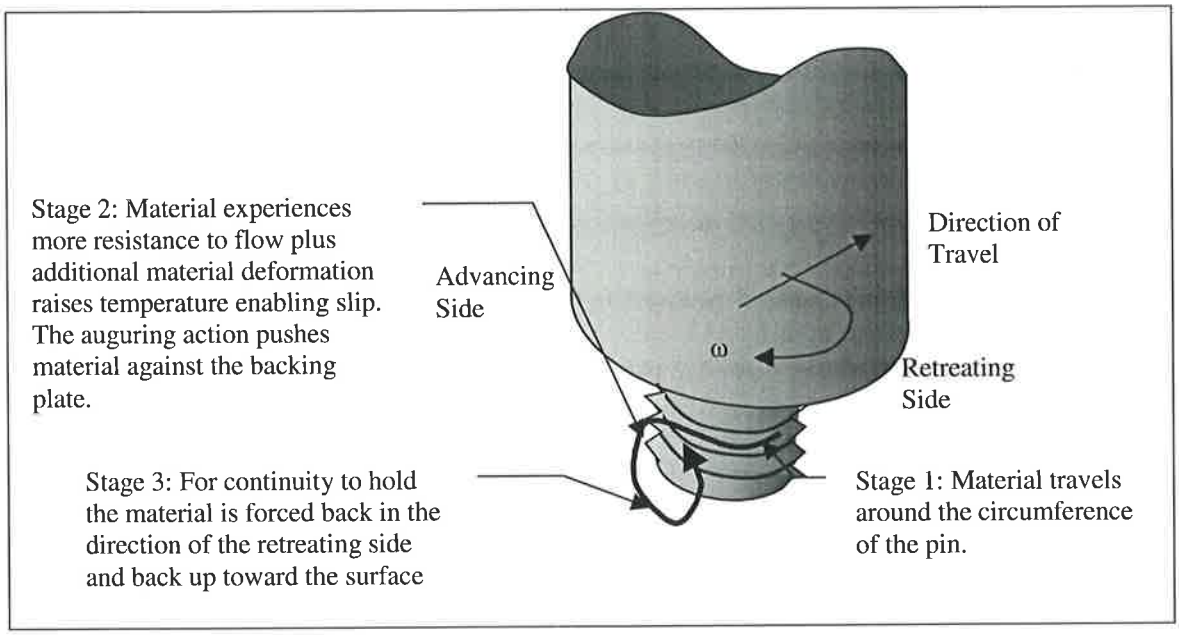

Figure 3-7 Theory for the Formation of Dynamically Recrystallised Region in Weld Bead Microstructure

No swirl was observed in the recrystallised region of a cold weld or in a weld made without a pin where the process tended toward extrusion. Even though the two welds display similar microstructures they are likely to be produced by two different processes. In the first case for the cold weld with a thread, the flow field around the pin is described by Figure 3-2. For the second, where no thread is involved slip occurs between the smooth tool and the workpiece material enabling the process to also tend toward extrusion. Note that in the first, the shear surface is within the workpiece material, while in the second it is between the tool and the aluminium. Since the shear stress obtained within the aluminium is much higher than between the steel tool and aluminium, the weld with the thread is much more effective. The smaller grain size in

the dynamically recrystallised zone remains and is a result of the greater deformation of the material which had to extrude around the pin.

The observed layering of the dynamically recrystallised zone is also consistent with the stick/slip flow of the proposed model. The regions between the layers will exhibit a larger degree of deformation resulting in the finer grain size between the layers. This layering of the microstructure was observed quite clearly in the pin retraction defect discussed in section 3.4.10.

The TMAZ is also explained adequately by this model. This region undergoes much less deformation so has a much larger grain size. This region corresponds to the extruded region in the far field shown in both Figure 3-2 and Figure 3-3.

The fluid model can also explain many of the observed flow features. It is difficult however, to see how the single slip surface could explain the observed flow features.

3.4.2 Flow Visualisation 2 – Welding of Dissimilar Metals

This method of visualising the flow involves the welding of two different metals and etching the material to show the difference between the two materials after they have been welded. Five papers have been written on this method by Biallas et. al. [35], Li et al. [41] and Murr et. al. [39,40] and Larsson et. al.[75]. All the papers demonstrated different features of the flow. The key features observed were:

- Layering of the two regions. This was demonstrated in the paper by Li et. al. and to a lesser extent the paper by Murr et. al. (Both from the University of Texas.) Both papers discussed the welding of 2024 to 6061, however the

second also discussed the welding of various other materials including copper. The first showed the layering that occur in the material in various directions. At a low welding speed the process seemed to tend toward extrusion with some secondary ripples and swirls at various points in the microstructure. The flow appeared exceedingly complex and difficult to explain. The extrusion part of the weld tends to occur around the top of the weld and may be explained by incomplete contact between the tool and the workpiece material. This was demonstrated by Colligan [26,27], and is discussed in section 3.4.4. The areas where swirling occurred tended to occur lower in the weld where there is better contact between the tool and the workpiece material. The swirls also demonstrated a certain amount of layering between the two materials. This is explained by the flow regime for a hot weld shown in Figure 3-3 and Figure 3-7. Very little information was provided on the higher rotational speed welds, so it was difficult to deduce what was occurring. It appeared as though the material was more fully mixed which is consistent with the process being hotter and therefore the material flowing around the pin as per Figure 3-3.

- In the paper by Biallas et. al. the central nugget was clearly visible. Both

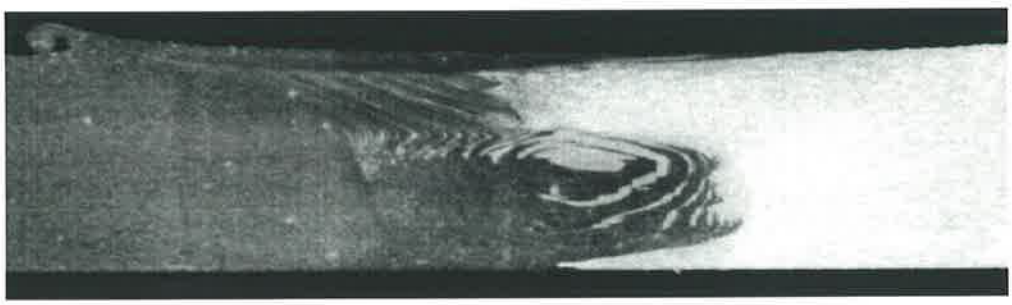

Figure 3-8 Welding of 5083 and 6082 [75]

materials were well mixed in layers in this region. This evidence is entirely consistent with the microstructure from a hot weld previously discussed in section 3.4.1.

- Larsson et. al. [75] investigated the welding of 5083 to 6082 which demonstrated similar features to those observed by Li et. al. except that the central swirl region was markedly more pronounced. One of these macro-sections is reproduced in Figure 3-8.

3.4.3 Flow Visualisation 3 – Marker Materials

Another method of flow visualisation was attempted by Reynolds et al.[24],[25] and involved the use of embedded marker materials which were placed on the advancing and trailing side of the weld at three different heights. ie. top, middle and bottom. The material being welded was 2195 Al while the marker material was 5454 H32 sheet. In the first paper [24], two different weld speeds were investigated, one giving a hot weld

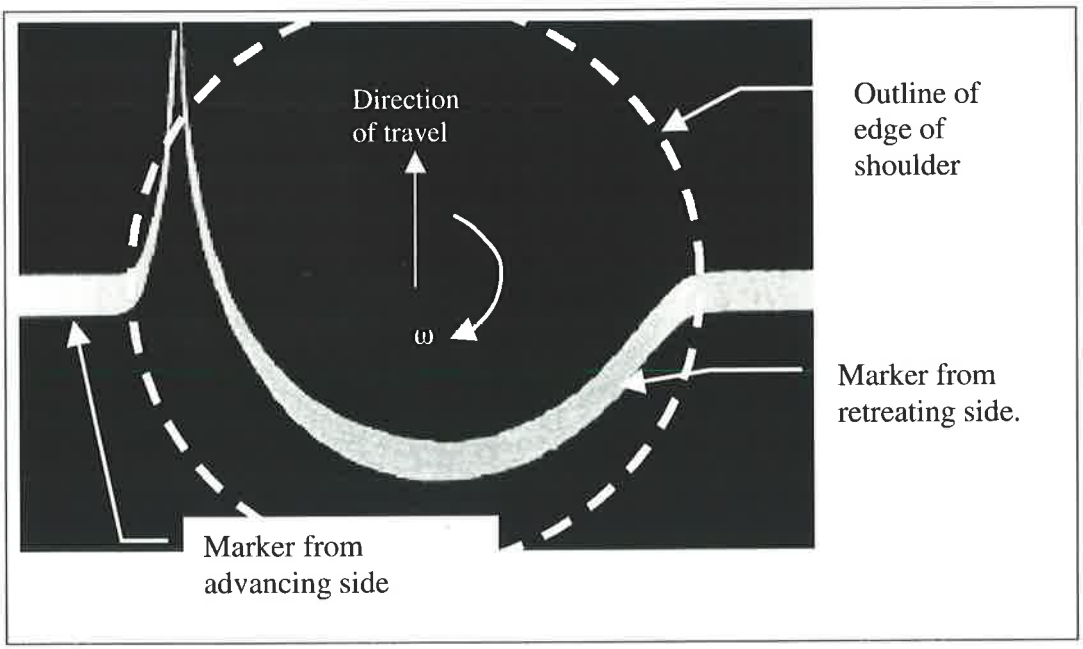

Figure 3-9 Marker Material Near Top Surface

and the other a cold one. The following results were obtained in this paper:

1. Top Layer Flow Pattern.

   After welding, both the hot and cold welds exhibited similar flow patterns in a layer at the top of the weld. The resulting flow pattern is illustrated in Figure 3-9 . The marker on the retreating side is swept around the tool, while the material on the advancing side is simply pushed forwards. There appears to be no mixing of material from the advancing and retreating sides.

2. Middle Layer Flow Pattern.

   Around the middle of the workpiece the flow patterns for the hot and cold welds were markedly different. See Figure 3-10 . In the cold weld the two markers remain effectively separate and remain on the same side that they started on. ie. the advancing side marker does not get taken around to the retreating side and vice versa. In contrast, the hot weld marker appears to have completely disappeared except for a few faint circles around the

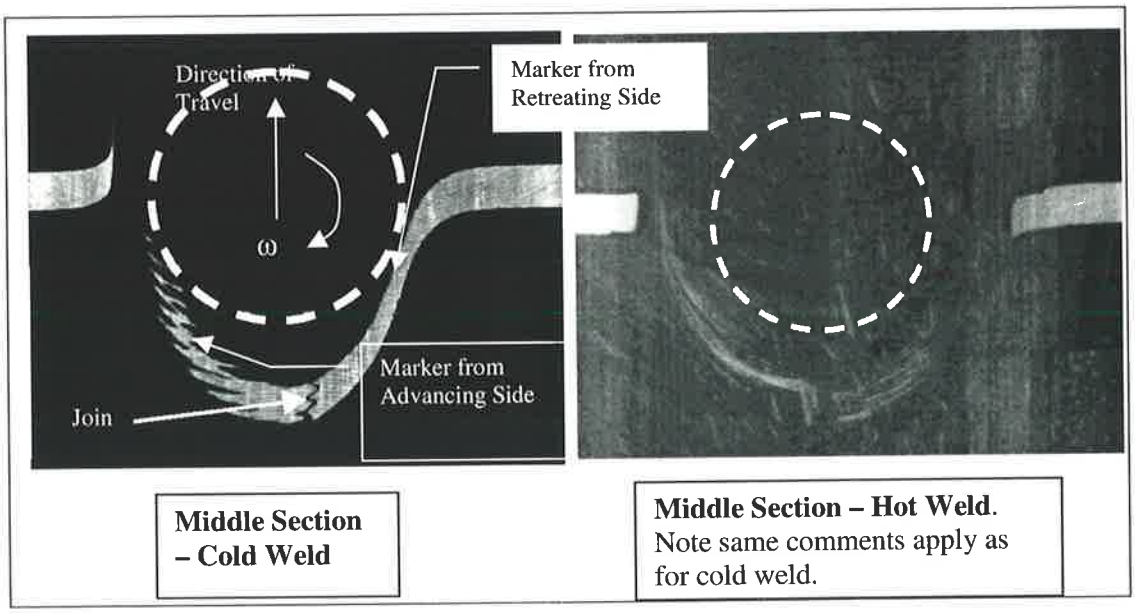

Figure 3-10 Markers from Middle Section of Weld

advancing side of the pin. One interesting feature of the middle level marker for the cold weld on the advancing side is that it shows a small kick forward while the rest of the material is pushed backwards. This may be explained by the material being pushed downwards from the shoulder above which is flowing in the same direction as the toolpiece. See Figure 3-10 .

3. 3 Dimensional Flow Pattern.

   Flow patterns from various layers through the cross section were combined to produce a 3-D plot of the resulting marker positions.

4. Plots of Layers Through the Cross Section.

   Plots were produced of the final marker positions across the various layers in Figure 3-12 for the cold weld and Figure 3-11 for the hot weld. These plots showed little mixing for the cold weld, with a slight twist in the centre where the pin went through the weld. For the hot weld there was significant mixing with some of the material from the top layer ending up at the bottom of the weld.

5. Plot of the Interface Between Advancing and Trailing Side Markers.

   Plots were produced showing the interface between the advancing and

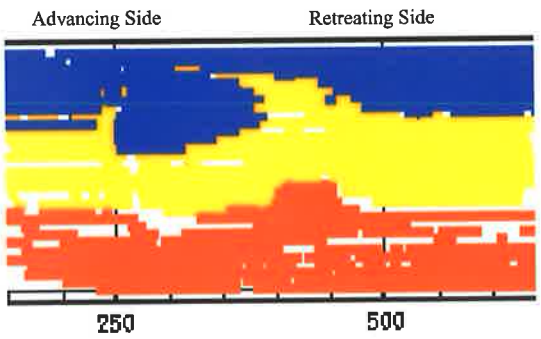

Figure 3-12 Marker Positions Across Layers for a Cold Weld

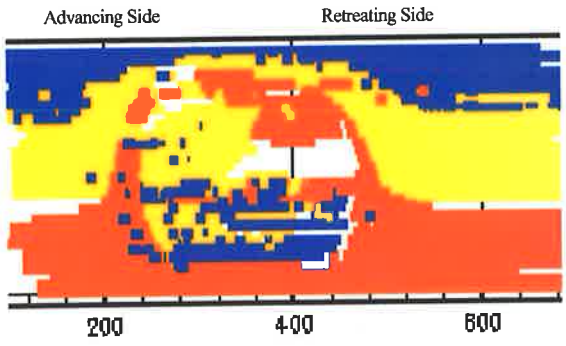

Figure 3-11 Marker Positions Across Layers for a Hot Weld

retreating side markers. (Figure 3-13 and Figure 3-14 from Reynolds et.al.) These flow patterns were similar to those obtained for the welding of dissimilar metals described in the previous section. The cold weld (Figure 3-13) showed a clearly defined interface between the advancing and retreating side materials, while the hot weld showed significant mixing of the two materials.

These results are consistent with the predictions of the flow model proposed in section 3.2.3. Where the material is cold then the process will tend towards extrusion as is clearly demonstrated by Figure 3-10 . The most interesting aspect of the observed weld is the 'jaggering' of the insert on the advancing side of the weld. It is believed that this is caused by the onset of the stick slip behaviour described in section. This only occurred on the advancing side because there is slightly greater material deformation and hence heat generation in this region.

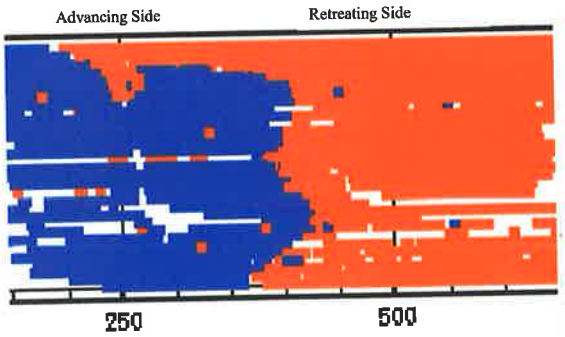

Figure 3-13 Interface Between Advancing and Retreating Side for a Cold Weld

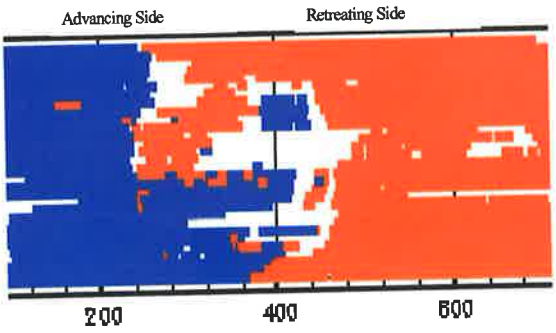

Figure 3-14 Interface Between Advancing and Retreating Side for a Hot Weld

From the visualised flow patterns Reynolds et. al. [24] concluded that the FSW process approximated an extrusion process. This conclusion would seem to be quite reasonable for the cold weld however it does not fit the results obtained for the hot weld which exhibited significant mixing. Reynolds et. al. stated that: 'We cannot with certainty make the same statement about weld #2(that the hot weld is an extrusion process); however, it seems likely that the welding process differs only in degree and not in kind between the two welds'. He clearly implied that although the hot weld was still essentially an extrusion process. However it seems reasonable that an alternative view could hold, namely that material slip against the tool results in significant material mixing causing the process to deviate from that of extrusion.

Finally, it is interesting to note that Figure 3-12 from Reynolds et. al. would seem to validate the conclusion drawn about the production of the Dynamically Recrystallised Zone in section 3.4.1. ie. The figure shows the resulting position of the layers in the micrograph have a slight anticlockwise twist around the position of the pin. This is exactly the result predicted by the theory in section 3.4.1.

3.4.4 Flow Visualisation 4 – Steel Markers

Colligan [26,27] proposed another method of flow visualisation which involved the placement of small steel balls (ϕ = 0.38mm) in the FSW material prior to it being welded. The material was then welded through the line of ball bearings. The tool was retracted mid-weld, enabling the flow pattern around the pin during welding to be observed. This is the only flow visualisation technique that enables this to be observed.

The materials that were welded were 6061-T6 and 7075-T6 Aluminium. To enable the flow to be observed at different positions, the line of steel balls was offset in the *y* direction (See Figure 1-1) by different amounts and the height of the ball bearings in the material was also varied.

The results from Colligan [27] are summarised below:

- The ball bearings that were near the top surface were dispersed reasonably randomly in the resulting weld. The ball bearings which started off on the advancing side of the tool ended up further down in the material than those on the retreating side. This confirms the results shown in Reynolds et al. [19] that indicated that the material on the top surface of the advancing side is swept around the pin and ends up on the top surface of the retreating side, while the retreating side material is swept down into the weld pool.
- Lower down in the material where the shoulder has less effect on the flow of the material, the ball bearings were swept around the pin surface. Their position was fairly consistent and did not display the large scatter that was observed for the ball bearings near the top surface. When looking at the cross section of the ball bearings in these positions their end position is usually higher than the start position.
- In several positions around the mid-section of the weld, the markers could end up in two distinct positions. (See positions 5, 9 and 10 in Figure 6 [27] and position 9 in Figure 7 [27])

- For the ball bearings which are near the edge of the pin on the advancing side, they often flow straight passed the pin with very little deflection. It is clear that they are not dragged around the surface of the tool.

Before discussing the results a point needs to be made about a potential error in the experimental procedure suggested by Graham [42]. Graham suggested that offsetting the position of the join, may effect the flow of the material due to the discontinuity in the material at this point. This effect is most significant for the welds where the steel markers are a considerable distance from the tool centre. Without further evidence, it is unclear whether this effect is or is not significant.

From Colligan's results the following conclusions can be made about the flow around the friction stir welding tool:

- The random dispersion of the markers around the top layer suggests that the flow must be stick/slip in this position. Section 10.5 demonstrates that, for material which is stably stuck to the surface of the tool the flow is continuous and laminar. Therefore it is suggested that this random flow is the result of an instability at the surface.
- In general the material is extruded around the tool. This is consistent with the findings in section 3.4.5, which shows that the material sticks to the surface of the tool in the lower section of the weld. The random flow, which is observed in several of the cases can be attributed to either a stick slip surface condition as mentioned above or the effect of the tool thread.

- Considerable movement in the vertical direction indicates that the screwing action of the threads is significant, even if the material may be stuck to them. A significant amount of material deformation occurs within the screw threads as well as in the far field beyond their reach. In some cases the final position of the material is higher than the initial start position, which indicates that the material has been forced upwards from underneath. Obviously the amount of material that moves down must equal the amount that moves upwards for continuity to hold.
- Colligan [27] found that although the two materials have a vastly different temperature at which melting occurs there was no appreciable difference in the flow patterns for the two welds. Neither the welding or rotational speeds were disclosed in the article.
- The single slip surface model is clearly discredited from the evidence presented by Colligan for under that model it would be impossible to get markers in such close proximity to the tool.

The flow patterns described by Colligan [26,27] largely agree with those found by Reynolds et. al. [24]. However Colligan did not distinguish between a hot and a cold weld, which could show the difference between slip and no-slip boundary conditions more clearly.

3.4.5 Flow Visualisation 5 – Shape of Material Around Tool During Welding

Colligan [26,27] also observed the weld zone microstructure that was obtained after the tool has been unscrewed from the workpiece material. This is shown in Figure 3-15. Note that the rate at which the tool retracted was synchronised with the screwing speed

so that the material was not disrupted. Colligan identified eight features which are described below:

- A – Initial butting surface intersection with section plane
- B – Material filling thread space
- C – Filled thread space in front of pin
- D – Void behind upper portion of pin
- E – Filled thread space behind pin
- F – Material flowing upward behind pin
- G – Material extruded under pin
- H – Material extruded under shoulder

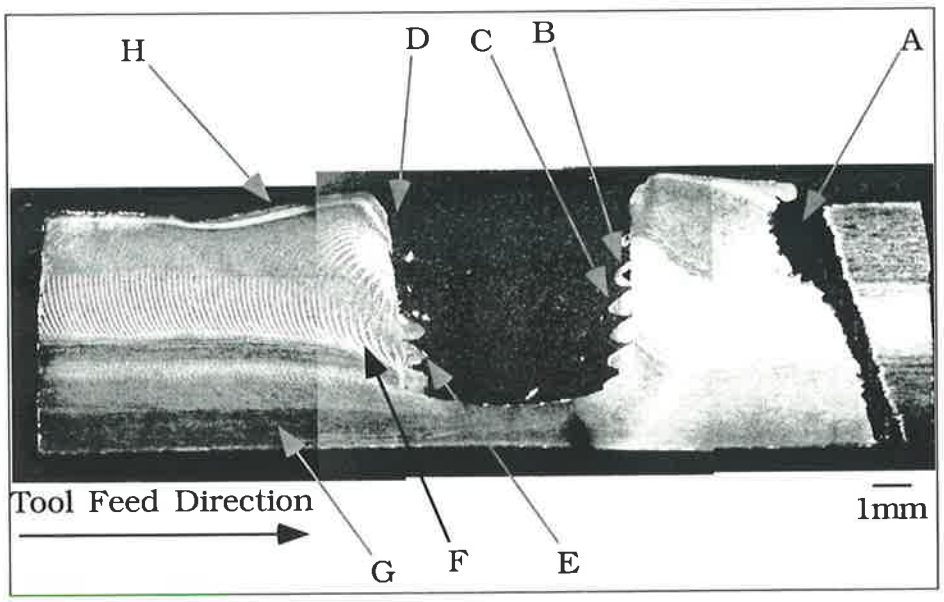

Figure 3-15 Pin Retraction Microstructure

Colligan's results indicate that the material does not fully fill the threads from the top to the bottom of the weld. In fact, on both the front and rear sides, the upper portion of the weld showed no evidence of the material having any contact with the threads in the toolpiece. About half way down the microstructure on the front side the material starts

to fill the threads. The process is gradual with the material being scraped downward by the vertical movement of the threaded pin. This situation is not observed on the reverse side of the pin. The first completely filled thread is observed about half way down the pin with no prior development. It is interesting to note that the first completely filled thread on the front side corresponds to the location of the first completely filled thread on the reverse side. Colligan [27] interpreted this observation as follows:

> 'Prior to the material fully filling the threads on the front side, the material is scraped vertically downwards. Once the material fills the thread cavity the tool is able to grab hold of the material and pull it round the back side of the pin where it is deposited.'

Finally, the banding which is observed in the cross section is similar to that observed by Leonard [36] and Mahony et al. [33]. It is believed that this may be caused by the stick slip flow of the material around the tool.

From this evidence the following conclusions can be made:

- It is unclear whether there is perfect contact between the pin and the workpiece material once the threads are fully formed as claimed by Colligan or whether there is still some degree of intermittent slip between the two. The banding, together with the intermittent movement of the markers in the material (eg position 9, Figure 6 [27])would suggest that the second effect is the more likely. Finally, Frigaard's[55] work on estimating the strain rate occurring in a FSW supports this position. See section 3.4.9. Note that if the rotational speed of the tool is 500rpm, then it will only take 0.12sec for a complete revolution. Therefore, it is entirely possible for some slip to occur

and to still obtain the correspondingly full threads on the reverse side of the thread, provided that the material can stick to the tool surface for at least part of the revolution.

- A fluid type model would obviously be inaccurate for the top part of the model where the material is clearly not in contact with the pin.
- Once again the single slip surface model is discounted by the evidence presented Colligan. Under that model one would expect a central nugget area with slip planes extending from the edge of the shoulder down into the pin. This is clearly not observed.

3.4.6 Experimental Evidence 1 – Variation in Normal and Rotational Forces

Two papers have been published which discuss the variation of heat produced with varying normal and rotational forces. These are by Midling and Rorvik [43] and McClure et. al. [12]. In the first paper the theoretical heat produced during a weld was calculated from the following equation:

$$q_o = \tfrac{4}{3}\pi\mu FNR \qquad \textbf{Eq. 3-8}$$

and compared with the size of the Heat Affected Zone (HAZ) which gave an indication of the actual heat produced. The material used was 7108.50-T79 alloy. In the second paper temperature measurements were made for the welding of 6061-T6, which has a relatively high solidus temperature (582°C) and is a relatively soft.

The papers showed that:

- There is a reduction in the heat produced with reduced vertical tool load, albeit a small change. Midling and Rorvik stated that the reduction in tool load resulted in slightly less heat being produced, which then resulted in an increase in the

workpiece yield strength and an increase in the coefficient of friction. The effect offset the reduced heat from reduced vertical load, so there was only a small change observed in the size of the HAZ.

- Reduced rotational speed of the FSW toolpiece also reduced the size of the HAZ, by a relatively small amount. Once again Midling and Rorvik stated the reason for the small change was due to the increase in the coefficient of friction offsetting the effect of the reduced rotational speed. These results were discussed in the section on friction welding (2.4.1). McClure et. al. found that while a reasonable increase occurred when changing the speed from 300 to 650rpm, a much smaller change occurred between 650 and 1000 rpm.

Reynolds et. al. [53] performed similar work, however measured the temperature in the weld in stead of the HAZ width and examined the parameter weld pitch, which they defined as:

$$\frac{\omega(\text{rpm})}{v(\text{ipm})} \qquad \textbf{Eq. 3-9}$$

Reynolds et. al. found that in general the weld temperature decreased when the weld pitch was reduced. However like Midling and Rorvik's results for the variation in rotational speed, the variation was quite minimal and in some cases showed a slight increase. It was unfortunate that they did not separate the two effects as this would have allowed a more systematic analysis.

Obviously Midling and Rorvik were working on the basis of sliding contact between the tool shoulder and the workpiece material. ie. The slip model. From these results the following conclusions can be made:

- The constancy of the heat input, which is largely independent of the rotational speed or the vertical load indicates that the temperature of the material is approaching the solidus. ie. Once the material has reached this temperature it is difficult to generate any more heat. ie.

  $\tau\omega = \text{const}$

  The observed change in the heat produced with increasing rotational speed are consistent with both single slip surface and fluid models provided a temperature dependent thixotropic material definition is used. Using this material definition only a small change will occur in the power requirement.

- The slight variation in the power input with tool load is inconsistent with both the fluid and single slip surface models. Very little or no change would be expected because increasing the vertical load will not change the shear strength of the material.

3.4.7 Experimental Evidence 2 – Tool Force Analysis

Johnson and Horrex [63] did some preliminary force analyses for the welding of 6082 and 5083 aluminium alloys. In the analysis the forces in both the x and y directions were measured, as well as the torque and the downward force. Some of the key results from this analysis are reproduced in Table 3-2.

Table 3-2

Alloy	Rotational Speed (rpm)	Traverse Speed (mm/min)	Force in Weld Direction (kN)	Force at 90° (kN)	Downforce (kN)	Torque (Nm)	Power (W)
6082-T6	710	40	0.6	0.6	6	12	892

Alloy	Rotational Speed (rpm)	Traverse Speed (mm/min)	Force in Weld Direction (kN)	Force at 90° (kN)	Downforce (kN)	Torque (Nm)	Power (W)
6082-T6	710	80	0.7	0.7	6	12	892
6082-T6	710	160	0.7	0.7	6	14	1041
6082-T6	1000	160	0.8	0.8	6	14	1466
6082-T6	1000	160	0.8	0.8	8-9.5	16	1676
6082-T6	1400	160	1.2	1.1	10	14	2053
6082-T6	1400	224	1.2	1.2	9.5	14	2053
6082-T6	1400	160	1.1	1.1	8.5	14	2053
5083-0	500	40	1.5	1.5	9.5	32	1676
5083-0	500	56	1.7	1.7	11	34	1780
5083-0	500	80	1.9	1.8	12	33	1728
5083-0	500	112	2.1	2.1	13.5	40	2094
5083-0	710	112	2.5	2.4	14.5	24	1784
5083-0	710	160	2.5	2.4	14.5	26	1933
5083-0	500	160	2.4	2.4	15.5	36	1885
5083-0	500	160	2.5	2.5	15.5	37	1937
5083-0	500	224	2.4	2.4	14.5	38	1990

A discussion of these results is presented below:

- The torque measurements for the 5083 are entirely consistent with what would be expected from the proposed slip if the welding temperature approaches the solidus. In this case total heat input will remain reasonably constant because any further heat generation will cause melting. Hence:

$$\tau\omega = \text{const}$$

Therefore an increased rotational speed will result in a reduced torque. Similarly an increased travel speed will result in slightly lower welding temperature, enabling an increase in the apparent coefficient of friction and energy input. This result can also be explained by the fluid and single slip surface models provided a temperature dependent, thixotropic material definition is used.

- When welding 6082 aluminium the torque measured by the transducer was largely independent of the weld rotational speed or weld travel speed. This is a significant deviation from the characteristics demonstrated by 5083. This can however be explained by the proposed slip model provided the welding temperature is significantly lower than the solidus. This is likely to be the case because of the material's lower yield strength and higher thermal conductivity when compared with 5083. See Table 3-3. This data was obtained from the aluminium handbook[59].

Table 3-3

Property	**6070 (Similar composition to 6082)**	**5083**
Thermal Conductivity at room temperature (W/mK)	172	120
Solidus Temperature (°C)	566	574
Yield Strength at room temperature (MPa)	145 (O temper)	172

The effect of different material properties on the thermal profile is discussed in the modelling work in section 8.2. As a result of the temperature being significantly lower than the solidus, the surface condition and material properties will remain much more constant. Therefore the shear stress at the surface of the tool and hence tool torque will remain more or less constant.

- Greater power was required to weld 6082 than the 5083 aluminium alloy which can be attributed to the 6082 having a greater thermal conductivity than the relatively poor conducting 5083. Hence more power will be required to plasticise the material.
- A surprising result for the 6082 alloy is shown with the horizontal forces which indicated that the force was more or less dependent on the rotational speed as opposed to the travel speed as one would expect. For the 5083 the observed horizontal force was largely independent of the rotational and travel speeds. No good explanation can be found for these observed characteristics.

These conclusions will of course need to be verified with temperature measurements.

3.4.8 Experimental Evidence 3 – The Effect of Varying Tool Geometry

Thomas et. al. [44] investigated various tool geometries, some of which are vastly different to the standard screwed pin with a flat shoulder. These included a plain, paddle, triangular, and whisk pins plus a few standard threaded tools.

The pin had twice the diameter that would normally be expected. The aim was not to produce good welds, but to test the effect of different tool geometries on the welding process. To do this an oversize probe was used.

Thomas et. al. found that the design of the pin had a large effect on whether a successful weld could be produced. The paddle, whisk and threaded pins gave the best results. Also, the coarser threaded pin gave better results than a finely threaded pin.

From these results the following conclusions can be drawn:

- The slip model predicts the observed results reasonably well.
    a) Cylindrical Tool.

        When the cylindrical probe is used there is very little resistance to flow around the surface of the probe, so the process approximates an extrusion process.

    b) Paddle Type Probes.

        When using the paddle, triangular or whisk probes the shape reduces the amount of slip that can occur between the probe and the workpiece material. Therefore, the process will act in a similar way to the fluid model. ie. Zero velocity at the tool workpiece interface. This will enable the tool to drag material from the front to the back of the probe, increasing the ability of the tool to produce a satisfactory weld without a groove. In this case the process will tend toward extrusion. See section 3.2.3.

    c) Threaded Probes.

        When using a probe with a fine thread, there was very little improvement over the plain cylindrical probe. However, the coarse thread achieved much

better results. The fine-threaded probe had little effect because the pitch angle was not sufficient to get a firm 'grip' on the plasticised material. Therefore the workpiece material essentially slides past the probe. When using the thread with a greater pitch, there is reduced slip between the material and the probe, which enables it to pull the material from the front to the back surface. Finally, it may also have an improved ability to scrape the material into the thread forms and producing a greater pressure in the material at the base. This will enable the tool to get a firm grip on the workpiece material and pull it from the front to the back of the probe.

- With a fluid type model no great difference would be expected between the various tool shapes. Since it has been assumed that the material is essentially stationary at the workpiece/tool interface, changing the shape of the tool will not have the same effect on the flow. This statement has assumed that the flow around the tool is essentially laminar, which would seem reasonable given the high viscosities involved. Note that if the flow were turbulent around the pin surface, then changing the tool shape would have a much greater effect. To understand why this is the case, consider the analogy with fully developed pipe flow. For laminar flow, the pipe roughness has no effect whatsoever on the pressure drop, however for turbulent flow the effect is quite significant.
- The single slip surface model cannot predict the observed results. Since the material is essentially stationary with reference to the pin with that model, altering the pin geometry should not alter the performance of the welding process.

3.4.9 Experimental Evidence 4 – Maximum Strain Rate Prediction

In a paper by Frigaard et. al. [55], the maximum strain rate that occurs during FSW was predicted from the Zener-Holloman parameter. The technique used is described briefly below and is based on work by McQueen and Jonas [56]:

1. Anneal the material after welding.
2. Using electron backscatter diffraction (EBSD) find the subgrain diameter, d_s in μm.
3. Find the Zener-Holloman parameter by the following formula for aluminium:

$$Z_h = 10^{\left(12.5\left(\frac{1}{d_s}+0.6\right)\right)} \qquad \textbf{Eq. 3-10}$$

4. Predict the maximum strain rate via the following equation:

$$\dot{\varepsilon} = \frac{Z_h}{\exp\left(\frac{18772}{T_p}\right)} \qquad \textbf{Eq. 3-11}$$

where T_p is the peak temperature (°K) obtained during welding for a particular position. Frigaard obtained this from his modelling work.

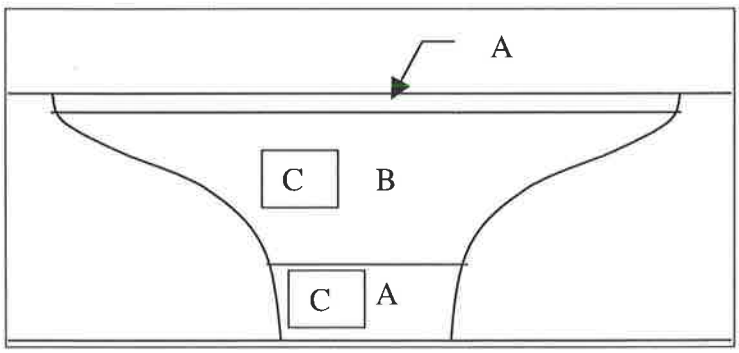

Figure 3-16 Recrystallised and Non-recrystallised

Referring to Figure 3-16, Frigaard identified 2 key regions in the FSW microstructure, namely:

Region A: Recrystallised Zone.

Region B: Non-recrystallised zone

Region C shown in this figure refers to the location of the EBSD measurements and the location of where the sub-grain diameter was calculated. Although the sub-grain diameter was not calculated for the region near the tool shoulder, it appears that it would be similar to that observed in the lower part of the weld.

A table of the key results from this work is shown below:

Alloy	Position	T_p(°C)	d(μm)	Z_h	$\dot{\varepsilon}$ (s^{-1})
6082-T6	B	550	4.8	1.28e+10	1.6
	A	540	3.5	1.10e+11	10.3
7108-T79	B	500	3.8	5.82e+10	1.7
	A	450	2.5	3.26e+12	17.3

Using this technique, Frigaard et. al. found the following interesting results:

1. The regions of highest strain rate are at the top surface adjacent to the tool and in the lower part of the weld. This is consistent with the pin retraction results by Colligan [26,27], who was able to show that complete contact between the tool and material only occurred at the tool shoulder and for the lower half of the tool thread. Therefore, the expected strain rates in these regions will be greater. Secondly, the deformation zone width is lower in this region, which will also result in higher strain rates.

2. The measured strain-rate is significantly below that which would be expected if the material had stuck to the surface of the tool. eg. Considering the lower part of the tool thread, the width of the deformed zone between the thread and the stationary material will be approximately 1mm (Reynolds [25]). Assuming that a pin size of 6mm was used, and a rotational speed of 500 rpm, then the approximate strain rate for material sticking to the surface of the tool will be $157s^{-1}$. This is an order of magnitude (10) greater than the values that have been measured. There are two possible causes for this low value of predicted strain rate:

    - The material slips against the tool.

      If the material slips around the tool then resulting strain rate will be significantly lower.

    - The material extrudes around the tool.

      In this case the material is stuck to the surface of the tool. Since there is very little flow into or out of the highly deformed region, the bulk of the material will extrude around the tool and will therefore have a much lower strain rate.

    Therefore, the evidence would suggest that Therefore, either the proposed slip model or fluid model can explain the low strain rate in the material.

Finally, Frigaard et. al. stated that the estimated value of strain rate is likely if anything to be an underestimate of the actual value.

3.4.10 Pin Retraction Defect

When welding a sample on the University of Adelaide friction stir welding machine, it was not possible to stop the traverse of the machine before the pin retraction sequence started. (See Figure 2-6) Therefore, the retraction hole was somewhat elongated. Fortunately, this defect enabled the layered flow of material around the tool to be clearly seen, which is seen in Figure 3-17. It does not appear that this layered flow is caused by the action of the threads, but rather a stick-slip surface condition. The only model that can adequately describe this type of flow is the proposed slip model.

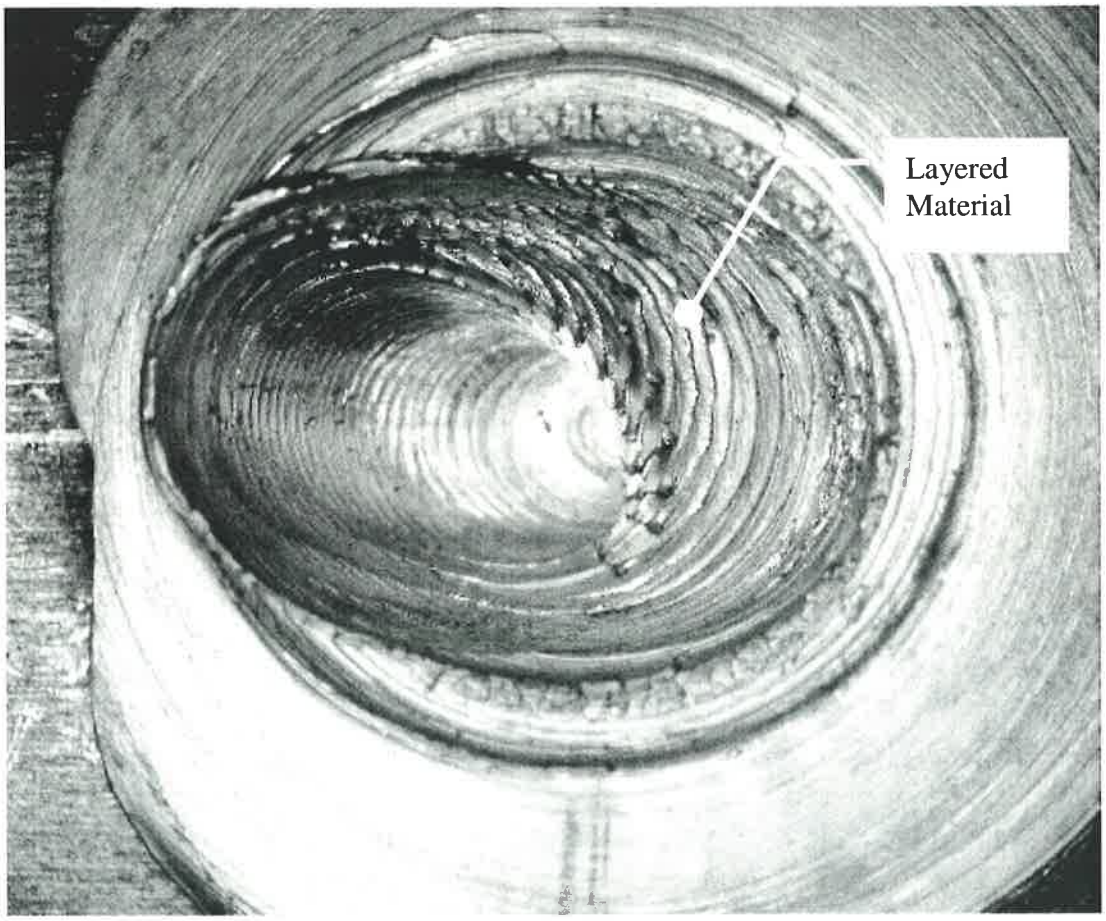

Figure 3-17 Pin Retraction Defect

3.5 Conclusions and Modelling Ramifications of the Various Flow Models

The proposed slip model is able to give a reasonable explanation of the flow visualisation, temperature and experimental evidence presented. It is certainly provides a better explanation than either the fluid or single slip surface models. Briefly a summary of the key findings are:

1. The flow of material around the tool appears to be predominantly by a stick-slip surface condition rather than being continuous or purely slip. It is believed that this stick slip behaviour is primarily caused by the mechanism of centres of unit seizure rather than surface/asperity melting.
2. In particularly cold welds the flow appears to be more continuous, with the material being extruded around the pin rather than the layered flow predicted by the stick slip behaviour identified above. A fluid model accurately describes the flow around the tool in this case.
3. The heat that can be generated by the process is limited by the solidus temperature. This does not necessarily imply that surface melting will occur. It is believed that some limited form of melting may occur in particularly hot welds with low travel and high rotational speeds. However, by and large the process is solid state.

The ramifications of this flow behaviour on modelling are that either one of the following two approaches must be employed.

1. Modelling as a Fluid.

   If one were to model the deformed zone using a fluid model and no slip, the stick slip behaviour could be modelled by introducing the concept of

viscosity hysteresis where the viscosity is dependent on temperature history of the material. This was proposed by Bendzsak and North [32] for the friction welding of. steel to aluminium. This situation is likely to be very similar to that occurring in FSW. The approach will of course only approximate the actual flow condition if the material is slipping at the surface.

2. Material Slip.

   In this approach, the material is allowed to slide along the surface of the tool and a shear stress is applied at the surface according to the surface temperature, slip velocity and the surface pressure. This surface condition is discussed in greater detail in section 10.4.1.3.

The final aspect that needs to be investigated is the modelling of the stick slip mechanism. The first mechanism, namely surface melting may be modelled relatively easily by adjusting the surface condition/material properties according to the temperature of the material. The second, namely the centres of unit seizure is significantly more difficult. Accurate modelling would require analysing the generation and subsequent annihilation of the seizure centres. Such a model would be exceedingly complex. However it is believed that the salient features of the effect are similar to the surface melting case. (ie. temperature fluctuation) Therefore, the process may be modelled in a similar manner.

Obviously the existence of a stick/slip surface condition will make modelling of the Friction Stir Welding process significantly more complex than if the material were modelled as a continuous solid. Not only are accurate predictions of the material

properties required, but also the parameters describing the interface between the tool and workpiece material. Therefore, one has to ask the question: 'Given the supposed complexity of the process and the interface existing between the tool and the material, is modelling warranted?' ie. Will the experiments required to fully understand the boundary surface conditions be so complex as to render it infeasible. One could argue that the current method of improving the process via trial and error will in the end be simpler than the time and effort required to produce a valid numerical model.

4 Experimental Results for Welding 12mm Thick 5083 Aluminium Alloy

4.1 Introduction

These experiments were done to assist the development of a valid thermal model of the process. This was done by:

- Determining the thermal profile produced when Friction Stir Welding 12mm 5083 Aluminium.
- Determining the torque and horizontal loads during the above process. This will enable the determination of the power input to the weld.

4.2 Measuring the Thermal Profile with Thermocouples

4.2.1 Method

Thermocouples were produced by welding the two wires of K-type thermocouple wire onto a piece of steel sheet using an electrical discharge unit. The excess sheet was cut off using tin snips, leaving a small thermocouple which could be poked down a 2mm diameter hole. Direct welding of the thermocouple wire to the aluminium workpiece material was attempted, however a good joint was not produced because of the dissimilar metals.

Having made the thermocouple, the wires were then connected to a 16 channel data logging unit, which was capable of scanning at a rate of 1 measurement per second. Unfortunately the scanning rate could not be increased. This did not seem to adversely affect the quality of the results since the process operates sufficiently slowly that this scanning rate was sufficient. See section 4.2.3. Fifteen of the channels were used to

accept thermocouple data. The last channel was used to accept a timing signal from the FSW control unit, which sent a 5V signal at the start of the weld run, enabling the start time of the weld to be clearly identified. This timing signal was then used to find the time when the centre of the tool passes the thermocouple. This point is indicated on the graphs shown in section 4.2.3.

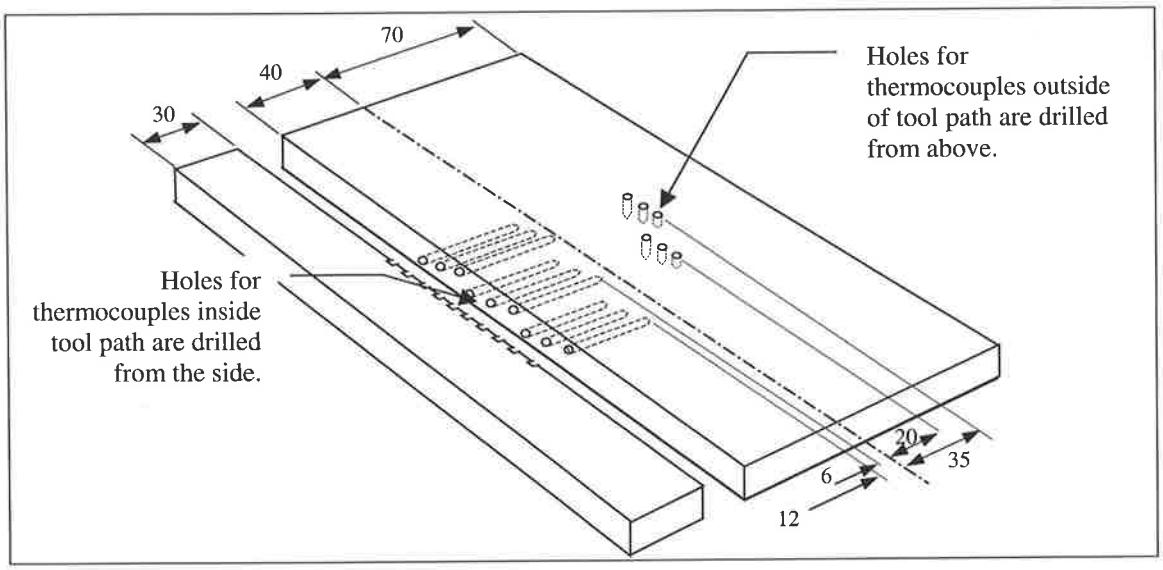

Figure 4-1 Thermocouple Arrangement

The standard thermocouple arrangement is shown in Figure 4-1. The thermocouples that were located near to or in the line of the weld were drilled from the side. The maximum length of the hole was restricted to 40mm, by the length of the drill. Therefore, the material was welded as a bead on plate and the plate was split 40mm from the weld centre-line. The split in the plate will cause a discontinuity across this surface and therefore some loss in the heat transfer. It was noted that the temperature of the smaller plate was lower in the corresponding position to that on the larger plate.

The presence of the thermocouples will affect the temperature profile to a small degree, however according to McClure et. al. [11] their effect was not believed to be significant.

It should be noted that McClure used ϕ = 0.92mm holes while our measurements used ϕ = 2mm holes.

Two weld runs were made using 12mm 5083 and were labelled 000313A and 000313B. The position of the thermocouples with the corresponding channel numbers for the data scan unit, as well as the start and finish positions for each of the weld runs is shown in Appendix C. The two layouts are identical except that the position of the first hole in 000313A was moved to the back of the plate because of tool bit breakage.

4.2.2 Results

4.2.2.1 Checking the Output of the Thermocouples

Before taking any measurements the output of the thermocouples was checked against a known temperature. This was done using ice water and steam. It was found that the error was generally below 1°C in all but two cases where the error was 2°C. Therefore one can be reasonably confident in the accuracy of the results.

4.2.2.2 Operating Data and Conditions

While the temperature data is being collected, data on various aspects of the machine's operation is collected by the Galil Motion Controller, which runs the FSW process. The aspects of the process which were monitored are:

- Horizontal (x) axis power.
- Vertical (z) axis position.
- z axis translational power.
- z axis rotational power.

Note that all the power data is given in terms of a percentage relative to their maximum possible value. The z axis position is given in terms of mm. The operating parameters for the two welds are summarised in Table 4-1.

Table 4-1

Parameter	**000313B**	**000313A**
Rotational Speed (rpm)	350	350
% Max Torque	31.5%	35.1%
Weld Rotational Power (kW) (See calibration curve in section 4.3.1)	3	3.3
Length of Weld (mm)	189	227
Time taken for Weld (sec)	110	126.7
Weld Speed (mm/s)	1.72	1.79
Plunge Rate (mm/min)	10	10
Dwell Time (sec)	5	5
Diameter of Shoulder (mm)	30	30
Type of Pin	12mm Taper Thread	12mm Taper Thread

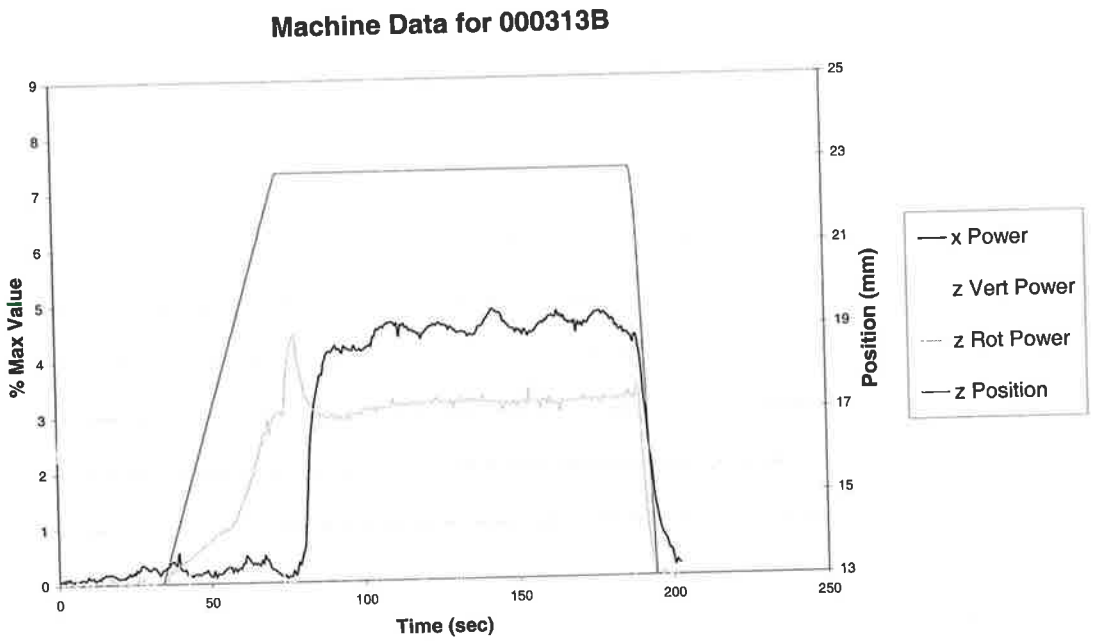

Figure 4-2 Operational Data for weld run 000313B

A graph showing the operating data for weld run 000313B is shown in Figure 4-2. A good weld was achieved with no corrections required for the z axis position (see Figure 4-2), enabling the rotational power and hence heat input to remain fairly constant over the duration of the weld. The x axis power was also fairly uniform. The good operational data was reflected in the quality of the weld, with very little flash being observed on the surface.

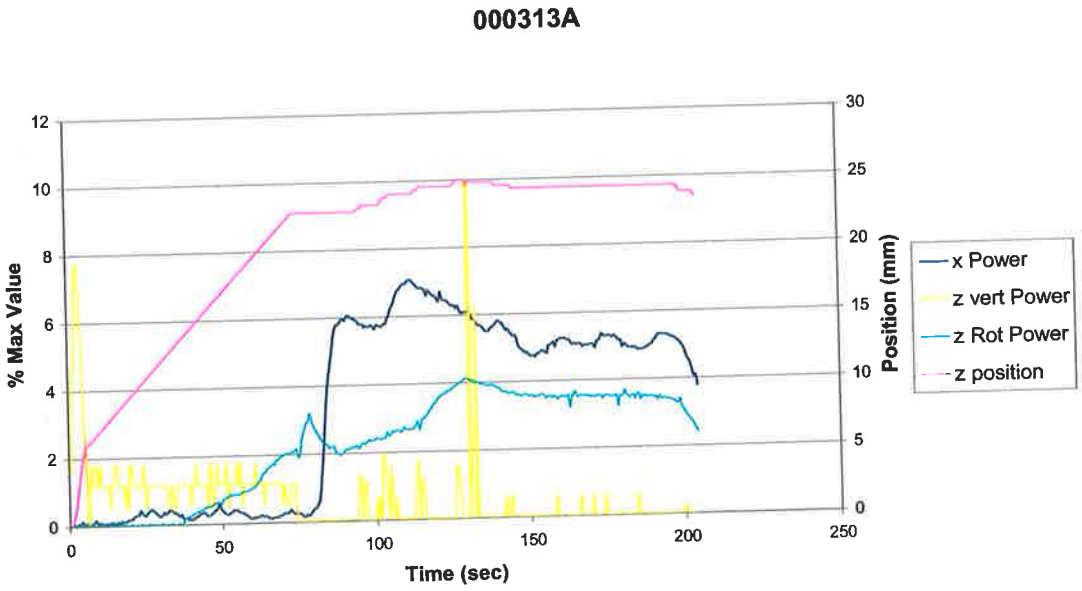

Figure 4-3 Operational Data for weld run 000313A

In contrast 000313A was plunged too deeply into the weld, resulting in excessive flash being deposited on either side of the tool. Secondly, the operational parameters were rather inconsistent as demonstrated by Figure 4-3. There were also several defects in the weld. Although the speed setting on the motion controller was identical for both welds, 000313A was in fact a slightly faster weld due to the lack of any encoder feedback in the control system. Finally the power consumed for 000313A which was calculated for the later part of the weld where it remained relatively constant was slightly higher than for 000313B. This may be attributed to a number of factors, namely:

- The greater traverse speed of this weld.
- The greater plunge, which resulted in some energy wastage in the production of the flash.

4.2.3 Temperature Data for 000313B

The temperature data proved most interesting and is shown in Figure 4-4, Figure 4-6 and Figure 4-5. Thermocouple data was obtained for all channels, however the thermocouple at the centre of the weld near the shoulder stopped reading once the probe had gone past. Presumably the intense mixing caused separation of the thermocouple wires, preventing it from reading data.

Thermocouple data for channels 9, 8 and to a lesser extent 7 (see data 12mm from centre-line in Figure 4-4, Figure 4-6 and Figure 4-5) were affected by the initial plunge of the tool into the material. ie. The transient effect caused by the plunge resulted in slightly higher temperatures prior to the probe passing these thermocouples.

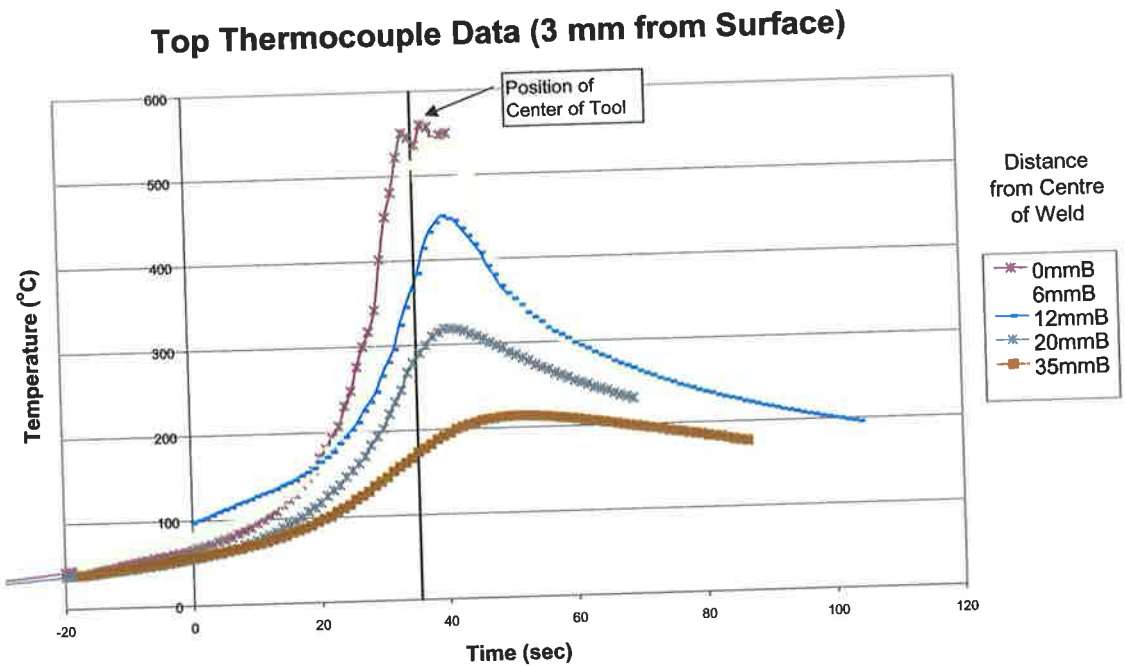

Figure 4-4 Thermocouple Data 3mm from Surface for 000313B

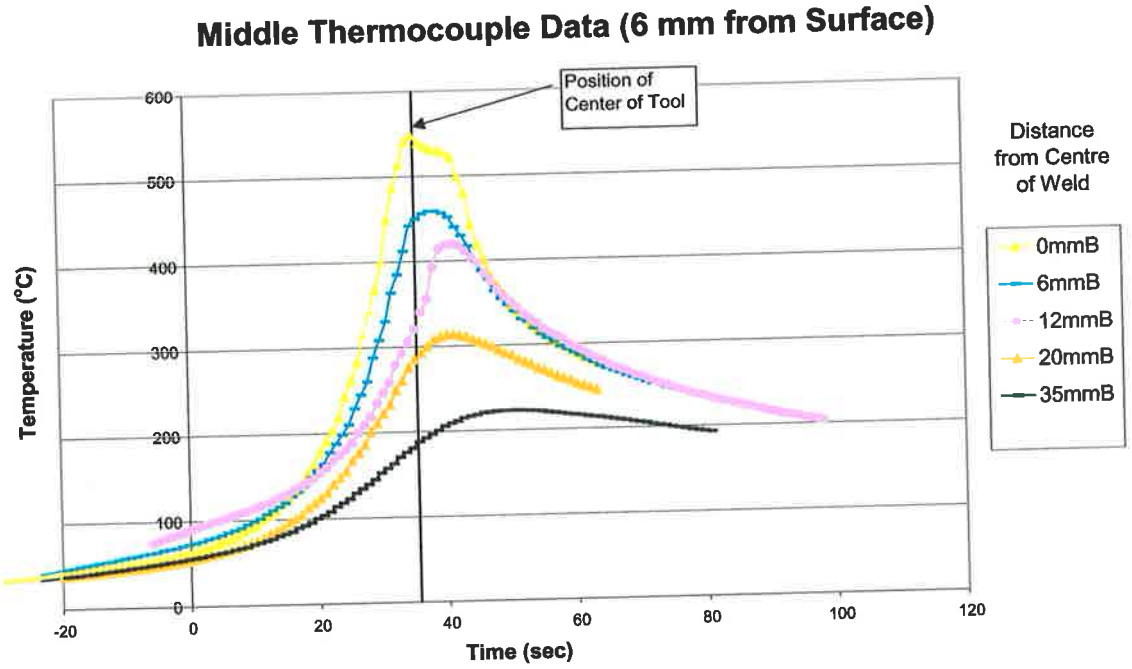

Figure 4-5 Thermocouple Data 6mm from Surface for 000313B

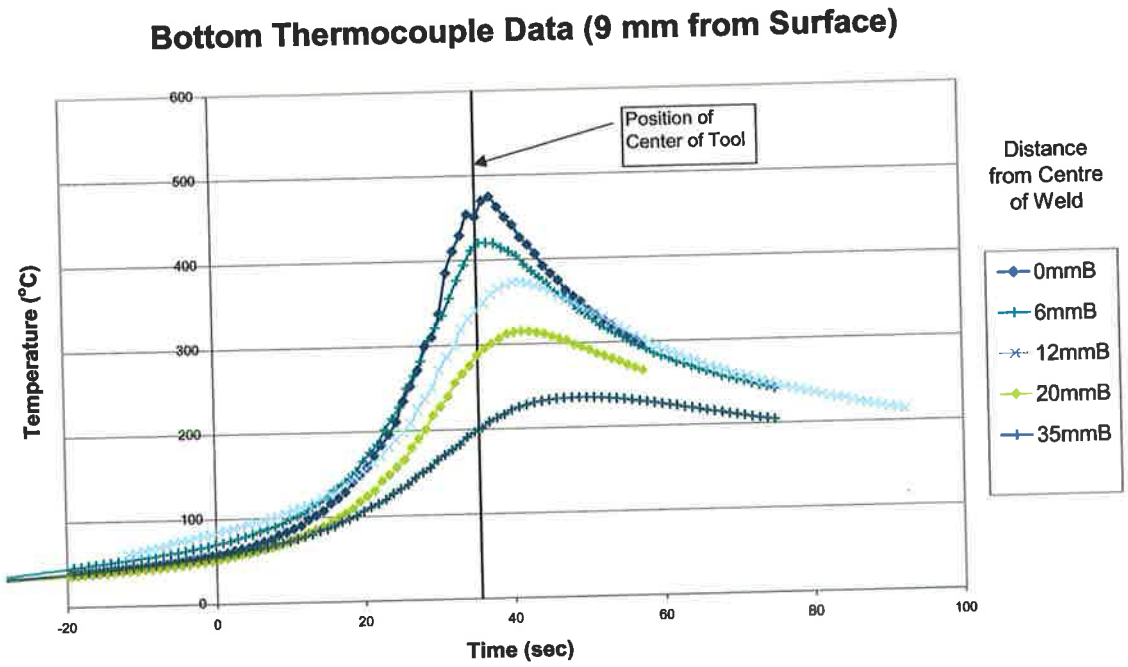

Figure 4-6 Thermocouple Data 9mm from Surface for 000313B

4.2.3.1.1 Top Surface Thermocouples (3mm from the surface)

Figure 4-4 shows that the thermocouples 3mm from the surface recorded the highest temperatures. It is interesting that there is very little difference in temperature between the thermocouples 0mm and 6mm from the centre-line. Presumably this is because of the intense mixing within this region evens out any temperature difference due to conduction. This is also supported by the fact that the temperature peaks in these positions are very flat, while thermocouples in the other positions demonstrate much sharper peaks. The thermocouples which demonstrate sharp peaks in the thermal profile are outside the intense mixing zone. The maximum temperatures of the thermocouples in the mixing zone were 560°C and 540°C for the 0mm and 6mm positions respectively. This compares with the solidus temperature for the material of 574°C. Hence it is highly likely that some degree of melting occurred at the material/tool interface.

Finally, the thermocouples which are furtherest away from the centre of the weld exhibit a much lower peak temperature, which is increasingly offset from the centre of the weld. This is no doubt due to the bow-wave effect of the thermal profile, which can be clearly seen in the thermal model modelling work in section 7.

4.2.3.1.2 Middle Thermocouples (6mm from the surface)

The results for the middle thermocouples (Figure 4-6) were similar to those obtained for the top set with the main difference being in the thermocouple 6mm from the weld centreline. When comparing it to the corresponding position 3mm from the surface:

- The peak for this thermocouple was much sharper

- The temperature of this thermocouple was significantly lower than either the thermocouple at the centre of the weld or the thermocouple above and at the same distance.

Both of these factors point to the fact that mixing of the material at this point was much less.

Finally the peak temperature for the thermocouple positioned along the centreline was 548°C, once again remarkably close to the solidus temperature of 574°C.

4.2.3.1.3 Bottom Thermocouples (9mm from the surface)

The thermocouples at the base of the plate (Figure 4-5) have a lower temperature again, particularly the thermocouple at the centre of the weld. This had a much sharper peak and demonstrated much less mixing than the two thermocouples above. Peak temperature was 478°C. Therefore, surface melting was unlikely to occur. The thermocouples further from the weld centre were progressively cooler, with the peak being further offset behind the weld centre due to the bow wave effect.

4.2.3.1.4 Comparison Between Thermocouples Equidistant from the Weld Centre

Another interesting comparison is that between thermal profiles of thermocouples equidistant from the centre of the weld. See Figure 4-7, Figure 4-8 and Figure 4-9. For the thermocouples near the centre of the weld and under the shoulder, the temperature at the top is significantly higher than at the base because most of the heat is generated at the shoulder of the tool. One exception to this are the thermocouples 3mm and 6mm from the top surface at the centre-line. (See Figure 4-7) The intense mixing plus the heat generation at the pin tends to even out the temperature distribution at this point.

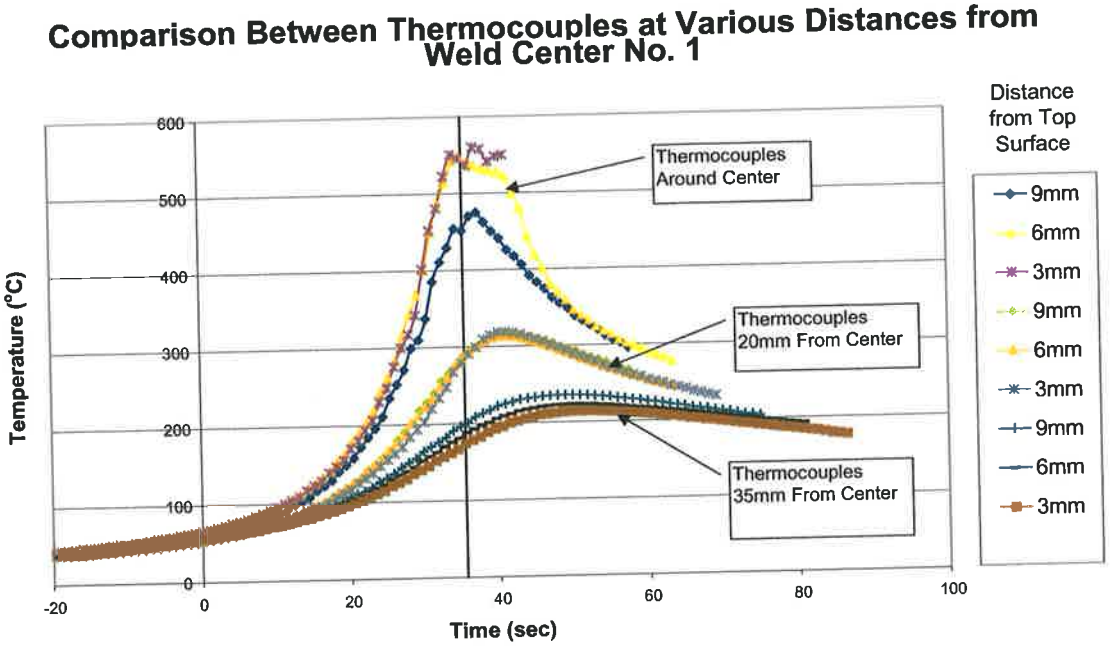

Figure 4-7 Comparison Between Thermocouples 0, 20 and 35 mm from the Weld

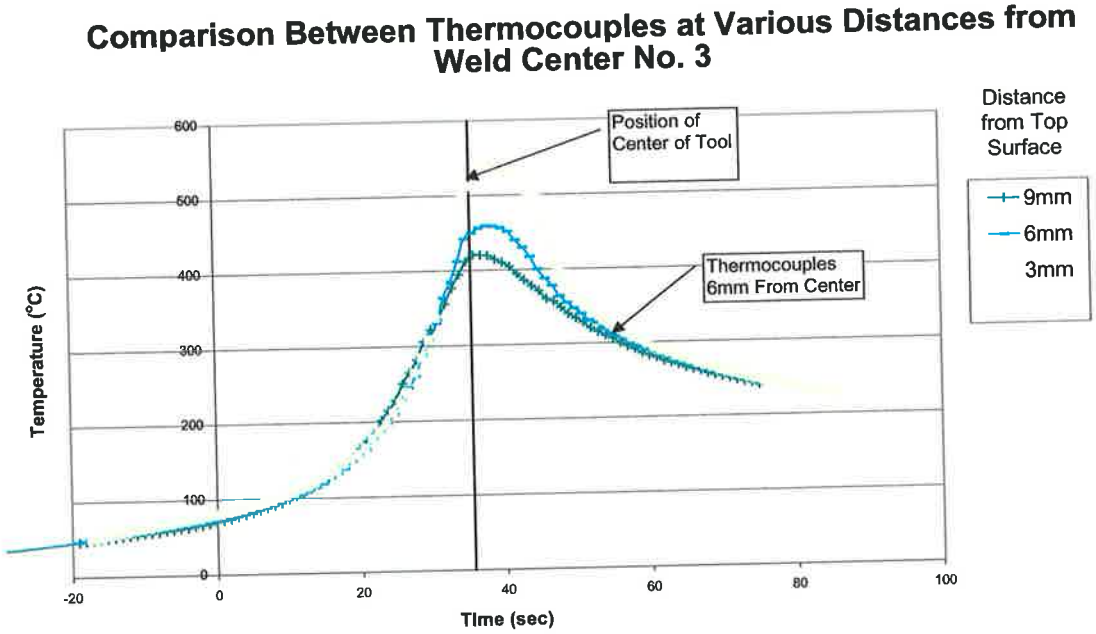

Figure 4-8 Comparison Between Thermocouples 6 mm from the Weld

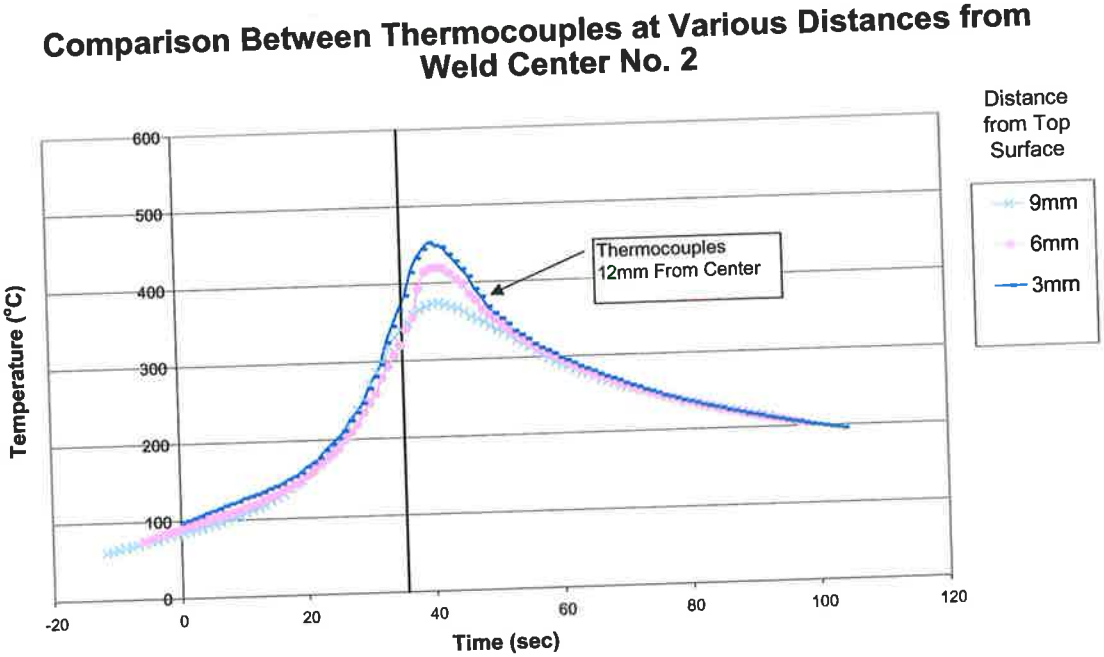

Figure 4-9 Comparison Between Thermocouples 12 mm from the Weld

For the thermocouples which are 20mm, from the centre, the thermal profiles are nearly identical.

Finally, for the thermocouples which are 35mm from the weld, the temperature at the top of the plate is in fact slightly cooler than that experienced at the base. It is believed that this is caused by the dual effect of air cooling and the plate clamp which is adjacent to the thermocouples in this position. Both of these factors assist the cooling of the plate on the top surface.

4.2.4 Temperature Data for 000313A

Despite this weld being done at a slightly faster speed and with more power, the temperature results were remarkably similar to those obtained for 000313B. It is believed that much of the extra power was used in producing the excessive flash.

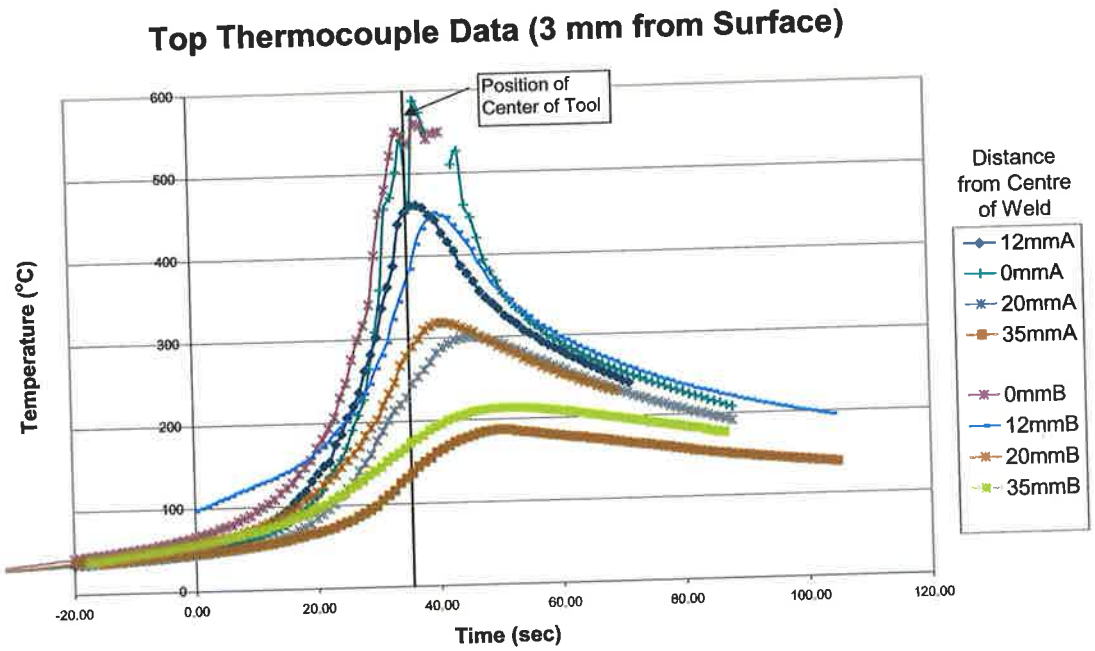

Figure 4-10 Comparison between 000313B and 000313A, 3mm below surface for positions 0, 12, 20 and 35 mm from centre-line.

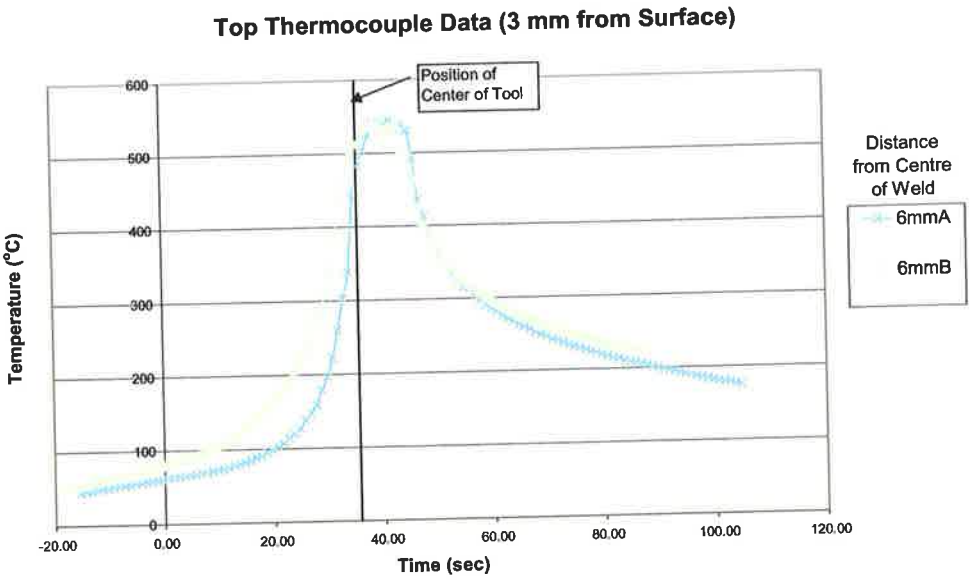

Figure 4-11 Comparison between 000313B and 000313A, 3mm below surface for 6mm from centre-line.

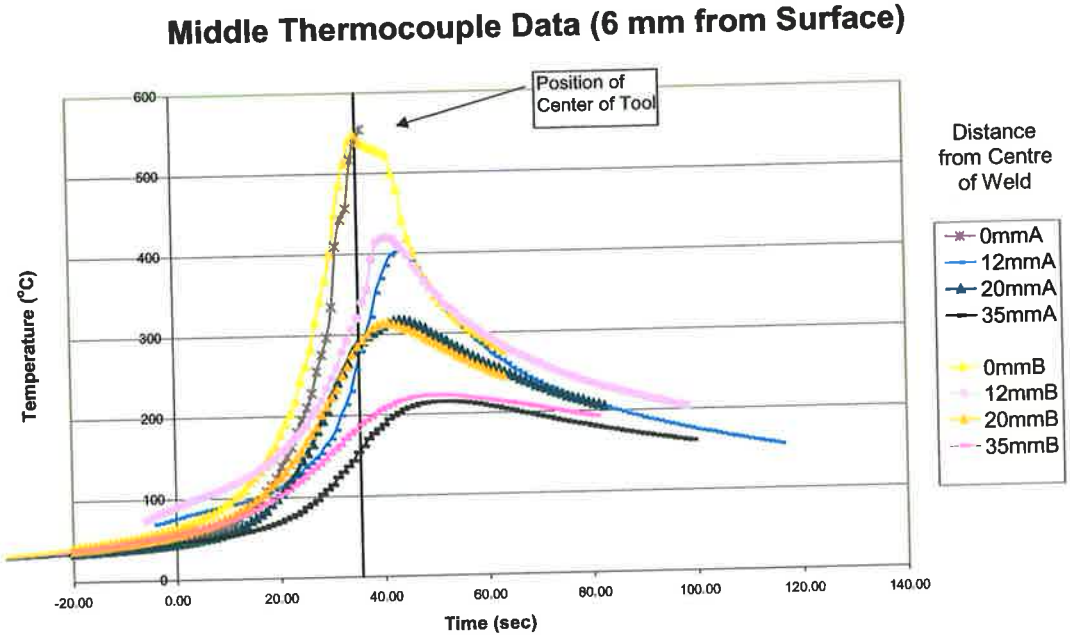

Figure 4-12 Comparison between 000313B and 000313A, 6mm below surface for positions 0, 12, 20 and 35 mm from centre-line.

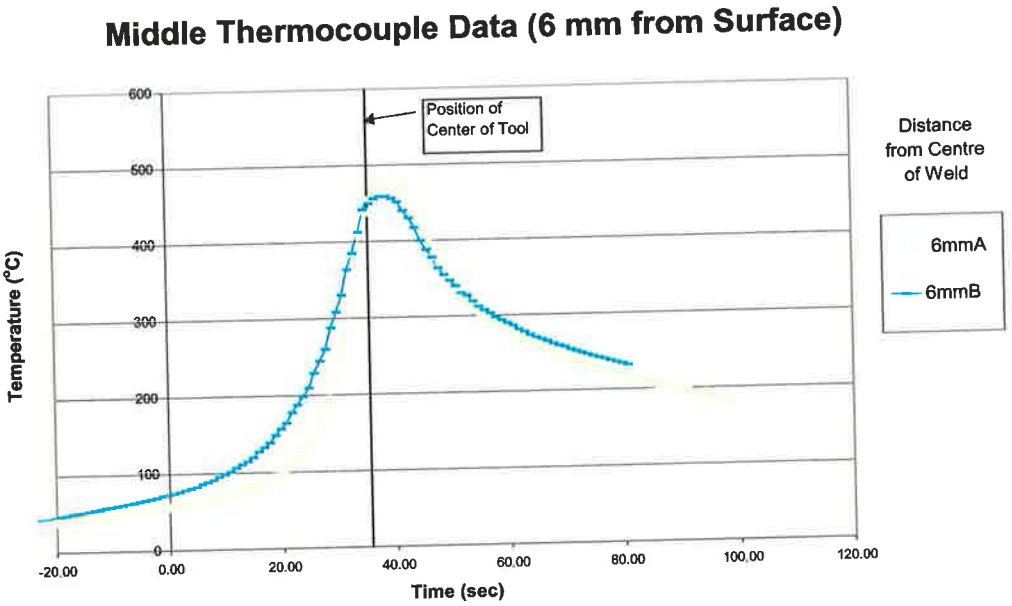

Figure 4-13 Comparison between 000313B and 000313A, 6mm below surface for 6mm from centre-line.

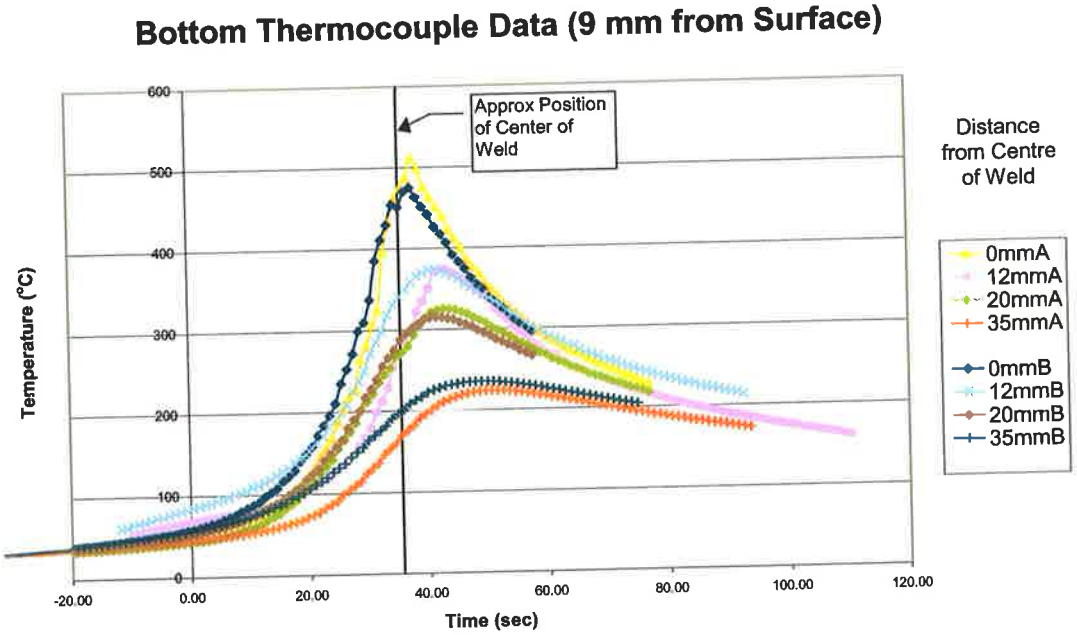

Figure 4-14 Comparison between 000313B and 000313A, 9mm below surface for positions 0, 12, 20 and 35 mm from centre-line.

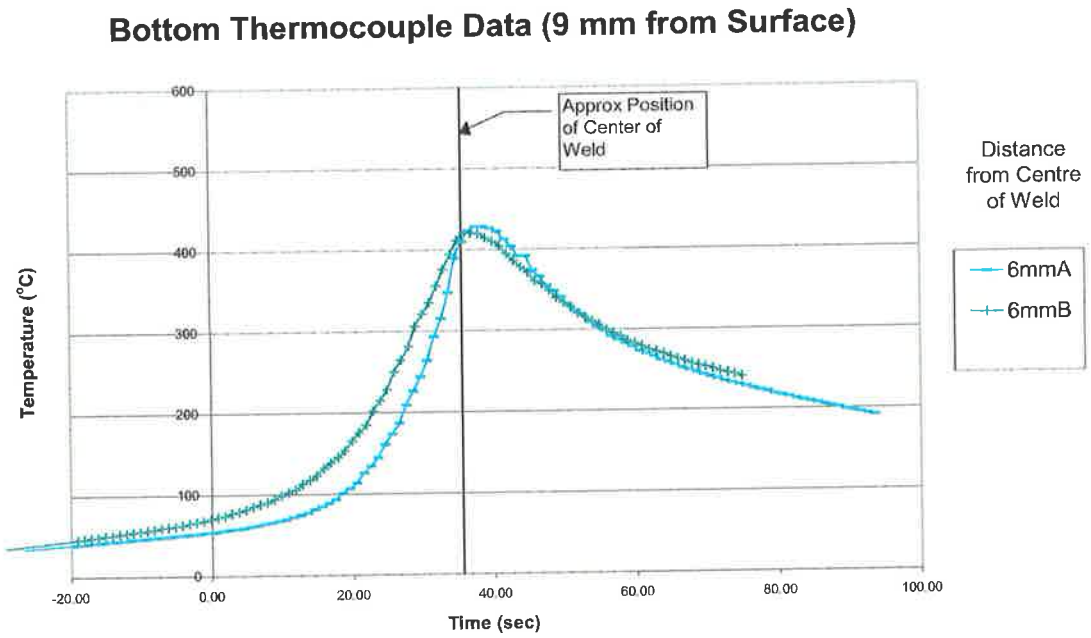

Figure 4-15 Comparison between 000313B and 000313A, 9mm below surface for 6mm from centre-line.

Rather than reproducing many of the same curves shown in section 4.2.3, graphs showing comparison between these results and those for 000313A are shown in Figure 4-10, Figure 4-11, Figure 4-12, Figure 4-13, Figure 4-14 and Figure 4-15.

The following observations can be made:

- The thermocouple mid-section in the weld stopped reading altogether and the thermocouple in the upper section of the weld did similarly, however later gave a reading after the tool had passed. See Figure 4-10.
- The speed of the traverse appears to have fluctuated slightly over the duration of the weld. This is demonstrated by the thermal profile for the thermocouple 3mm from the surface, 12mm from the centre of the weld. See in Figure 4-10. It is much closer to the centre of the weld than the corresponding profile in the 000313B weld.

4.2.5 Conclusions

Given more time a more thorough investigation of the thermal profiles obtained from a variety of operating conditions would be made. Nevertheless, the following conclusions can be made from the two experiments:

- The correlation between the thermal profiles of the two welds performed under similar operating conditions was high.
- The fact that the thermal profiles were so similar, while the weld qualities were so different suggests that an assessment of the thermal profile is not a valid way of determining whether or not a weld will be successful.
- Given that the two thermal profiles were so similar, the extra power required to weld 000313A appears to have been consumed in the production of the excessive flash.
- The temperatures measured in both welds were very near the solidus temperature for the material. Therefore, some form of surface melting is highly likely which limits the generation of heat.
- The thermocouples in the deformation zone exhibited fairly flat peaks in the thermal profile due to the mixing of the material in this region. The thermal profiles of thermocouples outside this region exhibited much sharper peaks.

4.3 Determining the Power Input

The verification of the thermal model requires that the heat input while welding should be known. This requires a knowledge of the torque produced by the FSW spindle and the horizontal load during welding. The heat input can be determined from these values plus the rotational speed of the spindle and the horizontal welding speed.

All the measurements have been done on the Butler Friction Stir Welding Machine. The vertical spindle motor of this machine is connected to an ABB ACS 600 Frequency Converter. This frequency converter produces a voltage, which depends on the output torque of the motor. The value varies between 0 and 10 Volts; 0 Volts indicating no load and 10 indicating that the motor is producing the full load torque. The value of this voltage is independent of the speed of the motor. The torque produced by the motor will not equal the torque at the spindle. There is a 2:1 gear reduction between the spindle and the FSW head plus there are bearings in the spindle head to support against horizontal loads and some losses will occur in the belt drive gear reduction. Referring to Figure 4-16, the actual power at the head will be equal to:

$$P_s = T_s\omega_s = 2T_m\omega_s - Q_{belt} - Q_{bearing} \qquad \textbf{Eq. 4-1}$$

Hence, taking the power from the motor only without considering the losses through the belt drive and bearings will give an incorrect result. To solve this problem, direct torque measurement at the spindle is required. This section describes how this has been achieved so that a relationship between %max torque of the motor and torque at the spindle can be found.

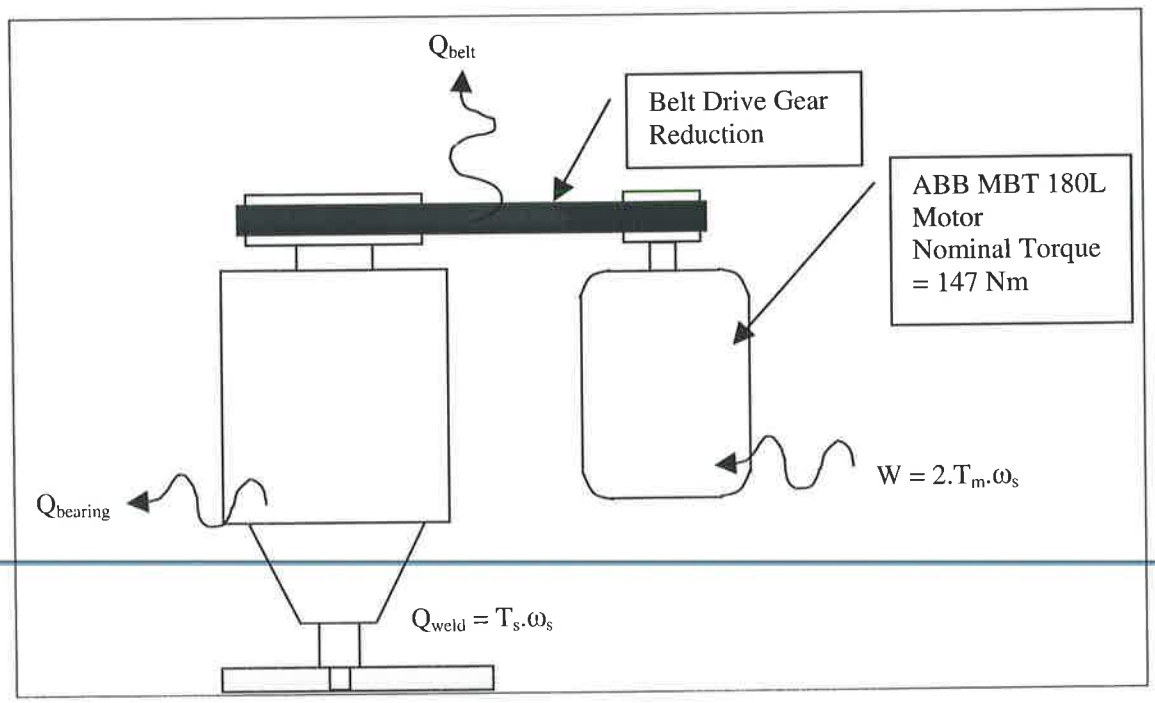

Figure 4-16 Spindle Drive on Butler FSW Machine

Measuring the horizontal load on the spindle is simpler. This is done by measuring the horizontal force with a load cell while welding, and is described in the second part of the document.

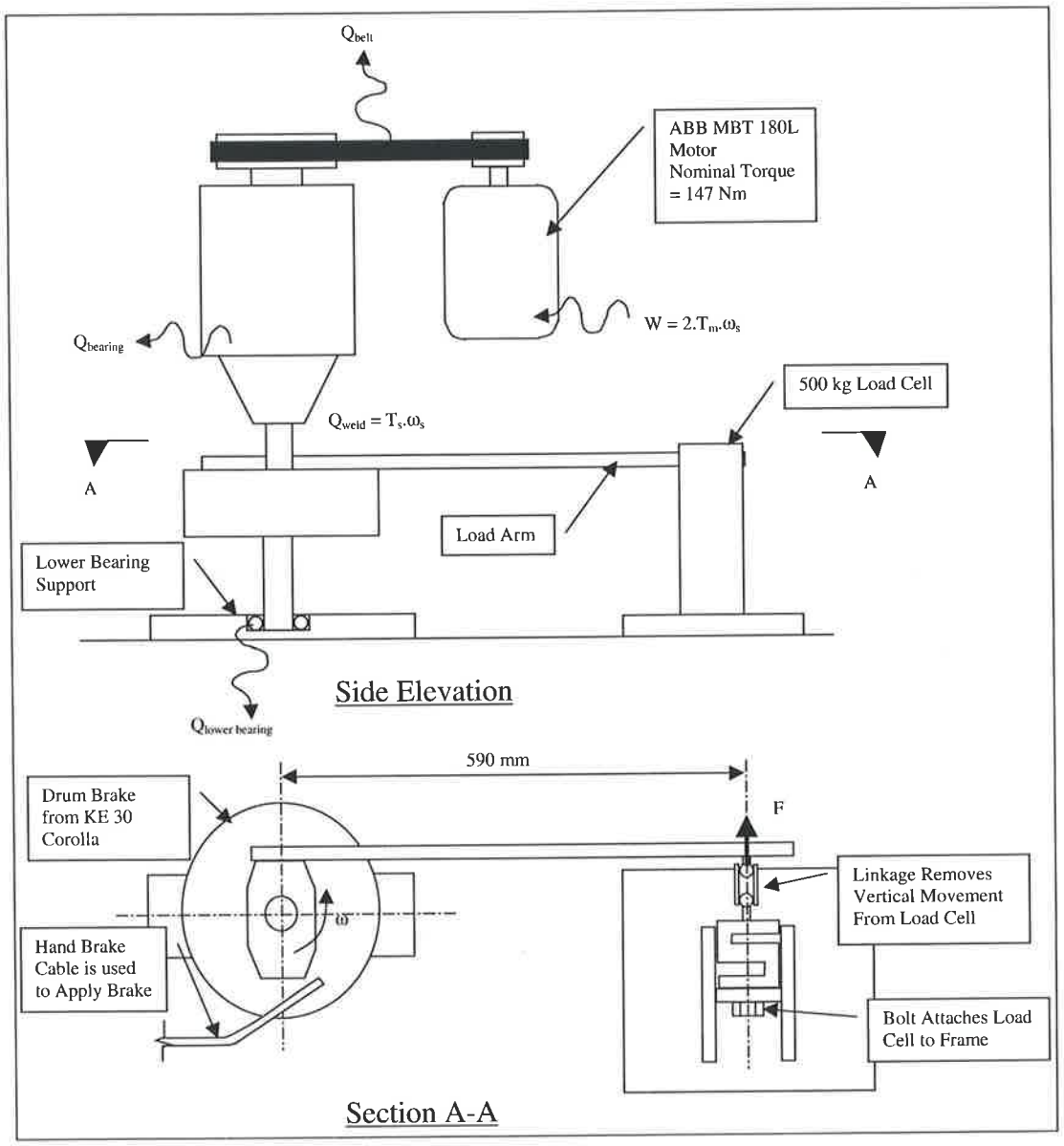

Figure 4-17 Layout of Torque Measuring Device

4.3.1 Torque Measuring Device

4.3.1.1 Description of Equipment

A layout of the equipment used for the Friction Stir Welding Torque Measuring Device is shown in Figure 4-17. The only problem with the design is the power loss from the lower bearing, which will tend to slightly lower the observed value of the force measured at the load cell. It is assumed that the resistance of this bearing is sufficiently low that it can be neglected. Note also that there is a linkage between the load cell and the load arm. This stops any vertical movement of the load arm being transferred to the load cell.

An energy balance on the system shows that:

$$0.59F\omega_s + Q_{belt} + Q_{bearing} + Q_{lowerbearing} = 2T_m\omega_s \qquad \textbf{Eq. 4-2}$$

Hence the force on the end of the load cell will be given by:

$$T_s = 0.59F = \frac{2T_m\omega_s - Q_{belt} - Q_{bearing} - Q_{lowerbearing}}{\omega_s} \qquad \textbf{Eq. 4-3}$$

The force measured at the load cell is output as a voltage from the load cell amplifier. This voltage is monitored by the Galil Motion Controller, which controls the operation of the equipment.

4.3.1.2 Problems with the Device Operation

When performing the experiment the following problems were encountered:

- There was significant oscillation of the load arm when the spindle was rotating. This was caused by the spindle not being parallel to the drum brake housing, due to a misalignment of the bearing. Hence at a radius of 0.59m

there was approximately 20mm oscillation of the load arm. Unfortunately, this oscillation may have also increased the energy loss in the system.

- There was significant noise in the readings from the load cell. Initially, it was thought that the noise was caused by the oscillation of the torque measuring device. However a test later showed that when the load cell was not connected there was still a significant amount of noise in the voltage output. Therefore, it was concluded that the noise was primarily caused by electrical RF noise from the spindle motor.

Because of these problems the following smoothing function was used when analysing the results:

$$T_i = \frac{T_{i-1} + 2T_i + T_{i+1}}{4} \qquad \textbf{Eq. 4-4}$$

This was repeated 10 times to get reasonably smooth data.

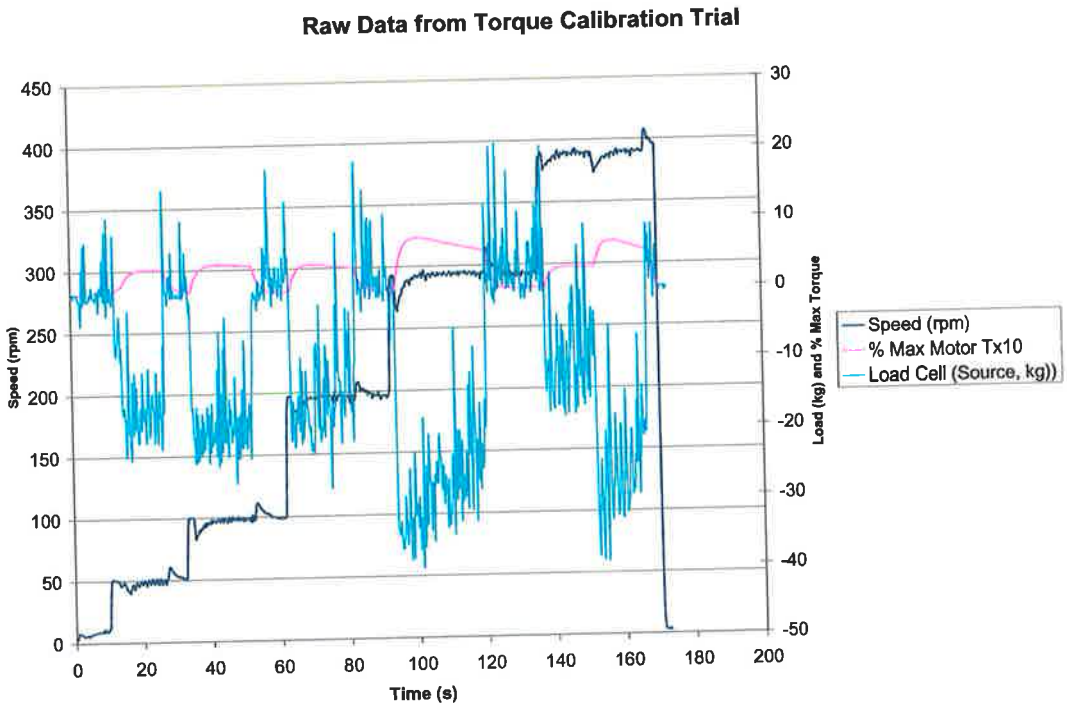

Figure 4-18 Raw Data

4.3.1.3 Results

The unsmoothed data is shown in Figure 4-18. The noise is clearly visible.

An example of the noise with no load on the load cell is shown in Figure 4-19. This clearly demonstrates that the bulk of the noise in the readings is not mechanical, but electrical. After smoothing this load data the curve shown in Figure 4-20 was obtained. Selected areas were then used to produce calibration plots between the input torque of the motor and the torque output from the torque-measuring device. The first graph shown in Figure 4-21 demonstrates that the calibration curve is independent of speed. The second graph (Figure 4-22) shows all the data plotted together with a trendline to giving the calibration curve between the two results.

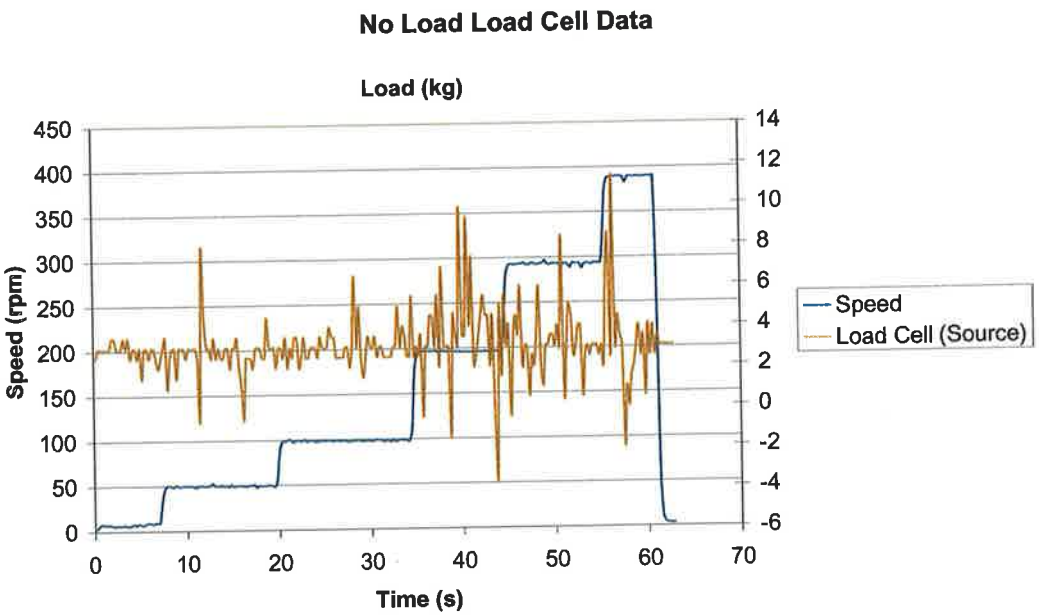

Figure 4-19 No Load, Load Cell Data

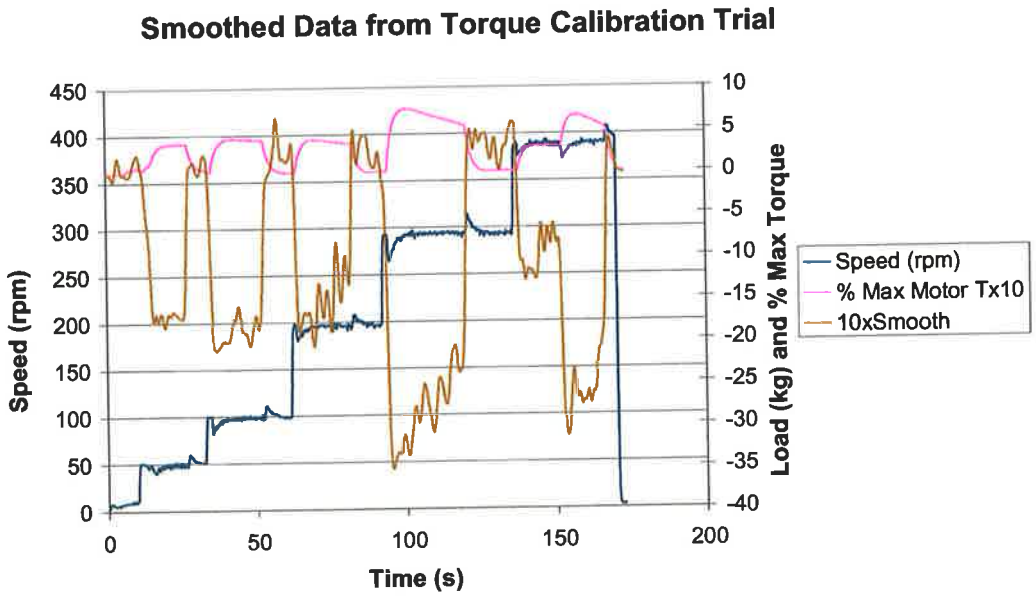

Figure 4-20 Smoothed Data

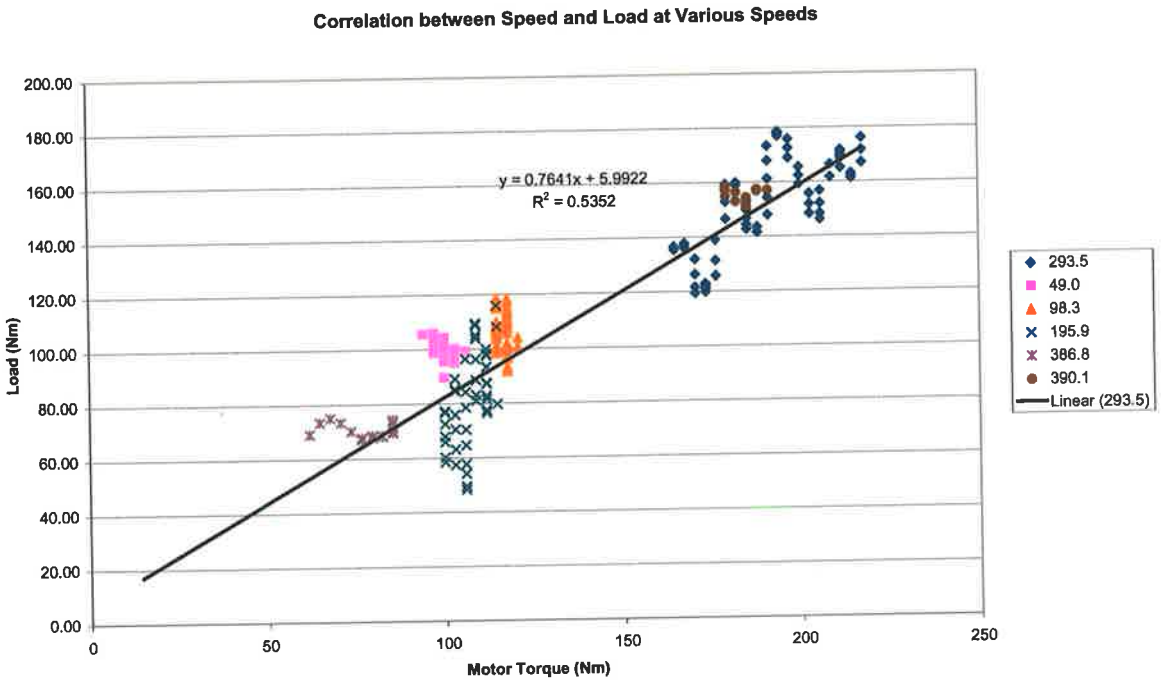

Figure 4-21 Results at Different Speeds for Motor Torque vs. Load Cell Torque (Nm)

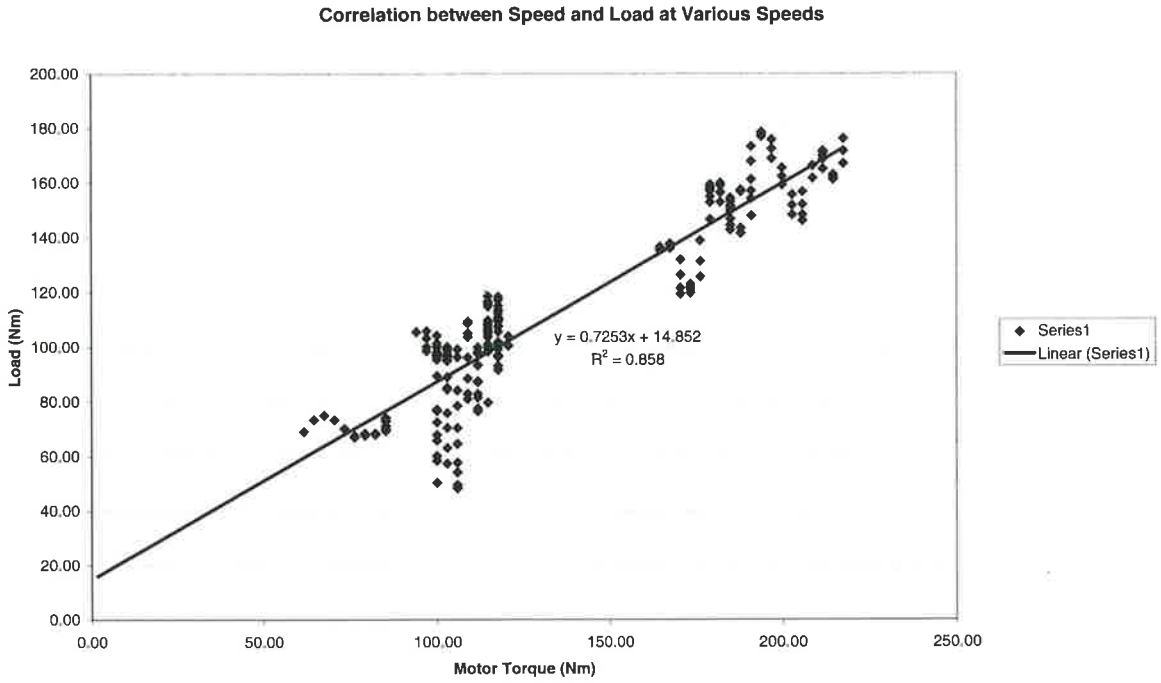

Figure 4-22 Results for Motor Torque vs. Load Cell Torque (Nm)

4.3.1.4 Discussion

One interesting feature that was observed in the results was how for a given setting on the hand brake, the load on both the load cell and the motor reduced over time. This was particularly noticeable at high speeds and braking loads and can be attributed to the brake pads heating up and losing their efficiency.

It was found that during weld 000313B, the %Max torque reading of the motor was 3.15. This resulted in a heat input of 2.96kW to the workpiece based on the calibration curve in Figure 4-22. The corresponding power output of the motor was 3.34 kW based on a nominal load of 147Nm. Hence there was a 12.9% energy loss through the drive system, based on the calibration curve. The comparison between the calculated heat input and that expected from modelling is discussed later in section 7.3.3 and 8.4.

4.3.2 Horizontal Force Measurement

4.3.2.1 Description of Equipment

The equipment for measuring the horizontal force is shown in Figure 4-23. The apparatus is simple. The only modification to the standard welding set-up is that the backing plate is mounted on rollers and a load cell is placed on the end of the assembly. The load cell acts in compression.

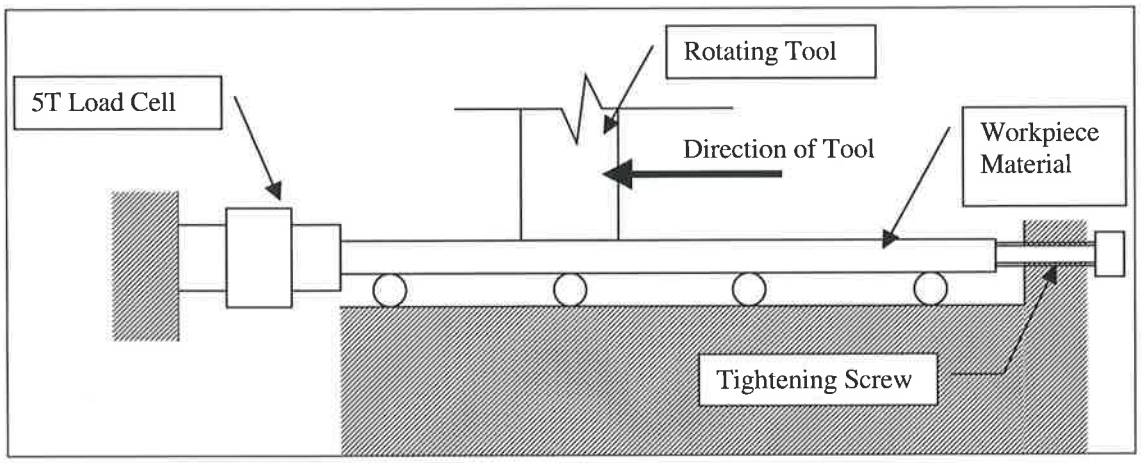

Figure 4-23 Layout of Horizontal Force Measurement

Note the tightening screw on the end of the plate. This was used to hold the plate firmly in position while welding. It was found that if this screw is tightened for the duration of the weld, the expansion of the plate causes an additional load on the load cell. Therefore once the tool had been plunged into the material the screw was released and the force of the tool holds the plate in position.

4.3.2.2 Method

Two welds were carried out and were labelled 000614C and 000614D. Both plates were 12mm thick 5083, 250 mm long and 110 mm Wide. The plates were welded as a bead on plate. Both of the welds used the operating parameters shown in Table 4-2.

Table 4-2

Speed (mm/min)	Speed (mm/sec)	Length of Travel (mm)
30	0.50	10
60	1.00	50
90	1.50	50
100	1.67	50

Also the following parameters were used:

- Dwell Time = 5 sec.
- Plunge: 10mm/min; 300 rpm
- Weld Rotational Speed = 350 rpm.

As mentioned previously, the *x* axis drive did not use a servo motor, however the total length of the weld was measured afterwards and found to be exactly 160mm on both welds. Therefore it was assumed that the welding distances prescribed by the above program were in fact achieved.

4.3.2.3 Results

Despite the fact that the original weld 000313B was a successful weld without a groove, the Bead on Plate Weld in this experiment was not successful, with a large groove occurring along the length of the weld. This was worse in the second weld (000614D). Since all the welding parameters were identical, the possible causes of this discrepancy were:

- Additional movement of the plate on the roller assembly resulting in a less effective weld.

- Wear on the tool, reducing its effectiveness.

Graphs plotting the results are shown in Figure 4-24 and Figure 4-25. The three values which are plotted are:

- Average Load (kg). The data has been smoothed by taking a running average of 10 readings. This is to remove the effect of electrical noise. Note that the data has not been adjusted so that zero kg is actually zero on the plot.
- Load (x-axis drive). This gives the % Max torque on this motor and is an indication of the motor's load. In general, these readings should correlate with those from the load cell.
- Spindle Torque. Once again this gives the % of the maximum torque on the spindle drive motor.

The average horizontal forces at the various travel speeds for each of the welds are shown in Table 4-3 and are plotted in Figure 4-26. The values have been adjusted to take away the zero offset of the load cell.

Table 4-3

Speed (mm/min)	000614C Load (kN)	0000614C Power (W)	000614D Load (kN)	0000614D Power (W)
60	4.04	4.04	3.61	3.61
90	4.98	7.47	4.32	6.48
100	5.27	8.78	4.37	7.29

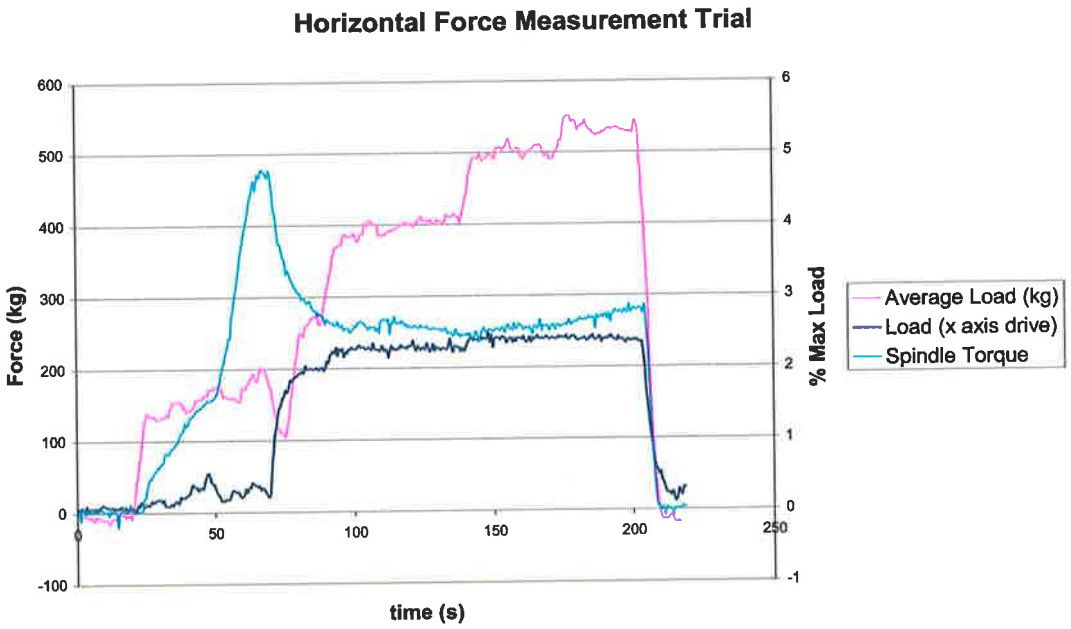

Figure 4-24 Horizontal Force Measurement for 000614C

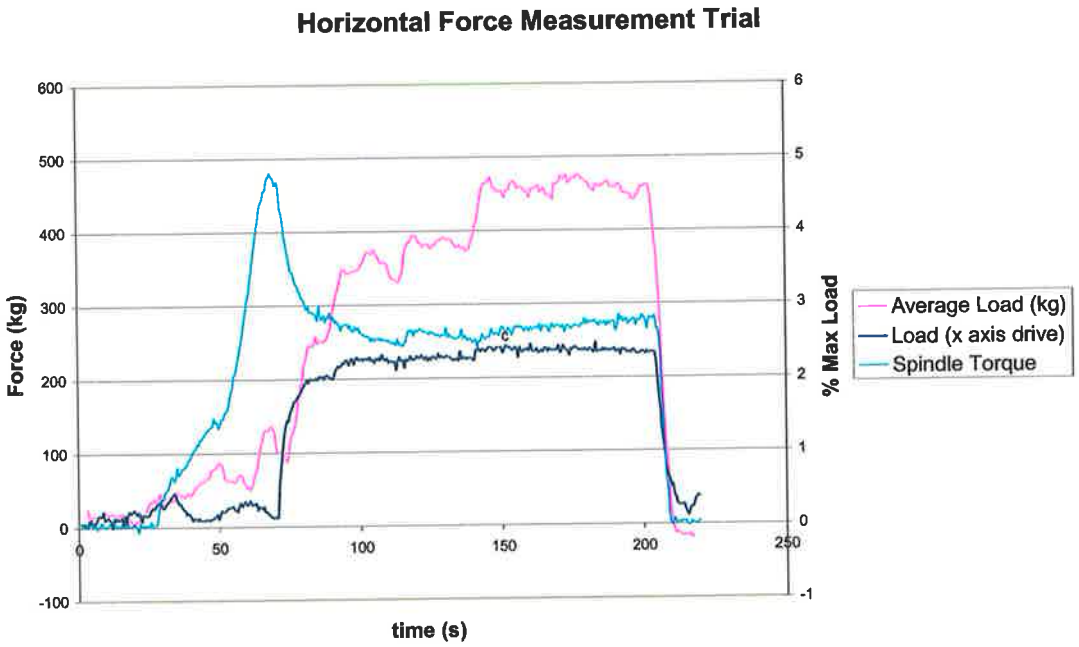

Figure 4-25 Horizontal Force Measurement for 000614D

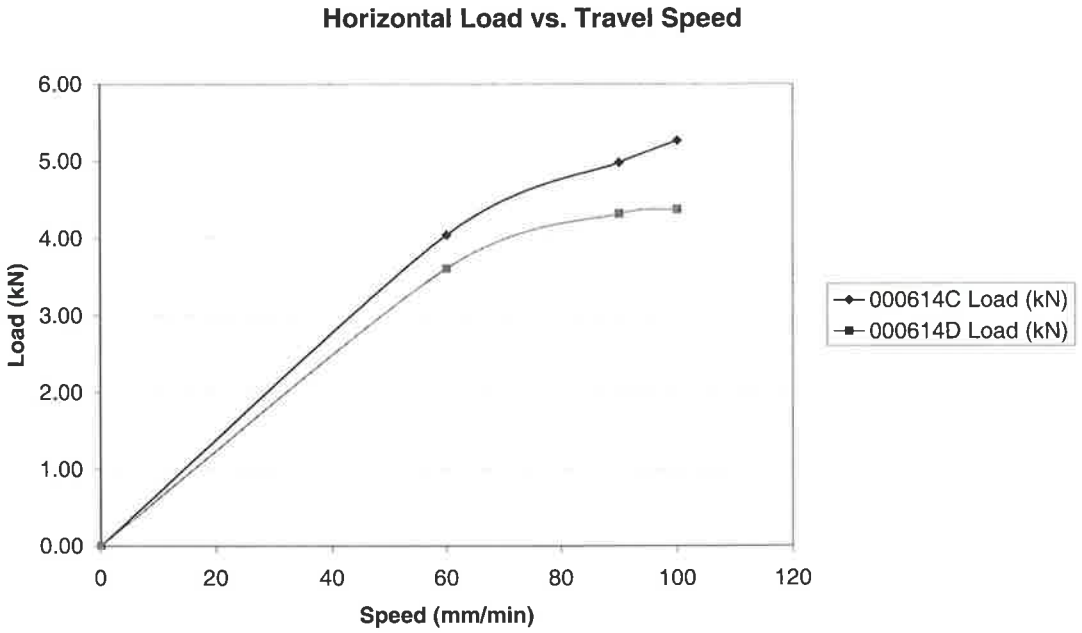

Figure 4-26 Horizontal Load vs. Travel Speed

4.3.2.4 Discussion

Even though the two welds were done under identical conditions, the results obtained were quite different, namely:

- The measured horizontal load across all welding speeds for the first weld was significantly higher than for the second.
- During the first weld the horizontal load was quite substantial during the plunge when it should be near zero.

The possible reasons for these discrepancies are:

- Although it was stated in section 4.3.2.1 that the tightening screw was loosened after the weld was started, there is a slight possibility that this may not have been done for the first weld. This would account for the both the higher overall loads and the non-zero horizontal force during the plunge. ie.

The heating of the plate causes it to expand, giving a non-zero horizontal load.

- The second weld had a greater plunge, increasing the vertical load on the spindle and hence also the horizontal load due to greater movement of material around the pin. ie. This weld had a much smaller groove.

In any case the discrepancy is not likely to be particularly important because the horizontal load is less significant than the torque of the spindle when it comes to heat input. The power input due to the horizontal drive is around 0.34% of that due to the spindle and is therefore not significant enough to be considered. The horizontal load will only be a concern when calculating the chance of a tool breakage.

Finally, it is worth comparing the measured values against those obtained by Johnson and Horrex [63] for 6mm thick 5083. The horizontal load at 100mm/min, is approximately twice the value that Johnson and Horrex obtained at 112mm/min and 710 rpm. This indicates that the horizontal load could be approximately proportional to the thickness of the material being welded. Secondly, Johnson and Horrex found that the horizontal load at higher traverse speeds virtually remained constant. No such observation was found in the above measurements, however the load did seem to flatten off with increasing traverse speed. See Figure 4-26.

5 Microstructural Analysis of 000313B

Microstructural analyses were done for the weld 000313B to confirm that a sound weld had been achieved and to examine the main features of the weld in greater depth.

5.1 Background to 5083 Microstructures

Surprisingly, very little has been published on the microstructural evolution of 5083, with much of the microstructural work to date being done on precipitation hardened alloys.

Threadgill and Leonard [76] discussed their microstructures briefly, making the following points about the observed microstructures:

1. The HAZ shows a reduction in the hardness due to the annealing out of vacancies and dislocations.
2. The Thermo-Mechanically Affected Zone (TMAZ) exhibits substantial work hardening, however most of this is lost due to the recovery induced by the high temperature in this region. Therefore there is no increase in hardness.
3. Finally the dynamically recrystallised region has the lowest hardness of all. This is because of the extremely low dislocation density in the recrystallised grains. The typical size of the grains in this area were found to be 10 μm.

This was supported by Larsson et. al. [75], who showed that the drop in hardness across a 5083 weld was minimal. Larsson et. al. believed that the small drop in hardness across the weld was due to annealing.

5.2 Light Microscopy

5.2.1 Pin Retraction Defect

The pin retraction defect from section 3.4.10 will be examined in greater depth. A photo of the defect from above is shown in Figure 5-1 which includes a ruler with 0.5mm graduations beside the weld.

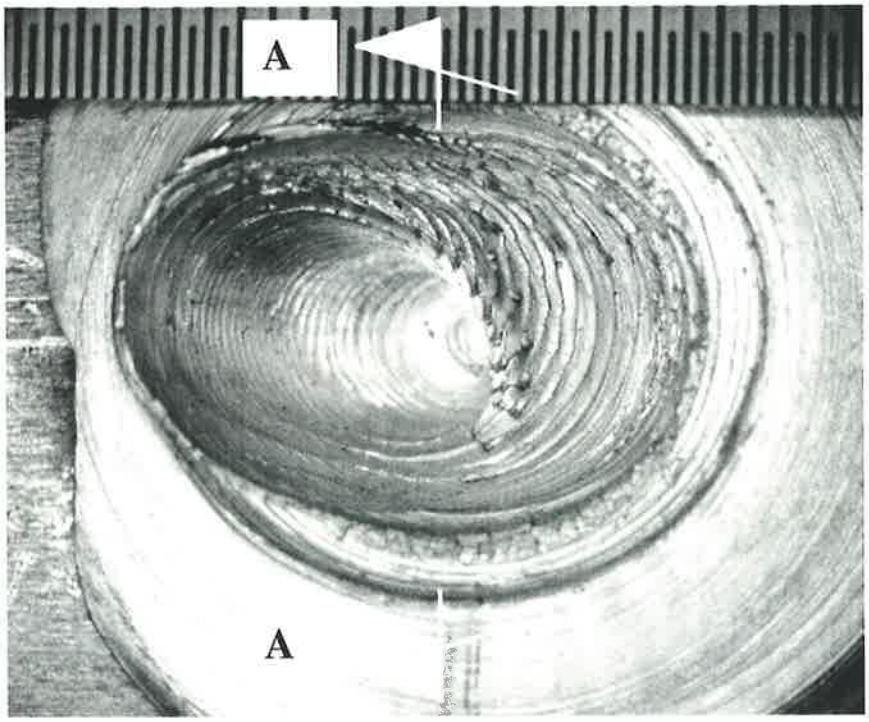

Figure 5-1 Pin Retraction Defect Size

From this image it can be ascertained that the distance between consecutive layers are approximately 0.7mm apart soon after the pin starts to retract and 0.5mm apart as it slows down. Assuming that the traverse speed is 1.72mm/s soon after the pin starts to retract, this corresponds to a period between the slip times of 0.4 sec. This is slower than the period of the spindle which is 0.171 sec. From this it can be inferred that the stick slip behaviour of the material does not coincide with the rotation of the spindle.

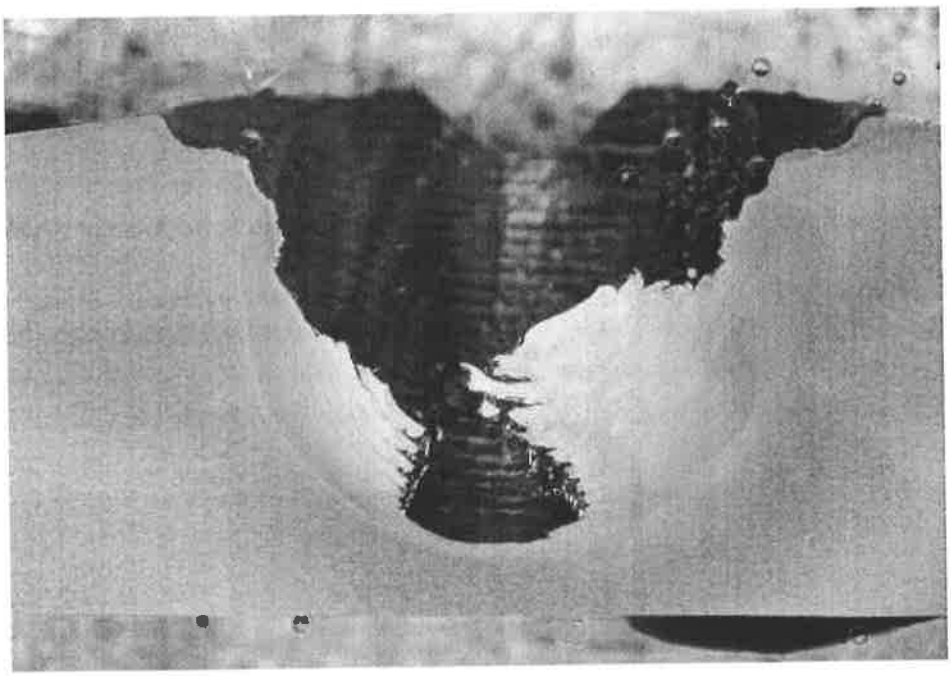

Figure 5-2 Section A-A Through Pin Retraction Defect

A section of the defect in Figure 5-1 is shown in Figure 5-2. Note that the sample was mounted on a clear substrate enabling the retraction area to be seen. From this section a partly formed dynamically recrystallised zone can be seen. Interestingly, the shape of

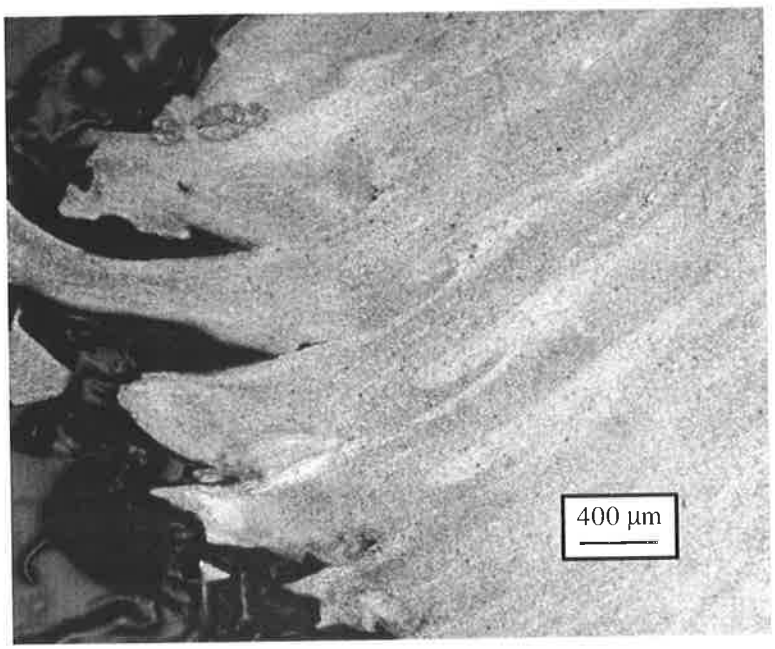

Figure 5-3 Layers in Retraction Defect (2.5x)

the flow lines in the dynamically recrystallised region were remarkably similar to those observed in a typical FSW microstructure. (Compare with Figure 5-5) ie. The fact that only half the material was present did not effect the basic shape of circular flow pattern. A close up view of the stir region of this is shown in Figure 5-3. The approximate width of the stir layers is 500 μm, which compares with the pitch of the tool thread of 4mm (4000 μm). Hence there is an order of magnitude difference.

Finally the area between the TMAZ and the dynamically recrystallised zone was examined and is shown Figure 5-4. It can be clearly seen how the grains are deformed up to 90° before they then start to recrystallise. This observation confirms that by Threadgill and Leonard [76].

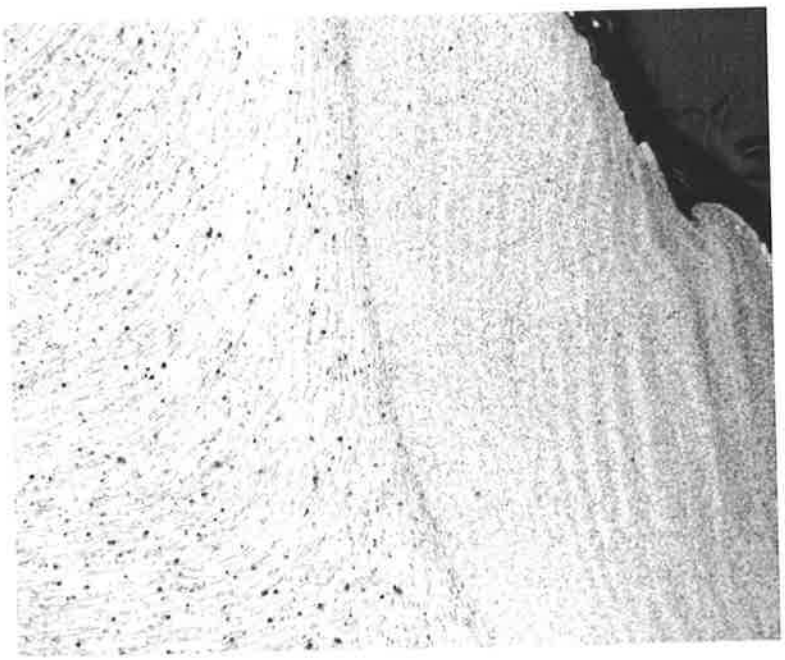

Figure 5-4 Boundary Between TMAZ and Dynamically Recrystallised Region (2.5x)

5.2.2 Through Weld Microstructure

Because it was not possible to fit a cross section of the weld sample onto a single base, it was divided into the two halves. The left half is shown in Figure 5-5.

It can be seen that the weld is reasonably sound. It is believed that the two holes near the top of the weld were caused by the thermocouple holes in that region. The HAZ,

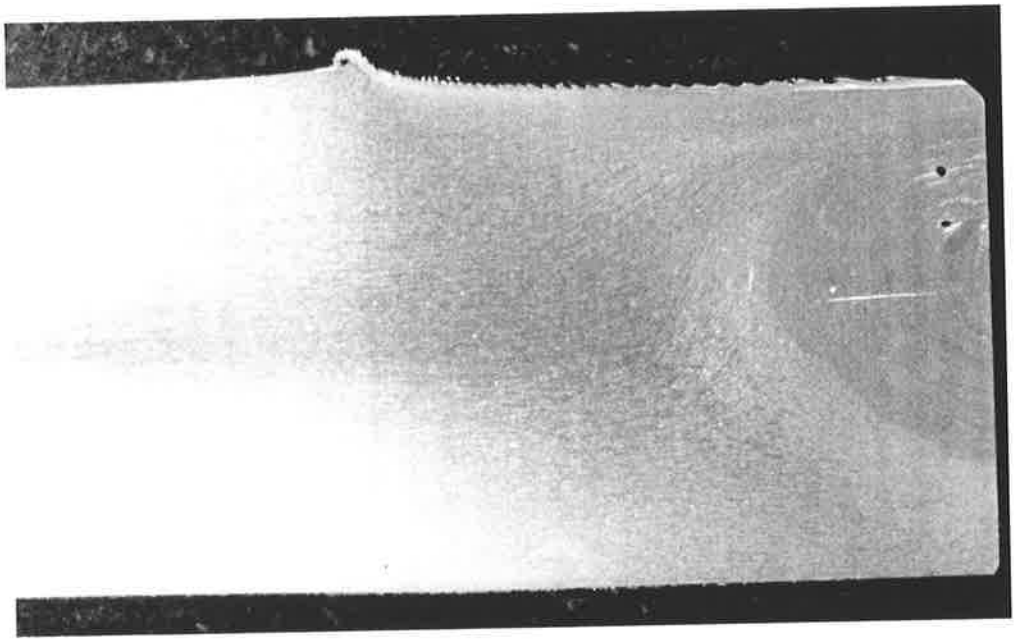

Figure 5-5 Left-Hand side Microstructure

TMAZ and recrystallised nugget region can be reasonably easily distinguished. Examining the base material at 50x magnification showed a layered microstructure in the direction of rolling. See Figure 5-7. It is difficult to distinguish the grains at this magnification. Some inter-metallic compounds can also be observed.

The microstructure in the weld region is quite different as is demonstrated by Figure 5-6. This shows equiaxed grains. Precipitate particles appear to have grown in size.

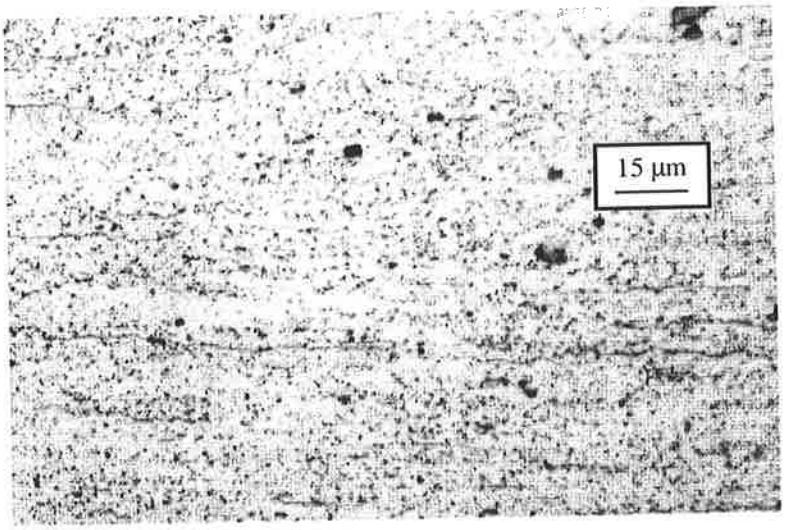

Figure 5-7 Base Material at 50x Magnification

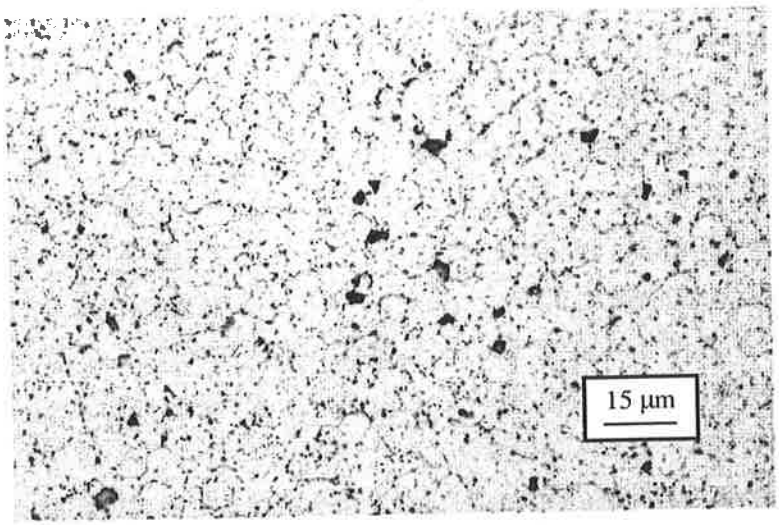

Figure 5-6 Stir region of Weld 50x

5.2.3 Longitudinal Cross Section Through Weld

The longitudinal cross section through the weld demonstrated similar features to those of the transverse weld microstructure. An overall section is shown in Figure 5-8 which shows the dynamically recrystallised zone and the HAZ and TMAZ at the base.

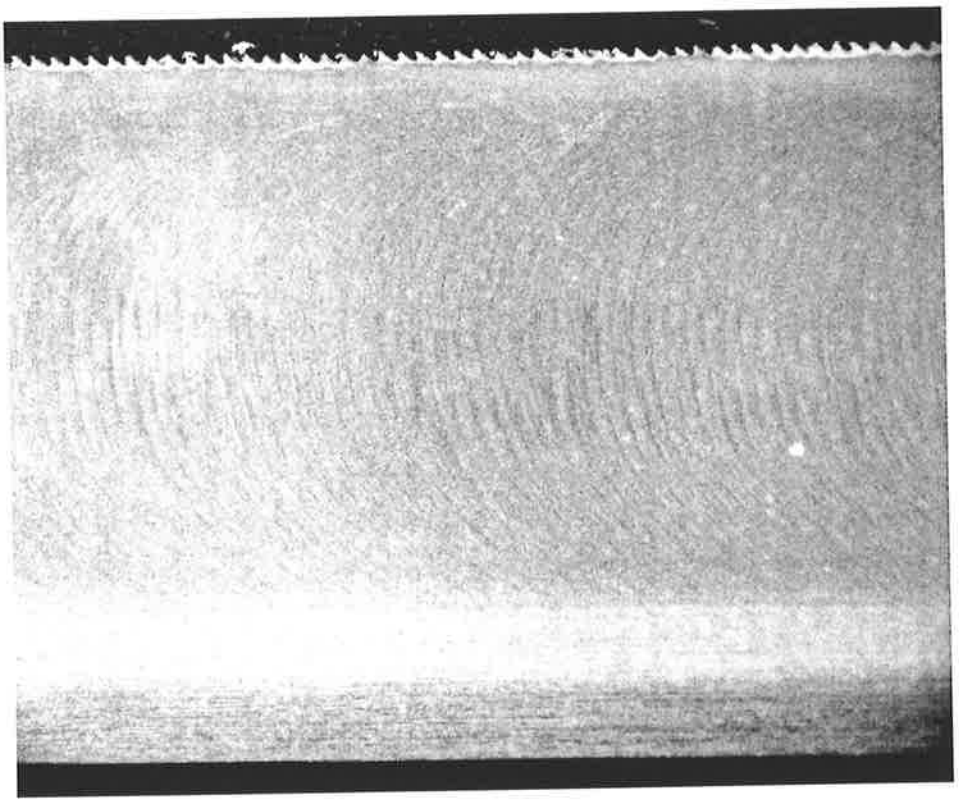

Figure 5-8 Longitudinal Section

Figure 5-9 shows an enlarged section of the stir region at 5x. Note that the streaks that are observed are voids caused by the presence of the thermocouples in the weld. This was verified by taking a second section which was not from the region where the

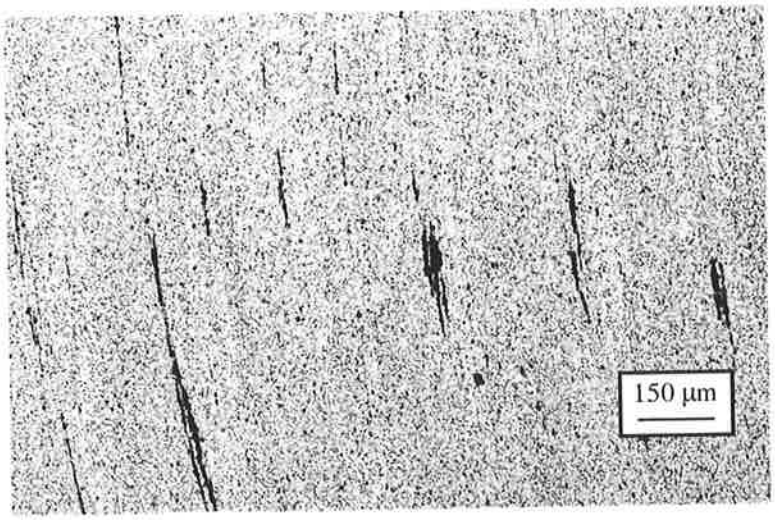

Figure 5-9 Through Weld 5x

thermocouples were located. Fortunately, these voids enable the layers of material to be distinguished more easily, which were approximately 135 μm apart. This is less than that observed for the pin retraction defect in the previous section. This spacing corresponds to a period of 0.08 sec at 1.72mm/s, which is significantly less than the rotational period of 0.17 sec. Hence the layering of the material does not appear to correspond to the rotation of the tool. Finally, Figure 5-10 shows the same section at 50x.

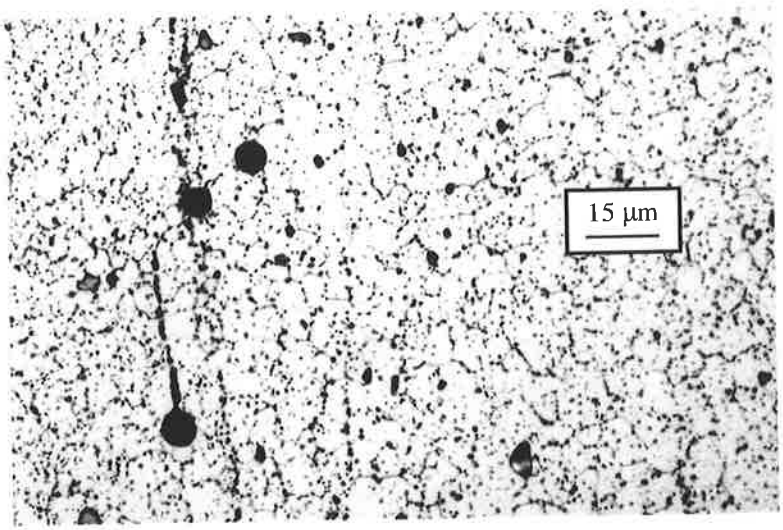

Figure 5-10 Streaks Occurring Through Weld 50x

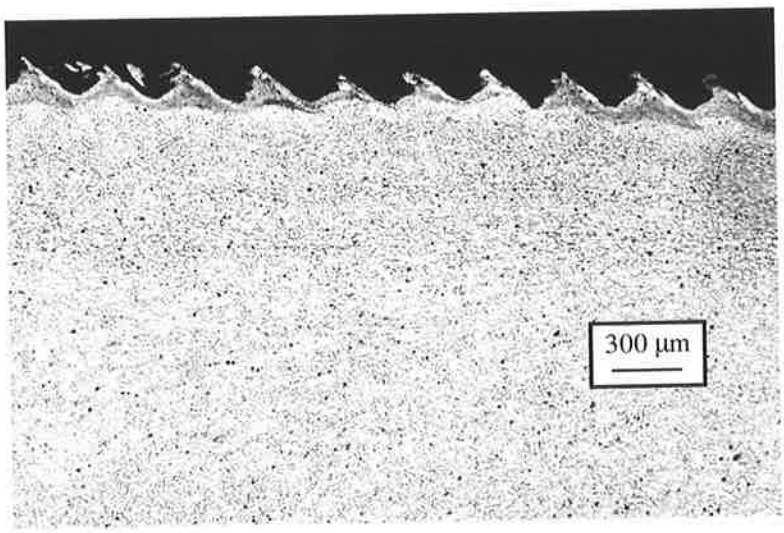

Figure 5-11 Top Surface of Weld 2.5x

A close up view of the top surface of the weld in Figure 5-11 clearly shows the serrated layer that is caused by the rotating shoulder. Closer inspection shows that the peaks are approximately 330μm apart. For a speed of 1.72mm/s this corresponds to a time of 194ms. Since the spindle period is 171ms, it appears that a peak is formed with every rotation of the spindle.

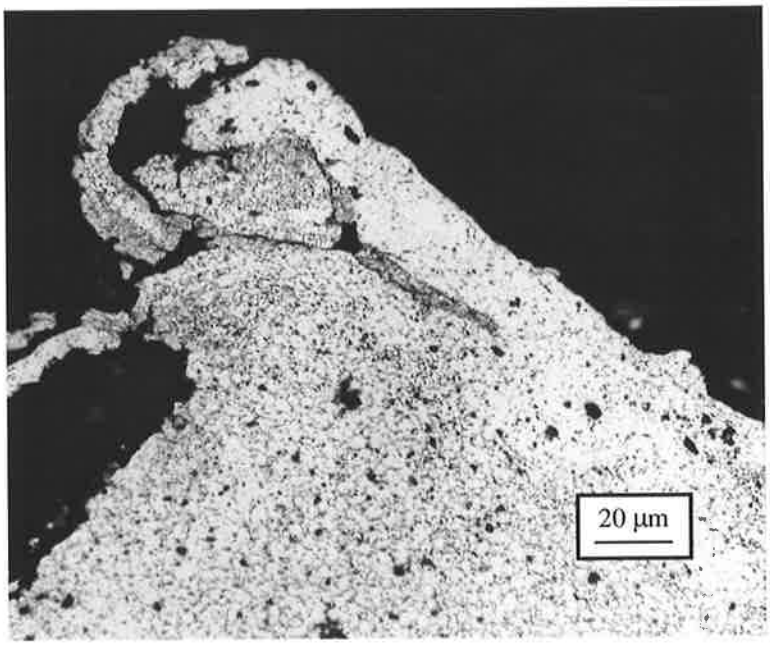

Figure 5-12 Close up View of Knife Edge Region 50x

A closer view of this serrated surface is shown in Figure 5-12. The photo demonstrates how the grain sizes in this region are significantly smaller (1-4μm), which is indicative of the high strain rates that occur in this region. Finally, there appears to be an accumulation of precipitates around the top surface.

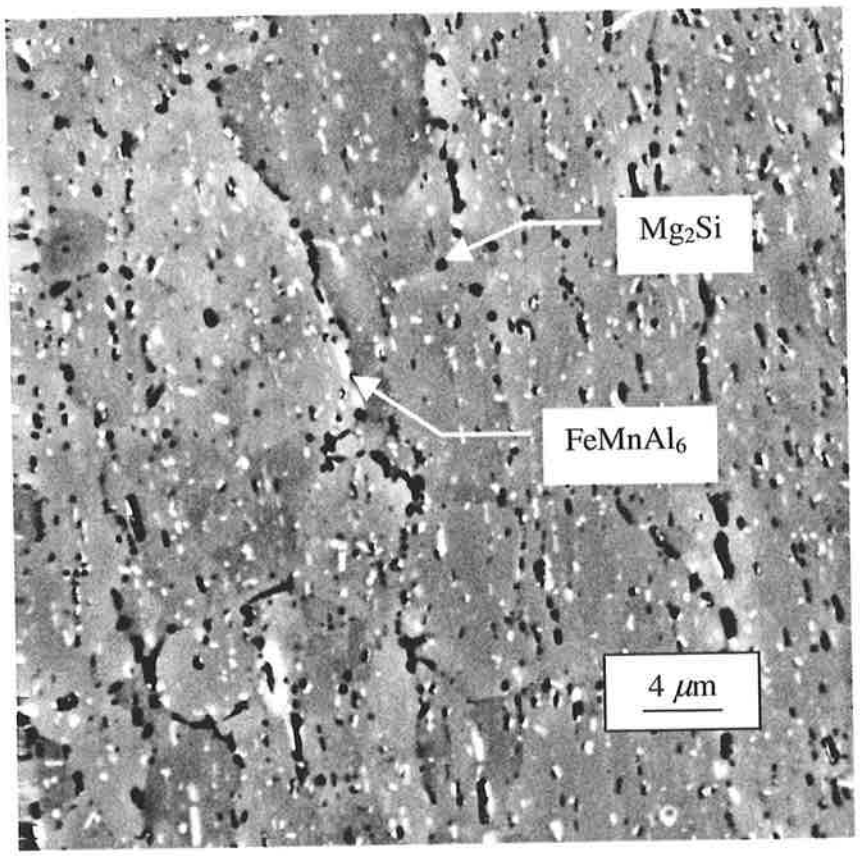

Figure 5-13 Back Scattered SEM Image of Base Material (x2500)

5.3 SEM Investigation of Longitudinal Weld

A back scattered image from the scanning electron microscope (SEM), is shown in Figure 5-13. The image shows long elongated grains in the direction of rolling. The grains are approximately 10 μm in length and have a width of 4 μm. The base grey material is $MnAl_6$, while the black inclusions in the image are Mg_2Si precipitates and the white inclusions are $FeMnAl_6$.

A similar image of the weld region is significantly different and is shown in Figure 5-14. The grains are equiaxed and far more easily distinguishable. Their size ranges from 3 to 10 μm, which is close to that reported by Threadgill and Leonard [76]. There

do not appear to be any bands of small and large grain sizes as reported by Leonard [36] for age hardened alloys, with the grain sizes being fairly randomly distributed. This observation is supported by Larsson et. al. [75] who found that a weld made in 6082 aluminium alloy did not exhibit any differences in grain size across the dynamically recrystallised region.

The precipitates in the weld region are far more spherical in shape and larger than those in the base material. They appear to have primarily nucleated on the Al grain boundaries, indicating that they have gone into solid solution when the material was heated and re-precipitated when cooled. Finally, the larger sized precipitate particles are likely to have over-aged.

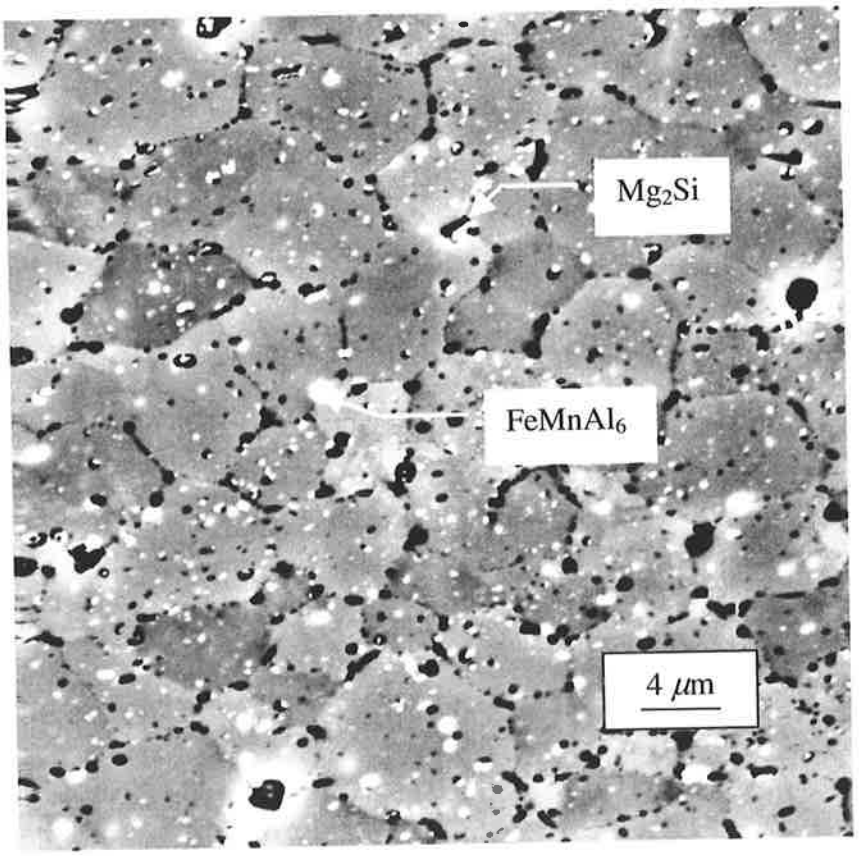

Figure 5-14 Back Scattered SEM Image of Weld Region (x2500)

The microstructure was examined on a slightly larger scale with the SEM to see if there was anything to distinguish the separate layers of material that are observed on the macro. Very little was found except for a line of $FeMnAl_6$ precipitates which are shown in Figure 5-15. This was however an isolated occurrence.

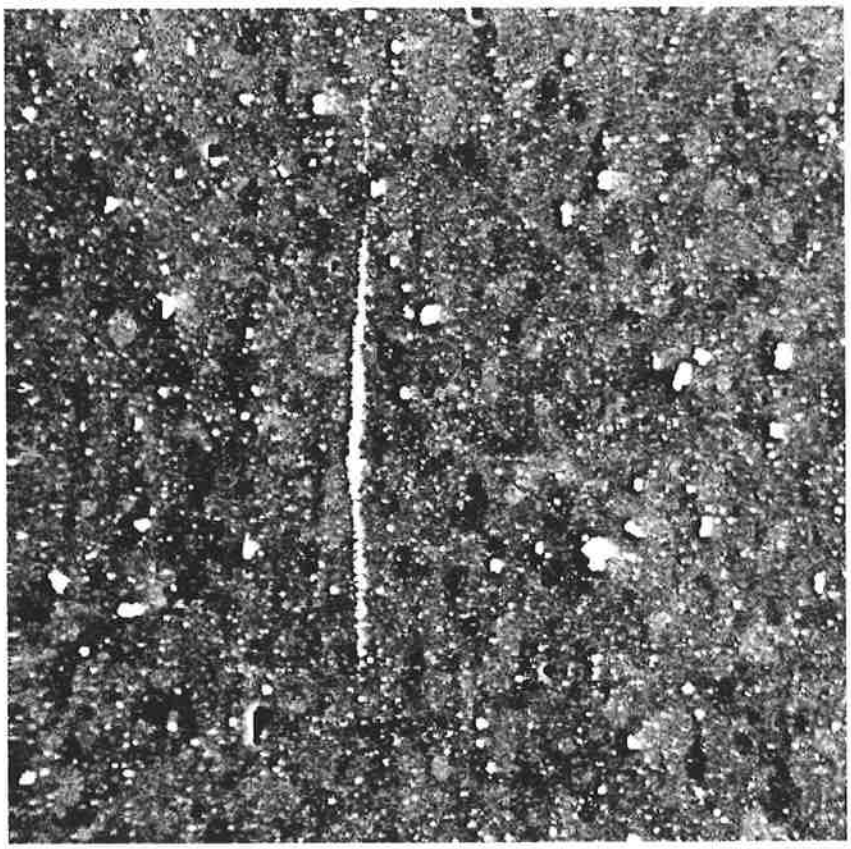

Figure 5-15 Line of $FeMnAl_6$ precipitate (x500)

5.4 Conclusions

This work has demonstrated the following:

- A sound weld was achieved, apart from a small amount of porosity caused by the thermocouple holes.
- The flow of material around the FSW tool when welding 5083 aluminium is in layers.
- This layered flow does not appear to correspond with the rotation of the tool.
- Differences in grain sizes between layers were not observed.

- The serrated top surface appeared to be produced by the rotation of the tool.
- There was no microstructural evidence for surface melting.

6 Theory for Calculating the Pin Heat Input

6.1 Introduction

All the numerical models up to this point in time have assumed that all the heat is generated at the shoulder. While McClure [12] has shown that the heat generation at the pin is relatively small for 6 mm plate, this assumption may become increasingly invalid as the thickness of the plate increases. To enable the model to more accurately represent the real process, the heat generation at the pin needs to be estimated.

Therefore, the following section shows:

1. The general equations describing the generation of heat in an element that undergoes deformation and has surface heat generation.
2. From the general equations developed in step 1, a few simple approaches are used to predict the heat generation around the pin during FSW.

6.2 Calculating the Heat Generated in an Element Undergoing Deformation

To calculate the heat dissipated during deformation, an element of the material will be considered first. In this analysis the following assumptions will be made:

- The solid interface is not attached to the surface of the element, but slides over the top. The energy dissipated by the sliding of this interface is one source of heat generation.
- The velocity of the element is arbitrarily set to zero. The actual value is irrelevant. What is important is the speed of the interface relative to the speed of the speed of the element, v_{rel}.

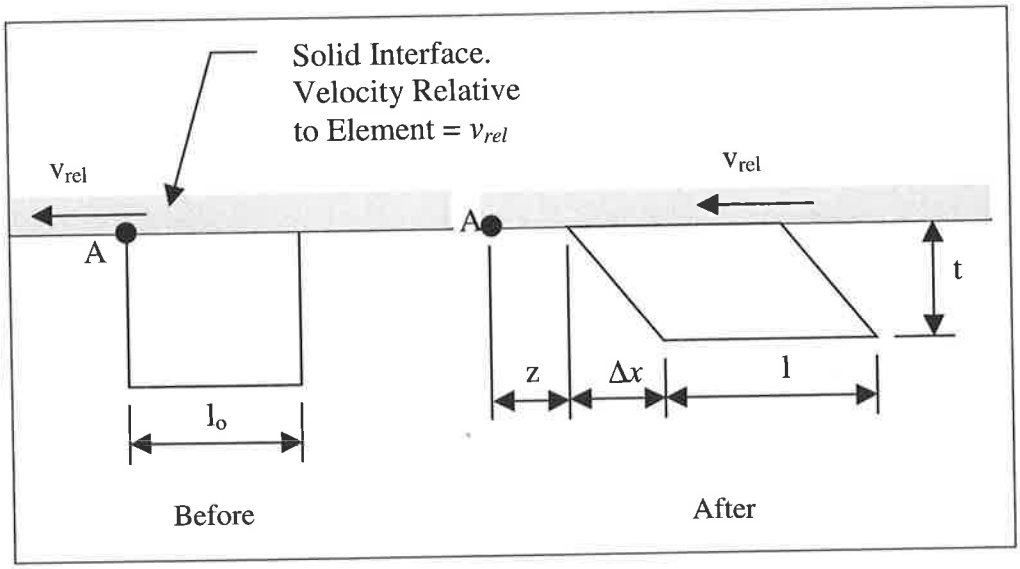

Figure 6-1 Deformation of an Element

Referring to Figure 6-1, the total heat generated in the element will be the sum of the heat generated due to deformation, Q_d and due to friction, Q_f. ie.

$$Q = Q_d + Q_f \qquad \textbf{Eq. 6-1}$$

The heat may be produced by either linear or shear deformation. The linear deformation is given by Kalpakjian [72]:

$$Q_{linear} = V\int \sigma d\varepsilon \qquad \textbf{Eq. 6-2}$$

Obviously the above equation is the area underneath the stress strain curve, multiplied by the element's volume. If we assume an average value of the yield or flow stress $\overline{\sigma}_y$, during the deformation, then the above equation simplifies to:

$$Q_l = V\overline{\sigma}_y\varepsilon \qquad \textbf{Eq. 6-3}$$

It can be easily shown that a similar relationship holds between the shear stress and shear strain rate:

$$Q_s = V\int \tau d\gamma \qquad \textbf{Eq. 6-4}$$

If τ is constant and equal to $\dfrac{\overline{\sigma}_y}{\sqrt{3}}$ then the heat produced by shearing is given by:

$$Q_s = \frac{V\overline{\sigma}_y \gamma}{\sqrt{3}} \qquad \textbf{Eq. 6-5}$$

Finally the heat generated by friction is given by:

$$Q_{friction} = F_r z \qquad \textbf{Eq. 6-6}$$

Note that for the case of columbic friction. (See discussion in section 2.3)

$$F_r = \mu p A \qquad \textbf{Eq. 6-7}$$

Therefore, the total heat produced is given by the following equations:

$$Q = V\overline{\sigma_y}\varepsilon + \mu p A z \quad \text{For normal strain only} \qquad \textbf{Eq. 6-8}$$

$$Q = V\overline{\sigma_y}\frac{\gamma}{\sqrt{3}} + \mu p A z \quad \text{For shear strain only} \qquad \textbf{Eq. 6-9}$$

where Eq. 6-8 is for linear deformation, and Eq. 6-9 is for shear deformation. Note that in the same way that stresses in different directions are not additive, the heat produced by the normal strain cannot be added to the heat produced by the shear strain. Their combined effect is discussed later in section 10.4. Finally by differentiating the above equations with respect to time, the heat generation rate is given by:

$$\dot{Q} = V\overline{\sigma_y}\dot{\varepsilon} + \mu p A v_{rel} \qquad \textbf{Eq. 6-10}$$

$$\dot{Q} = V\overline{\sigma_y}\frac{\dot{\gamma}}{\sqrt{3}} + \mu p A v_{rel} \qquad \textbf{Eq. 6-11}$$

Note that v_{rel} is the velocity of solid surface relative to the surface of the element.

6.3 Approximating the Heat Generation

To quantify the heat generated by the pin one has to make some broad assumptions about how the material flows around the threaded pin. There are in fact 3 possible methods which are illustrated in the following sections. Note that all the methods assume the following:

- The process is axisymmetric.

- The flow of material around the tool will not be considered. Note that this is really a consequence of the first assumption.
- Square threads are used.
- The pin is straight and not tapered.

6.3.1 Method 1 - No Slip Model

In this model it will be assumed that there is no slip between the pin and the workpiece, and that the material deforms on a surface passed the pin threads. This is shown Figure 6-2.

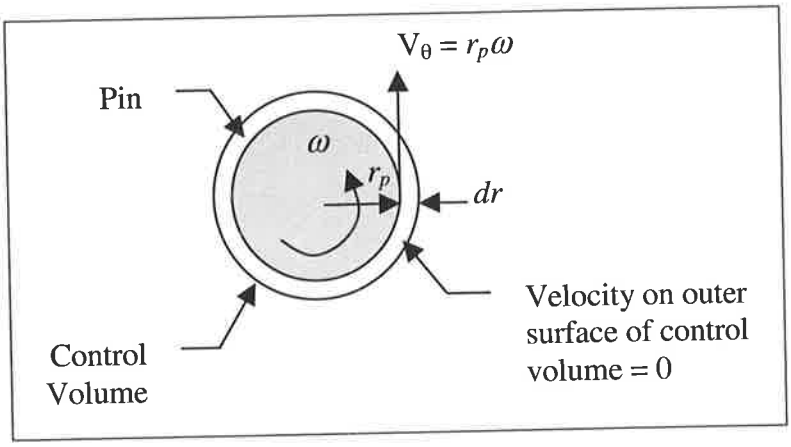

Figure 6-2 Heat Generation for No Material Slip

If shear is assumed to occur across an infinitely small plane dr, then applying equation Eq. 6-11 and knowing:

$\dot{\gamma} = \frac{dV_\theta}{dr}$ since velocity only varies in the radial direction

$V = 2\pi r_p h_p dr$

$v_{rel} = 0$ on both the inner and outer faces because it is assumed that the slip is zero.

Hence:

$$\dot{Q} = 2\pi r_p h dr \bar{Y}\left(\frac{1}{\sqrt{3}}\frac{dV_\theta}{dr}\right) \qquad \textbf{Eq. 6-12}$$

Cancelling out *dr* and letting

$$dV_\theta = V_\theta - 0 = r_p\omega$$

gives:

$$\dot{Q} = \frac{2\pi r_p^2 \omega h_p \overline{\sigma_y}}{\sqrt{3}} \qquad \textbf{Eq. 6-13}$$

6.3.2 Method 2 - Zero Friction Model

In this model it is assumed that the coefficient of friction between the workpiece material and the pin is zero. Therefore, the process effectively becomes an auguring

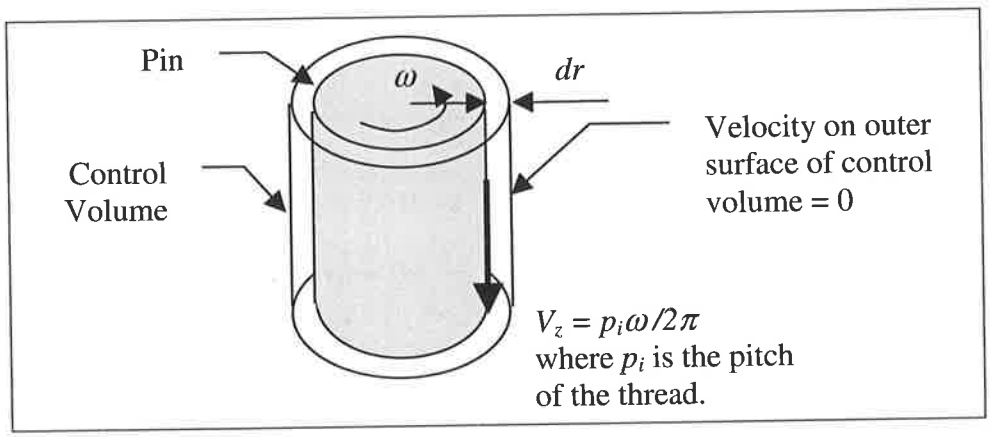

Figure 6-3 Heat Generation for Perfect Slip Model

process, where the material is constantly sheared downwards with the rotation of the pin. This is described diagrammatically in Figure 6-3.

Once again applying equation Eq. 6-11 for heat generation and noting that:

$\dot{\gamma} = \frac{dw}{dr}$ since velocity only varies in the radial direction

$V = 2\pi r_p h_p dr$

$\mu = 0$ between the pin and the workpiece material, therefore the heat generation due to sliding contact is zero.

The only difference between section 6.3.1 is that the velocity is now along the direction of the tool axis and:

$$dw = V_z - 0 = p_i \omega / 2\pi$$

Therefore:

$$\dot{Q} = \frac{r_p h_p p_i \omega \overline{\sigma_y}}{\sqrt{3}} \qquad \textbf{Eq. 6-14}$$

6.3.3 Method 3 – Combined Metal Deformation and Frictional Heating

The two methods described above provide two extreme cases. ie. No slip and slip without any friction. In reality a combination of the above two processes is likely to occur. Referring to Eq. 6-11 for the heat generation, it is necessary to find the friction at the interface and the strain rate to calculate the heat produced at the pin.

Consider an element of material travelling with the threads on the tool, as shown in Figure 6-4. The resultant velocity of the material, V_m is dependent on the velocity of the tool and the amount of slip. The resulting forces on this element are shown in Figure 6-5. Note:

- The total force on the element will equal the shear strength of the material times by the area.

- The direction of the V_m and τdA are identical. This is because the shear force must oppose the motion of the moving material.

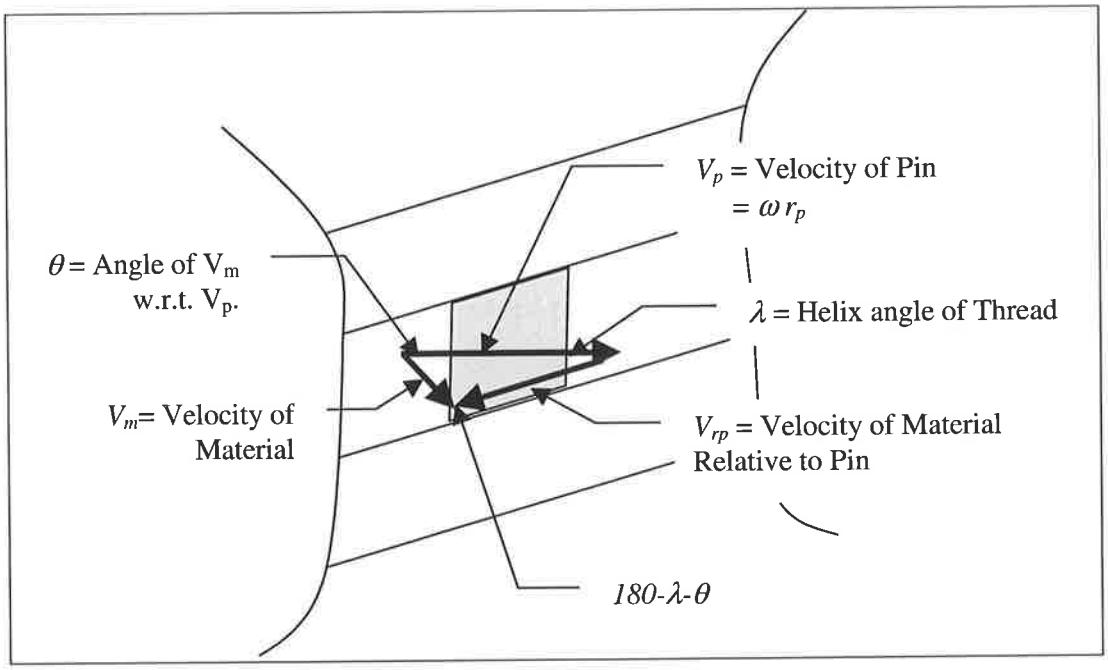

Figure 6-4 Description of Material Velocities

If the coefficient of friction is known, then the angle θ, which is the angle that V_m and τdA make with the horizontal direction is found by: (See Figure 6-5)

$$\theta = 90 - \lambda - \tan^{-1}(\mu) \qquad \textbf{Eq. 6-15}$$

Hence, the value of the coefficient of friction and the helix angle determines the direction of the material flow in the tool threads.

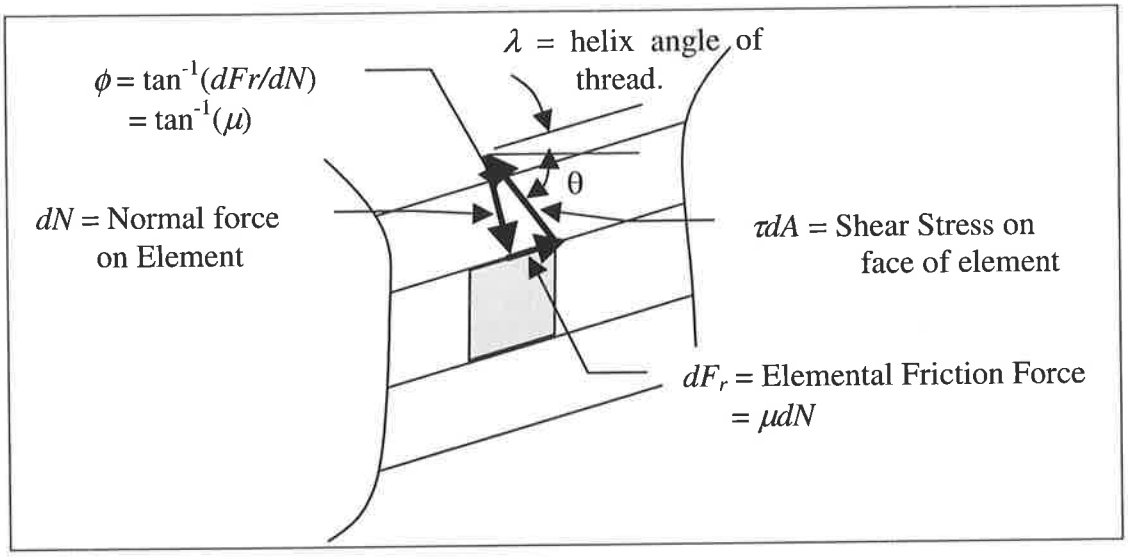

Figure 6-5 Description of Forces on Material Around Tool Threads

To calculate the heat produced it is necessary to find the following terms:

- V_m This will enable the heat generated by material deformation to be found.
- V_{rp} This will enable the heat generated by friction to be found.

Using the sine rule on the velocity triangle in Figure 6-4:

$$V_m = \frac{\sin\lambda}{\sin(180-\theta-\lambda)}V_p \qquad \textbf{Eq. 6-16}$$

$$V_{rp} = \frac{\sin\theta}{\sin(180-\theta-\lambda)}V_p \qquad \textbf{Eq. 6-17}$$

If the material is deformed across a radial thickness *dr*, then the strain rate of the material will be given by:

$$\dot{\gamma} = \frac{dV_m}{dr}$$

also the volume of the deformed material is given as per section 6.3.1 and 6.3.2:

$$V = 2\pi r_p h_p dr$$

Therefore referring to Eq. 6-11, the heat generated by material deformation simplifies to:

$$\dot{Q} = 2\pi r_p h_p \overline{\sigma}_y \frac{V_m}{\sqrt{3}} + \int V_{rp} dF_r \qquad \textbf{Eq. 6-18}$$

To determine the friction heat generation, dF_r is found from Figure 6-5, using Pythagorus's Rule:

$$dN^2 + (\mu dN)^2 = (\tau dA)^2$$
$$\Rightarrow dN = \frac{\tau dA}{\sqrt{1+\mu^2}} \qquad \textbf{Eq. 6-19}$$
$$\Rightarrow dF_r = \mu dN = \frac{\mu \tau dA}{\sqrt{1+\mu^2}}$$

Integrating this gives the following expression for the heat generated by friction:

$$F_r = \frac{2\mu\tau\pi r_p h_p}{\sqrt{1+\mu^2}} = \frac{2\mu\overline{\sigma}_y \pi r_p h_p}{\sqrt{3(1+\mu^2)}} \qquad \textbf{Eq. 6-20}$$

Substituting this into Eq. 6-18 gives:

$$\dot{Q} = 2\pi r_p h_p \overline{\sigma}_y \frac{V_m}{\sqrt{3}} + \frac{2\mu\overline{\sigma}_y \pi r_p h_p V_{rp}}{\sqrt{3(1+\mu^2)}} \qquad \textbf{Eq. 6-21}$$

Hence, the heat generation of the pin has been found from the dimensions of the pin, the yield strength of the material and the coefficient of friction. Note that the above equation simplifies to equation Eq. 6-13 when the material sticks to the surface of the tool. In this case the value of θ is zero. Therefore:

$$V_m = V_p$$

$$V_{rp} = 0$$

$$\mu = \tan\lambda$$

It is impossible, however for the flow described for the no-slip case in Figure 6-3 to actually occur. This would require a negative coefficient of friction which is clearly impossible. If the coefficient of friction is 0 then:

$$\phi = 0$$
$$\theta = 90 - \lambda$$
$$V_m = (\sin\lambda)V_p$$
$$V_{rp} = \sin(90-\lambda)V_p$$

Hence the material will flow on an angle 90° to the angle of the thread.

To further refine the model, heat generation caused by translation will be found. To do this, the system will be analysed in a similar manner to a drum brake. Figure 6-6 shows this diagrammatically. It is assumed that:

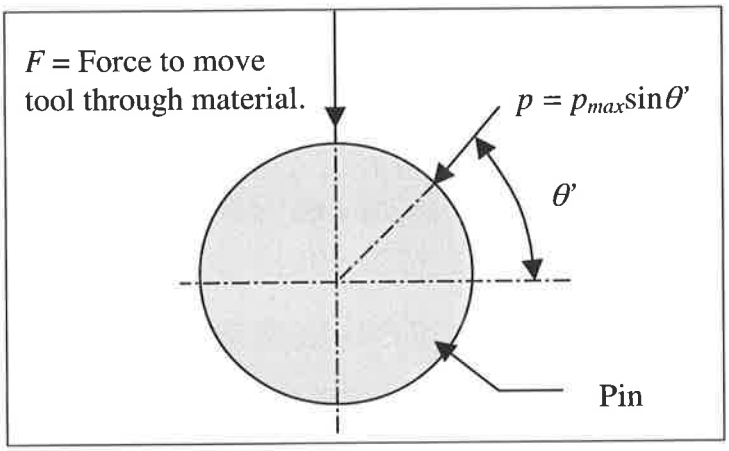

Figure 6-6 Drum Brake Analysis of Pin

a) Radial pressures caused by expansion of the material are negligible. It is believed that because the material has such low yield strength, the deformation caused by the pin negate the effects of thermal expansion.

b) The pressure varies sinusoidally around the circumference.

The total force, F in terms of the pressure at the surface is given by:

$$F = \int_0^{\pi} p \sin\theta' dA$$

Letting:

$$p = p_{max}\sin\theta'$$

$$dA = h_p r_p d\theta'$$

Hence:

$$F = \int_0^{\pi} p_{\max} \sin^2 \theta' h_p r_p d\theta'$$
$$= p_{\max} h_p r_p \left[\tfrac{1}{2}\theta' - \tfrac{1}{4}\sin 2\theta' \right]_0^{\pi}$$
$$= \frac{p_{\max} h_p r_p \pi}{2} \qquad \textbf{Eq. 6-22}$$

Hence p_{max} is found by:

$$p_{\max} = \frac{2F}{h_p r_p \pi} \qquad \textbf{Eq. 6-23}$$

The heat produced by friction is found by:

$$\dot{Q} = F_r v_{rel\theta} \qquad \textbf{Eq. 6-24}$$

where:

F_r = Tangential friction force at the interface

$$F_r = \int_0^{\pi} \mu p dA$$
$$= \int_0^{\pi} \mu p_{\max} \sin\theta' h_p r_p d\theta'$$
$$= \mu p_{\max} h_p r_p \left[-\cos\theta' \right]_0^{\pi}$$
$$= 2\mu p_{\max} h_p r_p$$
$$= \frac{4F\mu}{\pi}$$

$v_{rel\theta}$ = Velocity between the pin and the workpiece material in the direction of θ.

$= V_m \cos\theta$ (See Figure 6-4)

Therefore $\dot{Q}$ is given by:

$$\dot{Q} = \frac{4F\mu V_m \cos\theta}{\pi} \qquad \textbf{Eq. 6-25}$$

Hence, if the translational force can be obtained, it is possible to predict the heat generation.

Finally the total heat generation will be given by the following formula:

$$\dot{Q} = 2\pi r_p h_p \overline{\sigma}_y \frac{V_m}{\sqrt{3}} + \frac{2\mu\overline{\sigma}_y \pi r_p h_p V_{rp}}{\sqrt{3(1+\mu^2)}} + \frac{4F\mu V_m \cos\theta}{\pi} \qquad \textbf{Eq. 6-26}$$

This equation will be used in subsequent sections to estimate the heat generation due to the pin.

7 The Steady State Thermal Model

7.1 Basic Features

As discussed in section 2.1.4, the three analysis approaches that can be taken are the distributed circular source (analytic), an analytic solution based on Rosenthal's equation and finite element/volume technique. The later technique has been selected because it is believed to be more flexible and more easily adapted to different welding conditions. eg. different backing plates.

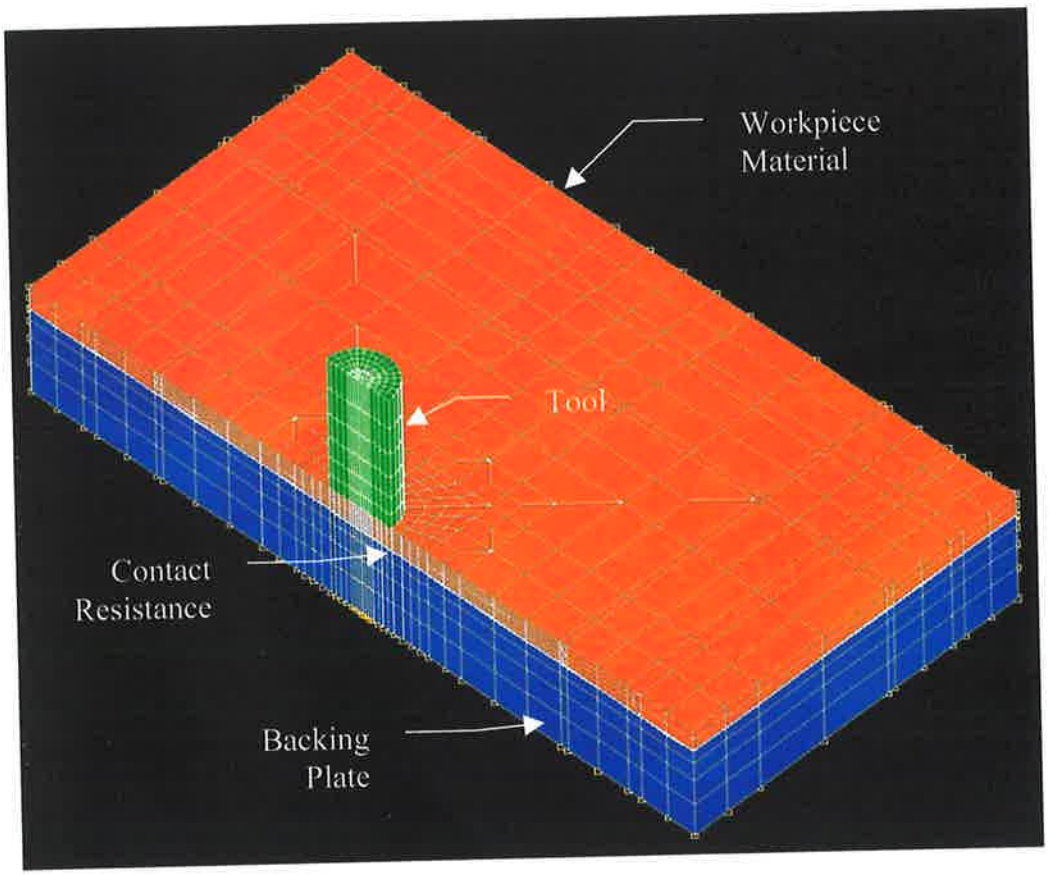

Figure 7-1 Standard Mesh for the FSW Thermal Model

The process has been modelled using the NISA [67] modelling package. A typical finite element mesh that is used to model the process is shown in Figure 7-1. Linear 8-

noded hexahedral shaped elements have been used for this mesh. The main components of the model are the tool, the backing plate, and the workpiece material. A pseudo material with reduced thermal conductivity is used to model the imperfect contact between the aluminium and the steel backing plate. Note the following assumptions:

- Only half the model is required because the other side is essentially a mirror image of the other side. As demonstrated in section 2.1.3 there is very little difference in the temperature between advancing and retreating sides despite the process being asymmetric.
- The model is considered to be quasi steady state with the workpiece effectively moving past a static tool.
- The clamps on top of the material have not been included. It has been shown later in section 7.3 that the contact resistance between aluminium and steel is high, so this simplification will not have a dramatic effect on the results. Secondly, the clamps are a sufficient distance from the tool that their effect on the heat transfer during the process will be small.

7.2 Boundary Conditions

The boundary conditions described below are the standard set used for setting up the model. Variations on this basic set of boundary conditions are considered later in the result section (7.3.1.5) to determine the effect of various parameters on the performance of the model.

7.2.1 Dirichlet Boundary Conditions

Dirichlet Boundary Conditions prescribe the value of a variable at a particular point. For a typical model, these are shown in Figure 7-2 and are described below:

(a) Nodal Velocities.

All the velocities for material constituting the backing plate, workpiece material and contact resistance are set equal to the welding velocity. The velocity of the tool is set equal to zero. ie. This is opposite to how a real welding situation works where the tool moves relative to the stationary workpiece.

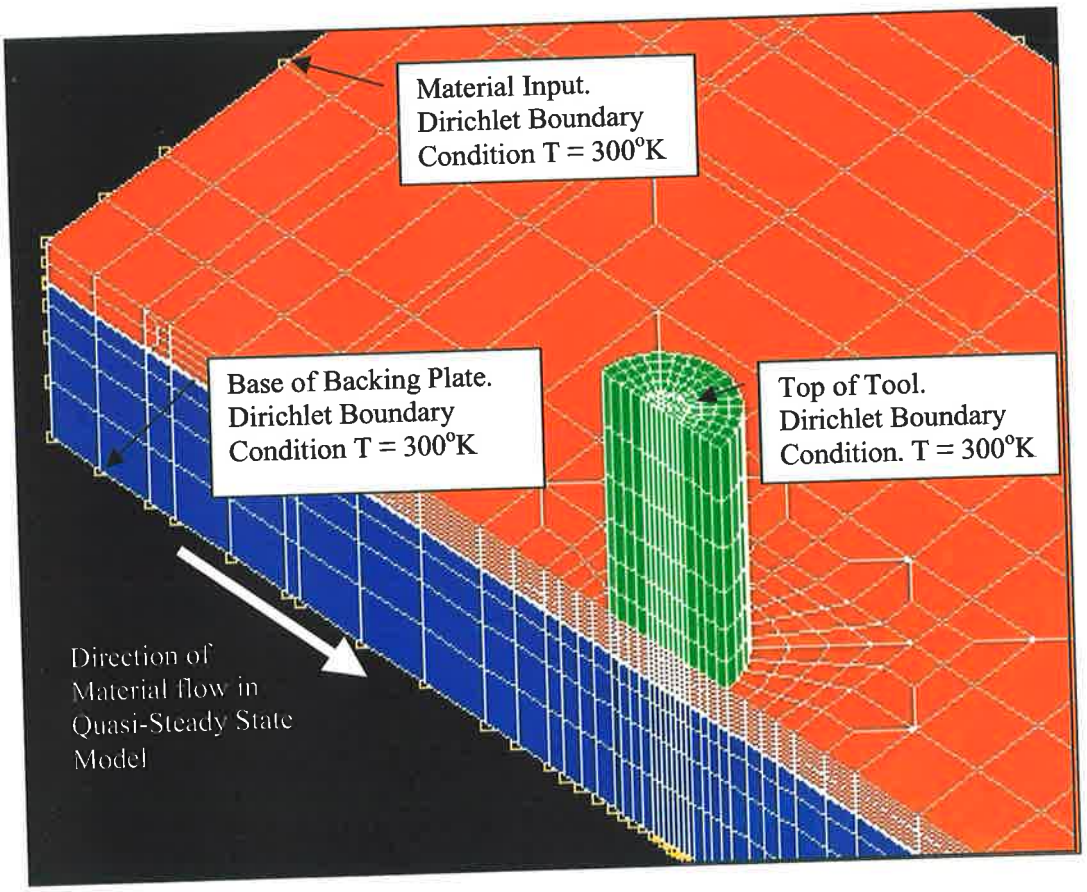

Figure 7-2 Dirichlet Boundary Conditions

(b) Nodal Temperatures.

The temperatures of the following nodes are set equal to ambient:

- Top face of the tool.
- Bottom face of the backing plate.
- Front edge of the material where it enters the model.

7.2.2 Neumann Boundary Conditions

The Neumann Boundary conditions are summarised in Figure 7-3. The boundary conditions are placed in the following areas:

(a) Convective Boundary Conditions.

The value of the heat transfer coefficient is described later in section 7.3.1.4.

The following faces have a convective boundary:

- Side of Tool.
- Top of Workpiece material
- Far edge of workpiece material

(b) Insulated Boundary Condition.

There is an insulated boundary along the mirror axis. This does not need to be specified, as the default for any finite element package is zero flux across

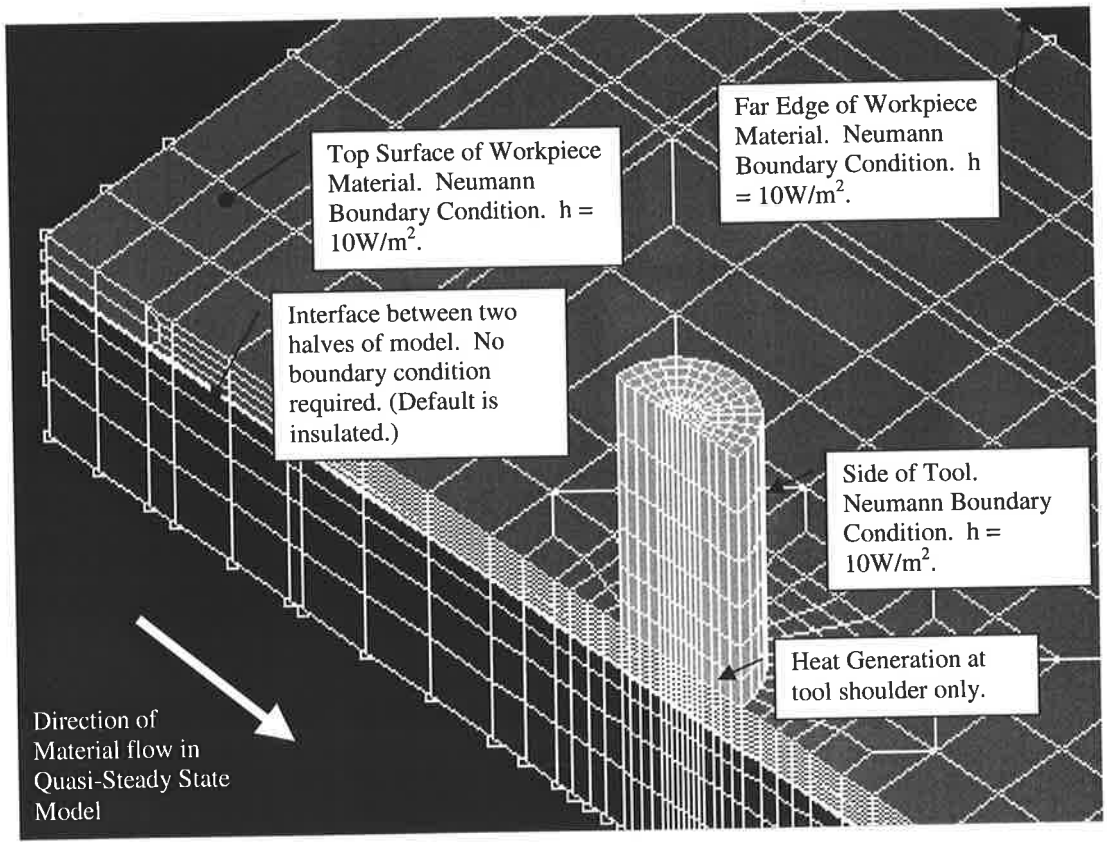

Figure 7-3 Neumann Boundary Conditions

the boundary.

(c) Heat Generation.

See section 7.3.1.3 for details.

7.3 Model Verification

Obviously the model needs to be validated. Validation has been carried out in two ways:

- Validation against previously published models. There are two papers where the data is sufficiently detailed that verification of the model is possible. They are Chao and Qi [2,3], and Russell and Shercliff [4].
- Validation against a set of our own experimental data.

7.3.1 Verification Against Chao and Qi [2,3]

This section describes the development of the model, testing of the effect of various boundary conditions and finally the values of parameters required for sensible results. It should be noted that the modelling work from Chao and Qi [2,3] was based on experimental results from McClure [11].

7.3.1.1 Material Properties

The material properties used in the model by Chao et. al. [14] are summarised in the table below:

Material	**Description**	**k (W/mmK)**	**c_p (J/kg K)**	**ρ (kg/mm^3)**
1 – 6061 T6	Workpiece material	0.18	896	2.7×10^{-6}
2 – Carbon Steel.	FSW Shoulder	0.040 (1% C Steel at 300°C)	465	7.85×10^{-6}

Material	**Description**	**k (W/mmK)**	**c_p (J/kg K)**	**ρ (kg/mm^3)**
3 – Carbon Steel	Backing Plate	0.052 (0.5%C Steel at 100°C)	465	7.85×10^{-6}
4 – Dummy Material	Contact Resistance	Max = 2.8×10^{-2} (Minimum thermal contact resistance) Min = 5.73×10^{-3} (Maximum thermal contact resistance)	0	7.85×10^{-6}

Note:

- The properties are given in terms of millimetres because this unit was used in sizing the model.
- The value of the thermal conductivity of aluminium is obtained by using the room temperature value of 167 W/mK (Note T6 temper) from the Aluminium Handbook [59] and multiplying this by a factor of 1.07. (See section 2.2.1) Therefore, the approximate value of the thermal conductivity is 180 W/mK
- c_p was obtained from aluminium handbook. [59]
- The properties for the steel backing plate and shoulder were the standard values obtained from Table A-2 of Holman [22]. Note that the thermal conductivity of the shoulder was taken at 300°C because this is a reasonable approximation of the average temperature at which it operates.

- The value of the thermal contact resistance from Holman [22] p55 for smooth aluminium was found to be:

$$R = 1/h_c = 0.18x10^{-4}(m^2K/W)$$
$$= 18(mm^2K/W)$$

Equating this to an equivalent thermal conductivity:

$$q = kA\frac{\Delta T}{\Delta x} = A\frac{\Delta T}{R}$$
$$k = \frac{\Delta x}{R}$$

For a value of Δx = 0.5mm, k=2.8x10^{-2}. The lower value of thermal conductivity (5.73x10^{-3}) was found when a value of 0.88 was used for the thermal contact resistance.

- The value of the specific heat of the dummy material was assumed to be equal to that of steel so that no errors occurred in the formulation.

Subsequent to this work a table of material properties for 6061-T6 was found in Chao and Qi [2] and are reproduced in Table 7-1:

Table 7-1

Temperature (°C)	**Thermal Conductivity (W/m°K)**	**Heat Capacity (J/kg°K)**	**Density (kg/m^3)**
-17.8	0.0162	904	2713
37.8	0.0162	945	2685
93.3	0.0177	978	2685
148.9	0.0184	1004	2667

Temperature (°C)	Thermal Conductivity (W/m°K)	Heat Capacity (J/kg°K)	Density (kg/m^3)
204.4	0.0192	1028	2657
260	0.0201	1052	2657
315.6	0.0207	1078	2630
371.1	0.0217	1104	2630
426.7	0.0223	1133	2602
571.1	0.0253	1230	2574

Note that there appears to be a 10^4 discrepancy between the values of Chao and Qi [2] and those in the Aluminium Handbook [59].

In any case the proposed values of thermal conductivity, specific heat and density while not being perfect, should be sufficient to give reasonable predictions from the model.

7.3.1.2 Geometry

The geometry used Chao and Qi is described in Table 7-2:

Table 7-2

Parameter	Chao and Qi [2,3]
Tool Radius (mm)	19
Material Thickness (mm)	6.4
Welding Speed (mm/s)	2
Tool Rotational Speed (rad/s)	42

7.3.1.3 Heat Generation

From section 2.1.2, the equation for the heat generation is given by Eq. 2-3:

$$q_o = \frac{2\pi\sigma_y \omega R_o^3}{3\sqrt{3}} = \frac{2}{3}\pi\mu P \omega R_o^3$$

Note that the inner radius has been ignored. The following heat input parameters were used for the model:

	Chao et. al [2,3]
f = Proportion of heat into the workpiece to the total heat input	**0.83**
Total Heat Input (kW)	1.69
Heat Input to the Workpiece only (kW)	**1.4**
Yield Stress (MPa)	N/A

Note:

- The values in bold are obtained directly from the paper and those in the normal font are calculated.
- The value of the f was obtained from Russell and Shercliff [4]. This was used because the article by Chao et. al. [2,3] provided the heat input into the workpiece material only. Therefore, a method of calculating the total heat input was required.

7.3.1.4 The Convective Heat Transfer Coefficient

The value of the convective heat transfer coefficient is not critical to the overall model performance, however a good value is required to reduce the modelling error. From Appendix B, a value of 10 W/m^2K will be used for both the horizontal plate and the rotating tool. This compares with the value of $30W/m^2K$ used by Chao and Qi [2,3].

7.3.1.5 Preliminary Results Showing the Maximum Temperature in the Weld and the Effect of Various Boundary Conditions

In the initial trial the maximum temperature that occurs in the weld was investigated. The model used the above input parameters, except that the convective heat loss off the top surface was $120W/m^2K$ and the conductivity of the steel tool was 0.052 W/mK and the backing plate was 0.059 W/mK. It is not believed that any of these differences will have a significant impact on the results.

The results show that the temperature in the new model is significantly lower than the value obtained by Chao and Qi [2,3] using the same heat input. ie. Around 330°C compared with 460°C. Because of the great difference in the two models, an investigation into the impact of changing the various boundary conditions was performed. The results of this investigation are summarised in Table 7-3.

Table 7-3

Analysis	Features	Maximum T(°C)	Comments
1	None	326	

Analysis	Features	Maximum T(°C)	Comments
2	• Thermal conductivity of the tool was forced to be very low. • The net heat input was reduced to 1.4 kW. ie. The value stated in the paper. • Dirichlet boundary condition on top of the tool was removed. These changes were done to model the effect of having all the heat input into the workpiece only.	301.6	The temperature is 25°C lower than the standard case. This indicates that the value of f used was probably too low and therefore needs to be increased.
3	• The value of thermal contact resistance was increased to the maximum value for aluminium quoted in Holman [40]. ie. $k = 5.73 \times 10^{-3}$ W/mmK.	345	The maximum temperature was increased by 20°C. This corresponds to a change of approximately 5%.

Analysis	**Features**	**Maximum T(°C)**	**Comments**
4	• Dirichlet Boundary Condition on top of the tool is removed.	338	12°C increase in temperature. i.e. a 4% change.
5	• Dirichlet Boundary Condition on bottom of backing plate is removed.	335.8	10°C increase in temperature. i.e. a 3.3% change
6	• Dirichlet Boundary Condition on top of the tool is removed. • Dirichlet Boundary Condition on bottom of backing plate is removed. • Thermal Contact Resistance increased to maximum value. ie. k = 5.73×10^{-3} W/mmK	369.1	43.1°C increase in temperature. i.e. a 14.3% change.
7	• Thermal conductivity of the workpiece material is reduced to the value at room temperature ie. k = 0.167 W/mmK	339.4	An 8% change in the value of thermal conductivity resulted in a 13.4°C increase in temperature. i.e. a 4.5% change.

Note:

- While none of the changes to the boundary conditions or the thermal contact resistance were significant, their accumulative effect could be significant. Their order from most significant to least significant was:
  - (a) Change in thermal contact resistance.
  - (b) Removing the Dirichlet BC from backing plate.
  - (c) Removing the Dirichlet BC from top of tool.
- Changing the value of the thermal conductivity had only a minimal effect on the maximum temperature of the workpiece material. Therefore its value is not critical to the model output.

7.3.1.6 Preliminary Results Showing the Temperature Profile Through the Weld and the Effect of Various Boundary Conditions

Figure 7-4 shows the line of nodes along which the results were taken. This enables a comparison of the temperature between the top and bottom of the weld.

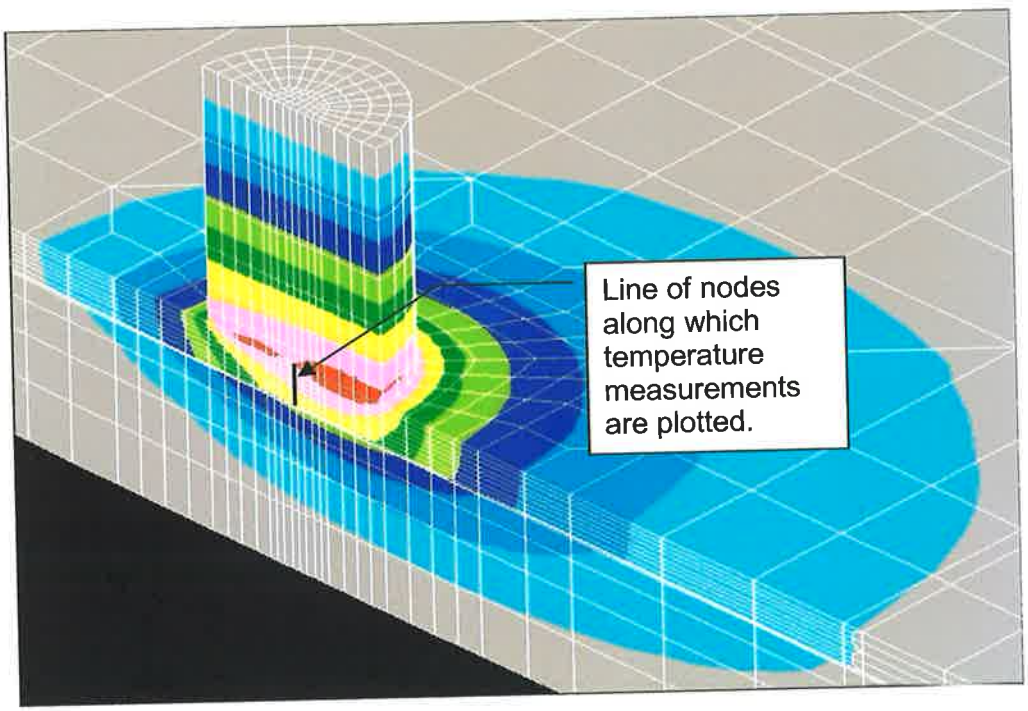

Figure 7-4 Line of nodes along which results were taken

These are shown below and are fairly self explanatory. The results indicate that none of the boundary conditions alter the results to a significant degree.

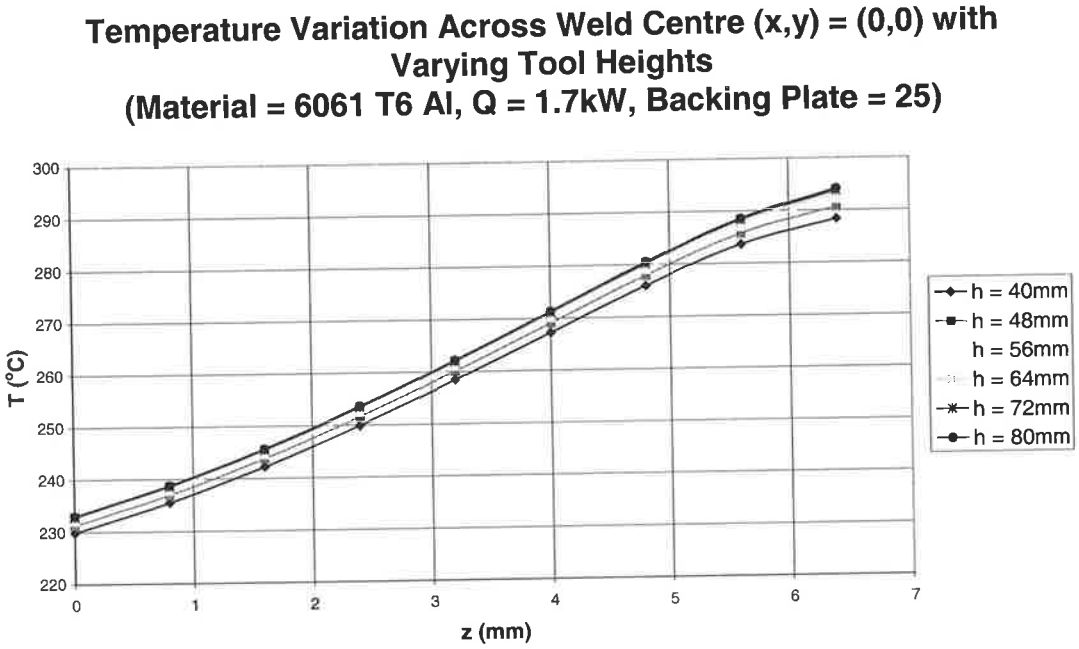

Figure 7-5 Temperature Variation with Varying Tool Heights

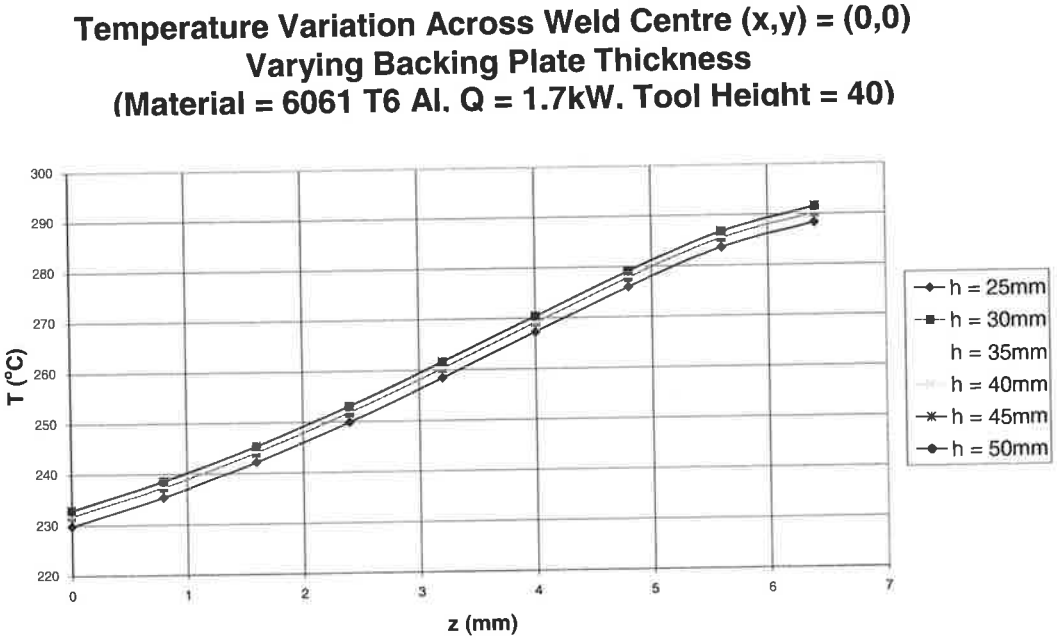

Figure 7-6 Temperature Variation with Varying Backing Plate Thicknesses

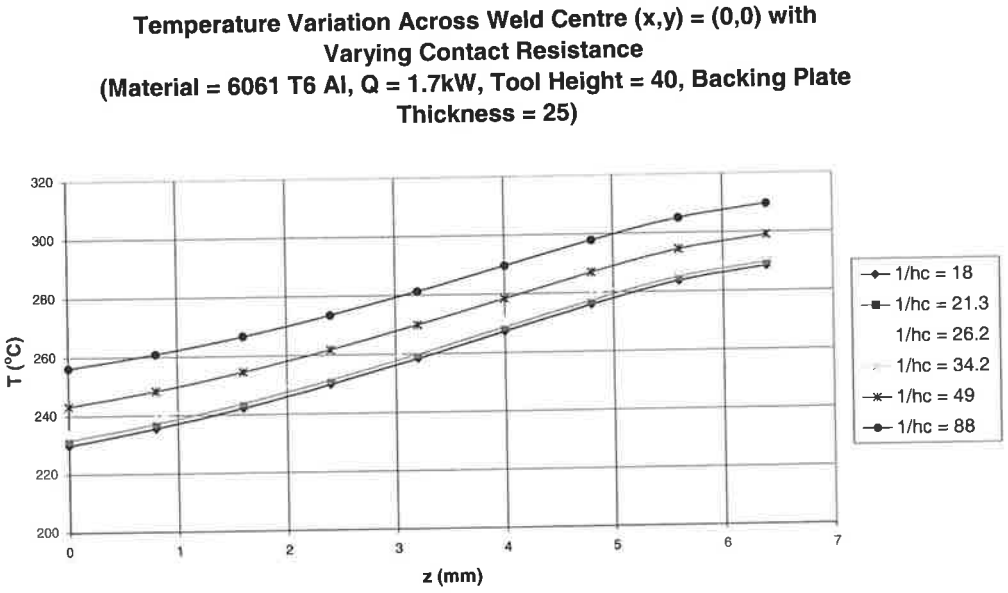

Figure 7-7 Temperature Variation with Varying Contact Resistance

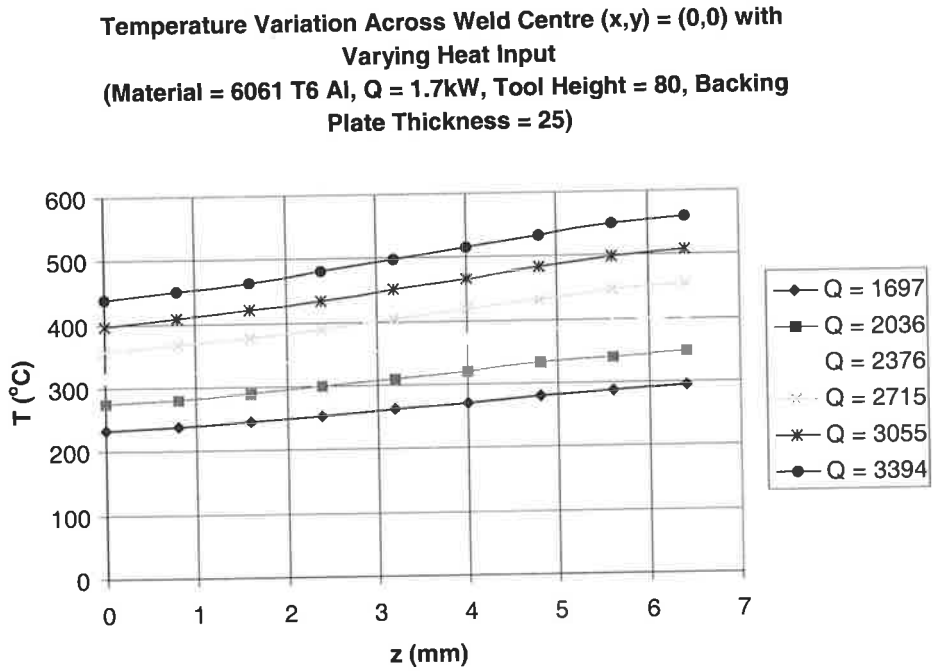

Figure 7-8 Temperature Variation with Varying Heat Input

Further to these results, graphs have been plotted of the temperature profile across the weld to model the results shown in Figures 4,5 and 6 from Chao and Qi [3]. Figure 7-9 summarises these three graphs. Figure 7-10 shows the heat input required to achieve the same maximum temperature in the weld, and Figure 7-11 shows the temperature profile when using a similar heat input to Chao and Qi.

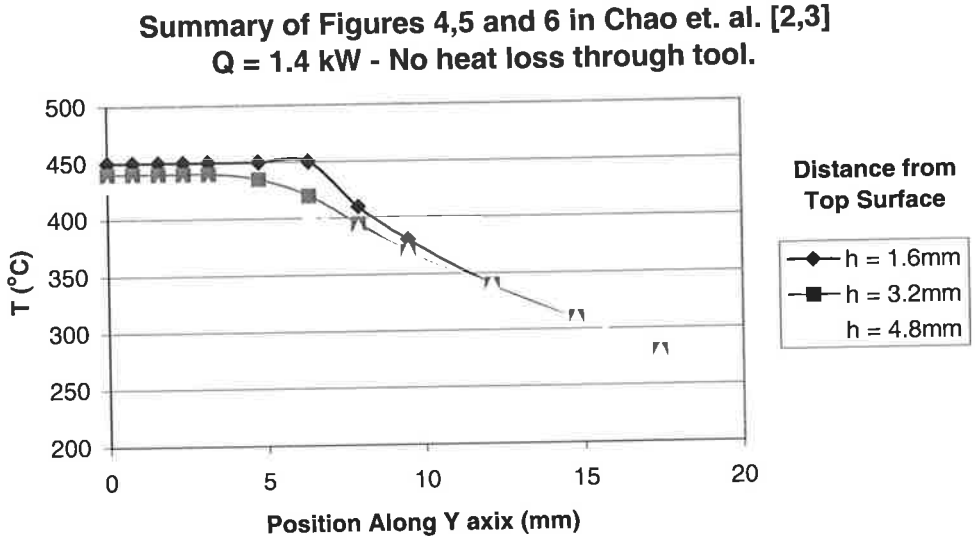

Figure 7-9 Temperature Profile Across the Weld for Chao and Qi Results

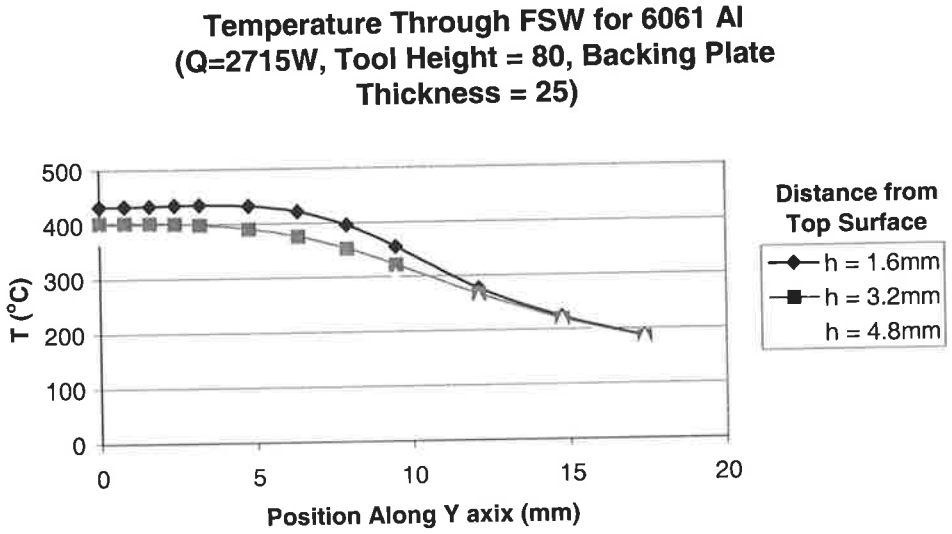

Figure 7-10 Temperature Profile Across the Weld for a heat input of 2715W

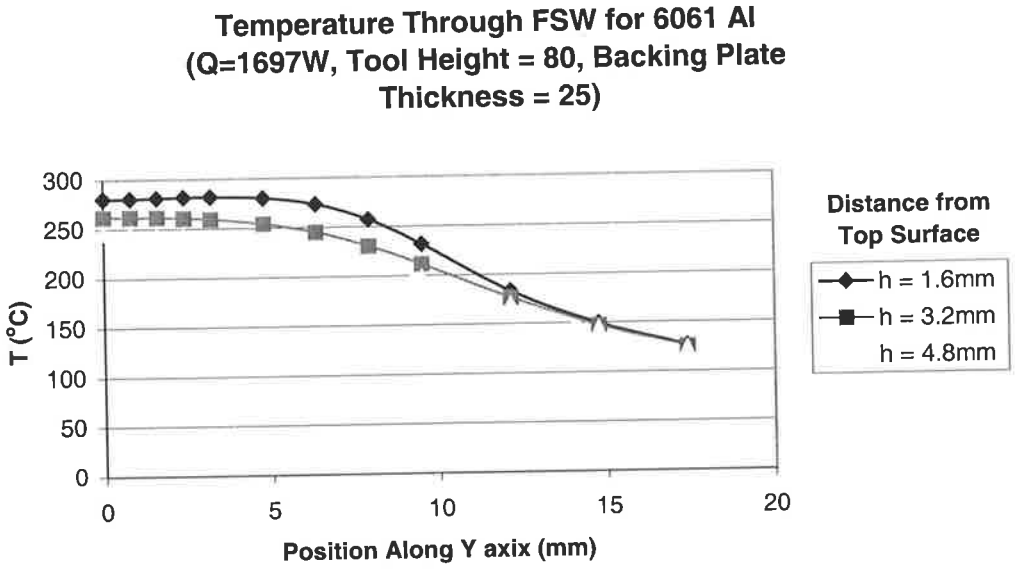

Figure 7-11 Temperature Profile Across the Weld for a heat input of 1697W

It is interesting to note that even where the maximum workpiece temperature is similar (Compare Figure 7-9 and Figure 7-10), the temperature gradient is much greater on our FSW model indicating that the heat loss into the backing plate is probably too high.

7.3.1.7 Copying the Model by Chao and Qi [2,3]

In an effort to identify the discrepancy between the two modelling methods it was decided to do an exact copy of the model produced by Chao and Qi. [2,3] ie Remove the backing plate and use a convective heat loss on the bottom surface and remove the tool and the associated heat loss from the model. From section 7.3.1.5 it is known that the heat loss through the tool does not have a significant impact on the result. Therefore, heat loss into the backing plate is likely to be the most significant factor. The results for this model are shown in Figure 7-12 and are practically identical to Chao and Qi's results in Figure 7-9.

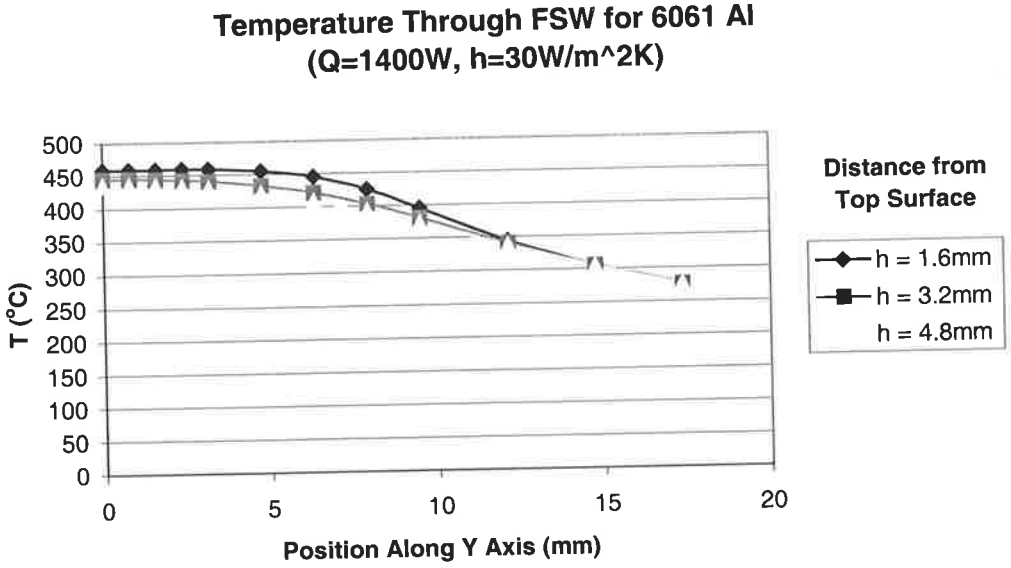

Figure 7-12 Results of a Finite Element Model Copying that Produced by Chao and Qi

Therefore, in an effort to more accurately predict the results obtained by Chao and Qi [2,3] using the revised model with backing plate and tool, the thermal contact resistance must be increased beyond that normally expected.

7.3.1.8 Parameters Required to Give Good Correlation with Chao and Qi [2,3] Model

The contact resistance and heat input required to give good correlation with experimental data are shown in Table 7-4.

Table 7-4

Parameter	Value
Contact Resistance	2500 mm K/W
Heat Input	1612 W

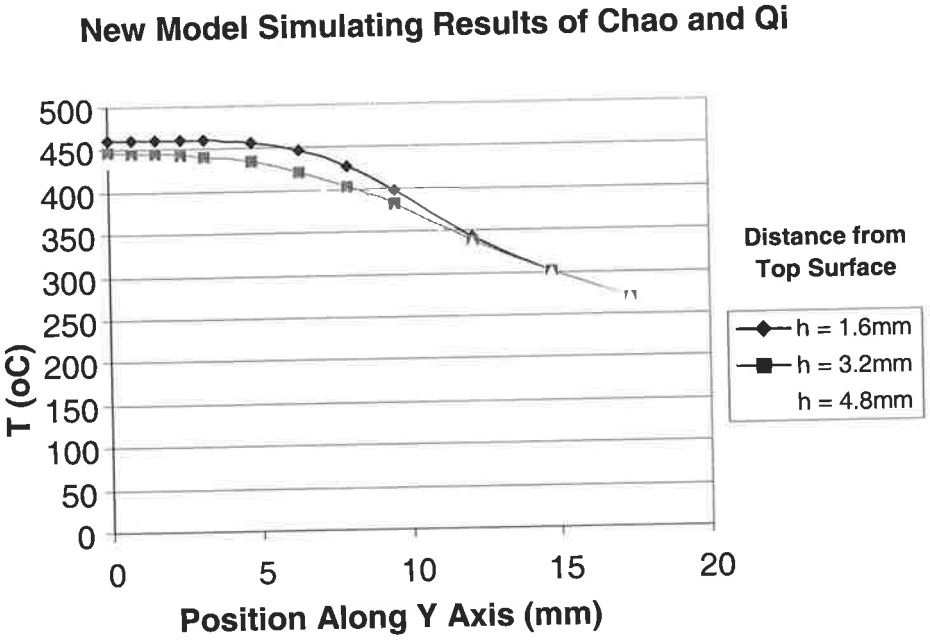

Figure 7-13 New Model Simulating Results from Chao and Qi [2,3]

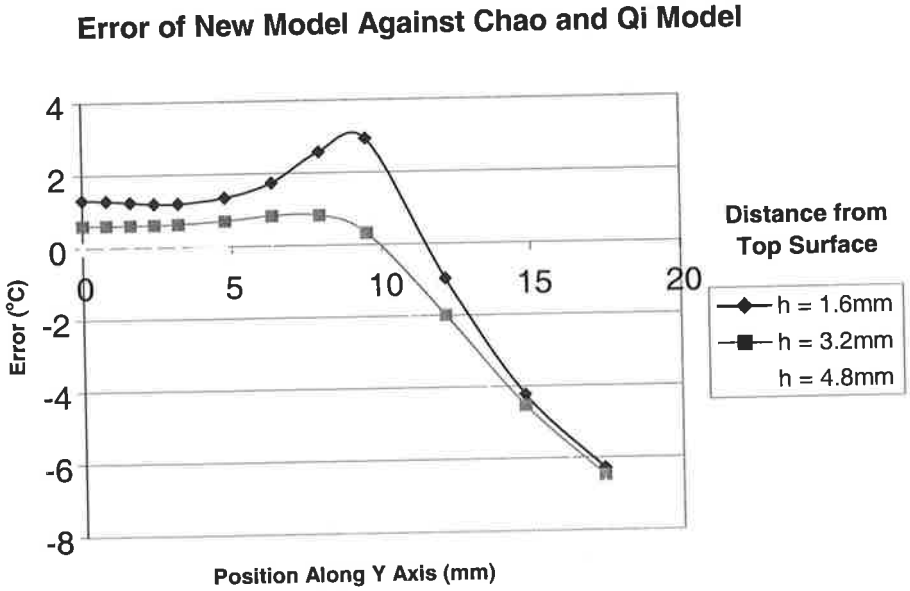

Figure 7-14 Error of New Model Against Chao and Qi Model

A graph of the output is shown in Figure 7-13 and a comparison with the Chao and Qi model is shown in Figure 7-14. Note that the error is less than 10°C. This contact resistance is substantially higher than those specified in standard engineering texts. (Holman [22]) This would seem to indicate that there is very poor thermal contact between the aluminium workpiece material and the backing plate.

7.3.2 Modelling of the Results by Russell and Shercliff [15]

7.3.2.1 Material Properties

The thermal properties when verifying the model by Russell and Shercliff [4] were identical to those used in the previous model except for the thermal conductivity of Aluminium. 2014-T6 aluminium was used, which has a thermal conductivity of 0.155 W/mmK at room temperature and therefore an approximate value of 0.17 W/mmK at 200°C.

7.3.2.2 Geometry

The geometry used by Russell and Shercliff is shown in Table 7-5.

Table 7-5

Parameter	**Russel and Shercliff [4]**
Tool Radius (mm)	25
Material Thickness (mm)	6.5
Welding Speed (mm/s)	1.33
Tool Rotational Speed (rad/s)	44

7.3.2.3 Heat Generation

The heat inputs used are shown in Table 7-6.

Table 7-6

	Russel and Shercliff [4]
f = Proportion of heat into the workpiece to the total heat input	**0.83**
Total Heat Input (kW)	**2**
Heat Input to the Workpiece only (kW)	1.66
Yield Stress (MPa)	**22**

Note that the values in bold are those obtained directly from the article. The values not in bold have been calculated.

7.3.2.4 The Convective Heat Transfer Coefficient

See section 7.3.1.4.

7.3.2.5 Preliminary Results Showing the Maximum Temperature in the Weld and the Effect of Various Boundary Conditions

The preliminary results when modelling the process described by Russell and Shercliff [4] are similar to those for Chao and Qi in section 7.3.1.5 and are summarised in Table 7-7. Note that once again these results have used a convective heat loss of 120 W/m^2K and conductivities of the tool and backing plate were 0.052 W/mK and 0.059 W/mK respectively.

Table 7-7

Analysis	Features	Maximum T(oC)	Comments
1	None	310.7	
2	The value of thermal contact resistance was increased to the maximum value for aluminium quoted in Holman [40]. ie. k = $5.73x10^{-3}$ W/mmK.	330.4	The maximum temperature was increased by 20°C, which corresponds to a change of approximately 7%. Hence the sensitivity of the model to this variable is higher than for the previous model.
3	Dirichlet Boundary Condition on top of the tool is removed.	329.2	18.5°C increase in temperature. i.e. a 6.5% change.
4	Dirichlet Boundary Condition on bottom of backing plate is removed.	339.3	29°C increase in temperature. i.e. a 10% change.

Analysis	Features	Maximum T(oC)	Comments
5	Dirichlet Boundary Condition on top of the tool is removed. Dirichlet Boundary Condition on bottom of backing plate is removed. Thermal Contact Resistance increased to maximum value. ie. k = $5.73x10^{-3}$ W/mmK	381.2	70.5°C increase in temperature. i.e. a 25% change
6	Thermal conductivity of the workpiece material is reduced to the value at room temperature ie. k = 0.155 W/mmK	325.4	An 8% change in the value of thermal conductivity resulted in a 14.7°C increase in temperature. i.e. a 5.1% change.

Comparing the above results with the results with the results from the model by Chao and Qi, section 7.3.1.5.

- The temperature under the standard conditions was lower than for the model from Chao and Qi.
- All the changes to the initial conditions had a much greater effect on the output temperature. The Dirichlet Boundary Condition on the back of the backing plate showed the greatest change in the overall weld performance.

ie. a 10% vs 3.3% change. This is because the greater overall heat input results in more of the heat being conducted to the base of the backing plate. Hence the effect of the Dirichlet Boundary Condition is much greater.

- Figure 4 from Russell and Shercliff [15] shows that the maximum welding temperature achieved was 360°C. It is unclear from the article at what position this temperature was taken. However given the value, it is unlikely to be in the centre of the weld.
- The temperature of this model seems to more accurately predict the results obtained by Russell and Shercliff.
- Once again changing the thermal conductivity has a relatively minor effect on the overall model result.

7.3.2.6 Copying the Model by Russell and Shercliff [4]

Because the position of the temperature profiles have not been specified in the modelling work by Russell and Shercliff [4], it is not possible to produce a model which directly copies the results. Therefore a model with increased contact resistance between the material and backing plate has not been attempted.

7.3.3 Verification Against a Known Set of Input Parameters

Because of the insufficient detail provided by previous modelling work (especially with regard to the actual heat input), it was decided to verify the model using our own set of experimental data. The acquisition of this data is described in section 4. The model will be based on the data obtained from one of the weld runs, 000313B. This weld was selected because of the minimal flash produced by this weld. As discussed in section 4.3.1.4, it is believed that the production of excess flash in the second weld resulted in

an overestimate of the power consumption. It is acknowledged that a more thorough validation of the model will require further experimental data.

7.3.3.1 Material Properties

The material properties used in the model are identical to those used in section 7.3.1.1 except that the thermal conductivity of the aluminium alloy is obviously different. 5083 aluminium was used, which has a thermal conductivity of 0.120 W/mmK at room temperature and therefore an approximate value of 0.13 W/mmK will be used for 100°C.

7.3.3.2 Geometry and Heat Input

These have been discussed previously in section 4.

7.3.3.3 Estimation of the Pin Heat Input

Because the model has been done with thick plate aluminium, an attempt to quantify the heat input at the pin has been made. This will then be introduced into the thermal models in section 7.3.3.4 to determine whether or not its effect is significant to the overall thermal profile of the weld.

To determine the heat input at the pin the procedure described in section 6 will be used. This requires the input parameters shown in Table 7-8.

Table 7-8

Parameter	Value	Comment
Temperature at Pin (°C):	550	See Experimental Results 000313B
σ_y (MPa) at 500(°C)	20	See comment below.

Parameter	Value	Comment
τ (MPa) at 500(°C)	11.55	$\frac{\sigma_y}{\sqrt{3}}$
r_p (mm)	6	
h_p (mm)	12	
ω (rad/s)	36.65	350 rpm
pitch (mm)	4	Estimated
λ	0.11	
F = Horizontal Welding Force (kN)	5.00	See section 4.3.2
Q_w = Heat Input from Welder (W)	3000	See section 4.3.1

Note that the approximate value of the yield strength of the material was found by the yield strength vs. temperature data in the Aluminium handbook [59] and then applying a strain rate multiplier to give an approximate value for a strain rate of 20/s (See section 3.4.9).

The calculated pin heat inputs are shown in Table 7-9.

Table 7-9

Method	μ	θ	Vp(m/s)	Vm(m/s)	Vrp (m/s)	Q	Qbrake	Qtot	% Qw
1	N/A	N/A	N/A	N/A	N/A	N/A	0	1149	38.29%
2	N/A	N/A	N/A	N/A	N/A	N/A	0	122	4.06%
3	0.2	1.27	0.219911	0.0237	0.214	343	9	352	11.73%
3	0.3	1.17	0.219911	0.0242	0.212	444	18	462	15.41%

Method	μ	θ	Vp(m/s)	Vm(m/s)	Vrp (m/s)	Q	Qbrake	Qtot	% Qw
3	0.4	1.08	0.219911	0.0250	0.209	537	30	567	18.88%
3	0.5	1.00	0.219911	0.0259	0.207	619	45	664	22.13%
3	0.6	0.92	0.219911	0.0271	0.205	692	62	754	25.13%
3	0.7	0.85	0.219911	0.0283	0.202	754	83	837	27.91%
3	0.8	0.79	0.219911	0.0297	0.200	808	106	915	30.49%

Estimates of the coefficient of friction can be found in Midling and Grong [48] who examined aluminium to aluminium friction welds and Midling and Rorvik [43] who examined the friction stir process. The first reference gave an estimate of 0.5, while the later gave an estimate of 0.2. Therefore, the pin heat input is likely to be between 10 and 20%. A value of 20% has been used, which is perhaps a little high depending on the surface condition which predominates in the weld. ie. Depending on whether the temperature approaches the solidus.

7.3.3.4 Model Types Developed

Three different thermal models have been developed to predict the results from this weld and are described below:

- Model 1. Heat was generated at the shoulder only.
- Model 2. 20% of the total heat input was generated at the pin.
- Model 3. 20% of the total heat input was generated at the pin and a reduced thermal contact resistance underneath the shoulder. This was done because in practice the contact resistance underneath the tool is likely to be reduced by the higher pressure in this position

A diagram showing the typical of the output from the NISA finite element modelling package is shown in Figure 7-15. This is for no heat input at the pin.

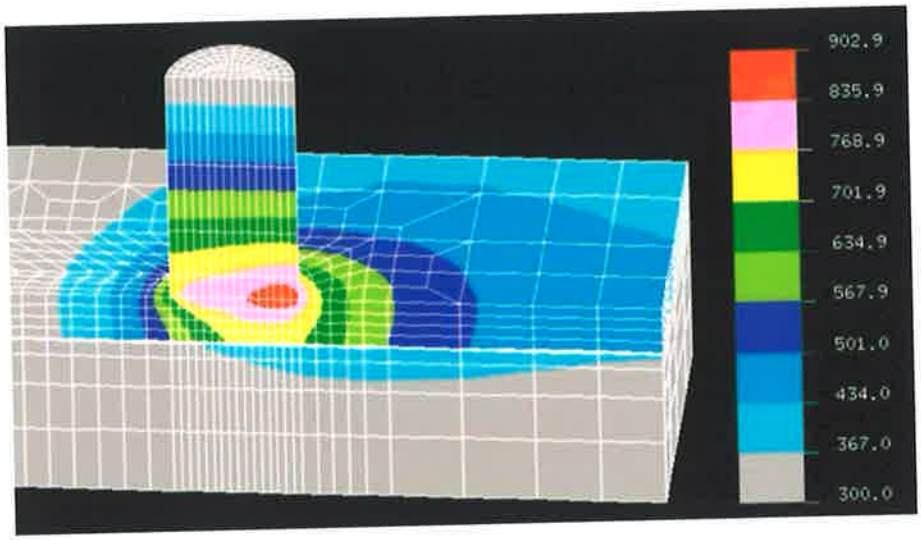

Figure 7-15 Thermal Contours Obtained for no Pin Heat Input

It was established that the heat inputs and contact resistances in Table 7-10 gave the best overall agreement between model and measured thermal cycles. The power consumptions used in the model were about 17% higher than that calculated from the motor. Once again the contact resistances stated in Table 7-10 are substantially higher than those specified in a standard engineering text, confirming the result from section 7.3.1.8. Note however that the contact resistance used in this model is less than half that used in the previous section. i.e. 1000 vs. 2500.

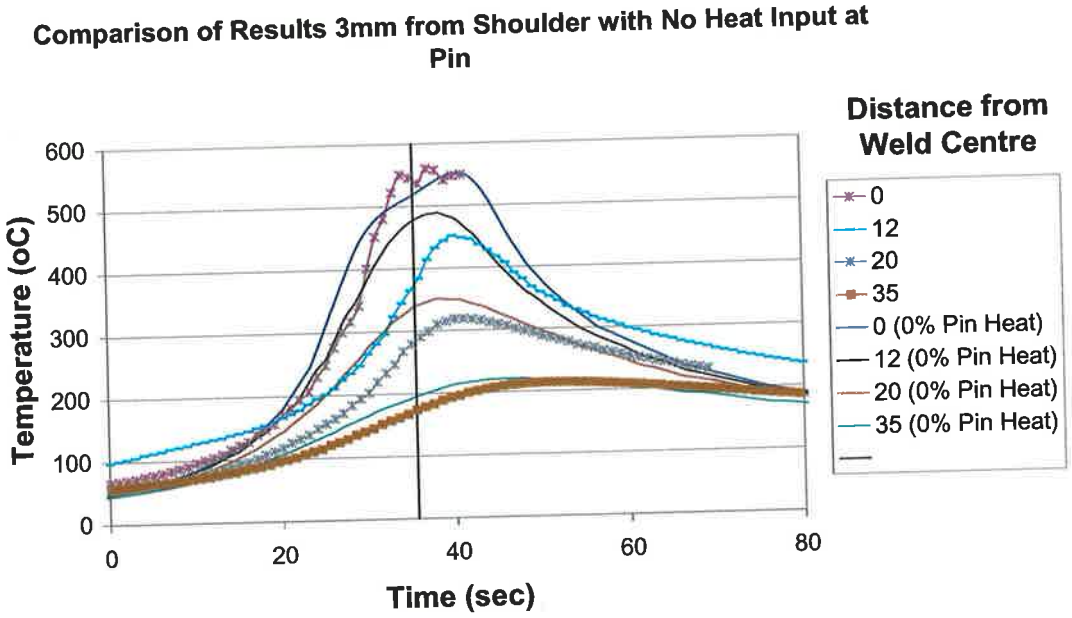

Figure 7-16 Comparison of Results 3mm from Shoulder with No Pin Heat Input

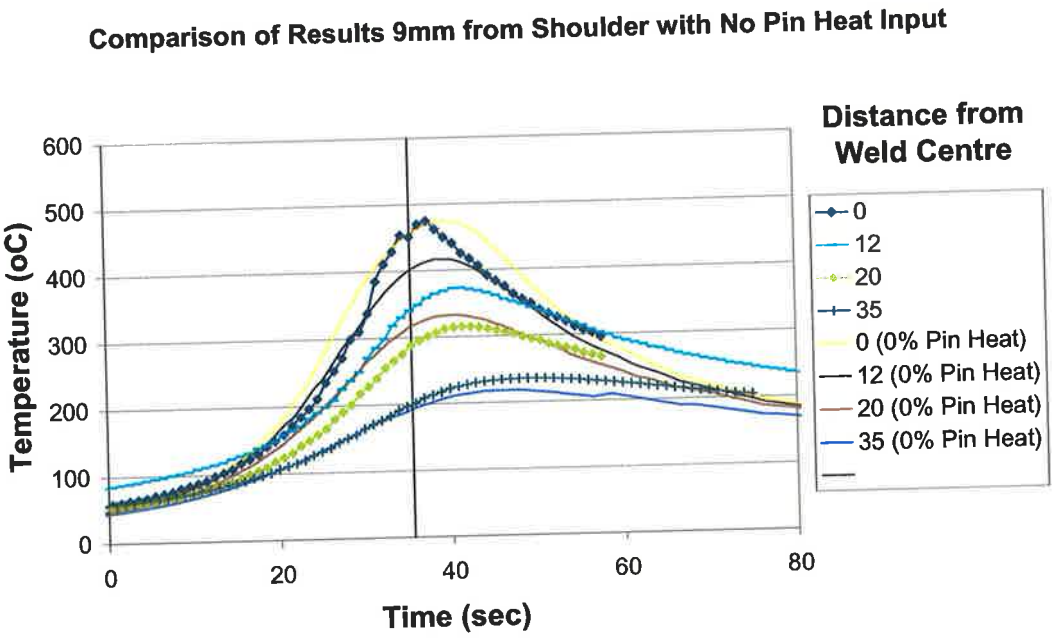

Figure 7-17 Comparison of Results 9mm from Shoulder with No Pin Heat Input

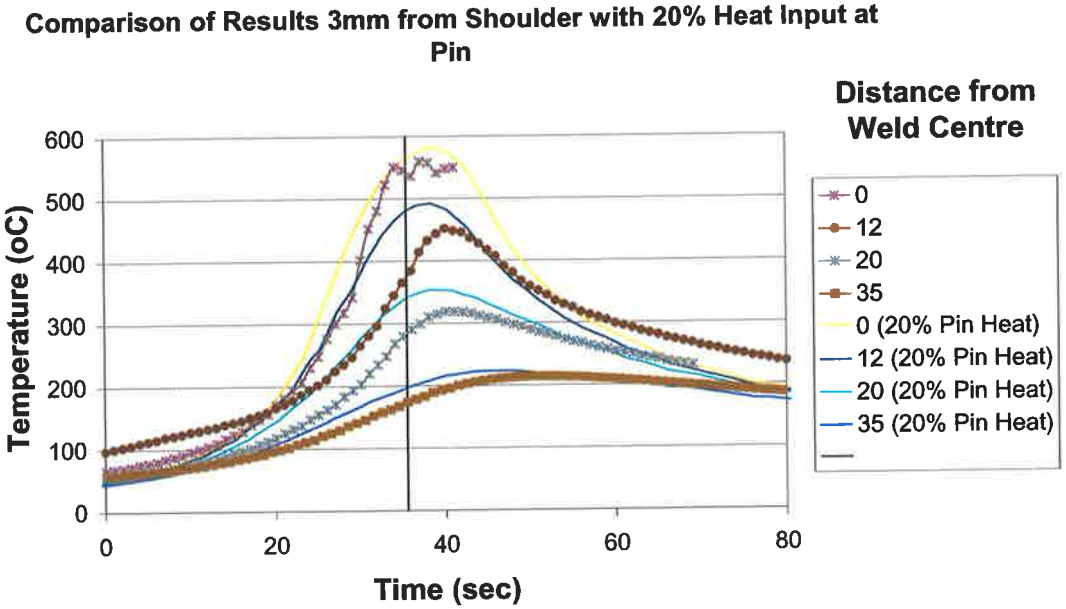

Figure 7-18 Comparison of Results 3mm from Shoulder with 20% Pin Heat Input

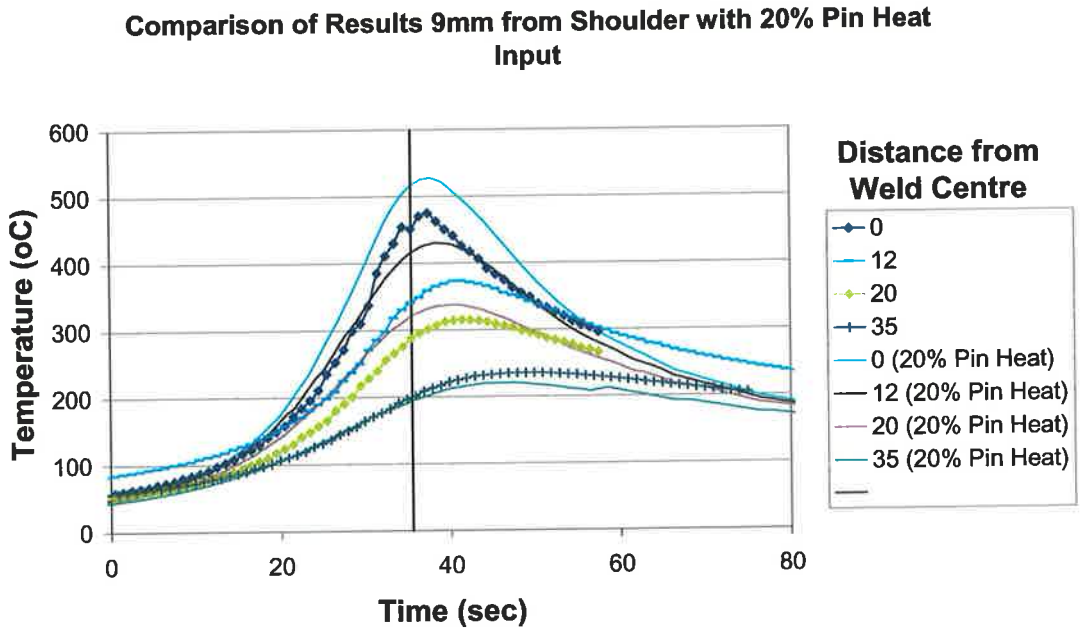

Figure 7-19 Comparison of Results 9mm from Shoulder with 20% Pin Heat Input

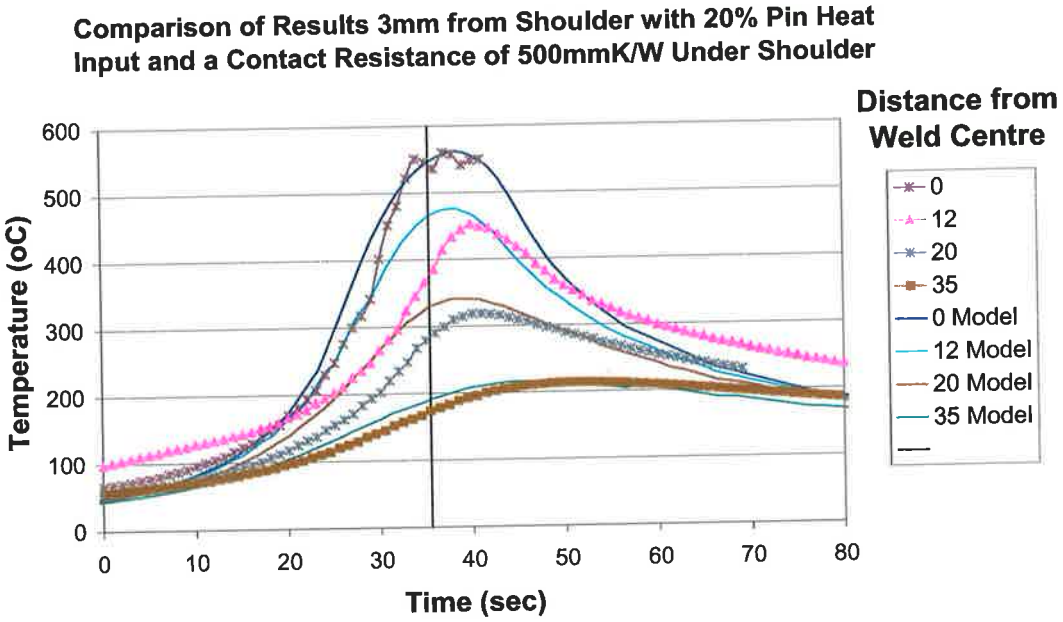

Figure 7-20 Comparison of Results 3mm from Shoulder with 20% Pin Heat Input and a Contact Resistance of 500 mmK/W Under Shoulder

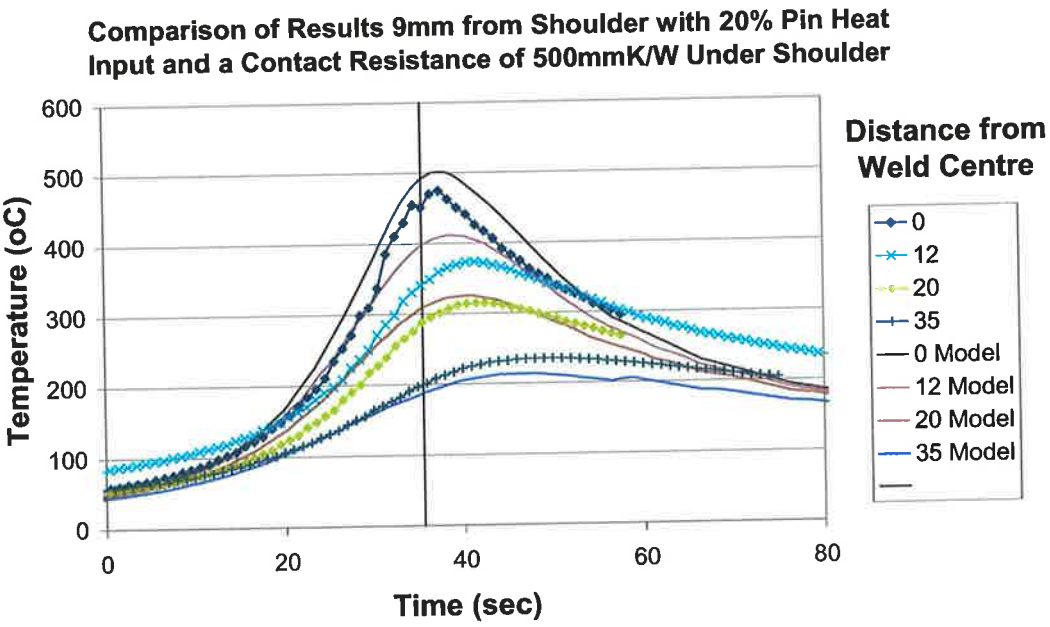

Figure 7-21 Comparison of Results 9mm from Shoulder with 20% Pin Heat Input and a Contact Resistance of 500 mmK/W Under Shoulder

Table 7-10

Model	Shoulder Heat (W)	Pin Heat (W)	Total Heat (W)	R_b	R_s	Thermal Profile
1	3474	0	3474	1000	1000	Figure 7-16 Figure 7-17
2	2940	588	3528	1000	1000	Figure 7-19
3	2940	588	3528	1000	500	Figure 7-20 Figure 7-21

Note:

- R_b = Contact Resistance of Backing Plate
- R_s = Contact Resistance of Shoulder

From these results the following points can be concluded:

- The accuracy of the thermal models is reasonable and the pin heat was found to have a relatively small influence on the calculated thermal cycle. All the models over predicted the thermal profile 12mm from the weld centre. This indicates that the heat generation under the shoulder at this point is too large.
- The model with no heat input at the pin gave good correlation with experimental data in the lower part of the weld, while the model with pin heat input showed better results toward top part of the weld. One of the reasons why the no pin heat model gave better results in the lower part of the weld may have been due to the lower contact resistance in this region caused by the high vertical load from the tool. This will assist heat conduction to

the backing plate, lowering the temperature of the workpiece material. Therefore, the greater heat loss is compensated by the lack of heat generation in this area. The effect of reduced contact resistance under the shoulder is modelled by the third model which gives reasonable results in this area.

7.3.3.5 Transient Thermal Model

Because of the reasonably significant discrepancy between the actual heat input and that predicted by the model shown above, it was decided to do a transient thermal model to see if there was any difference between the steady state results. A reasonably significant difference was found which is discussed in section 8.4.

7.4 Thermal Modelling of Thick Section Aluminium

At the University of Adelaide there is currently a project being undertaken on the Friction Stir Welding (FSW) thick section aluminium alloys. To assist this work, thermal modelling of the process has been done to enable a better understanding of the heat flows that occur during welding. This investigation will examine the welding of 5083, 7050 and a 1000 series aluminium alloy.

7.4.1 Input Parameters

7.4.1.1 Prediction of the Heat Generated by the Pin

To enable a reasonably accurate prediction of the heat distribution, an estimate of the heat generation around the pin will be made. This will be based on the formulas in section 6 and will use the input parameters shown in Table 7-11.

Table 7-11

Parameter	**5083 Value**	**7050 Value**	**1000 Series Value**	**Comment**
Temperature at Pin (°C):	500	500	500	See Experimental Results 000313B
σ_y (MPa) at 500(°C)	20	31.84	11.91	See comment below.
τ (MPa) at 500(°C)	11.55	18.38	6.88	$\frac{\sigma_y}{\sqrt{3}}$
r_p (mm)	8	8	8	
h_p (mm)	25	25	25	
ω (rad/s)	36.65	36.65	36.65	350 rpm
pitch (mm)	4	4	4	Estimated
λ	0.08	0.08	0.08	
F = Horizontal Welding Force (kN)	10.00			See section 4.3.2

For the three materials under investigation, an approximate value of this heat generation is shown in Table 7-12.

Table 7-12

Material	**Solidus Temp (°C)**	**Welding Temp (°C)**	**Analysis Type**	μ	σ_y(MPa)	Q(W)
5083	574	550	Friction Slip	0.2	20.08	1175
				0.3	20.08	1565

Material	**Solidus Temp (°C)**	**Welding Temp (°C)**	**Analysis Type**	μ	σ_y**(MPa)**	**Q(W)**
7050	524	500	Friction Slip	0.2	31.84	1859
				0.3	31.84	2471
1000 Series	646	500	Friction Slip	0.2	11.91	701
				0.3	11.91	935
			No Slip	N/A	11.91	2534

Please note the following features from the results:

- Where the yield strength is high, the heat generation rate is also high and vice versa.
- The results are reasonably sensitive to the coefficient of friction selected.
- Because the yield strength is so low and the solidus temperature is so high for the 1000 Series aluminium, it is believed that the material is more likely to stick to the surface of the tool. (See discussion in section 3.2.3.3) In addition to this, the conductivity of the material is much higher making it more difficult to heat up to the higher welding temperature. See section 7.4.1.

7.4.1.2 General Input Parameters

All the welds will be made using the following welding parameters:

- Plate Thickness = 25 mm.
- Plate Width = 70 mm.
- Shoulder Diameter = 40 mm.
- Pin Diameter = 16 mm.

- Weld Speed = 1 mm/s
- Weld Rotational Speed = 350 rpm.
- Ratio of pin heat input to total heat input = 30% (This ratio is independent of the material being used)

The weld travel and rotational speeds are a first estimate and may in fact not produce a good weld. The aim of the work is to compare the welding of various materials from a theoretical perspective rather than predicting whether a weld is or is not achievable.

The material properties shown in Table 7-13 are used for the model. In the preliminary work it has been assumed that the maximum temperature in the weld is equal to the solidus or insipient melting temperature for 5083 and 7050 alloys. For the 1000 series alloy, the maximum temperature will be significantly lower. See discussion in section 7.4.2.

Table 7-13

Material	**Description**	**Solidus Temp (°C)**	**k(W/mmK) T = 20°C**	**k(W/mmK) Welding Temp.**	**c_p (J/kgK)**	**ρ (kg/mm^3)**
1a – 5083	Workpiece Material	574	[1]120 x10^{-3}	[3]126 x10^{-3}	[1]896	[1]2.7x10^{-6}
1b – 7050	Workpiece Material	[5]524	[1]180x10^{-3}	[3]189 x10^{-3}	[1]896	[1]2.7x10^{-6}
1c – 1350	Workpiece Material	646	[1]234x10^{-3}	[3]246 x10^{-3}	[1]896	[1]2.7x10^{-6}
2 – Carbon Steel	FSW Shoulder			[2]40x10^{-3}	[2]465	[2]7.85x10^{-6}

Material	**Description**	**Solidus Temp (°C)**	**k(W/mmK) T = 20°C**	**k(W/mmK) Welding Temp.**	**c_p (J/kgK)**	**ρ (kg/mm^3)**
3 – Carbon Steel	Backing Plate			[2]52x10^{-3}	[2]465	[2]7.85x10^{-6}
4 – Dummy Material	Contact Resistance			[4]5.0x10^{-4}	N/A	N/A

Note:

[1] Properties are gained from the Aluminium Handbook.

[2] Properties from JP Holman. [22]

[3] Properties altered based on results from Holman. [22].

[4] Equivalent thermal conductivity of the contact resistance was found in section 7.3.3.

[5] Note that the eutectic temperature is 465°C and the temperature where incipient melting occurs for homogenised wrought material is 488°C. Hence the maximum temperature achieved during welding may be below the solidus temperature.

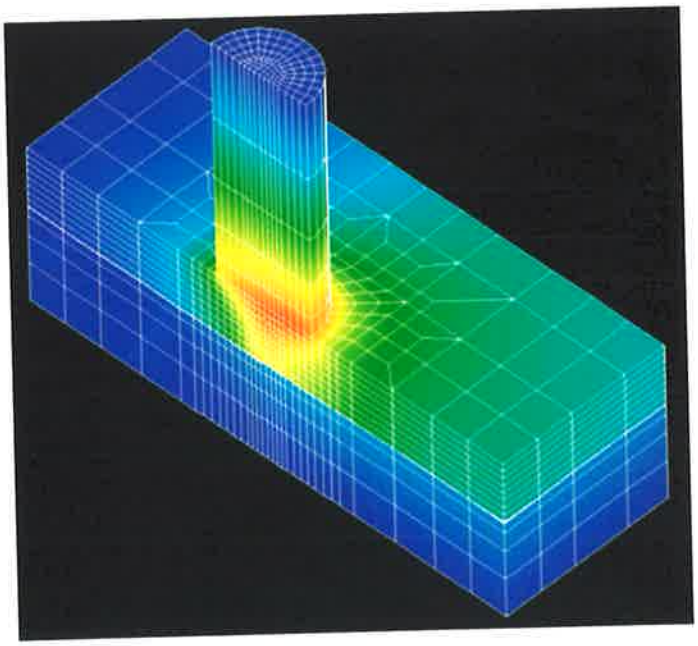

Figure 7-22 Thermal Profile Obtained for Steady State Model

7.4.2 Results

A diagram demonstrating the thermal contours obtained is shown in Figure 7-22.

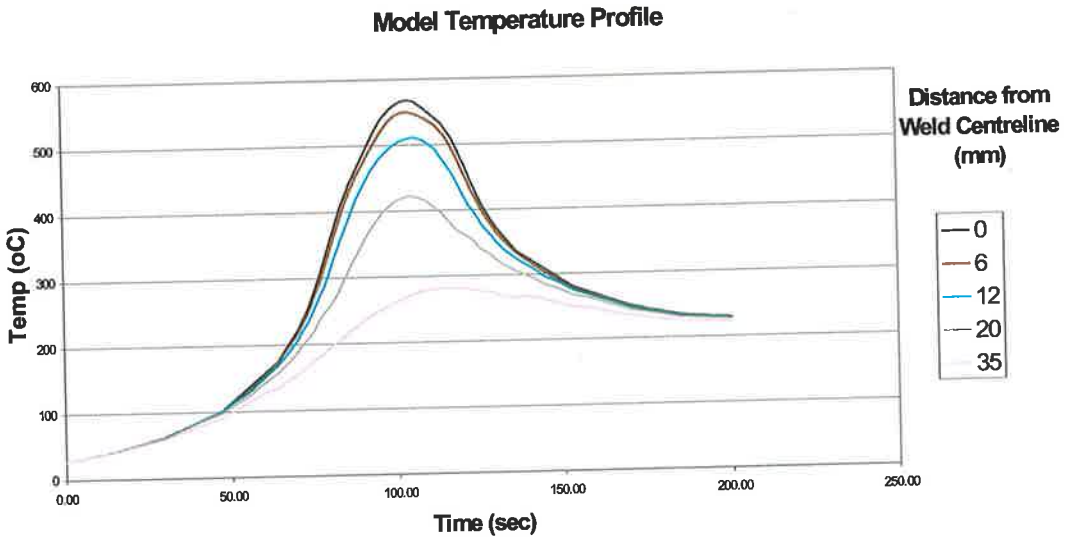

Figure 7-23 Temperature Profile 3mm from Top of Plate for 5083 Aluminium Alloy

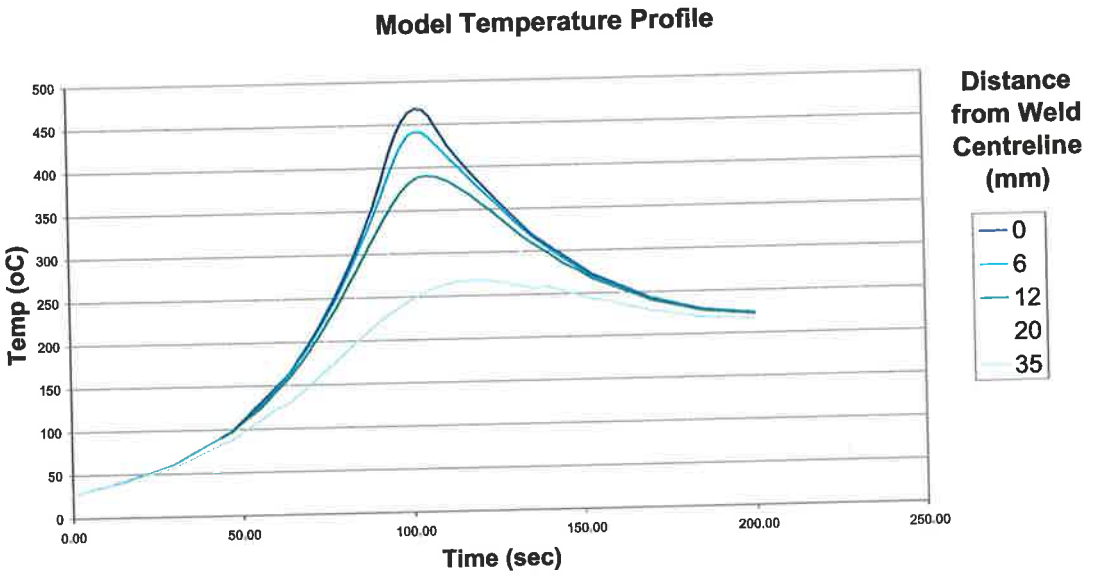

Figure 7-24 Temperature Profile 6mm from Bottom of Plate for 5083 Aluminium Alloy

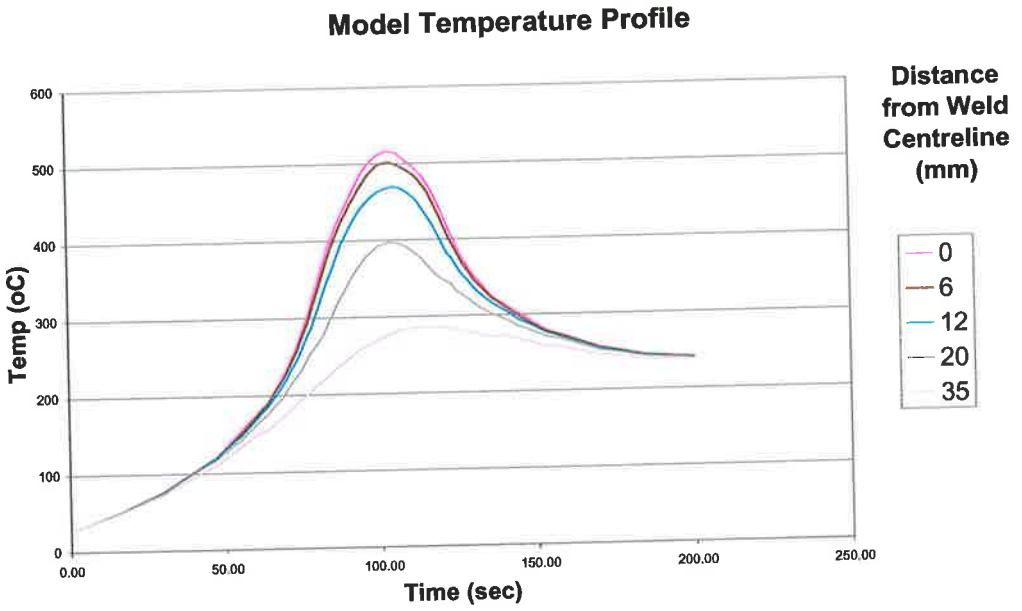

Figure 7-26 Temperature Profile 3mm from Top of Plate for 7050 Aluminium Alloy

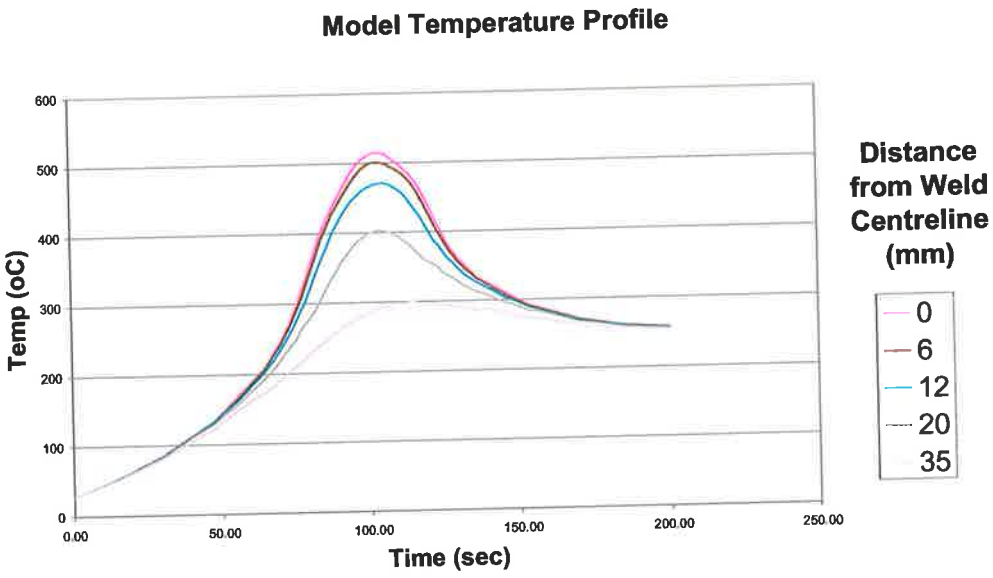

Figure 7-25 Temperature Profile 3mm from Top of Plate for 1350 Aluminium Alloy (Low Heat Input)

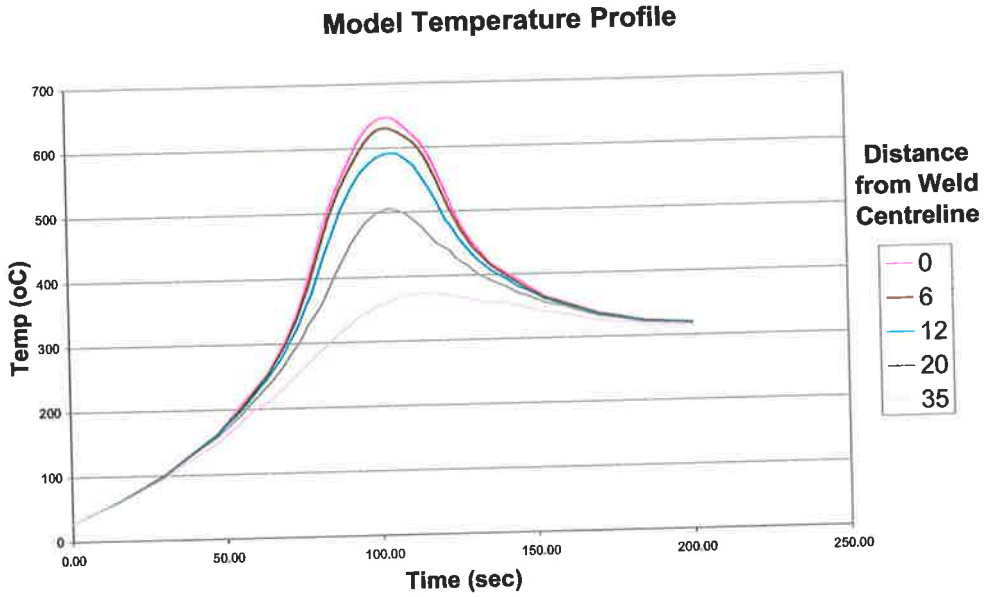

Figure 7-27 Temperature Profile 3mm from Top of Plate for 1350 Aluminium Alloy (High Heat Input)

Table 7-14

Material	Position	Figure	Q (W)	Q_s (W)	R_s
5083	3mm from Top	Figure 7-23	5000	284.48	0.0569
5083	6mm from Bottom	Figure 7-24	5000	284.48	0.0569
7050	3mm from Top	Figure 7-26	5800	256.84	0.0443
1350	3mm from Top	Figure 7-25	6600	256.36	0.0388
1350	3mm from Top	Figure 7-27	8400	326.26	0.0388

Note:

Q is the total heat input into the model.

Q_s is the heat loss through the shoulder.

R_s is the ratio of the heat loss through the shoulder to the total heat input.

A summary of these graphs and the corresponding operating parameters is shown in Table 7-14. Note that the heat conducted through the tool will be used for the transient thermal models which is discussed in section 8.2.

7.4.3 Discussion

The main points to note from these results are :

- Assuming that the maximum welding temperature will be equal to the solidus temperature for 5083 and 7050 will lead to a slight over-prediction of the heat input. This assumption has been used as a first estimate only. The validity of this assumption is discussed in section 3.3.
- Comparing Figure 7-23 and Figure 7-24 it is clear that while there is some reduction in the temperature around the base of the weld as opposed to the top, the difference is not great. The results around the bottom of the weld were not shown for the other two welds for the sake of conciseness.
- Initially one would think that more energy would be required to weld the harder, high alloy material than the softer, purer 1000 Series Alloy. However the opposite is indeed the case. The 1000 Series requires much more heat to achieve a welding temperature of around 500°C than the 7050 and certainly the 5083 Series aluminium alloys. This is because the 1000 Series aluminium alloy has a much higher thermal conductivity which tends to cool the weld. This is partially supported by the results from Johnson and

Horrex [63] discussed in section 3.4.7. In this work the better conducting 6082 required slightly more power to weld at the same traverse speed than the harder and poorer conducting 5083 aluminium alloy.

- The greater thermal conductivity of the 1000 series alloy also leads to a much flatter thermal profile for this material.
- The final weld temperature is much greater for the 1000 Series weld than for 5083 or the 7050 aluminium alloys. This is because of the greater amount of heat that has been put into the material.
- At the proposed welding parameters of 1mm/s and spindle speed of 350 rpm. it will be difficult to generate the required amount of heat of 6600 W for the 1000 Series aluminium and achieve the thermal profile shown in Figure 7-25. Assuming that the yield strength of the material is 12 MPa at a temperature of 500°C and that the material sticks to the surface of the tool as opposed to sliding then the maximum heat that can be produced by the tool is 6500W. Note that in this case the temperature is sufficiently below the solidus temperature that the material will tend to stick to the tool. (See section 3.2.3.3)
- The thermal profile shown in Figure 7-27 where the 1000 Series alloy reaches the solidus temperature has been included for the sake of comparison, but is not actually achievable in practice. This is because the heat requirement of 8400W is well beyond that which can be achieved even if the material were to stick to the surface of the tool. (Which is in itself impossible given that the solidus temperature has been reached and slip will occur at the surface.) The material at this temperature has an even lower yield strength than the already low value of 12MPa at 500°C further reducing

heat production. The only way that such a temperature could be achieved is if very high rotational speeds were used in conjunction with a low welding speed.

- There is an upper limit to the thermal profile. Greater rotational speeds or lower welding speeds will not increase the temperature to any great extent. This is because the material is already slipping so more heat cannot be produced by increasing the rotational speed. The only thing that may occur is a more even temperature distribution through the weld.

Therefore the problems encountered during welding are very much material dependent. When welding the 1000 Series aluminium alloys the main problem is in generating the heat necessary to plasticise the material and make the weld. On the other hand, when welding the 5083 and 7050 aluminium alloys the problem becomes one of avoiding the solidus temperature where surface melting may occur. Once the solidus has been reached, the heat generation will be drastically reduced because the material deformation is now much less. Secondly, because the shear stress exerted by the tool on the material is less, it will be much more difficult for the tool to drag the material behind the pin with a surface void being the result.

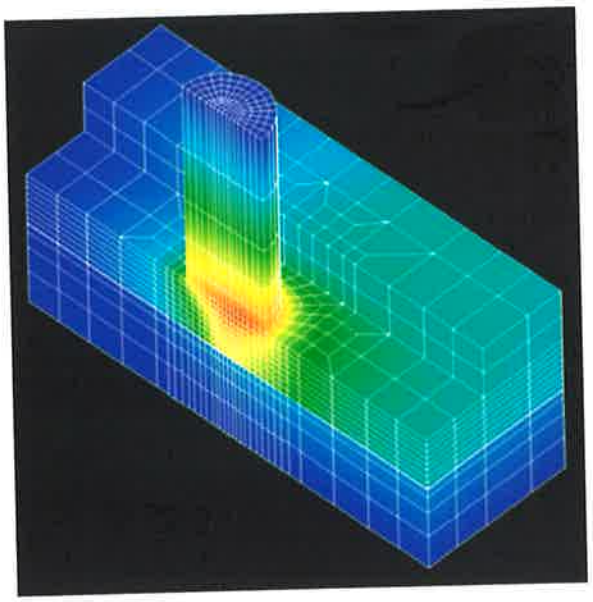

Figure 7-28 Thermal Contours Around Heat Sink Model

7.4.4 Heat Sink Model

One final investigation has been made, namely to see the effect of an odd shaped plate, which will act like a heat sink to the weld. This has been done to demonstrate the effect of irregular shaped parts on the heat input required. Examples of such parts are stiffeners and the welding of a T joint as opposed to a standard butt joint. The diagram showing the resulting thermal profile from such a weld is shown in Figure 7-28.

Generally, it was found that to achieve a similar thermal profile to those obtained in section 7.4.1, the heat inputs required an increase of between 4 -9%. This is summarised in table Table 7-15.

Table 7-15

Material	Normal Heat (W)	Modified Plate Heat Input (W)	% Difference
5083	5000	5200	4.00%
7050	5800	6200	6.90%
1000 Series	6600	7200	9.09%

Therefore a marginal increase in power is required when welding with a large heat sink on the side. The power increase required is greater for the materials with higher thermal conductivity.

8 Transient Thermal Model

Out of the various thermal models that have been reported on, the only author to publish results from a transient thermal model was Frigaard et. al. [8,10]. Frigaard stated that transient effects had an effect on the thermal profile, due to the heat reflection from the end of the plates. In addition, the transient thermal model will give an understanding how the temperature varies during the plunge sequence, and will give an indication about how long the tool needs to dwell before welding.

8.1 Mesh and Heat Generation

Two types of mesh have been used for the transient thermal model, which are shown in Figures 8-1 and 8-2. Both meshes use linear 8-noded hexagonal elements. Referring to Figure 8-1, the mesh which is used as the tool traverses the plate does not include the

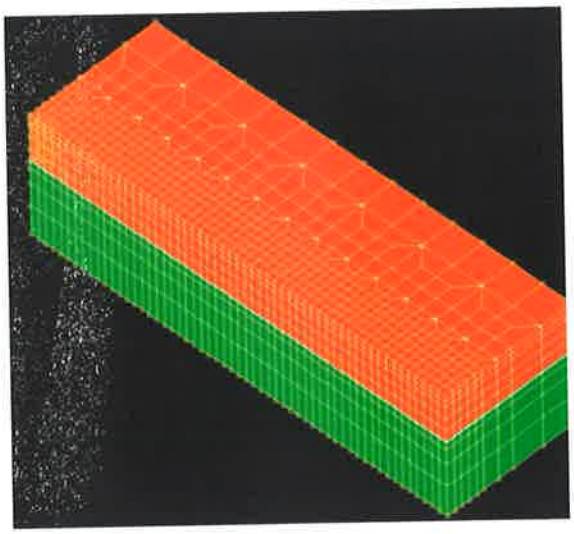

Figure 8-1 Transient Model Mesh During Traverse

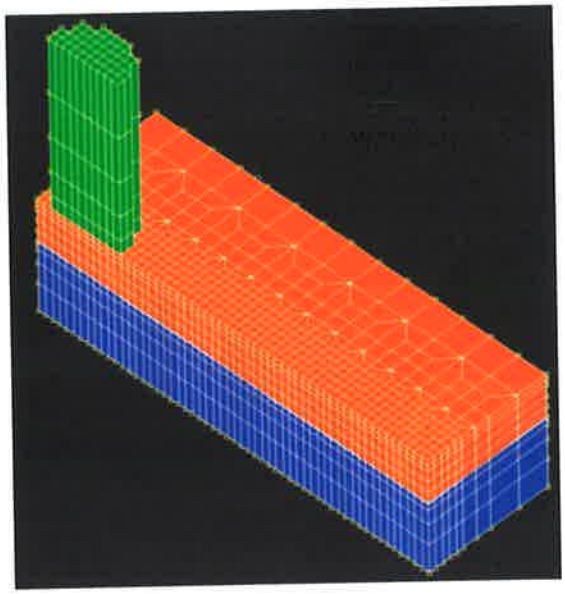

Figure 8-2 Transient Model Mesh During Start-up

tool in the model. This simplification is adapted because including the tool would require a moving mesh, making the model exceedingly complex. Therefore to avoid this situation, the heat conducted through the tool is subtracted from the total heat input which is then applied to the plate. The heat conducted through the tool was found for the steady state weld in section 7.4.1.

One cannot however apply such an approach to the start of the weld. When the tool is cold additional heat will be required to bring it up to welding temperature. Therefore, applying the same ratio of:

$$\frac{Q_{tool}}{Q_{total}} = \frac{(Heat\ loss\ through\ tool)}{(Total\ heat)}$$

to the start-up to that used during the weld will not be valid. Additionally the main

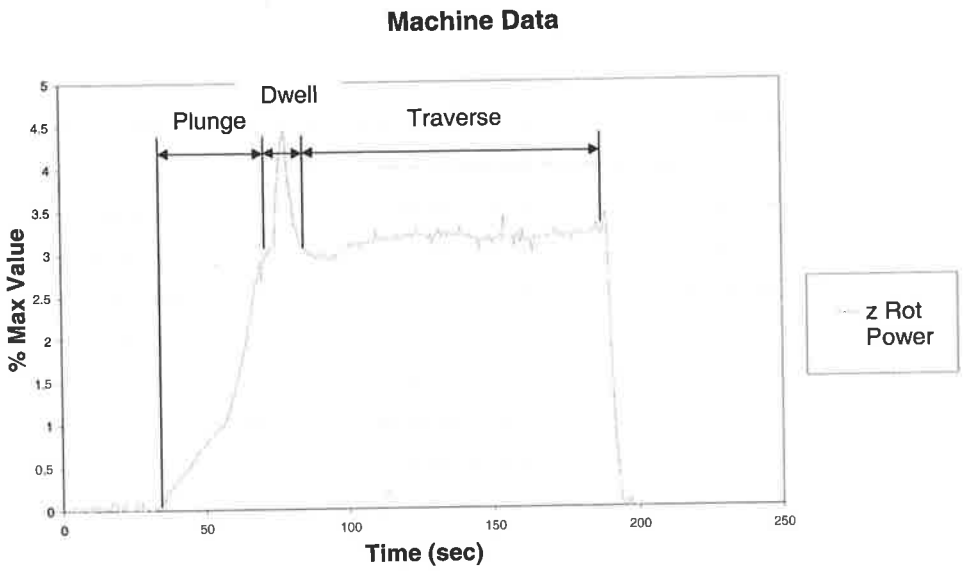

Figure 8-3 Power Input Profile While Welding 12mm Thick 5083

reason for not including the tool in the model for the traverse section of the weld (ie deforming mesh) is no longer valid. Therefore the tool is included in the mesh as shown in Figure 8-2. The temperature results from the start-up section are then used as the starting temperature for the remaining section of the weld.

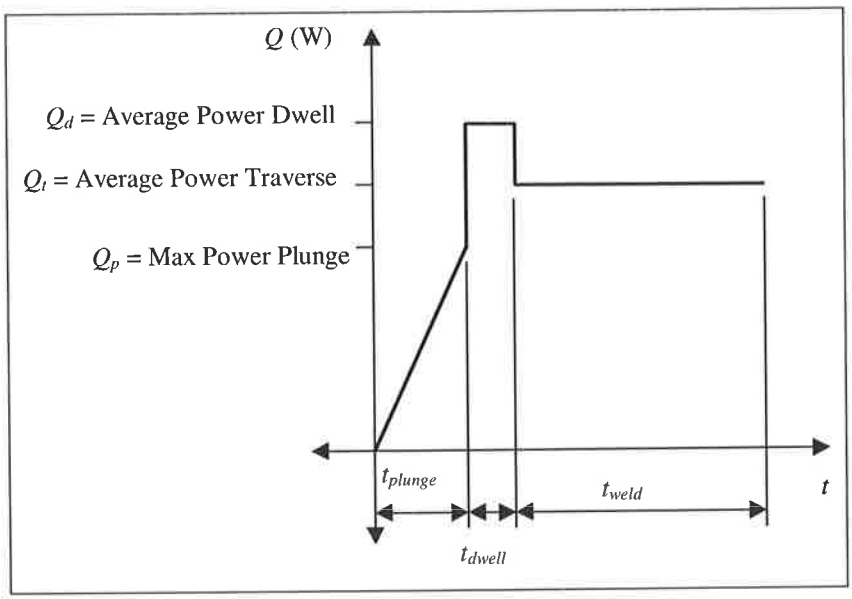

Figure 8-4 General heat input profile.

The main source of error with this approach is that during the plunge, only the pin is in contact with the material, so the only point of contact is between the pin and the workpiece material. In the model complete contact occurs between the tool shoulder and workpiece material for the duration of the start-up sequence. With this modelling approach this situation is unavoidable.

The heat input is not constant through the duration of the weld and has been divided into three main sections. Figure 8-3 shows the power input to the motor for a weld done on 12 mm plate. The three sections are identified on this diagram as the plunge, dwell and traverse sections of the weld. In an effort to simplify the heat input, the profile shown in Figure 8-4 has been used:

One further point that should be mentioned is that the convective heat loss around the periphery of the tool has been ignored in the initial start-up of the model. Since it may be shown that its value is less than 1% of the total heat input, its exclusion will have no significant impact on the result.

8.2 Transient Thermal Modelling of Thick Plate Aluminium

8.2.1 Input Parameters

The input parameters for the transient models are the same as for the steady state welds described in section 7.4, with the following additional parameters being used:

Table 8-1

Parameter	Value	Description
Plunge Rate	15 mm/min	The rate at which the tool is inserted into the workpiece material
Dwell Time	5 sec	The time that the tool waits and heats up the material before welding.
Length of Plate	224 mm	
Length of Weld	170 mm	

8.2.2 Results

Typical welding thermal profiles are shown for three positions in Figures 8-5, 8-6 and 8-7. Figure 8-5 shows the thermal profile in the weld just prior to the shoulder touching the workpiece material. Obviously all the heat generation at this stage will be around the pin. Figure 8-6 shows the temperature profile mid-weld which approximates that achieved for the steady state weld. Finally, Figure 8-7 shows the thermal profile near the end of the plate where the temperature increases due to the reflection of heat from the end of the plate. (or lack of conduction away.)

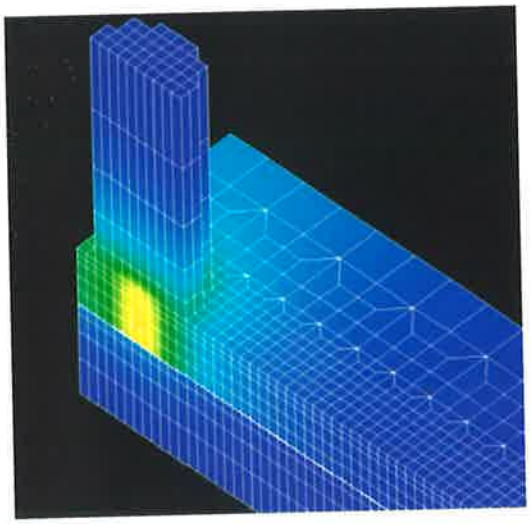

Figure 8-5 Thermal Profile During Start-up

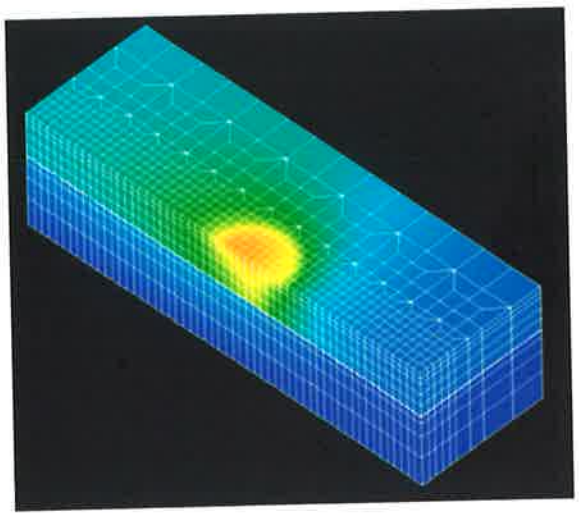

Figure 8-6 Thermal Profile Mid-Weld

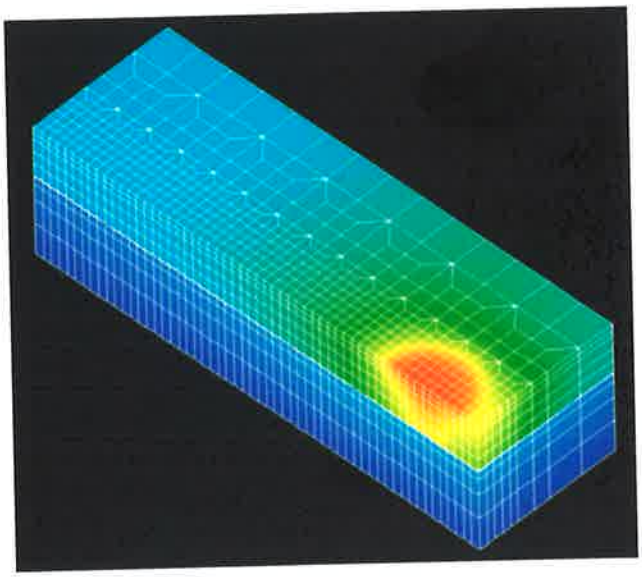

Figure 8-7 Thermal Profile End of Weld

A large amount of data is procured from such a model, so it is necessary to find a way of intelligently analysing the results. One way of doing this is to look at the maximum temperature achieved along lines of constant y and z position for each iteration (See Figure 1-1 for coordinate system.) and compare the results with the maximum value achieved for the weld thermal cycle found for the steady state weld in section 7.4.1. Such graphs are shown for the three welds in Figure 8-8, Figure 8-10 and Figure 8-9. These graphs clearly show:

- How the temperature raises toward the end of the plate. The weld will to a certain extent be self regulating in the fact that as the temperature rises, the

heat generation will decrease due to additional slip. This effect has not been included in the thermal model.

- The temperatures achieved differ quite widely from those achieved for the steady state welds in section 7.4.1. Initially, it was believed that an error had been made in the formulation, however subsequent checks showed that this was not the case. See section 8.3. It was also found that this deviation was greatest for the aluminium alloys with the highest thermal conductivity. It is believed that because aluminium is such a good conductor of heat the whole plate tends to get heated up during the initial plunge. Therefore, the heat required for the subsequent weld then tends to be much lower. It is expected that this effect would not be as great for longer length welds where the thermal profile will tend toward that achieved in the steady state.
- The analysis allows us to determine whether or not the dwell time of 5 seconds is appropriate.

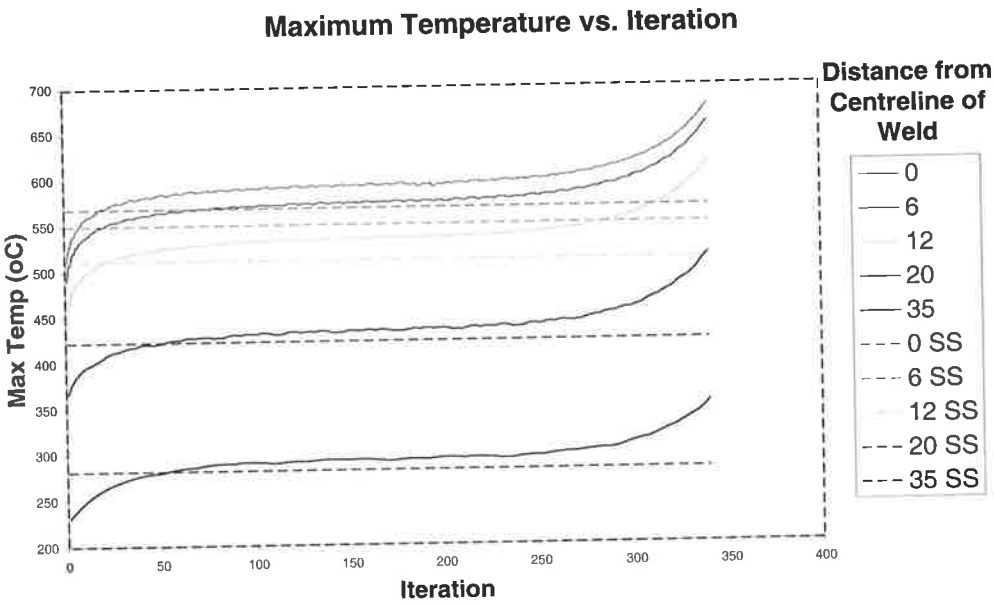

Figure 8-8 Transient vs. Steady State Maximum Temperatures 3mm from Top Surface for 5083 with 5 sec Dwell Time

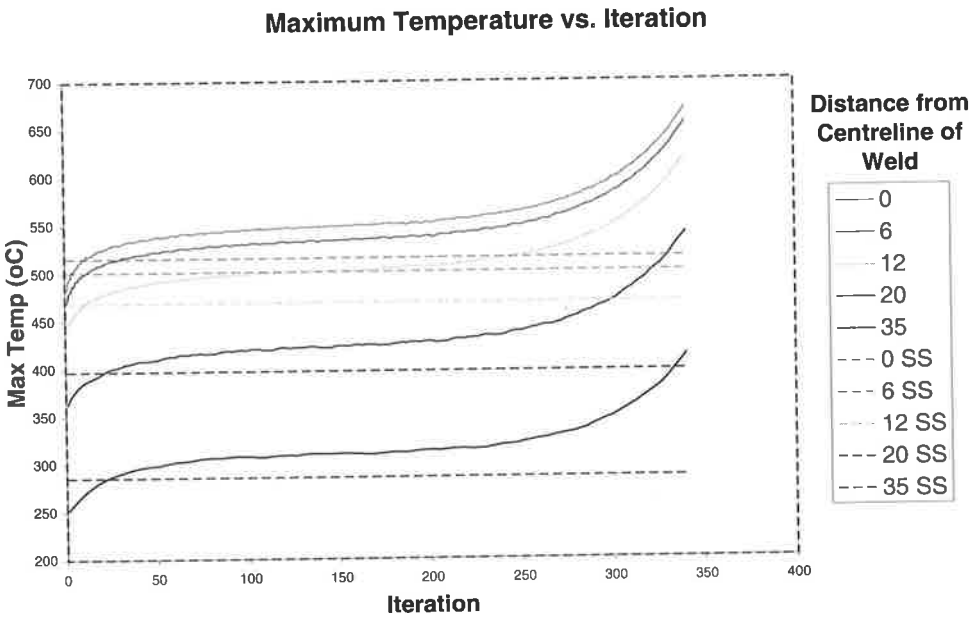

Figure 8-10 Transient vs. Steady State Maximum Temperatures 3mm from Top Surface for 7050 with 5 sec Dwell Time

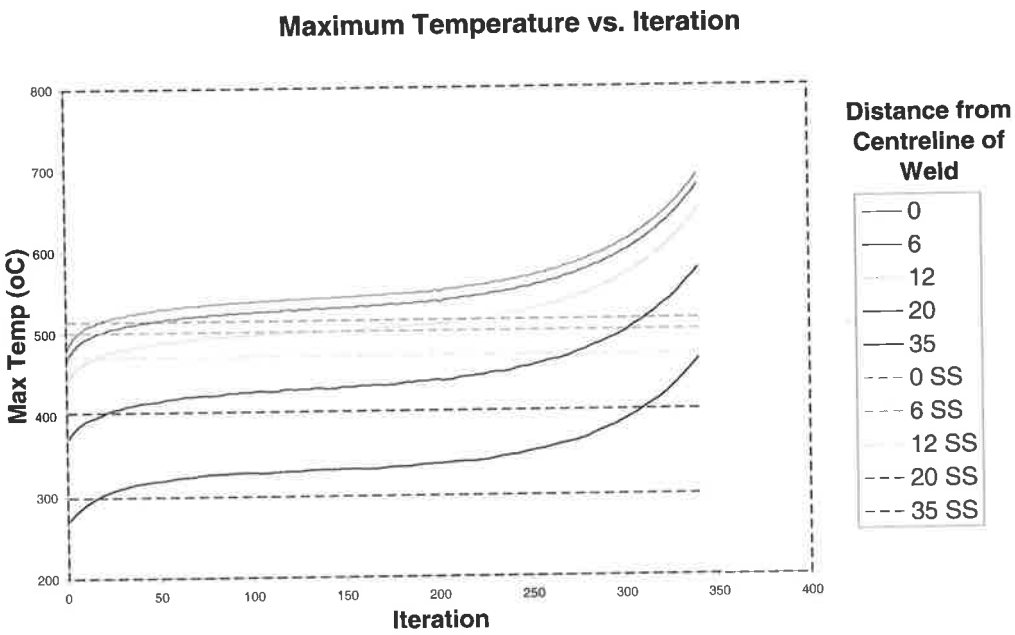

Figure 8-9 Transient vs. Steady State Maximum Temperatures 3mm from Top Surface for 1350 with 5 sec Dwell Time

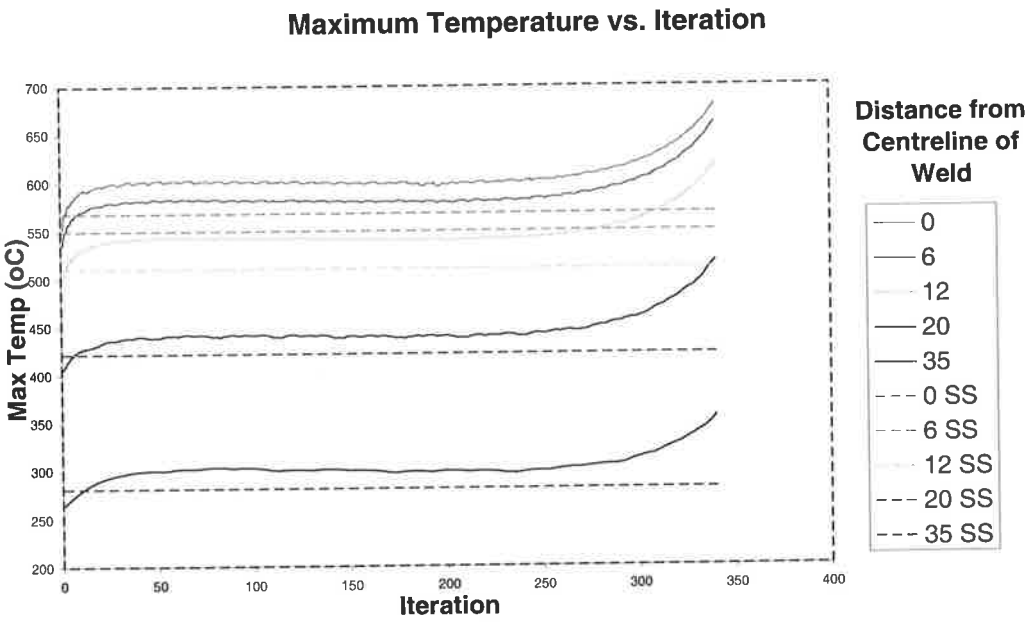

Figure 8-11 Transient vs. Steady State Maximum Temperatures 3mm from Top Surface for 5083 with 550 Maximum Temperature Set (14 sec dwell)

Finally, a different analysis was done for the 5083 aluminium alloy only, whereby the dwell time was increased till the maximum temperature had reached 550°C, before starting the traverse section of the weld. See Figure 8-11. It is interesting to note how the temperature raises quite sharply after the material has started to weld and then drops off as the tool moves further from the end region of the plate. This demonstrates how the end of the plate has a significant effect on the resulting thermal profile achieved during a weld.

8.3 Checking the Discrepancy in the Transient vs. Steady State Thermal Models

The above discrepancy between transient and steady state models was unexpected. Initially, it was believed that the discrepancy had been caused by one or more of the following:

- The tool had not been included in the transient model but was included in the steady state model. Therefore if the shoulder heat loss ratio, R_s was not calculated correctly then this may be one source of error.
- The new transient model used a different method for setting both the convective boundary conditions and applying the heat input. Therefore it may be possible that the new program may have produced some error.

To identify which if any of the above could have caused the discrepancy the following steady state test models were created.

- Model 1.

  This model was identical to the standard steady state model, except that the tool was removed. Therefore it was necessary to factor down the heat input by the shoulder heat ratio.

- Model 2.

  This model used the same mesh as the transient thermal model and used a modified version of the program which set the boundary conditions on the transient model.

A comparison between the proposed test models and the standard steady state model for 5083 described in section 7.4.2 is shown in Table 8-2. The results compare the maximum temperature in the weld at various distances from the centreline and 3mm

underneath the top surface. Interestingly, the first model over-predicted the temperature in the weld indicating that the shoulder heat loss ratio was slightly too low. The results for the second model were even more interesting. Rather than the overprediction of temperature that was expected, the test model actually consistently under-predicted the weld temperature by 20°C. It is believed that the difference was caused by the different mesh density.

Therefore it is possible to conclude that:

- The discrepancy between transient thermal model results and steady state thermal model results could not be explained by either the new mesh, heat application program or the fact that the shoulder had not been used in the model.
- We can be reasonably confident that the results presented in section 8.2.2 give a reasonable prediction of the temperature field if that heat input could be achieved.

Table 8-2

Distance from Weld Centre-line (mm)	Max Temperature (°C)			Error (°C)	
	Standard Model	Model 1	Model 2	Model 1	Model 2
0	568.28	587.61	546.41	19.33	21.87
6	550.07	568.29	529.73	18.22	20.34
12	510.99	524.87	492.82	13.88	18.17
20	422.25	424.86	398.78	2.61	23.47
35	281.48	283.06	265.23	1.58	16.25

8.4 Transient Thermal Modelling 12mm Thick 5083 Aluminium

Because of the discrepancies found between the steady state and transient thermal models in the previous section, it was decided to see whether transient effects could have been the cause of the over-prediction of the required heat input for the steady state model of 12mm thick 5083 in section 7.3.3. This is described in the following section.

8.4.1 Input Parameters

The input parameters for the transient models are the same as for the steady state welds described in section 7.3.3, with the additional parameters shown in Table 8-3 being used:

Table 8-3

Parameter	**Value**	**Description**
Plunge Rate	10 mm/min	The rate at which the tool is inserted into the workpiece material
Dwell Time	4 sec	The time that the tool waits and heats up the material before welding.
Length of Plate	224 mm	
Length of Weld	170 mm	
R_s	0.0779	Ratio of shoulder to total heat

It is interesting to note that R_s is much higher for the thinner plate material.

Two different heat inputs have been used which are summarised in Table 8-4

Table 8-4

	Total Heat	Pin Heat Input Ratio
Model 1	3500W	10%
Model 2	3000W	10%

Note:

- A pin heat input ratio of 10% has been used for both models which is a compromise between 0 and 20%.
- Due to the model construction it is not possible to have a region of reduced contact resistance underneath the tool.

8.4.2 Results

8.4.2.1 Model 1

Figure 8-12, Figure 8-13 and Figure 8-14 show a comparison between model 1 and the steady state thermal model 3 from section 7.3.3.4. Generally it was found that like

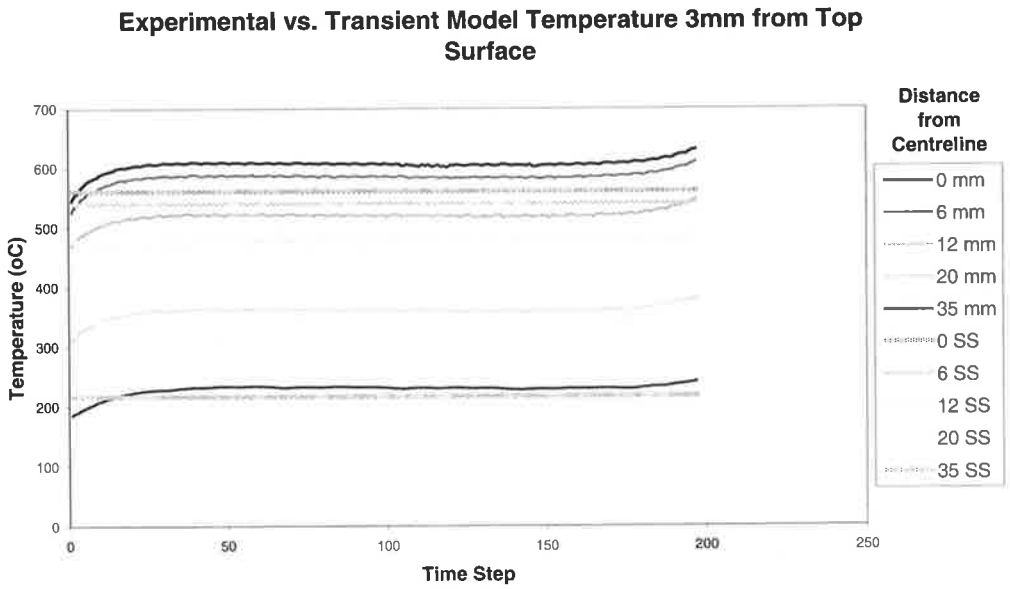

Figure 8-12 Transient vs. Steady State Results 3mm from Top Surface for Model

section 8.2.2, the transient thermal model predicted the much higher welding temperatures for the same heat input when compared with the steady state thermal model.

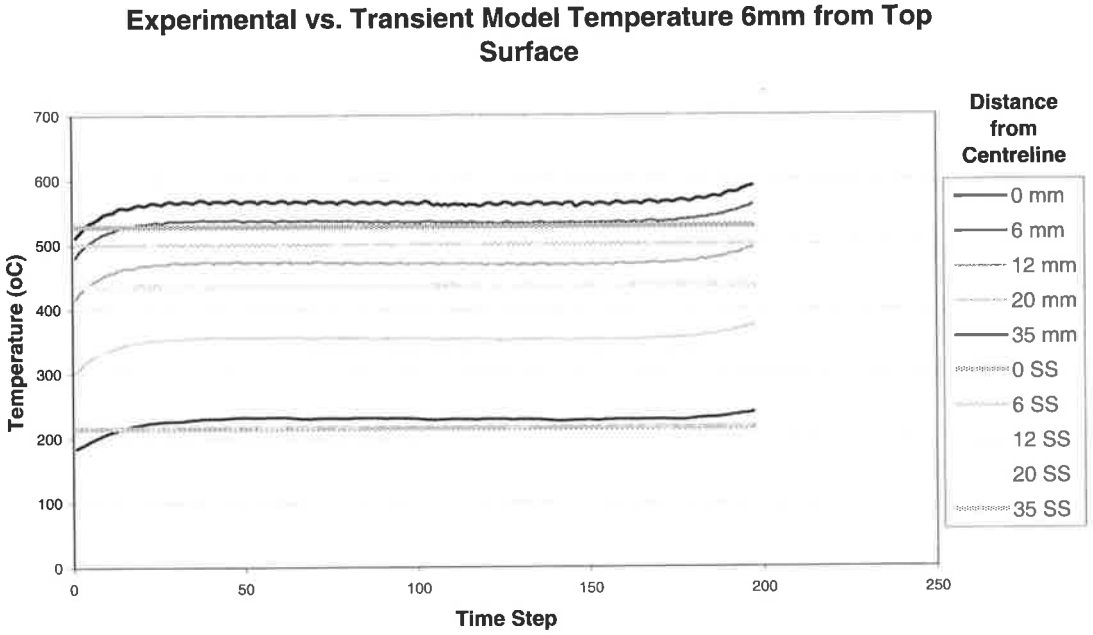

Figure 8-13 Transient vs. Steady State Results 6mm from Top Surface for Model 1

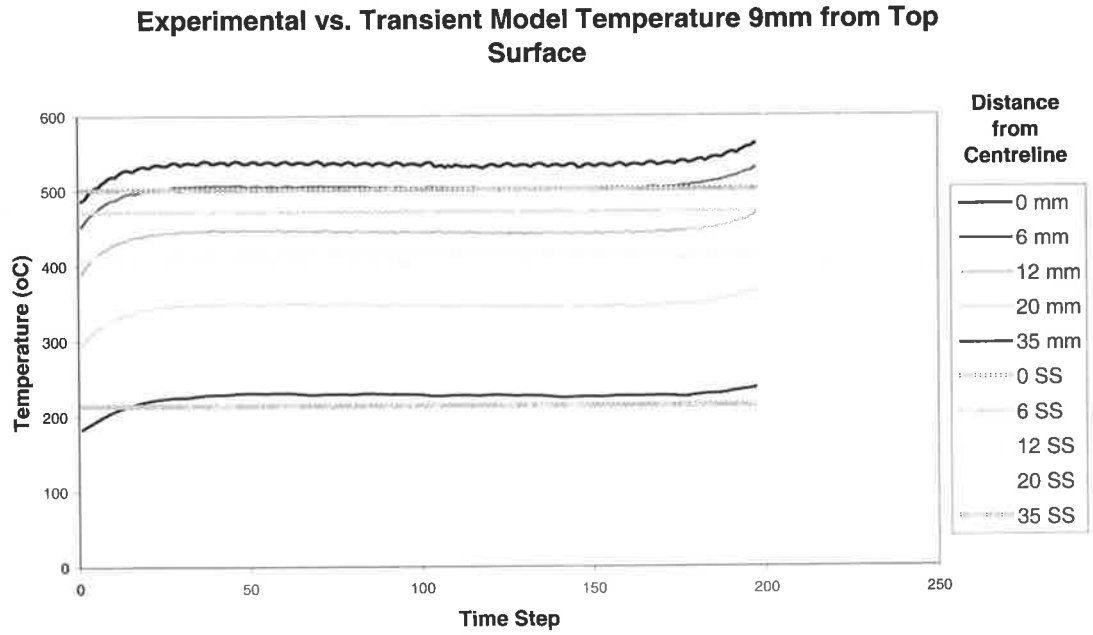

Figure 8-14 Transient vs. Steady State Results 9mm from Top Surface for Model 1

8.4.2.2 Model 2

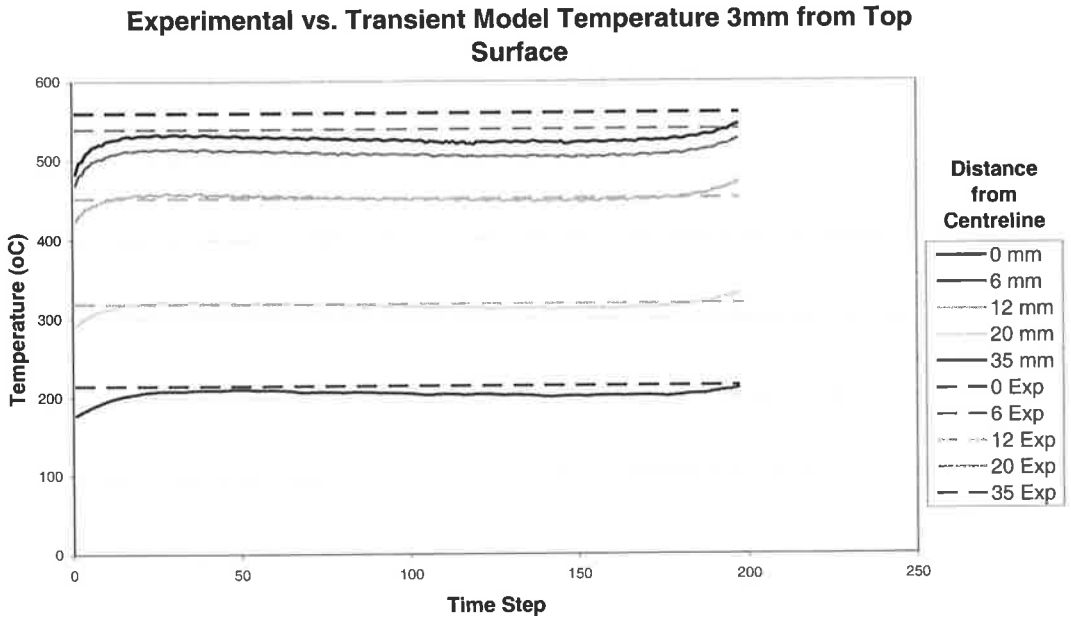

Figure 8-15 Experimental vs. Transient Results 3mm from Top Surface for Model 2

Graphs showing a comparison between experimental and the transient model for various distances from the top surface are shown in Figure 8-15, Figure 8-16 and Figure 8-17. Generally it was found that for thermocouple positions outside the mixing zone the correlation between experimental and model results was excellent. Interestingly, one of the positions of maximum discrepancy was for the thermocouples 35mm from the weld. This result confirms the experimentally determined heat input in section 7.3.3.2.

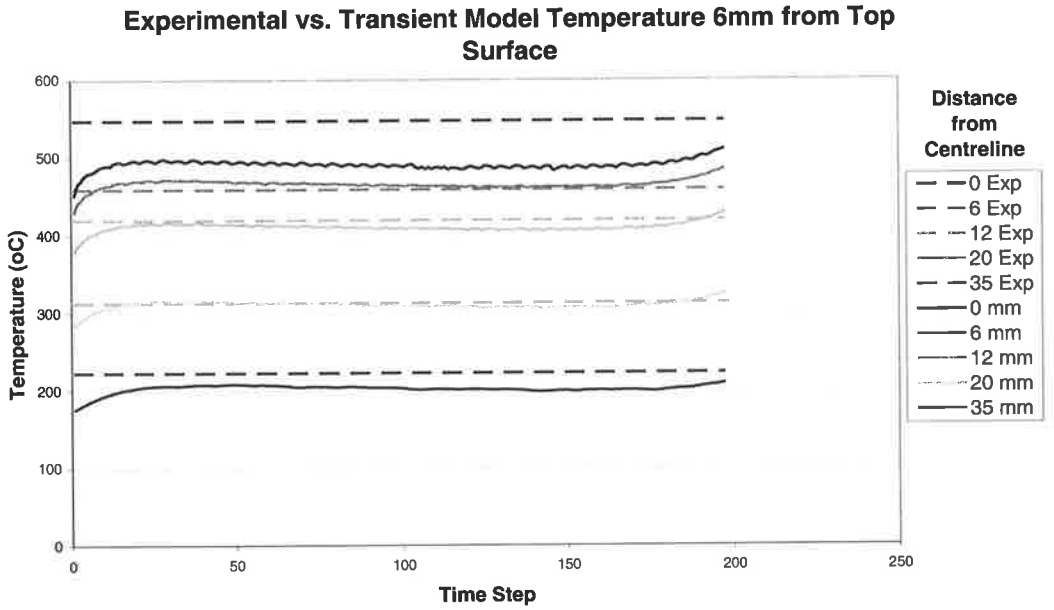

Figure 8-16 Experimental vs. Transient Results 6mm from Top Surface for Model

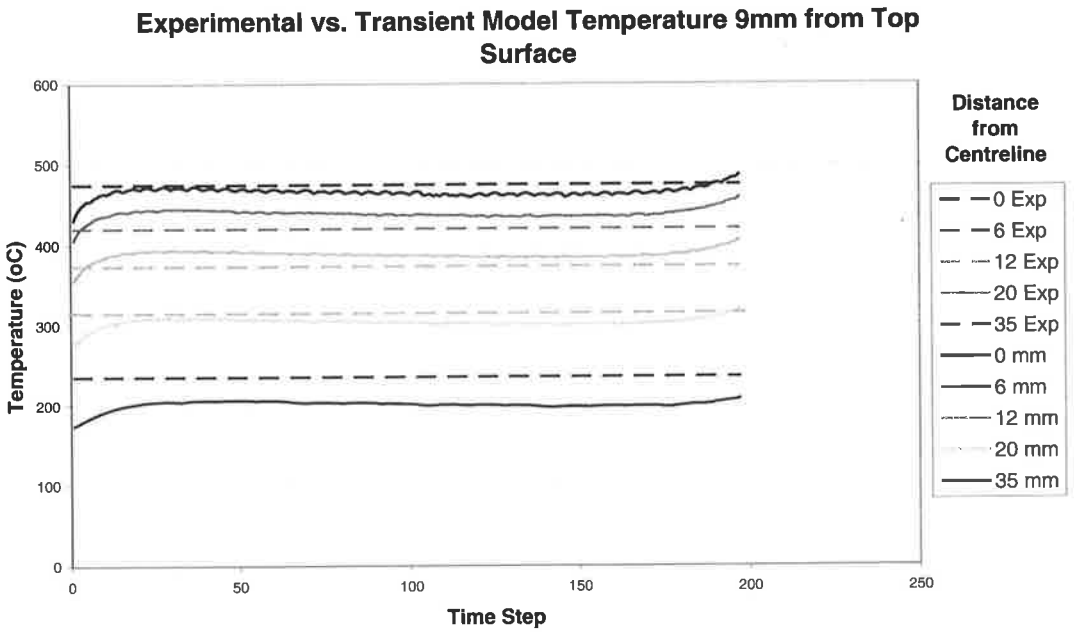

Figure 8-17 Experimental vs. Transient Results 9mm from Top Surface for Model

9 Experimental Results for Welding 25mm Thick 5083 Aluminium

9.1 Introduction

As mentioned in section 8.2, a project is being undertaken at the University of Adelaide for the Friction Stir Welding of thick plate aluminium. The objective of this work is to produce a successful weld. Temperature measurements were taken during the welds to:

- Validate the thermal models presented in section 7.4. Please note that there was insufficient time to complete this task.
- Enable a better understanding of the state of the material at the tool interface.

Some early temperature results from this work are presented in the following section. Please note that Mr. Rudolf Zettler, designed and manufactured the all mechanical equipment associated with this work.

9.2 Description of Equipment

In this work thermocouples were placed not only in the workpiece material but were also located within the FSW tool. The thermocouples located in the tool enabled the temperature at the tool/aluminium interface to be measured. Measuring the interface temperature in this way has the following advantages over similar measurements in the workpiece material:

- Because there is a large amount of plastic deformation in the workpiece material it is difficult to locate a thermocouple at the interface. This problem was identified by Smith et. al. [82] who found that there was significant movement of the thermocouple from the desired location.

- The temperature gradient through the tool is expected to be significantly less than the workpiece material. This is because the temperature at the tool is essentially in steady state during the welding period. Therefore locating the thermocouple at the interface becomes slightly less critical, although it is still necessary to get it as close as possible.

The thermocouples in the plate were inserted into 2mm diameter holes. The location of these holes is described in Appendix G. Please note that unlike the bead-on-plate weld in section 4 two plates were welded together, since a drill was found that enabled 70mm deep holes to be produced.

Mounting thermocouples in the spindle was more complex. Holes were drilled through the tool to enable the thermocouples to be located as close as possible to the tool surface in the following four locations:

- Shoulder.
- Top of the Pin.
- Middle of the Pin.
- Bottom of the Pin.

These thermocouples were then connected to an amplifier that was located on a slip ring which rotated with the tool. Amplifying the signal at the tool minimised the electrical noise, which would have been a problem if the thermocouples were connected directly through the slip ring. The amplified signal was then read by a data-logging unit.

9.3 Tool Design and Operating Parameters

The tool used for the weld had a scroll shoulder, similar to that developed by Dawes et. al. [83]. It also used a pin based on the Whorl design developed by Thomas and Gittos [81]. The diameter of the shoulder was 50mm and that of the top of the pin was 20mm. Details of the tool design will be provided by Zettler[85].

Finally, in making the weld, the parameters described in Table 9-1 were used:

Table 9-1

Parameter	Value
Rot Speed (rpm)	200
Travel Speed (mm/min)	50
Plunge (mm/min)	5
Dwell (sec)	10

9.4 Results

Unfortunately a satisfactory weld was not obtained for the initial weld run, with a running void being produced just below the top surface. However, the tool did weld perhaps 80-90% of the plate thickness, so it is believed that a slight adjustment of either the operating parameters or tool design will produce an acceptable weld. Despite this some very interesting temperature data was obtained. Figure 9-1 shows the temperature at the centreline for various distances from the top surface, and Figure 9-2 shows similar data except for 20 and 35mm from the weld centreline. The thermocouple which was located 19mm from the top surface and 20mm from the centreline failed, and did not give any useful results.

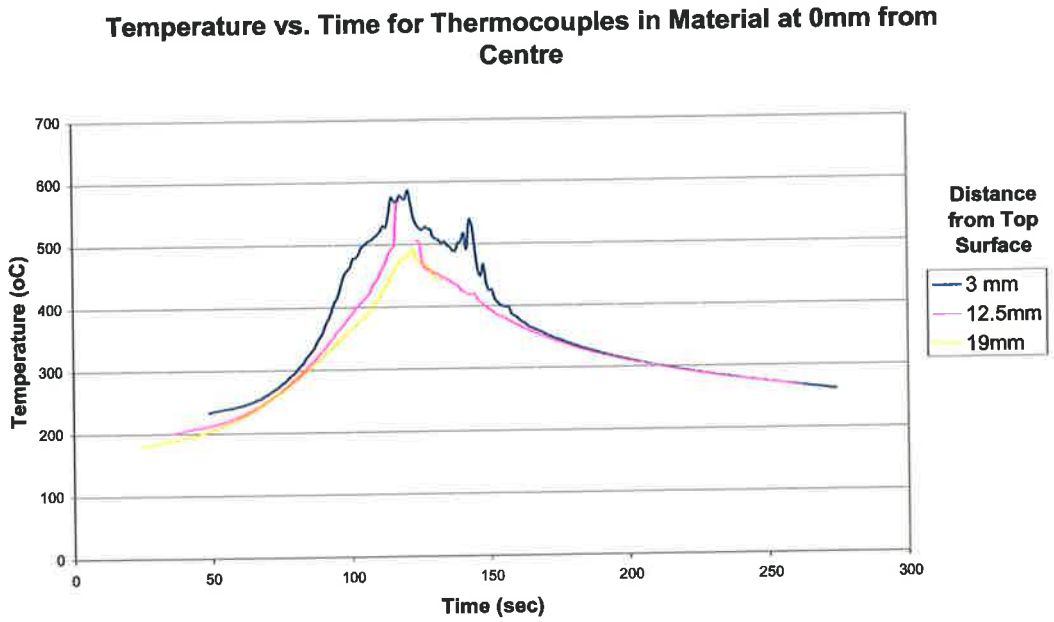

Figure 9-1 Temperature Data at Weld Centreline

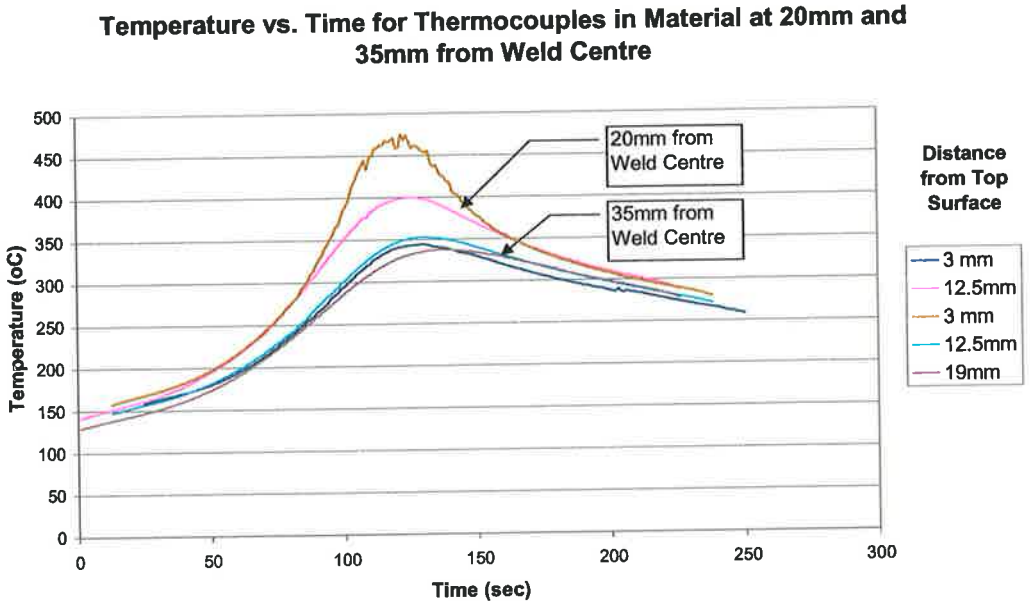

Figure 9-2 Temperature Data 20 and 35mm from Weld Centreline

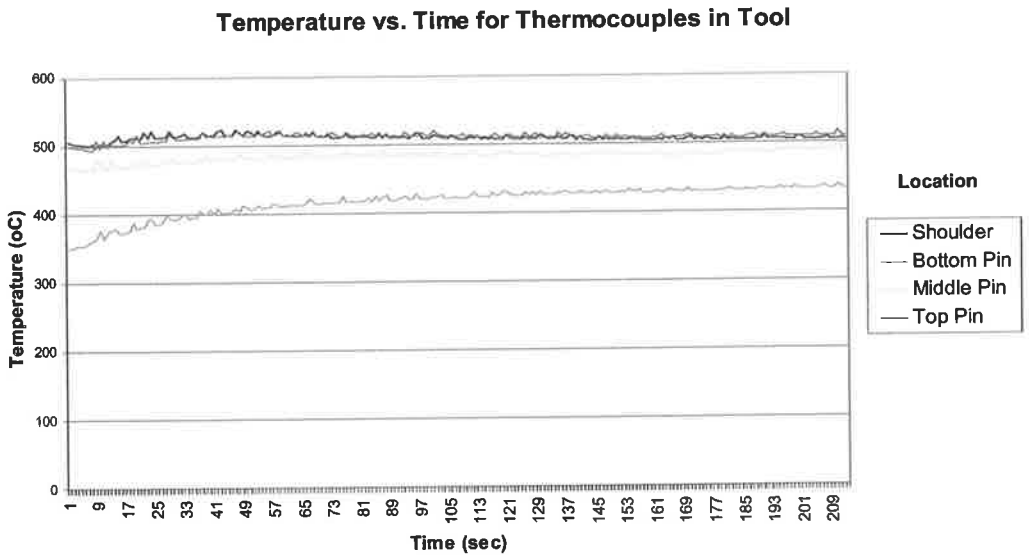

Figure 9-3 Temperature Data for Thermocouples Located in Spindle

Finally, the results for the thermocouples in the FSW tool are shown in Figure 9-3

9.5 Discussion

The temperature data on the weld centreline (Figure 9-1) showed some large fluctuations when the tool past near the thermocouple. The maximum temperature registered was around 574°C. There are two possible reasons why this high reading occurred:

- Surface melting occurs in the workpiece material in an extremely thin layer adjacent to the tool. This view is supported by the fact that the measured peak temperature is remarkably close to the solidus for 5083 aluminium. However if this occurs it is unclear why the temperature measured in the tool should be so much lower. There may have been a problem with the accuracy of the readings which was not verified prior to welding.

- Deformation of material around the thermocouple caused an incorrectly high temperature measurement. The maximum temperature in the material during welding is 510-530°C. If so this would imply that the results obtained for the thermocouples located within the deformation zone in section 4.2 are also incorrect.

It is unclear which of the above two scenarios is correct.

Another interesting feature of the data presented in Figure 9-19-1 is that both the thermocouples at 12mm and 19mm from the top surface show a sharp temperature rise as the tool approached, while the top thermocouple showed a sharp rise and then a flattening out as the pin got nearer. It is believed that this flattening out was caused by the close proximity of the shoulder during this period. The shoulder diameter of 50mm corresponds to a time interval of 60 seconds at a speed of 50mm/min. This length of time corresponds to the width of this region. Further to this observation the large spikes that are observed on the reverse side of the curve seem to correspond to the point where the periphery of the shoulder past the thermocouple. This would seem reasonable given the large deformation occurring in this region.

Next, the results from the thermocouples 20 and 35mm shown in Figure 9-29-2 will be discussed. Obviously the maximum temperature measured by the thermocouples gets progressively lower as the position moves away from the tool centreline. While the thermocouples 20mm from the centre showed quite a large temperature reduction through the thickness due to the proximity of the shoulder, the thermocouples 35mm from the tool showed very little variation through the thickness.

Another interesting comparison can be made between the general shape of the curves and those observed for the 12mm weld shown in section 4.2. Apart from the obvious spikes in the top thermocouple's results, the base level temperature of the plate is much higher. Even before the tool starts to traverse (the beginning of the temperature measurements) the temperature of the plate has risen to around 150°C during the dwell compared to 50-80°C for the 12mm thick weld. Secondly, the temperature flattens out to around 250°C after welding for the 25mm plate, compared to 200°C for the 12mm thick weld. This observation in part confirms the predictions of the modelling section 8 which stated that the transient characteristics of the weld varied greatly from the steady state result due to the initial preheating of the plate.

Finally, the results of the spindle mounted thermocouples will be discussed. The temperature at all points in the tool seemed to remain fairly constant for the duration of the weld, except for the thermocouple which was located at the base of the pin. This progressively increased over the duration of the weld. Therefore this part of the tool does not attain a steady state welding temperature. Table 9-2 compares the temperature measurements from the tool against the peak temperatures measured in the material.

Table 9-2

Location	**Tool (°C)**	**Material (°C)**
Bottom of Pin	400-430	490
Middle of Pin	480-490	500 Before Spike 568 After Spike
Top of Pin	510	530 Before Spike 574 Top of Spike

Shoulder	510	Not Available

A discussion of these results is presented below:

- The temperature measured in the material is consistently higher than that measured by the thermocouples in the tool. However the temperatures measured before the temperature spike were only 20°C lower than those measured in the tool for both the locations at the middle and the top of the pin.
- There was a much larger discrepancy between the measurements at the bottom of the pin. It is believed that this may in part have been caused by the different depths of the two thermocouples. The thermocouple in the tool was located right at the base of the pin, while that in the material was located 6mm from the bottom surface. Hence there was probably around a 4-5mm discrepancy between the two locations.
- The peak temperature measured in the material was remarkably close to the solidus temperature of 574°C.

9.6 Conclusions

This work has shown that:

- There is an inconsistency between the results from the thermocouples located in the plate and those located within the spindle. Further investigation will be required to determine the cause of this discrepancy.
- The thermocouples located in the plate reached temperatures near the solidus temperature for 5083, suggesting surface melting, provided these readings are correct.
- There is a significant build up of heat during the dwell, confirming that the transient characteristics of the weld vary significantly from the steady state.

10 Flow Modelling

10.1 Introduction

While the conduction based models can be used to predict the thermal cycles and estimate the microstructure formed during welding [4,10], they cannot yet accurately predict the conditions where a successful weld will be produced. (See section 2.1.8.1.) A more useful model is one that predicts the temperature and flow of material around the tool. This is described in the following section.

The work presented in the following sections presents a preliminary flow model under some simplifying conditions. It is far from complete, and much work needs to be done before a useful numerical model can be developed. Much of the work will involve the determination of physical properties such as flow stress vs. strain rate relationships, and friction and surface behaviour at high strain rate and temperature. Despite this, the following section describes a method, which will enable successful flow models to be produced in the future.

10.2 Modelling Technique

Because of the complexity of the model it is divided into two separate models, the global thermal model and the local thermal/flow model. The regions described by these two models are shown in Figure 10-1.

The global thermal model is the same as the thermal model described in section 7 and is used to predict the temperature on the boundary of the flow model. The temperature at

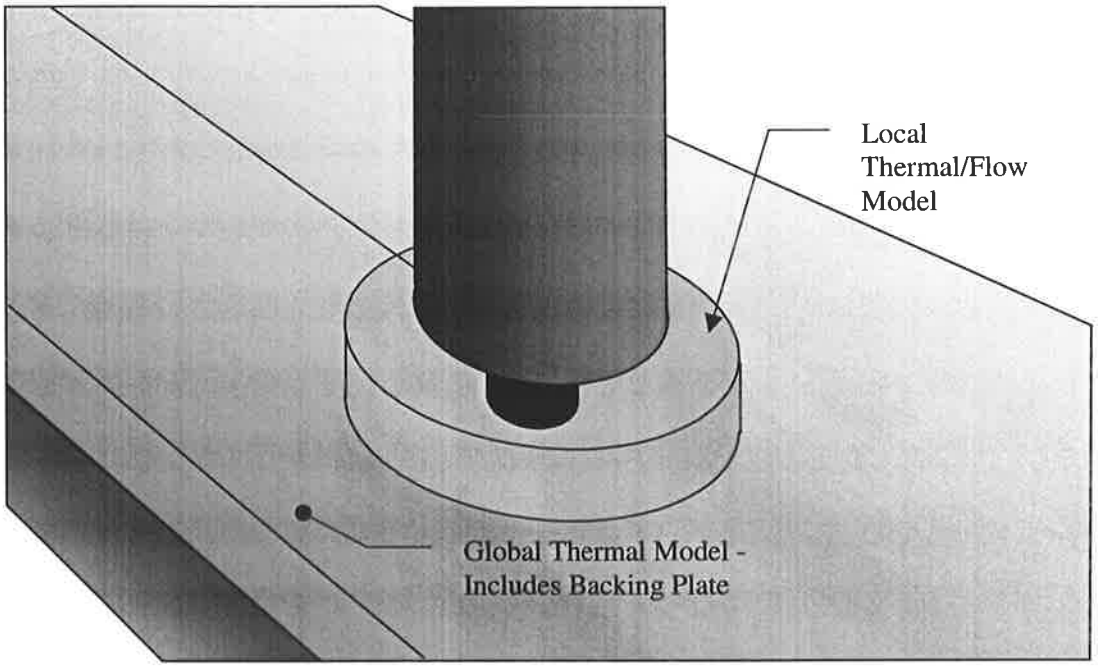

Figure 10-1 Diagram Showing Regions Covered by Local Flow and Global Thermal Models

the boundary of the flow model is influenced by backing plate type, distance from the centre of the weld to the edge of the plate, preheat and the thermal conductivity of the tool. By not including these characteristics in the flow model it is kept as simple and small as possible.

A second benefit of this approach is that it will allow the analysis of different flow directions without the need to recreate the whole mesh. Analysing a new flow direction may be done simply by:

- Changing the direction of the flow on the boundary.
- Changing the position of the front of the model when applying the temperatures at the boundary of the global thermal model.

10.3 Mesh Generation

One of the more difficult aspects of the work has been the generation of the mesh for the local flow model. The mesh generation program primarily uses quadratic, 20-noded hexahedral elements for the mesh. However some quadratic 15-noded wedge elements are used around the top and bottom of the tool thread. Presently, this meshing program models the workpiece material only and does not include the pin or the tool. To maximise the adaptability of this program, it has been made flexible so that mesh can be produced for various tool geometries. eg. thread pressure angle, pitch, overall rake angle of the pin, and thread thickness. This enables both the plain probe and Whorl™ tools from Thomas and Gittos [81] to be effectively modelled. An example of the mesh that can be produced by this program is shown in Figure 10-2 and Figure 10-3. Note the different mesh densities. Only half of the model has been shown in both cases.

The advantage of the existing meshing program is that changes to the mesh geometry can be made quickly allowing various tool profiles to be analysed in a short space of time. Another advantage is that the mesh is reasonably efficient. The disadvantage of this approach is that the automatic meshing program cannot (at this stage) model recently developed tools by Thomas and Gittos [81] which vary quite considerably from the standard threaded pin. It is however believed that:

- With some modification the mesh generation program could model standard Triflute™ tool relatively easily.
- Modelling the MX Triflute™ tool design would be a significantly more difficult although not impossible.

Finally, it should be noted that the meshing program does not include the tilt angle of the tool. (See section 1)

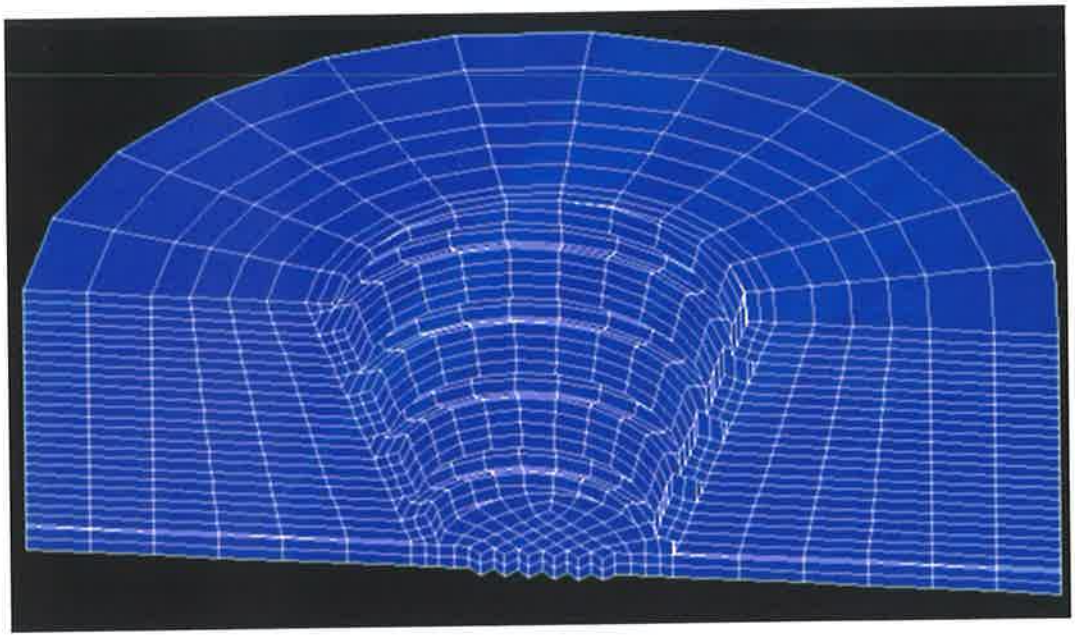

Figure 10-2 Example of a Fine Thread Mesh

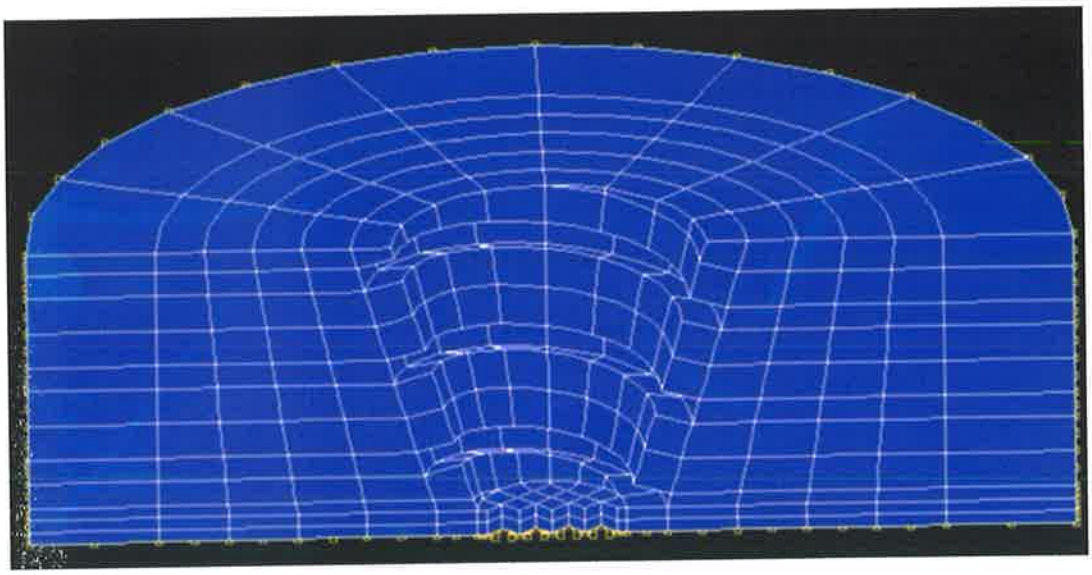

Figure 10-3 Example of a Coarse Thread Mesh

A description of some of the basic theory behind this mesh generation program is described in Appendix D.

10.4 Fastflo Modelling

Two different software packages have been used to model the process. Fastflo [21] was initially selected because of its flexibility. This software enables the user to apply their own differential equations and boundary conditions to the problem. Therefore, it is possible to apply slip boundary conditions, which are not available in many standard finite element solvers.

However for reasons which will become apparent later in this section this solver was not entirely successful. Therefore to obtain better results, a second package NISA[67] was used. This is described in section 10.5.

10.4.1 Theory

Normally the derivation of differential equations governing the flow is not required provided a standard solver is used. However, section 10.4.2 describes how the finite element package Fastflo [21] has been used which requires the input of the equations which govern the flow.

10.4.1.1 Momentum Equations

To derive the equations governing the material flow, the Cauchy equations that apply to fluid flow will be used and are found in Gerhart et. al. [73] p 347:

$$\rho\left(\frac{\partial u}{\partial t}+u\frac{\partial u}{\partial x}+v\frac{\partial u}{\partial y}\right)=-\frac{\partial p}{\partial x}+\frac{\partial \sigma_x}{\partial x}+\frac{\partial \tau_{xy}}{\partial y}$$
$$\rho\left(\frac{\partial v}{\partial t}+u\frac{\partial v}{\partial x}+v\frac{\partial v}{\partial y}\right)=-\frac{\partial p}{\partial y}+\frac{\partial \sigma_y}{\partial y}+\frac{\partial \tau_{xy}}{\partial x} \qquad \textbf{Eq. 10-1}$$

Note that the above equation may be rewritten in vector notation for 3 dimensions as:

$$\rho\left(\frac{\partial \boldsymbol{v}}{\partial t}+\boldsymbol{v}.\nabla\boldsymbol{v}\right)=-\nabla p+\nabla\cdot\boldsymbol{S} \qquad \textbf{Eq. 10-2}$$

where:

v = Velocity vector

p = Pressure at a point (Note Compressive pressure is positive.)

$$\boldsymbol{S} = \begin{bmatrix} \sigma_x & \tau_{yx} & \tau_{zx} \\ \tau_{xy} & \sigma_y & \tau_{zy} \\ \tau_{xz} & \tau_{yz} & \sigma_z \end{bmatrix} = \text{Deviatoric Stress} \qquad \textbf{Eq. 10-3}$$

The deviatoric stress tensor is defined as the amount by which the stress in the material varies from the zero stress value. It is different to the total stress tensor which is defined as:

$$\boldsymbol{\sigma} = \boldsymbol{S} - p\boldsymbol{I} \qquad \textbf{Eq. 10-4}$$

or if we define the mean stress as:

$$\sigma_m = \tfrac{1}{3}\sigma_{ii} = -p \qquad \textbf{Eq. 10-5}$$

ie. the mean stress has the opposite sign of p, then σ may be written as:

$$\boldsymbol{\sigma} = \boldsymbol{S} + \sigma_m \boldsymbol{I} \qquad \textbf{Eq. 10-6}$$

and the Cauchy equations rewritten as:

$$\rho\left(\frac{\partial \boldsymbol{v}}{\partial t} + \boldsymbol{v}.\nabla\boldsymbol{v}\right) = \nabla \cdot \boldsymbol{\sigma} \qquad \textbf{Eq. 10-7}$$

One interesting consideration with this equation is the value of the Reynolds number, which determines the ratio of the momentum to shear forces in the solution. If the Reynolds number is sufficiently low, then the non-linear term may be neglected from the calculation so the Cauchy equations which are then simplified to:

$$0 = \nabla\boldsymbol{\sigma} \qquad \textbf{Eq. 10-8}$$

A similar procedure was used by Bendzsak and North [29,32] for modelling friction welding. The Reynolds number is given by:

$$\mathrm{Re} = \frac{\rho V l}{\mu} \qquad \textbf{Eq. 10-9}$$

Typical values of the parameters are:

$\rho = 2700$ kg/m^3 for aluminium.

V = Velocity of Material passed the pin:

= 0.002m/s

l = Characteristic length = diameter of tool = 0.006m

μ = Viscosity. A low-end estimate will be obtained from the values of stress vs. strain rate using equation 5.61 in Gerhart et. al. [73]:

$$\mu = \frac{\sigma}{2\dot{\varepsilon}}$$
$$= \frac{20\times10^6}{2\times1}$$
$$= 10\times10^6\ Pa.s$$

Hence the Reynolds number will have an approximate value of:

Re = 3.24x10^{-9}

so the effect of momentum will be negligible. Another consequence of this result is that when using commercial finite element solvers, only the steady state solution is required because the effect of momentum forces from the previous time step are negligible. It should be noted that this assumption is no way invalidated by the stick slip flow of material that is believed to occur around the tool. (See section 3.2.3.) It is believed that this transient effect is a result of the transient nature of the temperature adjacent to the tool. This change in temperature affects the material properties and therefore the flow. Therefore such effects must be included in the heat flow analysis which is discussed in section 10.4.1.4.

10.4.1.2 Solution Algorithm in Fastflo

In addition to the momentum equation in section 10.4.1.1 the problem will require the definition of:

1. Material constitutive equation. The simplest form of the equation will be used, which from section 2.2.2.1 may be given as:

$$\bar{\sigma} = C\dot{\bar{\varepsilon}}^{m} \qquad \textbf{Eq. 10-10}$$

2. If the density of the material is assumed constant throughout, then the continuity equation will be:

$$\nabla \cdot \boldsymbol{v} = 0 \qquad \textbf{Eq. 10-11}$$

3. The strain rate tensor:

$$\dot{\boldsymbol{\varepsilon}} = \tfrac{1}{2}\left(\nabla \boldsymbol{v} + (\nabla \boldsymbol{v})^{\mathrm{T}}\right) \qquad \textbf{Eq. 10-12}$$

4. The effective strain rate in the material: (Equation 6.227, Bathe [66])

$$\dot{\bar{\varepsilon}} = \sqrt{\tfrac{2}{3}\dot{\boldsymbol{\varepsilon}} \cdot \dot{\boldsymbol{\varepsilon}}} \qquad \textbf{Eq. 10-13}$$

5. The deviatoric stress tensor, $\boldsymbol{S}$ in the material from the following relationship:

$$\boldsymbol{S} = \lambda \dot{\boldsymbol{\varepsilon}} \qquad \textbf{Eq. 10-14}$$

where λ is a scaler constant and has units of MPa.s. (Compare equation 6.225 Bathe [66]). Taking the dot product of both sides and substituting for the equivalent stress and strain from equations 6.227 Bathe gives:

$$\begin{aligned} &\sqrt{\tfrac{2}{3}}\sqrt{\tfrac{3}{2}\boldsymbol{S} \cdot \boldsymbol{S}} = \lambda\sqrt{\tfrac{3}{2}}\sqrt{\tfrac{2}{3}\dot{\boldsymbol{\varepsilon}} \cdot \dot{\boldsymbol{\varepsilon}}} \\ &\sqrt{\tfrac{2}{3}}\bar{\sigma} = \lambda\sqrt{\tfrac{3}{2}}\dot{\bar{\varepsilon}} \\ &\Rightarrow \lambda = \tfrac{2}{3}\frac{\bar{\sigma}}{\dot{\bar{\varepsilon}}} \end{aligned} \qquad \textbf{Eq. 10-15}$$

Therefore the deviatoric stress tensor is found by substituting this back into Eq. 10-10. Note that if we substitute the material constitutive equation we get:

$$\lambda = \tfrac{2}{3}C\dot{\bar{\varepsilon}}^{m-1} \qquad \textbf{Eq. 10-16}$$

Substituting for the equivalent strain rate gives the following relationship for λ:

$$\lambda = \tfrac{2}{3} C \left(\frac{1}{3} \left(\nabla \boldsymbol{v} \cdot \nabla \boldsymbol{v} + \nabla \boldsymbol{v} \cdot (\nabla \boldsymbol{v})^T \right) \right)^{\frac{m-1}{2}} \qquad \textbf{Eq. 10-17}$$

Note that commercial finite element packages [67] use a slightly different procedure which is based on a power law relationship for the viscosity.

6. Substituting the above relationship for the deviatoric stress, into the momentum equation:

$$\nabla \cdot \boldsymbol{\sigma} = 0$$

$$\nabla \cdot \boldsymbol{S} + \nabla p = 0$$

$$\nabla \cdot \left(\lambda \frac{1}{2} \left(\nabla \boldsymbol{v} + (\nabla \boldsymbol{v})^T \right) \right) + \nabla p = 0 \qquad \textbf{Eq. 10-18}$$

Note that p is positive in tension, which is opposite to the conventional direction.

To solve the above equations, the augmented Lagrangian solution procedure is used from the Fastflo user manual [21]. Briefly:

Make the following substitution for the pressure:

$$p_n = p_{n-1} - \mathrm{Pen} \nabla \cdot \boldsymbol{v}_n \qquad \textbf{Eq. 10-19}$$

and using the previous value of λ, ie λ_{n-1} the following equations may be obtained:

$$0 = \nabla \cdot \left(\lambda_{n-1} \frac{1}{2} \left(\nabla \boldsymbol{v}_n + (\nabla \boldsymbol{v}_n)^T \right) \right) + \nabla p_{n-1} - \mathrm{Pen} \nabla (\nabla \cdot \boldsymbol{v}_n)$$

$$p_n = p_{n-1} - \mathrm{Pen} \nabla \cdot \boldsymbol{v}_n \qquad \textbf{Eq. 10-20}$$

$$\lambda_n = \tfrac{2}{3} C \left(\frac{1}{3} \left(\nabla \boldsymbol{v}_n \cdot \nabla \boldsymbol{v}_n + \nabla \boldsymbol{v}_n \cdot (\nabla \boldsymbol{v}_n)^T \right) \right)^{\frac{m-1}{2}}$$

These equations are then solved iteratively with the solver until the solution converges.

10.4.1.3 Boundary Conditions for the Momentum Equation

The two possible boundary conditions are:

- No-Slip.

  This is obviously the simplest case. For the boundary where the tool meets the workpiece material: (Note material moves around stationary tool.)

  $$\boldsymbol{v} = \{u,v,w\} = \{0,0,0\} \qquad \textbf{Eq. 10-21}$$

  Secondly, for the nodes which are on the boundary of the local/flow models the velocity will be will have the following value:

  $$\begin{aligned} u &= \pm r\omega \sin\theta - V_{weld}\cos(\theta_{weld}) \\ v &= \pm r\omega \cos\theta - V_{weld}\sin(\theta_{weld}) \\ z &= 0 \end{aligned} \qquad \textbf{Eq. 10-22}$$

  Note that the sign depends on the particular quadrant being investigated.

- Slip.

  The following boundary condition is used for the interface between the shoulder and the workpiece material:

  $$\boldsymbol{v}\cdot\boldsymbol{n} = 0$$

  $$\boldsymbol{\sigma}\cdot\boldsymbol{n}\cdot\frac{\boldsymbol{v}}{|\boldsymbol{v}|} = f(p,\Delta v_s.T) \qquad \textbf{Eq. 10-23}$$

  $$\boldsymbol{\sigma}\cdot\boldsymbol{n}\cdot(\boldsymbol{v}\times\boldsymbol{n}) = 0$$

  The slip condition for the interface between the thread and the workpiece material is a slightly modified version of the above:

  $$\boldsymbol{v}\cdot\boldsymbol{n} = 0$$

  $$\boldsymbol{\sigma}\cdot\boldsymbol{n}\cdot\frac{\boldsymbol{v}}{|\boldsymbol{v}|} = f(\boldsymbol{\sigma}\cdot\boldsymbol{n}\cdot\boldsymbol{n},\Delta v_s.T) \qquad \textbf{Eq. 10-24}$$

  $$\boldsymbol{\sigma}\cdot\boldsymbol{n}\cdot(\boldsymbol{v}\times\boldsymbol{n}) = 0$$

Note that at the interface between the material and the shoulder a uniform pressure is artificially set. This is because the pressure at this point is due to the elastic properties of the material. ie. The material constitive equation in Eq. 10-10 considers the stress caused by plastic deformation only and not elastic. Because the deformation on the top surface is largely elastic in the vertical direction, the stress in the material and therefore the pressure at the interface will tend to zero. In any case the shear stress applied to the material is not highly dependent on the surface pressure. See section 3.4.6.

One further point should be noted about the slip boundary condition. When using the finite element method it is usual to define either the actual value at the boundary (essential boundary condition) or the flux or stress that occurs at the boundary. (natural boundary condition) Therefore, the slip boundary condition is really a combination of the two. From discussions with Nick Stokes [84], implementing both may cause problems in the way that the software solves the problem. Therefore, to avoid this problem the boundary condition can be specified entirely as a natural one by implementing the following equation:

$$\boldsymbol{\sigma} \cdot \boldsymbol{n} = f(p, \Delta \boldsymbol{v}_s, T) \cdot \frac{\boldsymbol{v}}{|\boldsymbol{v}|} + \sigma_n \cdot \boldsymbol{n} \qquad \textbf{Eq. 10-25}$$

where:

$\boldsymbol{\sigma} \cdot \boldsymbol{n}$ is the stress vector defined at the boundary.

$f(p, \Delta \boldsymbol{v}_s, T) \cdot \frac{\boldsymbol{v}}{|\boldsymbol{v}|}$ is the function for the shear stress, which of course opposes the direction of the material flow.

$\sigma_n \cdot \boldsymbol{n}$ is the value of the stress normal to the boundary which forces the velocity to equal 0 normal to the surface. It is proposed that one way of determining σ_n would be from the following relationship:

$$\sigma_n = C_1\left(C_2(\boldsymbol{v}\cdot\boldsymbol{n}) - \sigma_{np}\right) + \sigma_{np} \qquad \textbf{Eq. 10-26}$$

where:

σ_{np} is the normal stress from the previous iteration.

C_2 is a very large constant which, when multiplied by the velocity normal to the boundary produces a normal stress in the opposite direction to force it to equal zero.

C_1 is a very small constant which avoids an instable solution which would occur if the solution just depended on $C_2(\boldsymbol{v}\cdot\boldsymbol{n})$.

10.4.1.4 Defining the Differential Equations for Heat Flows During FSW

The differential equation defining the heat transfer due to conduction and convection which is not steady state is given by: (See equations 4-1 and 5-22 Holman [40])

$$\rho c_p \frac{\partial T}{\partial t} + \rho c_p \boldsymbol{v}\cdot\nabla T = k\nabla^2 T + \dot{Q} \qquad \textbf{Eq. 10-27}$$

where:

$\dot{Q}$ = is the heat generation in the material due to shearing.

$= V 2\mu\dot{\boldsymbol{\varepsilon}}\cdot\dot{\boldsymbol{\varepsilon}}$ (W/m^3) (From FIDAP theory manual p2-6 [74])

$= VC\left[\tfrac{2}{3}\dot{\boldsymbol{\varepsilon}}\cdot\dot{\boldsymbol{\varepsilon}}\right]^{(1+m)/2}$ See Appendix E.

Note that this ignores the heat generation at the surface which will be considered later in the definition of the boundary condition.

There are two possible approaches to solving the above equation:

- Method 1.

  If we assume that the temperature field around the tool is independent of time, then we can assume that either:

  (a) $\frac{\partial T}{\partial t} = 0$ if the frame of reference is the stationary workpiece material in the far field.

  (b) $\frac{\partial T}{\partial t} = \omega r\left(-\sin\theta\frac{\partial T}{\partial x} + \cos\theta\frac{\partial T}{\partial y}\right)$ if the frame of reference is the rotating tool. See Appendix F.

  While this solution method is considerably simpler than the second method shown below, it will not allow any stick/slip behaviour of the material flow around the tool to be analysed.

- Method 2.

  The temperature field at a particular point will vary and will therefore require the term $\frac{\partial T}{\partial t}$ to be included in the heat equation.

Note that a consequence of the first approach when using standard finite element solvers is that only the steady state solution is required.

Finally, the momentum and heat equations are very much interlinked. ie. The temperature field will determine the properties of the material, which in turn will effect the velocity profile, which in turn determines the heat generation which affects the temperature field.

10.4.1.5 Boundary Conditions for the Heat Equation

The analysis will require the following boundary conditions:

a) At the interface between the local and global models the temperature of the Local Flow Model will be:

$$T_{lm} = T_{gm} \qquad \textbf{Eq. 10-28}$$

where:

T_{lm} = Temperature of local model node.

T_{gm} = Temperature of global model node.

b) At the interface between the tool and the workpiece material the heat generation will be:

$$\dot{Q} = \sigma \cdot n \cdot v \qquad \textbf{Eq. 10-29}$$

Note that this only applies to the model where slip occurs between the workpiece material and the tool.

10.4.2 Tool Design

The mesh was designed to simulate the tool that was used for weld run 000313B. See section 4. This tool had the characteristics described by Table 10-1. Note for a definition of the parameters used in Table 10-1 see Figure D-1 in Appendix D.

Table 10-1

Characteristic	Value
p (mm)	4
s(mm)	1
d (mm)	1.5
$\phi_n(^o)$	0
R_a (mm)	2.85
R_b (mm)	6

Characteristic	Value
t_{min} (mm)	1
t_{max} (mm)	12
R (mm) (Shoulder Radius)	15
R_m (mm) (Model Radius)	20

10.4.3 Results

Preliminary results for the flow around the pin under the following conditions have been obtained:

- Rotational Speed = 350 rpm
- Temperature = 400°C.
- Translational Speed = 0mm/s
- Boundary Conditions = No-Slip

Even for this very simple case the results obtained are very interesting and are shown in Figure 10-4 to Figure 10-6. Figure 10-4 shows the absolute velocity profile of the material flowing around the tool. Obviously the velocity of the material is highest around the periphery of the tool for the no-slip case. Figure 10-5 shows the velocity in the vertical direction. The blue areas demonstrate the material moving toward the backing bar, while the yellow areas show the material moving back toward the shoulder. Figure 10-6 shows the pressure of the material around the pin.

Note:

- The pressure is significantly higher around the bottom where the material is being 'screwed' toward the backing bar.
- There are regions of high pressure around the bottom of the tool threads and regions of low pressure on the topside.

- To show greater detail, the pressure range has been artificially restricted. The black regions are the areas where the pressure is out of range.

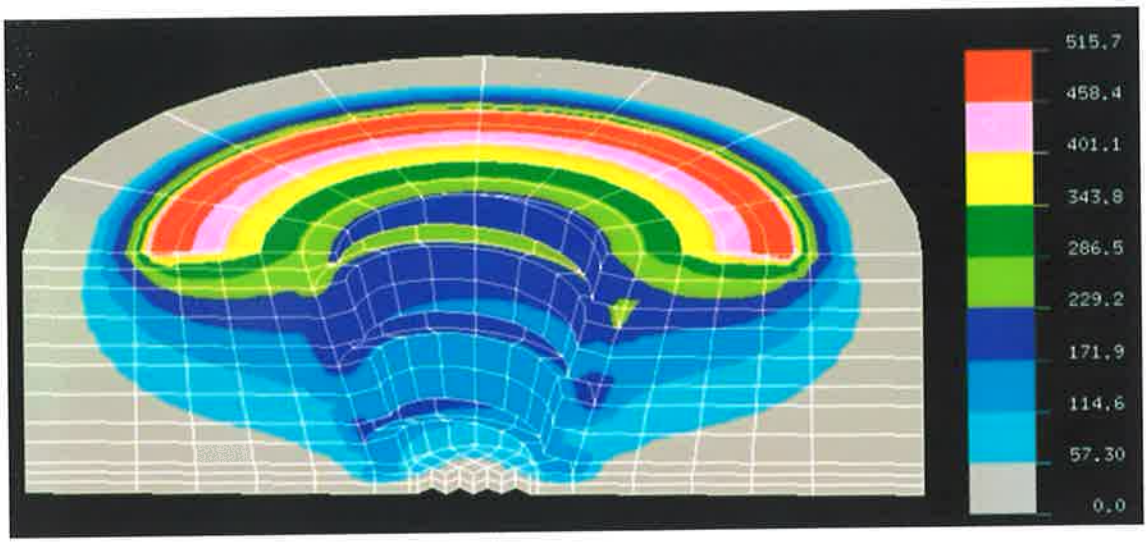

Figure 10-4 Absolute Velocity of the Material Flowing Around the Tool (mm/s)

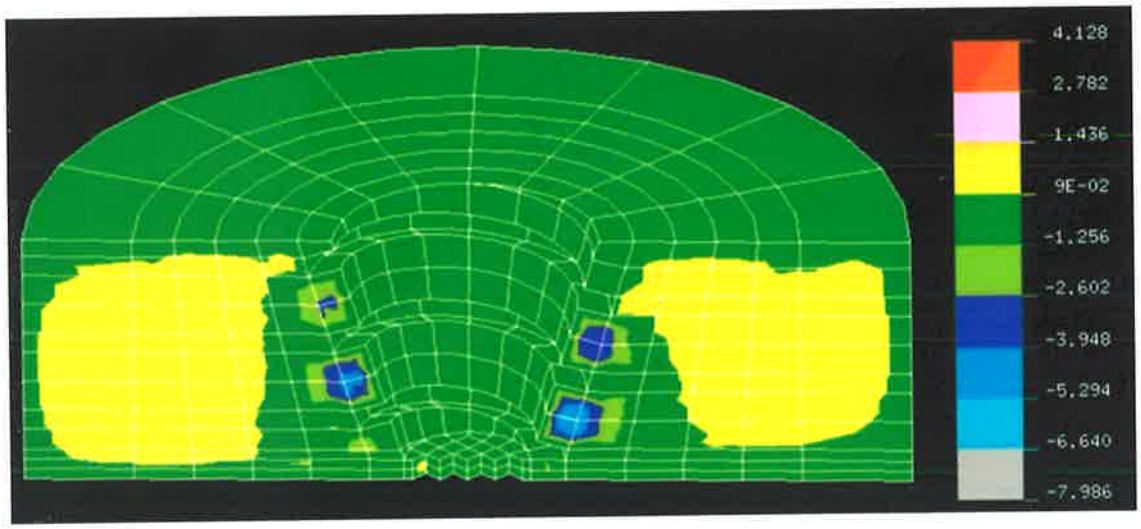

Figure 10-5 Velocity in the Vertical Direction (mm/s)

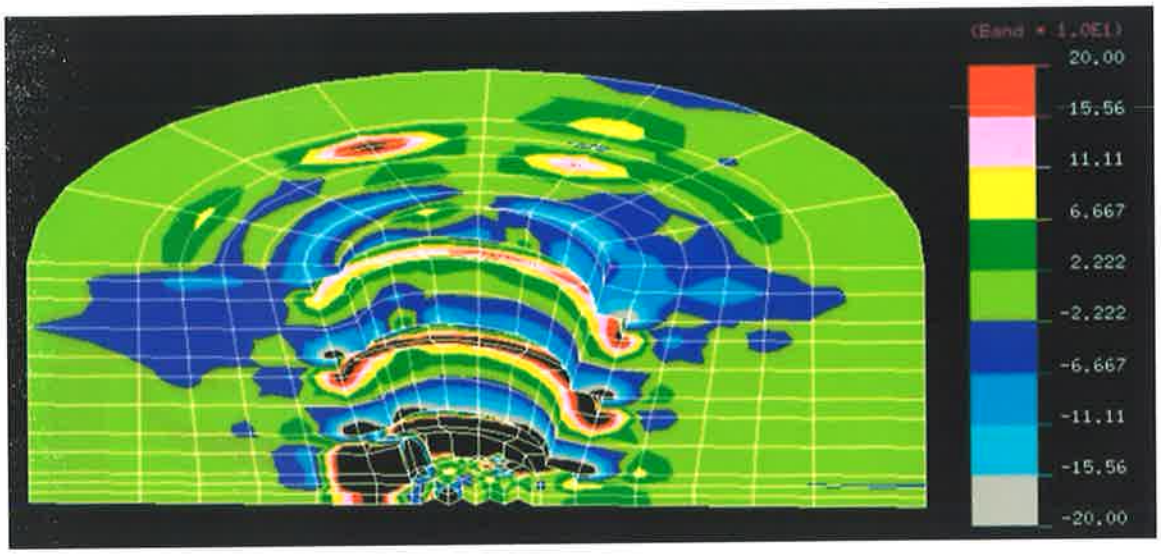

Figure 10-6 Pressure Distribution (MPa)

When a 1.72 mm/s translational velocity is included in the model, all the results look fairly similar to the non-translatory model because the translational speed is small relative to the peripheral velocity of the shoulder. (515 mm/s). The most interesting difference is in the pressure distribution around the tool, which shows a significant reduction in the pressure on the trailing side. See Figure 10-7. An analysis of the low pressure region in conjunction with the temperature field may be one way of quantifying whether or not an acceptable weld will be produced.

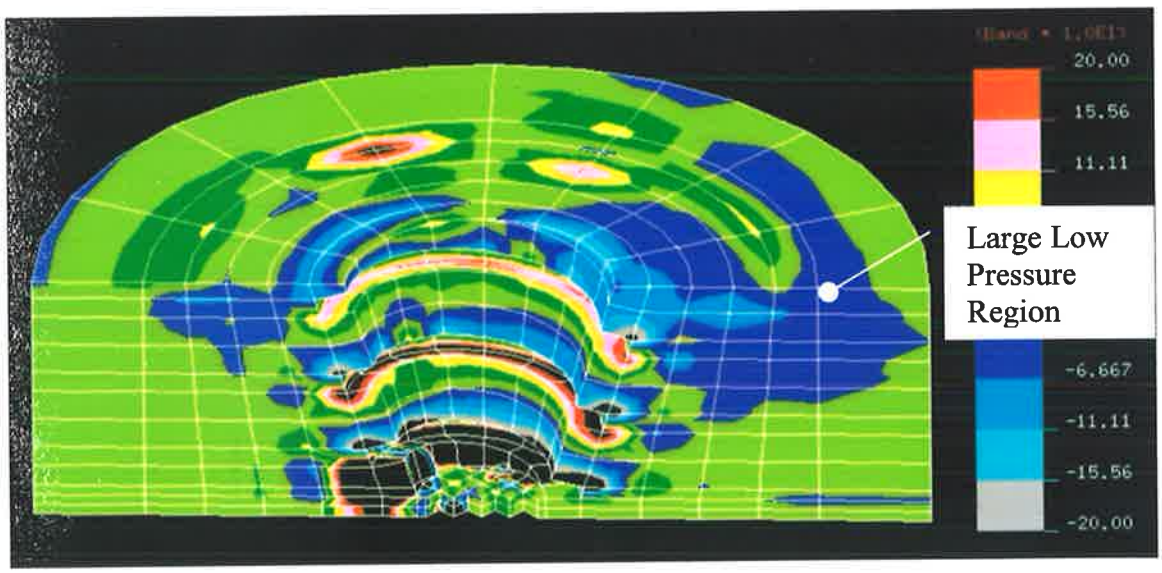

Figure 10-7 Pressure distribution on with 1.72mm/s translation

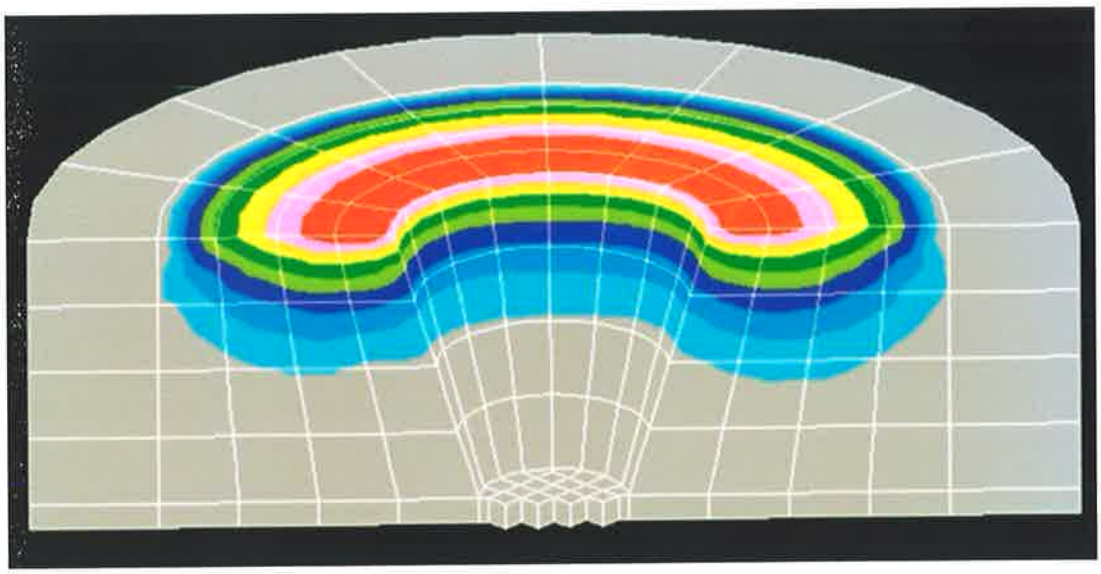

Figure 10-8 Constant Shear Stress Model

Finally, a very simple model was attempted which applied a constant rotational shear stress to the top surface of an unthreaded mesh. This result is shown in Figure 10-8 for a model with no translational flow. Interestingly the position of maximum flow velocity has now moved from the shoulder edge toward the pin. It is believed that this more accurately represents the flow situation around the shoulder in a typical FSW.

10.4.4 Problems in Using the Fastflo Finite Element Solver

The problems experienced in using this package were:

- Calculated pressures showed erratic behaviour.

  Spikes in the pressure distribution are clearly apparent from Figure 10-6 and Figure 10-7. In an effort to solve this problem, the penalty parameter in the formulation was adjusted. (See section 10.4.1.2) This was however not successful. Another possible cause of this error could be the large mesh size. This was not changed because of the already large solution times.

- Lack of an effective pre or post-processing program to complement the finite element solver.

While Fastflo is provided with a 2 dimensional graphical display program, displaying the results for 3 dimensional problems required the use of a 3rd party post-processor. Therefore the NISA modelling package was used for post-processing which required the writing of a conversion program.

- Difficulty in debugging code.

  It was found that the Fastflo code often gave a different answer to the intended result, with the problem being difficult to detect because there was no debugging facility provided. This problem resulted in an incorrect result for the material constant λ. The calculated value remained relatively constant over the mesh. Therefore, the solution represented one at constant viscosity rather than the power law viscosity that was required. Correcting this error meant that the solution no longer converged because of the high velocity gradients near the pin. (See NISA solution in section 10.5)

While most of the above problems could no doubt be solved with sufficient time, it was found that the effort required to obtain the results was extremely high. Therefore, it was felt that time could be more profitably spent using a standard solver, which had been thoroughly tested. This is described in the following section.

10.5 NISA Modelling Results

Modelling with the NISA finite element package proved far more successful and much easier to implement than the Fastflo solution because a standard finite element solver was used. Please note that the operating parameters for weld run 000313B (see section 4) were used for the modelling work in this section.

10.5.1 Solution Method

Referring to sections 10.4.1.1 and 10.4.1.4, a consequence of the material having a large viscosity is that only the steady state solution needs to be analysed for both the momentum and heat equations, provided the transient aspects at the surface are not considered. Therefore, the NISA steady state incompressible fluid solver [67] was used for the analysis.

10.5.2 Boundary Conditions

10.5.2.1 Velocity Boundary Conditions

The boundary conditions for this model are similar to those used for the Fastflo solution described in section 10.4.1.3 except that the frame of reference was changed to the stationary plate. The boundary conditions for the model will be:

- Tool.

  The set velocities for each of the nodes in this area are: **Eq. 10-30**

  $$v = \{u,v,w\} = (\pm r\omega \sin\theta, \pm r\omega \cos\theta, 0)$$

  Note that the ± sign depends on the quadrant being used.

- Outer Boundary.

  The velocities set in this region are:

  $$\begin{aligned} u &= V_{weld} \cos(\theta_{weld}) \\ v &= V_{weld} \sin(\theta_{weld}) \\ z &= 0 \end{aligned}$$ **Eq. 10-31**

10.5.2.2 Temperature Boundary Conditions

Because the model is being used to simulate the results of the experiment 000313B, the temperature results from steady state Model 3 in section 7.3.3.4 were applied on the outer boundary.

10.5.3 Mesh Generation

A similar mesh to that used in section 10.4 was used with the same tool design as described in section 10.4.2. There were additional improvements made to the mesh which are summarised below:

- Mesh Density.

  The mesh density used in section 10.4 was extremely coarse to enable a solution to be obtained in a realistic time. Because the NISA solver is far more efficient and the processor being used much faster, the mesh density was increased significantly.

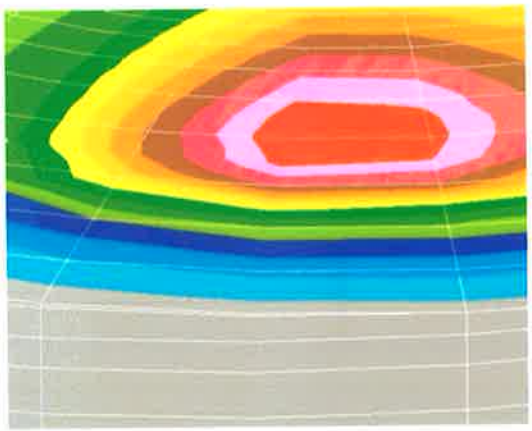

Figure 10-10 Temperature Instability

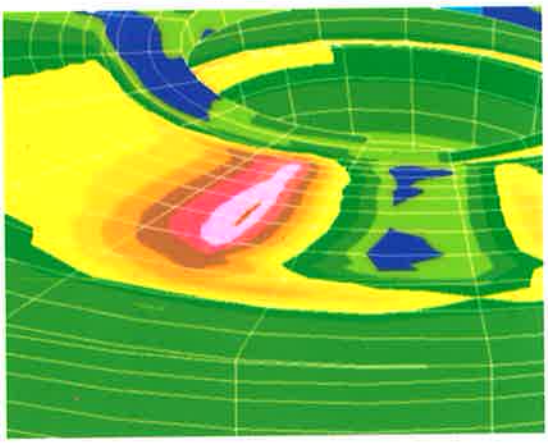

Figure 10-9 Pressure Instability

- Square Elements around Top Layer.

  It was found that extremely large velocity gradients occurred near to the tool surface. This resulted in instabilities in the pressure and temperature solution which are shown dramatically in Figure 10-10 and Figure 10-9. To solve this problem a layer of square elements was generated around the top surface. Secondly, the degree to which the wedge elements were distorted was minimised.

These two changes resulted in the mesh shown in Figure 10-11 being used.

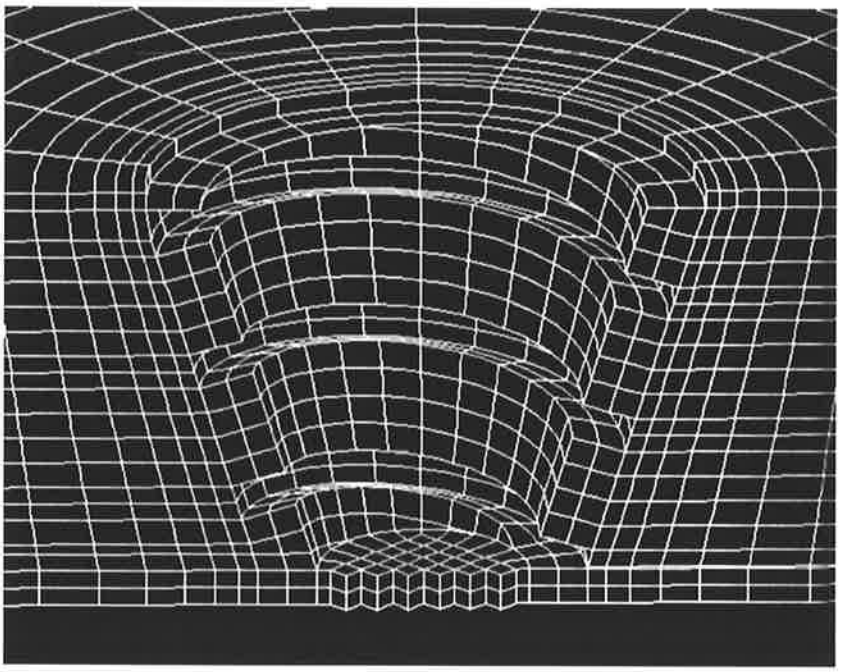

Figure 10-11 Improved Mesh for NISA Solution

Note that distorted elements around the base of the model still occur, however, since the deformation is fairly small in this region, they do not appear to cause any significant error in the solution.

10.5.4 Material Properties

The initial work considered only one set of material properties which were based on those provided by the Forge 2 Database[18] described in section 2.2.2.1. This data enabled an approximate value for the material constant C to be obtained. Eq. 2-19 was used, however it was divided by 10 to give reasonable values. The reasons for this are explained in section 2.2.2.1. ie.

$$\sigma = 200\exp(-0.00429T)\dot{\varepsilon}^{0.089} \qquad \textbf{Eq. 10-32}$$

To enable a faster solution time the material constant, C was assumed to be independent of temperature, so the above equation was simplified to:

$$\sigma = 20\dot{\varepsilon}^{0.089}$$

$$\sigma = 20\dot{\varepsilon}^{0.089}$$

for a temperature of 550°C. (approximately) From this equation, the effective viscosity can be calculated from Eq. 2-18. For a strain rate exponent, m equal to 0.089 the effective viscosity is 16.5 MPa.s.

10.5.5 Results

The results for a single time step (one position of the tool) are presented below:

10.5.5.1 Velocity Contours

The effective velocity around the tool is shown in Figure 10-12. This clearly shows how the low strain rate exponent causes an extremely steep velocity gradient at the tool surface. To enable the velocity contours beyond this thin boundary layer to be viewed, the maximum velocity for plotting was set to 10mm/s. The resulting contours for this case are shown in Figure 10-13. Interestingly the location of maximum velocity beyond this thin boundary layer has now shifted toward the top part of the pin.

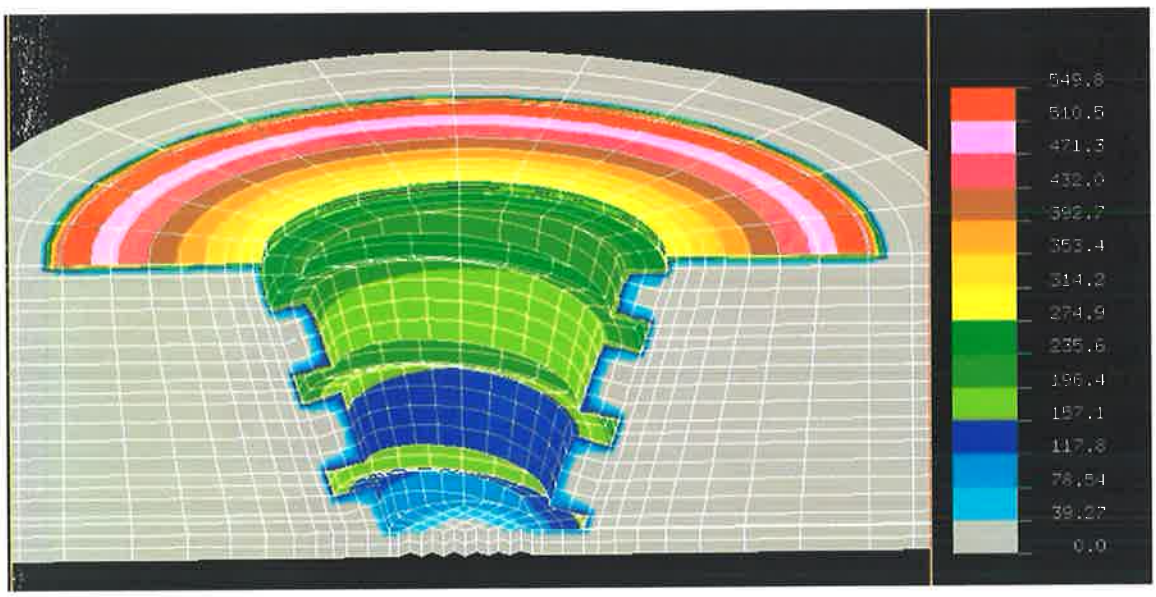

Figure 10-12 Effective Velocity Around the Tool (mm/s)

This figure also enables the deformation zone to be viewed, which corresponds reasonably well to the edge of the TMAZ in a typical FSW. Finally, contours of the velocity in the vertical (z) direction were plotted and are shown in Figure 10-14. The blue regions show movement of material downwards toward the backing plate.

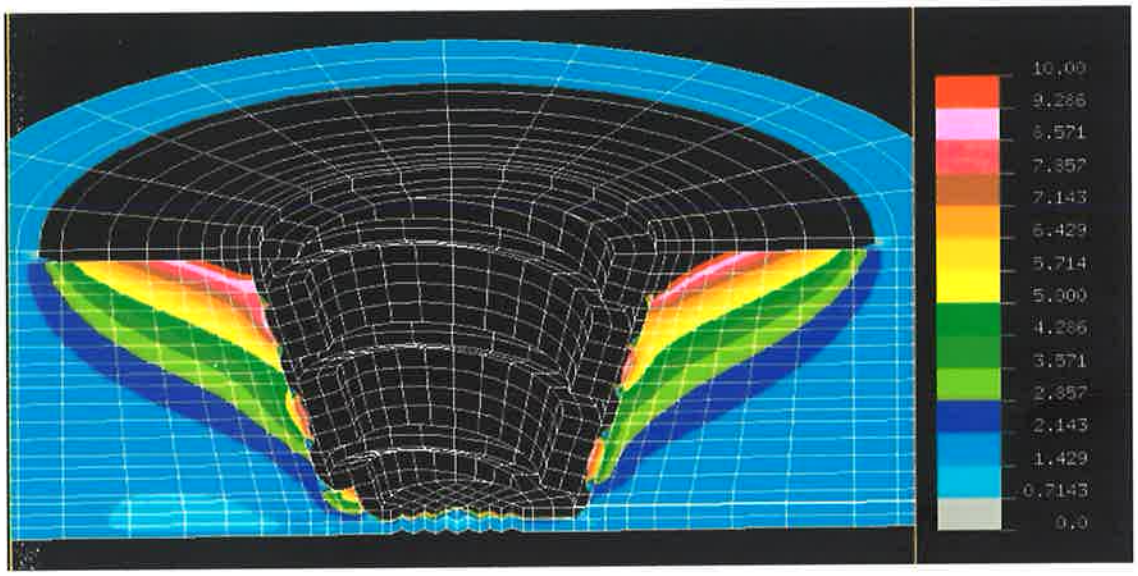

Figure 10-13 Effective Velocity with Maximum Velocity of Contours Set to 10mm/s

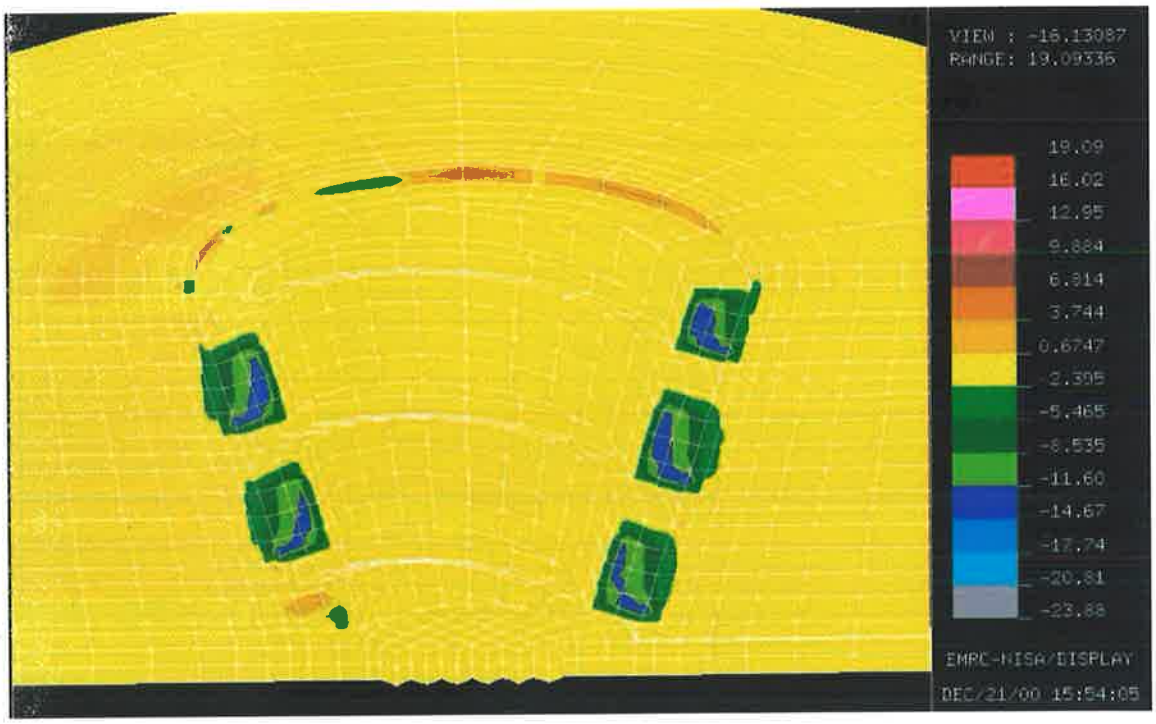

Figure 10-14 Velocity of Material in the Vertical (z) Direction (mm/s)

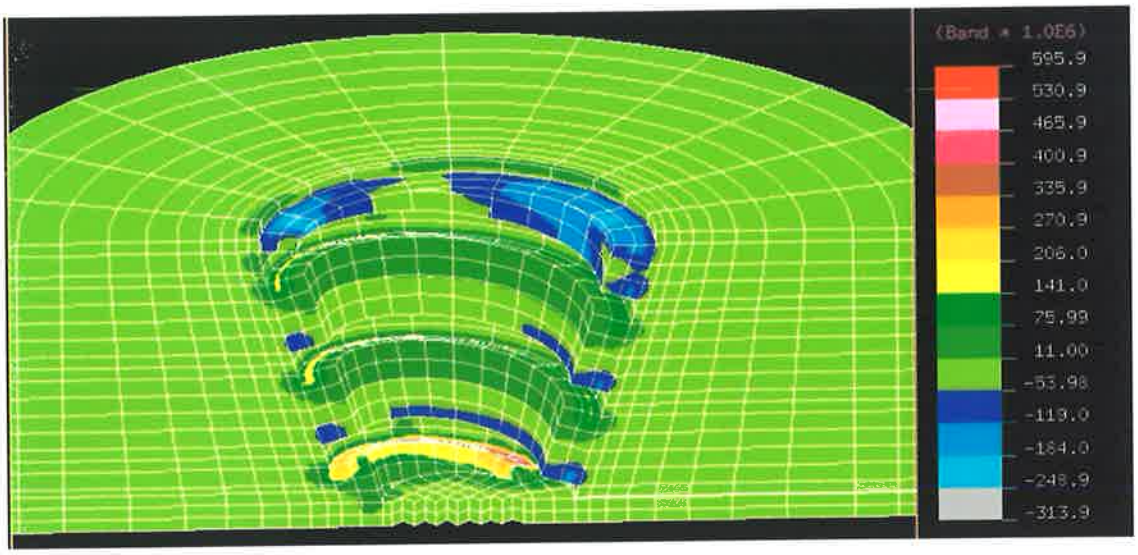

Figure 10-15 Pressure Contour Plot Around Tool (Pa)

10.5.5.2 Pressure Distribution

The pressure results from the NISA package show a significant improvement over those obtained using Fastflo. Figure 10-15 shows the contours without any limit to the contour plotting, and Figure 10-16 shows the same results with a ±100 MPa limit. The

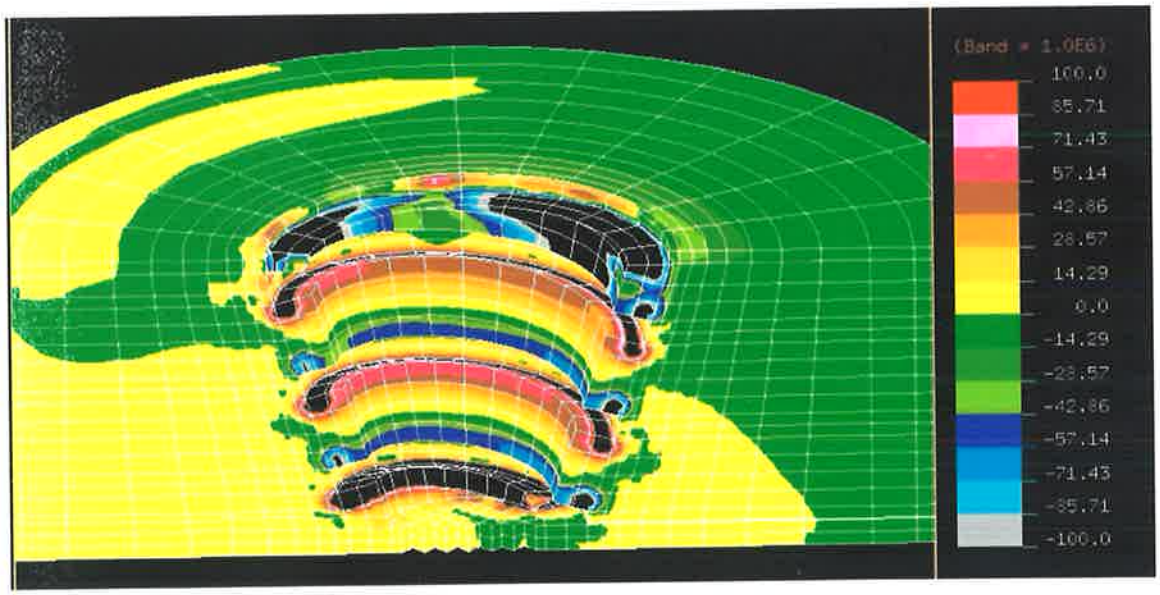

Figure 10-16 Pressure Distribution with Restricted Pressure Range (Pa)

high pressure regions can be clearly seen on the bottom of the threads and the low pressure regions on the top. The region where the pressure was lowest was around the top of the tool thread. Unlike the Fastflo model there was no large low pressure region extending behind the tool. Finally the material underneath and in front of the tool had a slightly larger pressure.

10.5.5.3 Temperature Distribution

Although the material properties were not temperature dependent, the thermal profile obtained from the material deformation could be calculated. This is shown for the half model in Figure 10-17, and for the full model in Figure 10-18. Note that the temperature at the boundary was set from the results of the steady state thermal model.

The maximum temperature in the weld calculated from the material deformation was 1080°K, or 807°C. The result is obviously too high, but is a reasonable first estimate. This will obviously be improved if surface slip or better material properties can be obtained. Another interesting result from the full model shown in Figure 10-18 is that

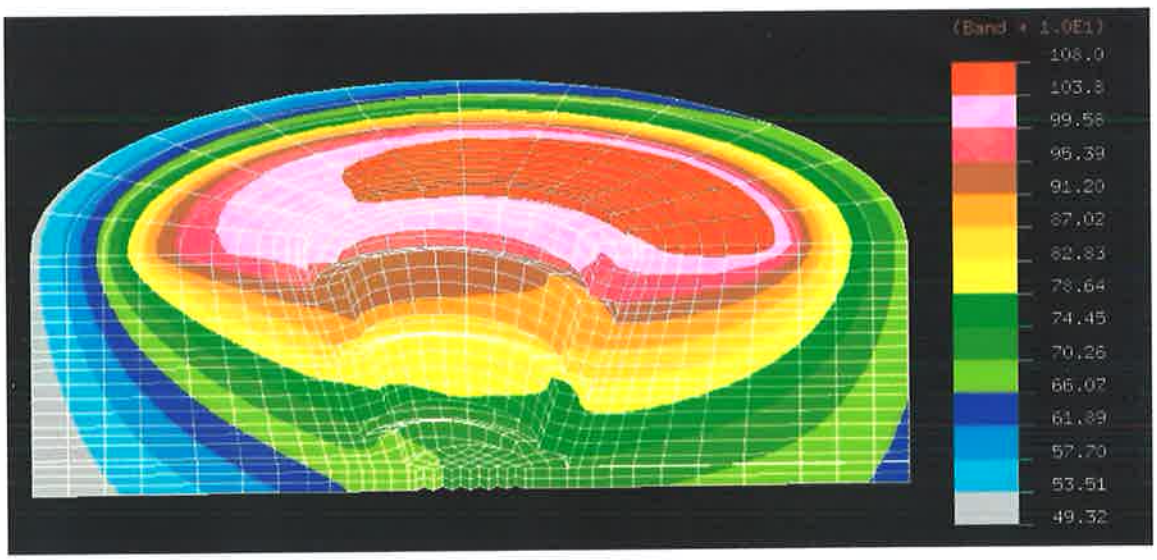

Figure 10-17 Temperature Contours Around Weld (°K)

the temperature profile around the tool isn't actually symmetric about the x-axis. The rotation of the tool seemed to transfer the hottest region toward the advancing side of the tool.

10.5.5.4 Flow Visualisation

Unfortunately the velocity contours in section 10.5.5.1 did not allow the flow around the tool to be visualised. Therefore, an arrow plot of the flow was done. When performing this arrow plot the size of the arrows were proportional to the magnitude of the velocity. Therefore, the high velocity gradient made it difficult to observe the flow of material in the far field. This problem was solved by modifying the data so that all points had a velocity magnitude of 1.

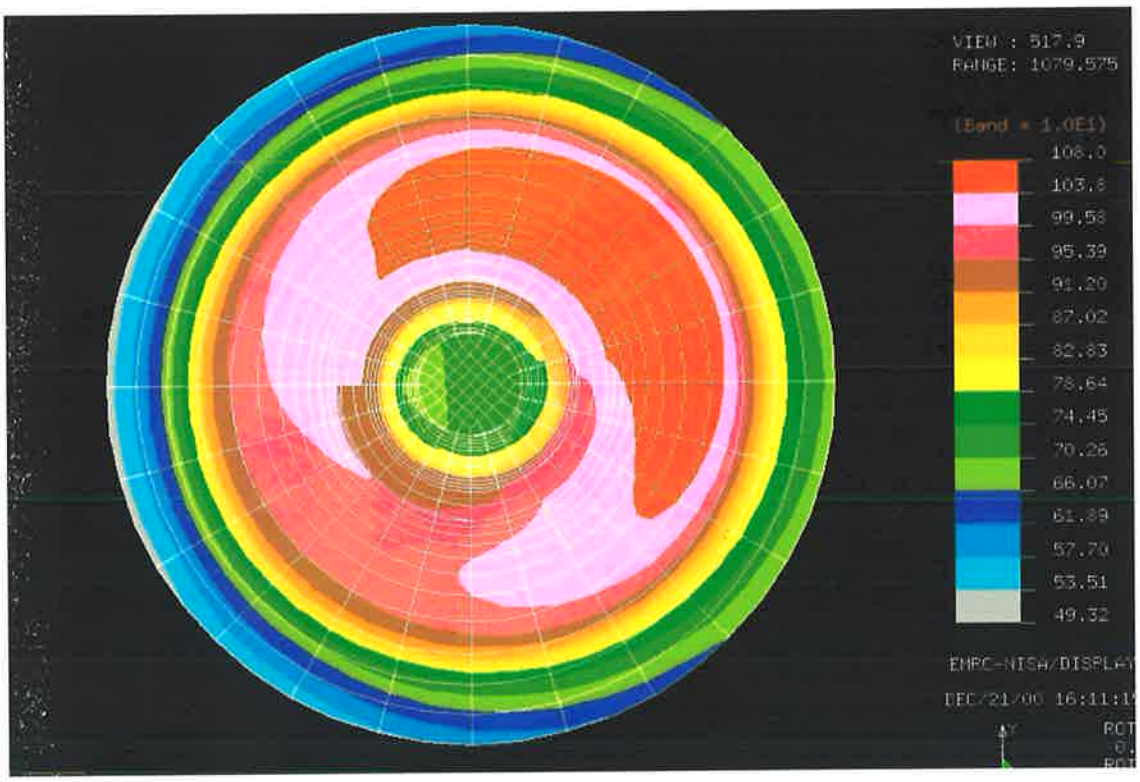

Figure 10-18 Plan View of Temperature Contours for the Full Model (°K)

Figure 10-19 shows the results for the material on the *x-y* plane around the bottom of the tool, and Figure 10-20 shows the same result for material mid-section. Both show how extrusion of material around the tool is affected by the tool rotation. Secondly, a stagnation point on the advancing side, which is further away from the tool for the section taken through the middle. Obviously the material movement is influenced by the shoulder to a much greater extent at this location. The region of material deformation extends much further into the material than would be expected in a real FSW. It is believed that temperature dependent material properties will produce a better result.

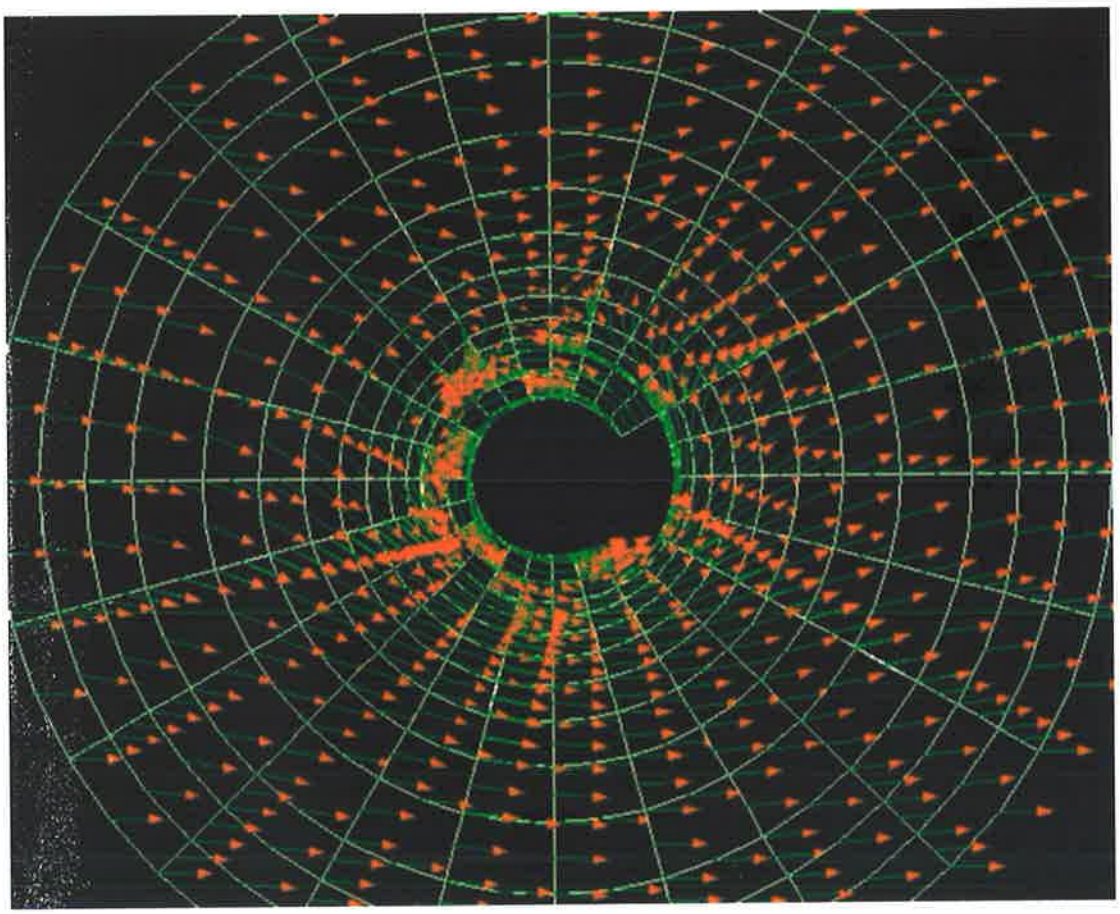

Figure 10-19 Arrow Plot of Material Around the Bottom of the Tool

Figure 10-21 shows the flow of material in the x-z plane in front of the tool, and Figure 10-22 shows a similar plot behind the tool. These two figures clearly show the downward movement of material caused by the tool threads. The flow around the base seems to be a little confused. This could be improved by a higher mesh density in this region.

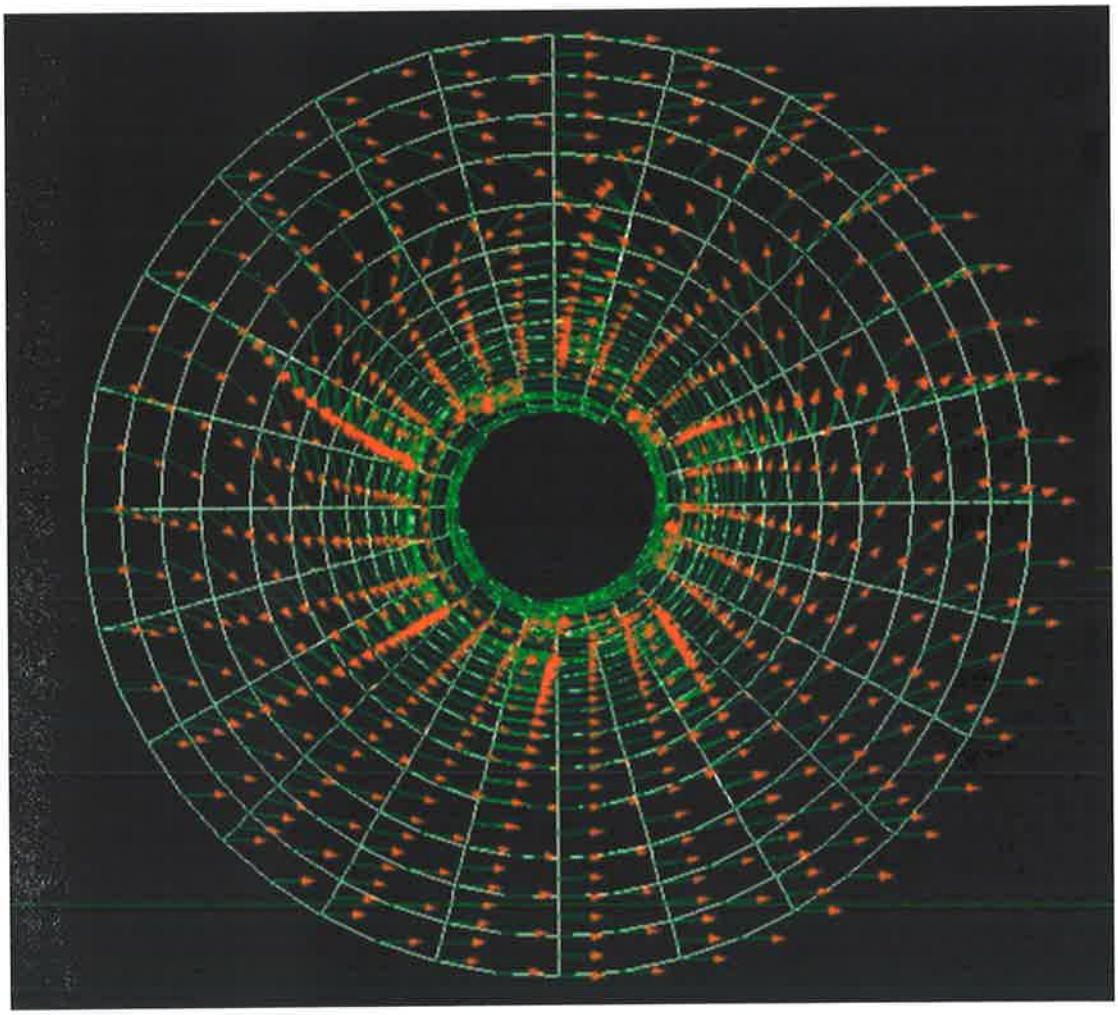

Figure 10-20 Arrow Plot of Material Around the Middle of the Tool

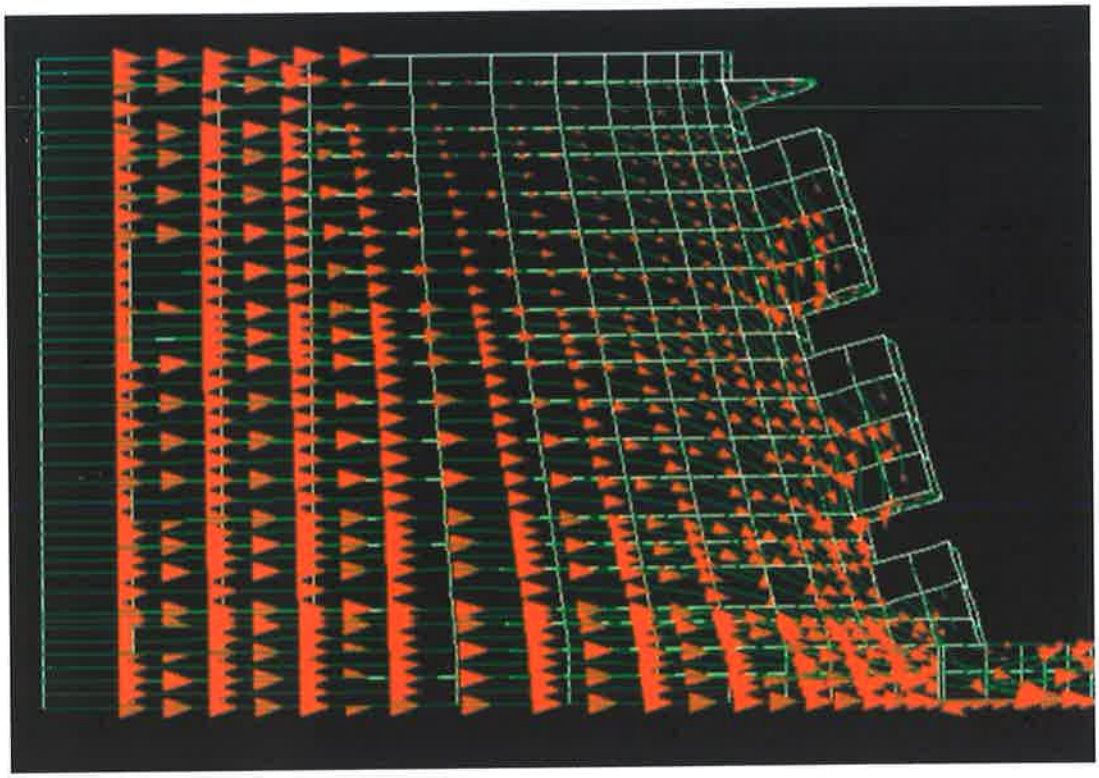

Figure 10-21 Flow of Material in Front of the Tool

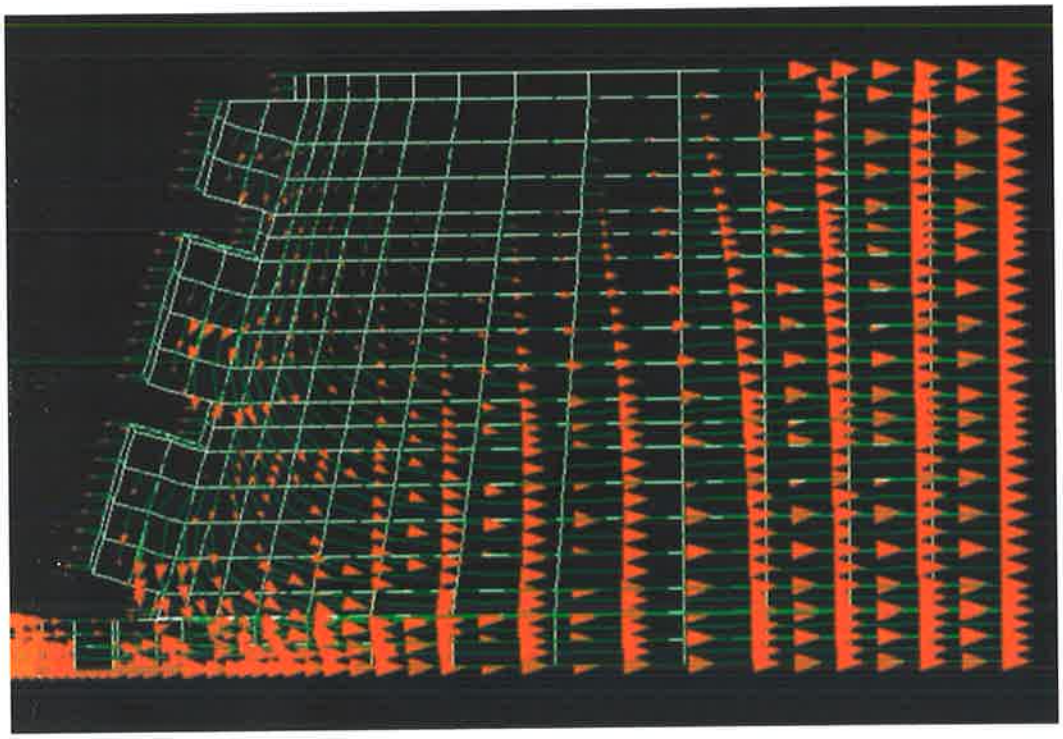

Figure 10-22 Flow of Material Behind the Tool

Finally, a similar section through the thickness was taken along the *y-z* plane and is shown in Figure 10-23. This diagram demonstrates how the flow in the *z*-direction is much greater on the advancing than the retreating side of the tool. This at least partially supports the theory for the formation of the 'onion ring' described in section 3.4.1. At the stagnation point there is some movement of the material up and to the left. This region seems to correspond to the 'dog-leg' which is observed in a typical friction stir weld. See section 3.4.1. Note however the location of the actual 'dog-leg' is much closer to the pin in the FSW microstructure. A model with temperature dependent properties would improve this result.

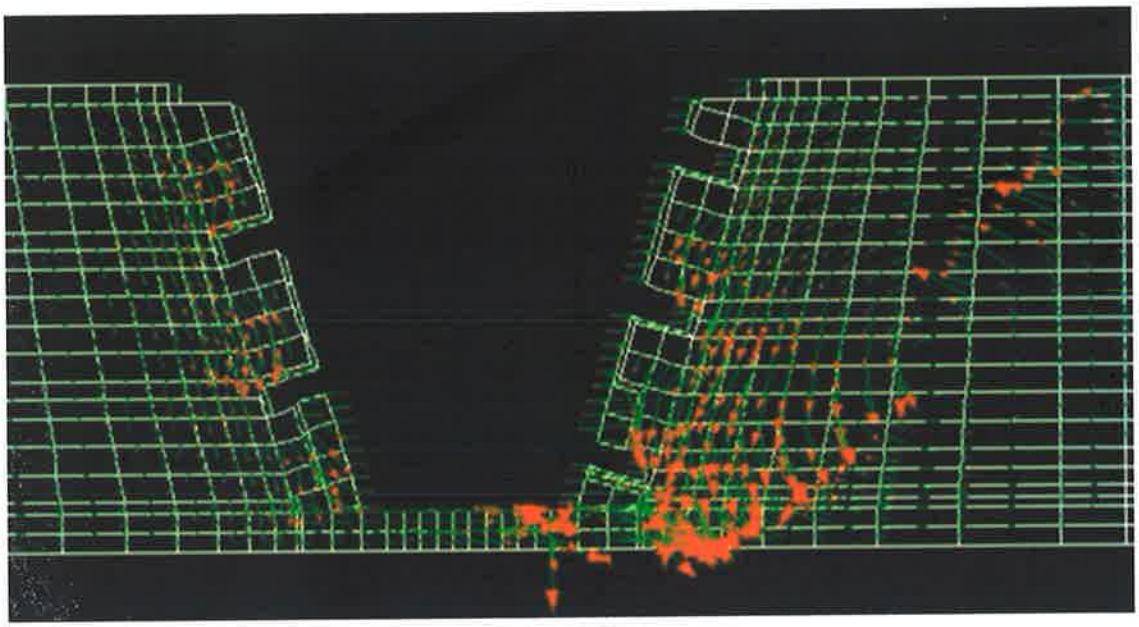

Figure 10-23 Flow of Material on the Side of the Tool (*y-z* Plane)

11 Conclusions and Future Direction

11.1 Conclusions

Friction Stir Welding is process that is gaining increased acceptance as a viable industrial process. Modelling of the process, while perhaps not being particularly useful at this stage will in the very least assist our understanding of how the process works. Fully developed, modelling has the potential to be a tool that will enable rapid improvements to the process to be made assisting the technology's already rapid acceptance as a viable joining technique.

This thesis is very much the first step in the process and has demonstrated:

- A Literature Search and a Theory Describing the Flow Around the Tool.

  The literature search covered areas which were believed relevant to the modelling of FSW. This included previously developed models for both friction welding and FSW, as well as material properties. An expanded theory for how the material flows around the tool was developed which introduced the concept of stick slip flow. This theory was evaluated against flow visualisation and experimental data.

- Steady State Thermal Models.

  A steady state thermal model was developed, which has enabled a greater understanding of the heat flows during the process. This model expanded upon previously developed thermal models and included heat generation at the pin. This heat generation was calculated from a new theory. The model

also included the tool and backing plate. Finally, the model was verified against a set of experimental data.

- Transient Thermal Models.

  A transient thermal model was developed which enabled the variation in weld temperature during the weld to be visualised. This model included the plunge and dwell sequences and was able to demonstrate that, for a short length weld, the temperature varied quite considerably from the steady state model. Finally, a transient model of 12mm 5083 gave extremely good correlation with experimental data.

- Flow Models.

  An automatic meshing program was developed which enabled the modelling of a plain probe, and Whorl™ friction stir welding tools. This mesh was then used to predict the flow of material around a tool using two finite element solvers, Fastflo and NISA. The NISA package gave the better results which enabled the heat generation around the tool as well as the flow to be predicted. Arrow plots were produced of the flow around the tool, which demonstrated extrusion of material around the tool, the downward movement of due to the tool threads, and a stagnation point on the advancing side of the tool.

- Microstructural Investigation of a 5083 Weld.

  This work demonstrated the layered flow of material that occurs around the tool by examining the 'so-called' pin retraction defect. The differences in the microstructure between the dynamically recrystallised zone, thermo-mechanically affected zone and base material were observed. Some SEM work was done which enabled the grains and constituent particles in the weld

to be more easily distinguished. Finally the width of the layers in the dynamically recrystallised zone of the microstructure were determined and compared with the rotation of the tool. It was found that the layering in the microstructure did not coincide with the rotation of the tool.

- Preliminary Temperature Measurements of a 25mm Thick 5083 FSW.

  Some preliminary temperature measurements were presented which compared the temperature obtained in the material against temperature measurements from thermocouples located within the tool. The results showed a discrepancy between two locations with the thermocouples in the material giving a higher reading which was equal to the solidus. Therefore it was unclear whether or not surface melting was occurring during the weld.

11.2 Future Work

To obtain a model that is able to predict whether or not a successful weld can be achieved will require the flow model to be developed to a greater extent. It is clear that the models presented are not yet capable of doing this. Therefore, it is suggested that the following improvements be made:

- Include Heat Loss Through the Tool.

  The present flow model has not included any of the heat loss that occurs through the tool. This could be achieved relatively easily by estimating its value from the steady state model and applying this as a heat loss to the nodes on the top surface.

- Improve the Mesh.

  The current meshing system while being able to model tools which have the standard threaded profile, cannot be easily adapted to the new MX Triflute tools that have been developed by TWI [81]. Secondly, the meshing system

has not included the tilt angle of the tool or a concentric ring or scroll design for the shoulder [83]. One way of implementing complex geometries easily would be the use of a solid modelling package with an automatic meshing tool.

- Incorporate Slip into the Model.

  As discussed in section 3.2.3 it is highly likely that some degree of slip occurs at the material/tool interface, which is very much dependent on the temperature. Therefore, such an effect will need to be incorporated into the model. This may be done by either incorporating a slip boundary condition as discussed in section 10.4.1.3, or by setting the viscosity temperature relationship such that there is a sharp drop in viscosity once the temperature approaches the solidus temperature. Either approach should work. The first approach has the advantage that it will not require such a fine mesh in the vicinity of the tool enabling faster solution times, while the second has a much simpler boundary definition.

- Better Material Data.

  This is one of the main areas that is lacking in the current investigation. It will be necessary to gain information about the stress vs. strain rate characteristics of a particular material, plus how this material interacts with the rotating steel tool. Not only will this information be useful for modelling the process, but it should in the very least suggest what rotational speed should be used for a particular material. ie. It is believed that like friction welding [60], there is a critical rotational speed at which heat liberation is maximised. This could potentially be used to optimise tools where the pin rotates separately to the shoulder.

- Tool Force Analysis.

  In the current work no tool force analysis has been implemented. This could be reasonably easily implemented by analysing the stress data in the material at the surface of the tool.

- Iterative Approach to Solving Flow Model.

  Ultimately it is hoped that one could obtain a model where no initial heat input need be specified. ie. Given the material properties, tool design and process characteristics, what will be the resulting heat input, temperature in the material, tool forces and material pressure. This is the 'Holy Grail' of modelling. To do this with the modelling approach suggested in this document, it will be necessary to use an iterative approach between the global thermal and local flow models. This is described diagrammatically in Figure 11-1.

- Incomplete Tool Contact with Material.

  It has been shown by Colligan [26,27] that there is not necessarily complete contact between the tool and material, especially around the top of the pin. Including this effect in the model would require a deforming mesh in this region. While improving the accuracy of the model it is questionable whether it would give significantly better results.

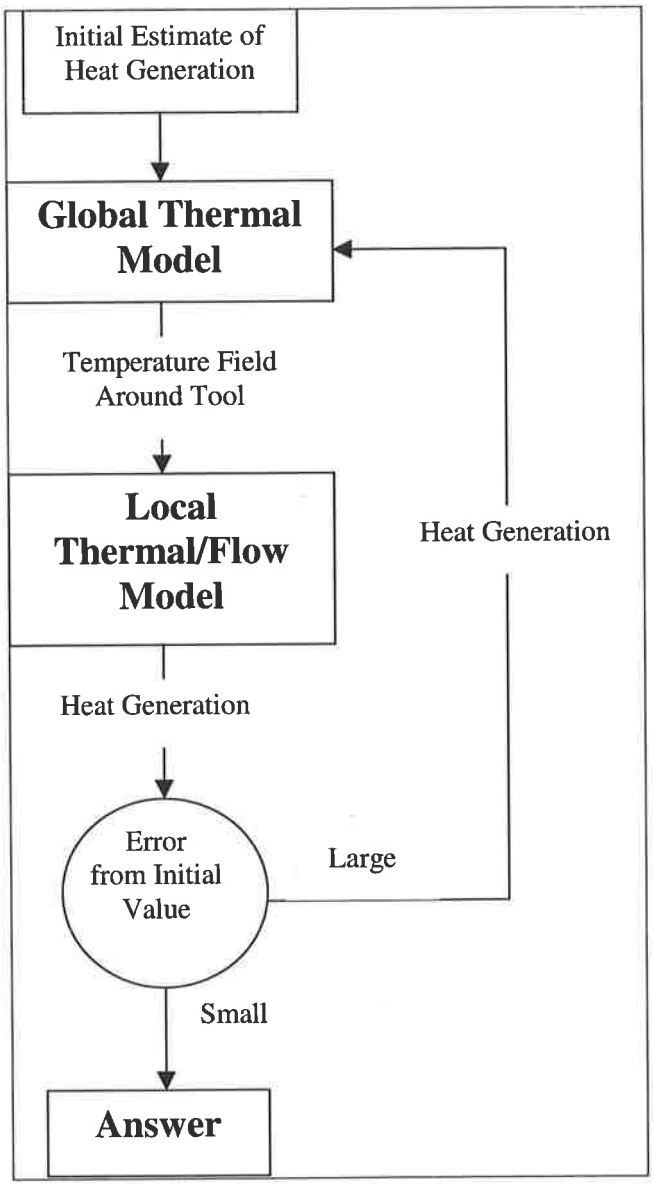

Figure 11-1 Iteration Between Global Thermal

12 References

1. Thomas, WM, et. al. Friction Stir Butt Welding, US Patent No. 5, 460,317.
2. Chao YJ, Xinhai Q, Thermal and Thermo-Mechanical Modelling of Friction Stir Welding of Aluminium Alloy 6061-T6, *Journal of Materials Processing & Manufacturing Science (USA), 7, (2), 163-172, Oct. 1998.*
3. Chao YJ, Xinhai Q, Heat Transfer and Thermal-Mechanical Analysis of Friction Stir Joining of AA6061-T6 Plates, *1st International Symposium on Friction Stir Welding at Thousand Oaks, Cal June 1999.*
4. Russell MJ, Shercliff HR, Analytic Modelling of Microstructure Development in Friction Stir Welding, *1st International Symposium on Friction Stir Welding at Thousand Oaks, Cal June 1999.*
5. Russel MJ, Shercliff HR, Analytic Modelling of Friction Stir Welding, *INALCO '98, TWI, Cambridge, UK, 1998.*
6. Russel MJ, Shercliff HR Development and Modelling of Friction Stir Welding, *Technical Report ISSN 0309-6505, Department of Engineering, University of Cambridge, UK (12), 1997.*
7. Andersson CG, Andrews RE, Dance BGI, Russell MJ, Olden EJ, Sanderson RM, A Comparison of Copper Canister Fabrication by the Electron Beam and Friction Stir Processes, *2nd International Conference on Friction Stir Welding, Gothenburg Sweden 2000.*
8. Frigaard O, Grong O, Midling OT, Modelling of Heat Flow Phenomena in Friction Stir Welding of Aluminium Alloys, *INALCO '98, TWI, Cambridge, UK, 1998.*

9. Frigaard O, Bjorneklett B, Grong O, Midling OT, Process Modelling Applied to Friction Stir Welding of Al-Mg-Si Alloys, *Aluminium Alloys: Their Physical and Mechanical Properties (Japan), 1477-1482, July 1998.*

10. Frigaard O, Grong O, Bjorneklett B, Midling OT, Modelling of the Thermal and Microstructure Fields During Friction Stir Welding of Aluminium Alloys, *1st International Symposium on Friction Stir Welding at Thousand Oaks, Cal June 1999.*

11. McClure JC, Feng Z, Tang T, Gould JE, Murr LE, A Thermal Model of Friction Stir Welding, *5th International Conference on Trends in Welding Research.*

12. McClure JC, Tang W, Guo X, Murr LE, Nunes A, Heat Input and Temperature Distribution in Friction Stir Welding, *Journal of Materials Processing & Manufacturing Science (USA), 7, (2), 163-172, Oct. 1998.*

13. Feng Z, Gould JE, Heat Flow Model for Friction Stir Welding of Aluminium Alloys, *Journal of Materials Processing & Manufacturing Science (USA), 7, (2), 185-194, Oct. 1998.*

14. Gould JE, Feng Z, Ditzel P, Preliminary Modelling of the Friction Stir Welding Process *EWI, Columbus Ohio, US, 1996.*

15. Nunes AC, Stewart MB, Adams GP, Romine P, A Combined Experimental and Analytical Modelling Approach to Understanding Friction Stir Welding, *Developments in Theoretical and Applied Mechanics (USA), 472-484, 1998.*

16. Dong P, Lu F, Hong JK, Cao, Analysis of Weld Formation Process in Friction Stir Welding, *1st International Symposium on Friction Stir Welding at Thousand Oaks, Cal June 1999.*

17. Ulysse P, Three Dimensional Modelling of the Friction Stir Welding Process, *Review Copy.*

18. Forge 2®V2.8 Software, *Trasvalor S.A.*

19. Hosford WF, Caddell RM, Metal Forming, Mechanics and Metallurgy, *Prentice Hall, Inc, Englewood Cliffs, NJ.*

20. NISA, *Engineering Mechanics Research Organisation.*

21. Fastflo, *CSIRO Division of Mathematical and Information Sciences.*

22. Holman JP, Heat Transfer, *McGraw Hill.*

23. Stewart MB, Adams GP, Nunes AC, Romine P, A Combined Experimental and Analytical Modelling Approach to Understanding Friction Stir Welding, *Developments in Theoretical and Applied Mechanics, Volume XIX, 1998.*

24. Reynolds AP, Lockwood WD, Digital Image Correlation for Determination of Weld and Base Metal Constitutive Behaviour, *1st International Symposium on Friction Stir Welding at Thousand Oaks, Cal June 1999.*

25. Reynolds AP, Visualisation of Material Flow in Autogenous Friction Stir Welds, *Science and Technology of Welding and Joining 2000 Vol 5, No. 2, pp. 120-124.*

26. Colligan K, Dynamic Material Deformation During Friction Stir Welding of Aluminium, *1st International Symposium on Friction Stir Welding at Thousand Oaks, Cal June 1999.*

27. Colligan, K, Material Flow Behaviour During Friction Stir Welding of Aluminium, *Welding Journal, July 1999.*

28. North TH, Bendzsak GJ, Smith C. Material Properties Relevant to 3-D FSW Modelling. *2nd International Symposium on FSW, Gothenburg Sweden.*

29. Bendzsak GJ, North TH, Li Z. Numerical Model for Steady-State Flow in Friction Welding, *Acta Metallurgia et Materialia. Vol. 45, No. 4 pp 1735-1745, 1997.*

30. Kong HS, Ashby MF, Friction-Heating Maps and Their Applications, *MRS Bulletin/October 1991.*

31. Moal A, Massoni E, Finite Element Simulation of the Inertia Welding of Two Similar Parts, *Engineering Computations, Vol. 12, 497-512 (1995)*

32. Bendzsak GJ, North TH, Numerical Modelling of Fluid Dynamics and Heat Transfer in Friction Welding, *Mathematical Modelling of Weld Phenomena 4, pp. 429 – 443.*

33. Mahony MW, Rhodes CG, Flintoff JG, Spurling RA, Bingel WH, Properties of Friction-Stir Welded 7075 T 651 Aluminium, *Metallurgical and Materials Transactions Vol 29A, July 1998 pp 1955-1964.*

34. Kinchen DG, Li Z, Adams GP, Mechanical Properties of Friction Stir Welds in Al-Li 2195-T8, *1st International Symposium on Friction Stir Welding at Thousand Oaks, Cal June 1999.*

35. Biallas G, Braun R, Dalle Donne C, Staniek G, Kaysser WA, Mechanical Properties and Corrosion Behaviour of Friction Stir Welded 2024-T3, *1st International Symposium on Friction Stir Welding at Thousand Oaks, Cal June 1999.*

36. Leonard AJ, Microstructure and Ageing Behaviour of FSWs in Aluminium Alloys 2014A – T651 and 7075-T651, *2nd International Symposium on FSW, Gothenburg Sweden*

37. Dalle Donne C, Biallas G, Ghidini T, Raimbeaux G, Effect of Weld Imperfections and Residual Stresses on the Fatigue Crack Propagation in Friction Stir Welded Joints, *2nd International Symposium on FSW, Gothenburg Sweden.*

38. Larsson H, Karlsson L, Stoltz S, Bergqvist Eva-Lena, Joining of Dissimilar Al-alloys by Friction Stir Welding, *2nd International Symposium on FSW, Gothenburg Sweden.*

39. Murr LE, Trillo EA, Li Y, Flores RD, Nowak BM, McClure JC, Solid State Flow Associated with the Friction-Stir Welding of Dissimilar Metals, *Fluid Flow Phenomena in Metals Processing, The Minerals Metals & Materials Society 1999.*

40. Murr LE, Ying Li, Trillo EA, McClure JC, Fundamental Issues and Industrial Applications of Friction-Stir Welding, *Materials Technology (UK) (UK), 15, (1), 37-48, Mar. 2000*

41. Li Y, Murr LE, McClure JC, Solid State Flow Visualisation in the Friction-Stir Welding of 2024 Al to 6061 Al, *Scripta Materialia, 1999 Apr 9, 40(9) pp 1041-1046*

42. Graham D, Personal Communication.

43. Midling OT, Rorvik G, Effect of Tool Shoulder Material on Heat Input During Friction Stir Welding, *1st International Symposium on Friction Stir Welding at Thousand Oaks, Cal June 1999.*

44. Thomas WM, Munn I, Smith PT, Friction Stir Welding of an Aluminium Alloy - Effects of Tool Geometry, *TWI, World Centre for Materials Joining Technology*

45. Threadgill, PL, Friction Stir Welding - The State of the Art, *TWI Research Report, 1999.*

46. Mitlea I, Radu B, Thermal Field Numerical Analysis in Case of Friction Welding of Dissimilar Metals, *Mathematical Modelling of Weld Phenomena 4.*

47. Crawford-Swift, First Friction Stir Welding Machine in the Weld, *Materials World (UK), 8, (2), 7, Feb. 2000.*

48. Midling OT, O Grong, A Process Model for Friction Welding of Al-Mg-Si Alloys and Al-SiC Metal Matrix Composites - I. HAZ Temperature and Strain Rate Distribution, *Acta Metallurgia et Materialia Vol 42 No. 5 pp 1595-1609 1994.*

49. Grong O, Metallurgical Modelling of Welding, *The Institute of Materials, London, 1994*

50. Shercliff H, Ashby MF, The Prediction of Case Depth in Laser Transformation Hardening, *Metallurgical Transactions, A, Vol. 22A, 1991, pp. 2459-2466*

51. Rosenthal D, Schmerber R, Thermal Study of Arc Welding, *Welding Journal, 1938, Vol. 17, no. 4, pp. 208-214.*

52. Grong O, Metallurgical Modelling of Welding of Aluminium Alloys, *Mathematical Modelling of Weld Phenomena 3*

53. Reynolds AP, Lockwood WD, Seidel TU, Processing-Property Correlation in Friction Stir Welds, *Materials Science Forum Vols. 331-337 (2000) pp. 1719-1724*

54. Myhr OR, Grong O, Process Modelling Applied to 6082-T6 Aluminium Weldments – I. Reaction Kinetics, *Acta Metallurgia et Materialia. Vol 39, No. 11, pp 2693-2702, 1991.*

55. Frigaard O, Grong O, Hjelen J, Gulbrandsen-Dahl, Midling OT, Characterisation of the Subgrain Structure in Friction Stir Welded Aluminium Alloys Using the SEM-EBSD technique, *1st International Symposium on Friction Stir Welding at Thousand Oaks, Cal June 1999*

56. McQueen HJ, Jonas JJ, Treatise on Materials Science Technology, "Plastic Deformation of Materials", *Academic Press, New York, NY, 1975, Vol. 6, pp 393-493*

57. Juvinall RC, Marshek KM, Fundamentals of Machine Component Design, *John Wiley and Sons, 1991*

58. Bogaard RH, Ho CY, Thermal Conductivity of Selected Aluminium Alloys - A Critical Review, *Thermal Conductivity 19, Cookeville, Tennessee, USA, 20-23 Oct. 1985*

59. Davis JR, ASM Specialty Handbook, Aluminium and Aluminium Alloys, *ASM International, 1993.*

60. Vill VI, Friction Welding of Materials, *American Welding Society Inc. NY, 1962.*

61. Nguyen TC, Weckman DC, A Thermal and Microstructure Evolution Model of Direct-Drive Friction Welding of 1045 Steel, *Mathematical Modelling of Weld Phenomena 4*

62. Midling OT, Grong O, A Process Model for Friction Welding of Al-Mg-Si Alloys and Al-SiC Metal Matrix Composites - II. HAZ Microstructure and Strength Evolution, *Acta Metallurgia et Materialia Vol 42 No. 5 pp 1611-1622 1994*

63. Johnson R, Horrex NL, Preliminary Examination of Forces Generated During the Friction Stir Welding Process, *TWI Research Report, January 2000.*

64. Larsen-Basse, Basic Theory of Solid Friction, *ASM Handbook, Volume 18, Friction Lubrication Wear, Technology, The Materials Information Society*

65. Avitzur, Betzalel, Friction During Metal Forming, *ASM Handbook, Volume 18, Friction Lubrication Wear, Technology, The Materials Information Society*

66. Bathe, KJ, Finite Element Procedures, *Prentice Hall, Inc, Englewood Cliffs, NJ*

67. NISA/3D-Fluid Users Manual, *Engineering Mechanics Research Corporation*

68. Sample VM and Lalli LA, Effects of Thermo-Mechanical History on Hardness of Aluminium, *Materials Science and Technology, January 1987, Vol. 3.*

69. North T, Private Communication.

70. Seetharaman V, Jata KV, Semiatin SL, Plastic Flow and Microstructure Development During High Temperature Deformation of a Friction Stir Welded 7050 Aluminium Alloy, *2nd International Conference on Friction Stir Welding, Gothenburg Sweden 2000.*

71. Bendzsak GJ, North TH, Smith CB, An Experimentally Validated 3D Model for Friction Stir Welding, *2nd International Conference on Friction Stir Welding, Gothenburg Sweden 2000.*

72. Kalpakjian S, Manufacturing Processes for Engineering Materials, *Addison Wesley Publishing Company, 1991*

73. Gerhart PM, Gross RJ, Hochstein JI, Fundamentals of Fluid Mechanics, 2nd Edition, *Addison Wesley Publishing Company, 1995.*

74. Fluid Dynamics International, FIDAP 7.0 Theory Manual.

75. Larsson H, Karlsson L, Svensson LE, Characteristics of Friction Stir Welds in AA5083 and AA6082 Aluminium, *6th International Conference on Aluminium Alloys, Japan 1998.*

76. Threadgill PL, Leonard AJ, Macro and microstructural features of friction stir welds in various materials, *TWI Research Report, December 1999.*

77. Askeland DR, The Science and Engineering of Materials, Third S.I. Edition, *Stanley Thornes Publishers Ltd.*

78. Arbegast WJ, Fundamental Model of the Friction Stir Weld Process, *AeroMat 2000 Conference, Seattle (Abstract Only).*

79. Jones J, Arbegast WJ, Application of Neural Net Models to Friction Stir Welds, *AeroMat 2000 Conference, Seattle (Abstract Only).*

80. Lockwood WD, Reynolds AP, Mechanical Response of Friction Stir Welds, *AeroMat 2000 Conference, Seattle (Abstract Only).*

81. Thomas WM, Gittos MF, Development of Friction Stir Tools for the Welding of Thick (25mm) Aluminium Alloys, *TWI Research Report, December 1999*

82. Smith CB, Bendzsak GB, North TH, Hinrichs JF, Noruk JS, Heideman RJ, Heat and Material Flow Modelling of the Friction Stir Welding Process, *Proceedings of the*

9th International Conference in Computer Technology in Welding, Detroit, MI, Sept.

83. Dawes CJ, Staines DG, Spurgin EJR, Tool Developments for Friction Stir Welding of 6mm Thick Aluminium Alloys, *TWI Research Report, December 1999.*
84. Stokes N, Private Communication. (Author of Fastflo Finite Element Solver)
85. Zettler R, Friction Stir Welding of Thick Aluminium Plate, *Unpublished Work.*

Appendix A

Proof of Strain Rate Relationship

Knowing Eq. 2-14 and Eq. 2-17 and

$$\sigma_y = C\bar{\dot{\varepsilon}}^m \qquad \textbf{Eq. A-1}$$

In equation from Gerhart et. al. [73]:

$$\sigma_x = 2\mu\dot{\varepsilon}_x \qquad \textbf{Eq. A-2}$$

Rewriting this in terms of equivalent stress and strain rate gives:

$$\bar{\sigma} = 2\mu\bar{\dot{\varepsilon}} \qquad \textbf{Eq. A-3}$$

If power law viscosity is being used then from NISA[67]:

$$\mu = \mu_0 \mathrm{I}^{m-1}$$

$$\mathrm{I} = \sqrt{2\dot{\boldsymbol{\varepsilon}} \cdot \dot{\boldsymbol{\varepsilon}}} \qquad \textbf{Eq. A-4}$$

$$\dot{\boldsymbol{\varepsilon}} = \tfrac{1}{2}\left(\boldsymbol{v}_{i,j} + \boldsymbol{v}_{j,i}\right)$$

Also, noting the definition of equivalent strain rate from Eq.10-13

$$\bar{\dot{\varepsilon}} = \sqrt{\tfrac{2}{3}\dot{\boldsymbol{\varepsilon}} \cdot \dot{\boldsymbol{\varepsilon}}} \qquad \textbf{Eq. A-5}$$

Therefore:

$$\mathrm{I} = \sqrt{3}\bar{\dot{\varepsilon}} \qquad \textbf{Eq. A-6}$$

Equating Eq. A-1 with Eq. A-3:

$$C\bar{\dot{\varepsilon}}^m = 2\mu\bar{\dot{\varepsilon}}$$

Substituting in Eq A-4:

$$C\bar{\dot{\varepsilon}}^{m-1} = 2\mu_o \mathrm{I}^{m-1}$$

Substituting Eq. A-6:

$$C\bar{\dot{\varepsilon}}^{m-1} = 2\mu_o \sqrt{3}^{m-1} \bar{\dot{\varepsilon}}^{m-1}$$

Hence:

$$\mu_o = \frac{C}{2\sqrt{3}^{m-1}} \qquad \textbf{Eq. A-7}$$

Appendix B

Calculating the Convective Heat Transfer Coefficient

B.1 Horizontal Flat Plate

A procedure is discussed on p. 350 Holman [22] for the free convective heat transfer coefficient from a horizontal flat plate.

To calculate its value the following values are required:

- Characteristic Length. From Eq. 7.39:

$$L = \frac{A}{P}$$

For a square plate 0.2m in length:

Substituting $A = 0.2\text{x}0.2 = 0.04\text{m}^2$

$P = 4\text{x}0.2 = 0.8\text{m}$

$\Rightarrow L = 0.05\text{m}$

- Grashoff Number:

$$Gr_L = \frac{g\beta(T_w - T_\infty)x^3}{\nu^2}$$

Where:

$x = L = 0.05\text{m}$

$g = 9.81\ \text{m/s}^2$

T_w = Average Wall temperature

$= 250^\circ\text{C}$

T_f = Temperature that fluid properties evaluated at

$= (T_w+T_{amb})/2 = (250+20)/2 = 135^oC$

β = Temperature Coefficient of Thermal Conductivity

$= 1/T(^oK) = 1/(273+135) = 2.5x10^{-3}$

ν = Average Viscosity of air

$= 25.9x10^{-6}$

$\Rightarrow Gr_L = 1.05x10^6$

Note that the properties of air were obtained from Table A-5 Holman [22].

- Prandtl Number:

  Pr = 0.689 Table A-5 Holman [22]

Therefore:

$GrPr = 723\ x10^3$

From Table 7.1 Holman [22], C = 0.54 and m = 0.25 for use in the following equation:

$\overline{Nu_f} = C(Gr\,\mathrm{Pr})^m$ Eq 7.25 Holman [22]

$\Rightarrow Nu = 15.7$

Finally, the convective heat transfer coefficient is given by:

$$Nu = \frac{hL}{k}$$

where: k = Thermal conductivity of air

= 0.03365 W/mK (Table A-5 Holman [22])

This gives a value for the convective heat transfer coefficient of **10.6 W/m^{2}K**.

B.2 Vertical Cylinder

This analysis has been done for the rotating tool with a Φ = 40mm and a height of 100mm. The analysis has been done for free convection off a stationary cylinder and will therefore slightly underestimate the actual heat transfer coefficient for a rotating tool. In any case the heat loss due to convection is relatively small compared to the total heat input so any error will not have a significant impact on the results.

To determine whether or not the cylinder can be analysed as a vertical flat plate, use equation 7-27 from Holman [22].

$$\frac{D}{L} \geq \frac{35}{Gr_L^{0.25}}$$

Calculating the Grashoff number as for the horizontal flat plate except that $L = 0.1$m:

$$\text{Gr} = 7.31\text{x}10^6$$

Therefore:

$$\left(\frac{40}{100} = 0.4\right) \leq \left(\frac{35}{(7.31e6)^{0.25}} = 0.673\right)$$

Hence required condition for this analysis does not hold.

Hence use equation 7.28 from Holman [22]:

$$Nu = 0.68 + \frac{0.67Ra^{0.25}}{\left[1 + (0.492/\text{Pr})^{9/16}\right]^{4/9}}$$

where:

- $Pr = 0.689$
- $Ra = GrPr = 7.31\text{x}10^6\text{x}0.689 = 5.04\text{x}10^6$

Therefore $Nu = 24.28$.

This corresponds to a convective heat transfer coefficient of:

$$h = Nuk/x = 24.28 \text{x} 0.03365/0.1 = \mathbf{8.17\ W/m^2K}$$

Hence a value of 10 will be reasonable, especially given that the above estimate will underestimate the value for a rotating cylinder.

Appendix C

Position of Thermocouple Holes for the Welding of 12mm Thick 5083 Aluminium Alloy

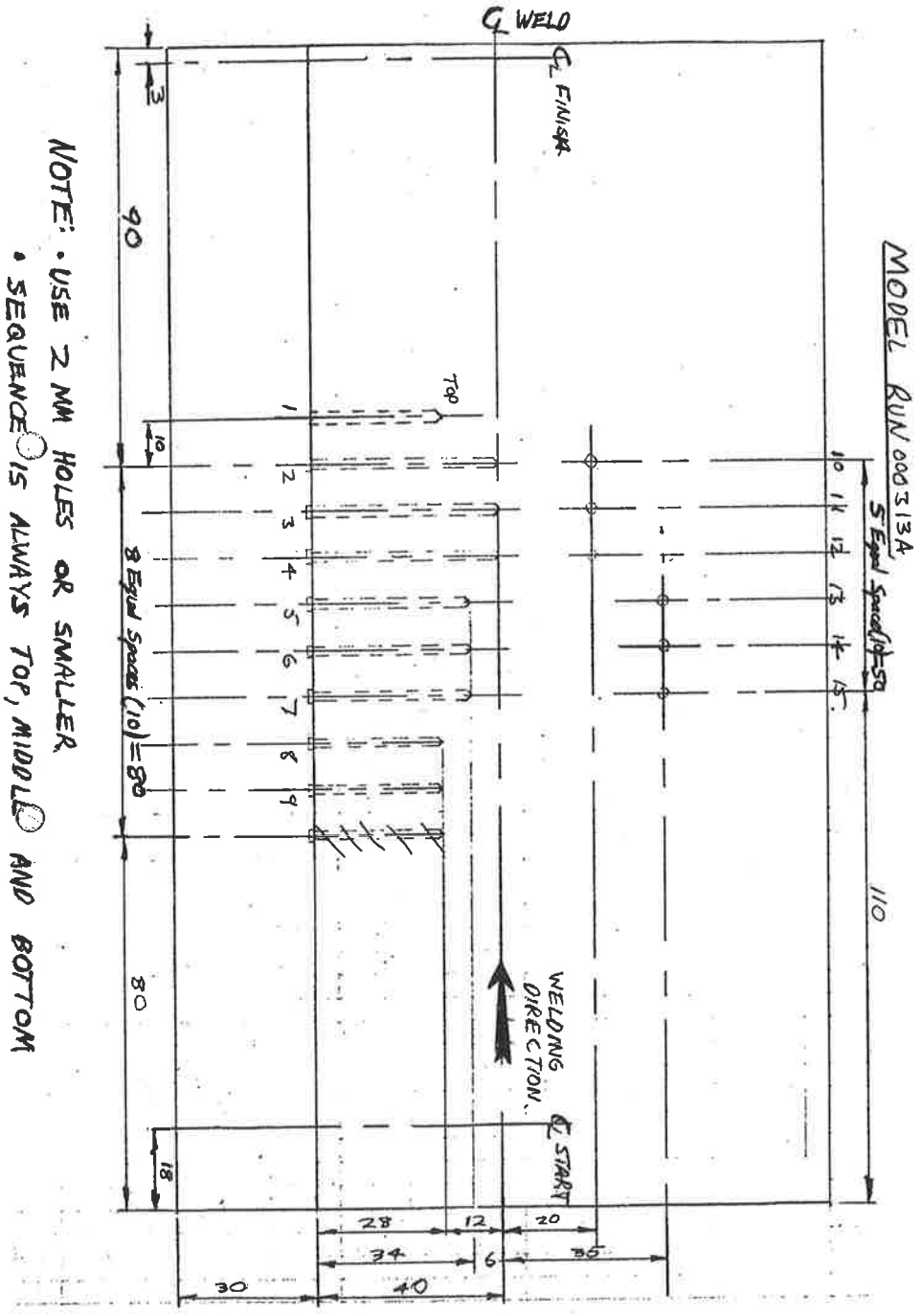

MODEL RUN No. 000313B

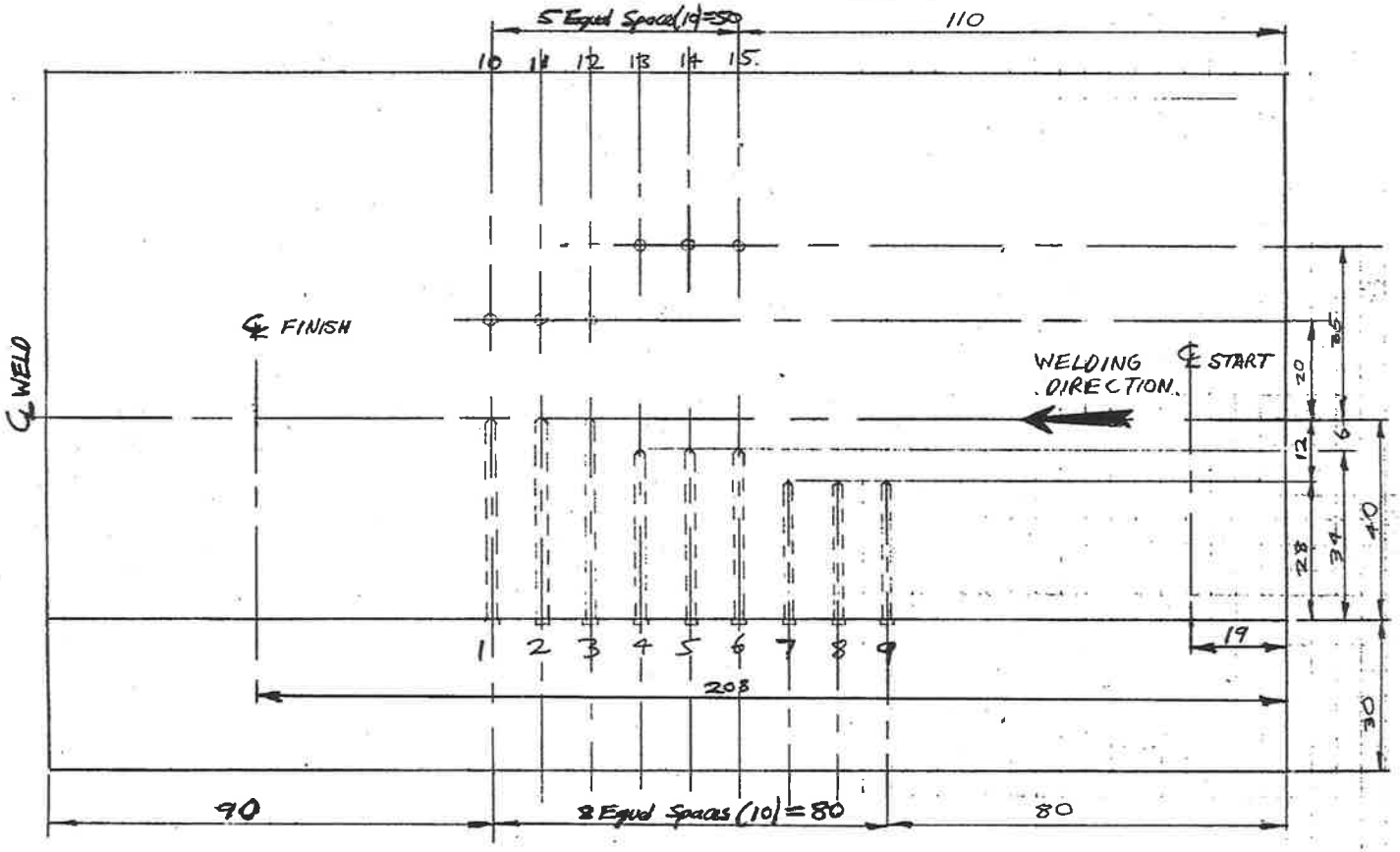

NOTE: • USE 2 MM HOLES OR SMALLER
• SEQUENCE IS ALWAYS TOP, MIDDLE AND BOTTOM

Appendix D

Basic Theory for the Mesh Generation Program

D.1 Setting Up the Model Mesh for the Local Thermal/Flow Model

The mesh for the local thermal model is reasonably complex because of the complex geometry of the pin. The following work describes some of the basic theory behind the program used to generate the mesh.

D.2 Description of Pin Geometry

Before developing the equations describing the nodal coordinates of the mesh, it is necessary to define the main features of the pin and the nomenclature to be used. A diagram showing this information is shown in Figure D- 1

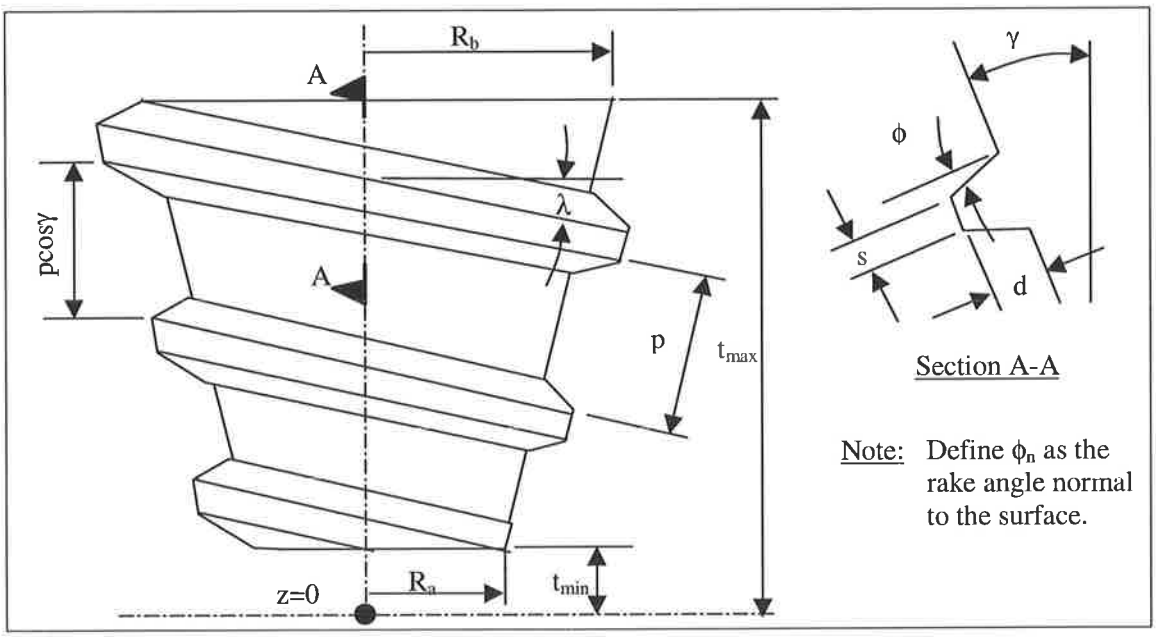

Figure D- 1 Inclined Thread Geometry

Note the following relationships between the parameters:

$$\tan\phi_n = \cos\lambda \tan\phi$$

$$\tan\gamma = \frac{R_b - R_a}{t_{\max} - t_{\min}}$$

D.2.1 Description of Helix

The fundamental concept in describing the thread of the pin mathematically is the description of a helix. For a helix which starts at a height $t_{\min}$ and finishes a height $t_{\max}$, and is conically shaped:

$$r = R_a + \frac{(R_b - R_a)}{t_{\max} - t_{\min}}(z - t_{\min})$$

If the pitch is p and the start angle is θ_0, then:

$$z = t_{\min} + (p\cos\gamma)\frac{\theta - \theta_0}{2\pi}$$

Substituting for z in the first equation gives:

$$r = R_a + \frac{(R_b - R_a)}{t_{\max} - t_{\min}}(p\cos\gamma)\frac{\theta - \theta_0}{2\pi}$$

for: $t_{min}<z<t_{max}$

ie. Both a and r are given by the single variable θ.

D.2.2 Description of Thread Form by Helix Approach

The shape of a tool thread may be described by series of helixes. Therefore, to find the nodes that describe the shape of the screw, the above description of a helix will be used.

Referring to Figure D- 2, we will assume that the base helix will be described by point 1. Therefore, if we let $\theta_0 = 0$ then the equation for point 1 is:

$$r_1 = R_a + \frac{(R_b - R_a)}{t_{max} - t_{min}}(p\cos\gamma)\frac{\theta}{2\pi}$$

$$z_1 = t_{min} + p\cos\gamma\frac{\theta}{2\pi}$$

To find the equation of point 2, refer to Figure D- 2. The length of the face of the thread, k is:

$$k = d\sqrt{1+\tan^2\phi}$$

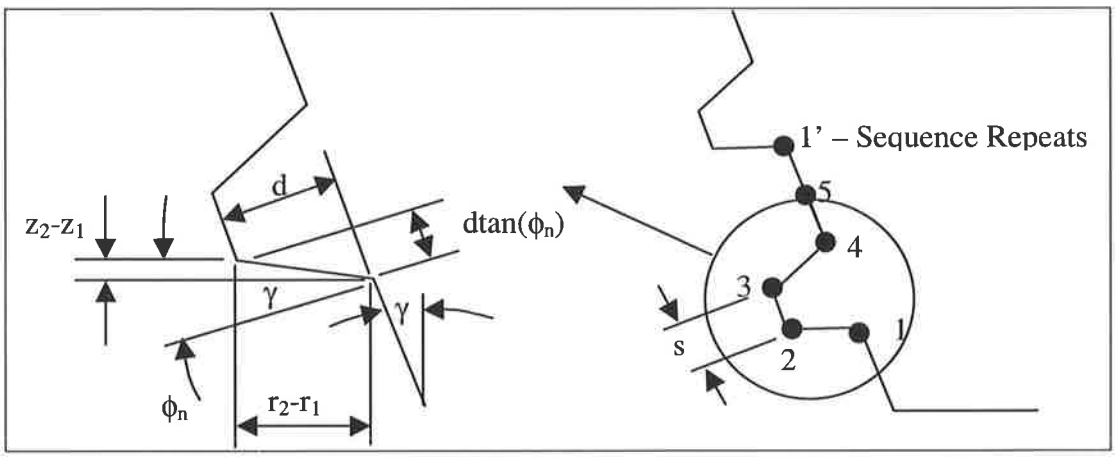

Figure D- 2 Description of Nodes that Make Up Tool Thread

Therefore, r_2 is given by:

$$r_2 - r_1 = \cos(\phi_n - \gamma)d\sqrt{1+\tan^2\phi_n}$$

$$z_2 - z_1 = \sin(\phi_n - \gamma)d\sqrt{1+\tan^2\phi_n}$$

For point 3:

$$r_3 - r_2 = s\sin\gamma$$
$$z_3 - z_2 = s\cos\gamma$$

For point 4:

$$r_4 - r_1 = (s + 2d\tan\phi_n)\sin\gamma$$
$$z_4 - z_1 = (s + 2d\tan\phi_n)\cos\gamma$$

Finally for point 5:

$$r_5 - r_1 = \left(\frac{p+s}{2} + d\tan\phi_n\right)\sin\gamma$$

$$z_5 - z_1 = \left(\frac{p+s}{2} + d\tan\phi_n\right)\cos\gamma$$

Determining the position of the rest of the grid points will involve a similar procedure. Note that the actual program has been written to allow additional grid points between 1 and 2, 2 and 3 etc, so that the mesh can be made as fine as required.

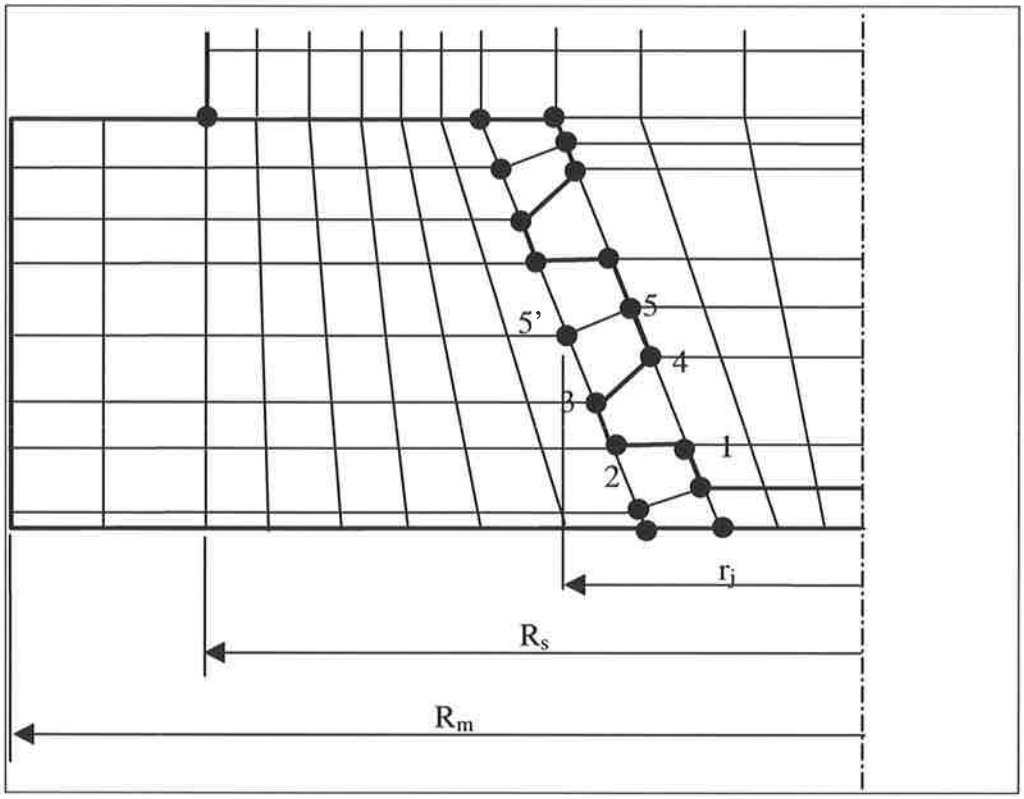

Figure D- 3 Remaining Model Nodes

Figure D- 3 describes the layout of the rest of the nodes. To determine the nodal positions of the rest of the mesh the following procedure will be used:

1. Calculate the nodal position of 5' by the following equations:
   $$r_{5'} - r_3 = (p-s)\sin\gamma$$
   $$z_{5'} - z_3 = (p-s)\cos\gamma$$

2. If it is assumed that there are N_1 elements between the surface of the tool and R_s, then the nodal positions will be given by:

$$r_{ij} = r_i + (R_s - r_i)\frac{j}{N_1}$$

where:

- r_i is the nodal radial position corresponding to one of the nodal radial positions for 2, 3 and 5' nodes.
- 0<j<N

Alternatively, if the size of the elements increases exponentially by the following relationship

$$\Delta r = Ae^{bj}$$

where A and b are constants, and the ratio between the largest and smallest element is defined by r:

$$r = \frac{\Delta r_N}{\Delta r_1} = e^{b(N-1)} = r$$

Hence b is given by:

$$b = \frac{\ln r}{n-1}$$

It may be shown that:

$$A = \frac{R_s - r_i}{\sum_{j=1}^{N} e^{bj}}$$

Hence r is given by:

$$r_{ij} = r_i + \sum_{j'=1}^{j} Ae^{j'b}$$

Finally, the heights of the nodes are given by:

$$z_{ij} = z_i$$

3. The position of the nodes beyond R_s will be given by the following equations, if there are N_2 elements between R_s and R_m. This only applies to the 2,3 and 5' nodes.

$$r_{ij} = R_s + (R_m - R_s)\frac{j}{N_2}$$

$$z_{ij} = z_i$$

Appendix E

Material Heat Generation

Another way of calculating this value in terms of the material constants C and m is described as follows. From equation 6.227 in Bathe [55] as:

$$\bar{\varepsilon} = \sqrt{\tfrac{2}{3}\boldsymbol{\varepsilon}\cdot\boldsymbol{\varepsilon}}$$

where: $\boldsymbol{\varepsilon}$ is the strain tensor given by:

$$\boldsymbol{\varepsilon} = \begin{bmatrix} e_{xx} & e_{yx} & e_{zx} \\ e_{xy} & e_{yy} & e_{zy} \\ e_{xz} & e_{yz} & e_{zz} \end{bmatrix}$$

Note that if the strain rate is constant at a particular point then the principal strains can be written in terms of the constant strain rate as:

$$\varepsilon_i = \dot{\varepsilon}_i t$$

Therefore the effective strain can be written as:

$$\bar{\varepsilon} = t\sqrt{\tfrac{2}{3}\dot{\boldsymbol{\varepsilon}}\cdot\dot{\boldsymbol{\varepsilon}}}$$

Differentiating both sides with respect to time gives the following equation for the effective strain rate:

$$\dot{\bar{\varepsilon}} = \sqrt{\tfrac{2}{3}\dot{\boldsymbol{\varepsilon}}\cdot\dot{\boldsymbol{\varepsilon}}}$$

From section 6:

$$\dot{Q} = V\bar{\sigma}_y\dot{\varepsilon}$$

and substituting the equivalent strain rate above and the material constitutive equation , Eq 2-14:

$$\dot{Q} = VC\left[\tfrac{2}{3}\dot{\boldsymbol{\varepsilon}}\cdot\dot{\boldsymbol{\varepsilon}}\right]^{(1+m)/2}$$

Appendix F

Determining an Equation for $\frac{\partial T}{\partial t}$ for a Rotating Frame of Reference with a Constant Temperature Field in the Stationary Frame of Reference

To transfer the identity $\frac{\partial T}{\partial t}$ into a derivative with respect to position consider the following simple case of a solid bar moving horizontally past a stationary coordinate system with velocity, v. It will be assumed that the bar is being heated and that this heating process is steady state. Therefore at a position $x = x_o$ and time $t=t_o$ the temperature of the bar will be $T = T_o$. See Figure F-1.

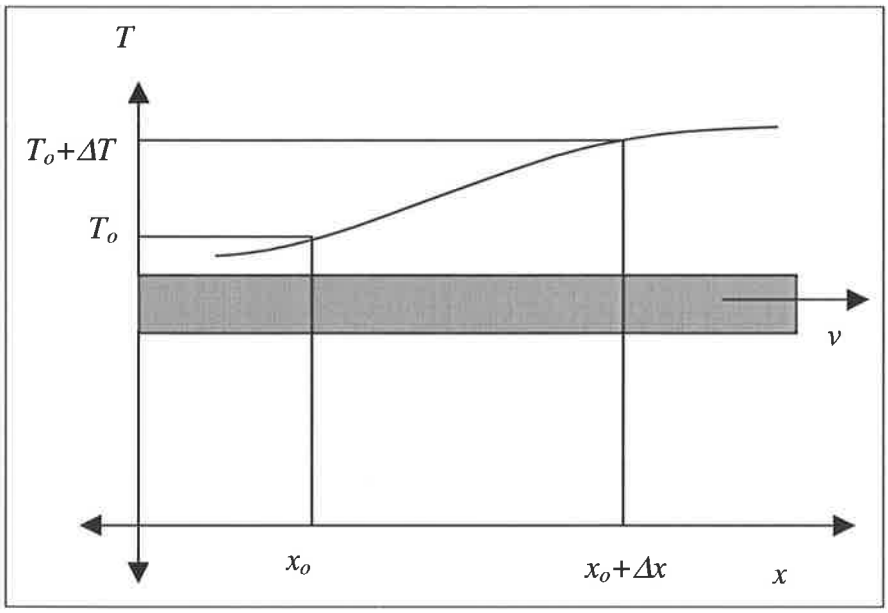

Figure F-1

Now consider the bar at a new position $x = x_o+\Delta x$, where the temperature of the bar has increased to $T=T_o+\Delta T$. If we consider a particular point on the bar, which is at x_o at t_o, then it will be at the position $x_o+\Delta x$ at $t_o+\Delta t$.

Finally, since:

$$\Delta x = v\Delta t$$

Therefore:

$$\frac{\partial T}{\partial t} = v\frac{\partial T}{\partial x}$$

In a rotating coordinate system a similar condition will hold except:

$$\Delta\theta = \omega\Delta t$$

Therefore:

$$\frac{\partial T}{\partial t} = \omega\frac{\partial T}{\partial \theta}$$

Converting this to Cartesian coordinates by the following equation:

$$\frac{\partial T}{\partial t} = \omega\left(\frac{\partial T}{\partial x}\frac{\partial x}{\partial \theta} + \frac{\partial T}{\partial y}\frac{\partial y}{\partial \theta}\right)$$

Finally:

$$x = r\cos\theta$$
$$y = r\sin\theta$$

so:

$$\frac{\partial T}{\partial t} = \omega r\left(-\sin\theta\frac{\partial T}{\partial x} + \cos\theta\frac{\partial T}{\partial y}\right)$$

Appendix G

Position of Thermocouple Holes for the Welding of 25mm Thick 5083 Aluminium Alloy

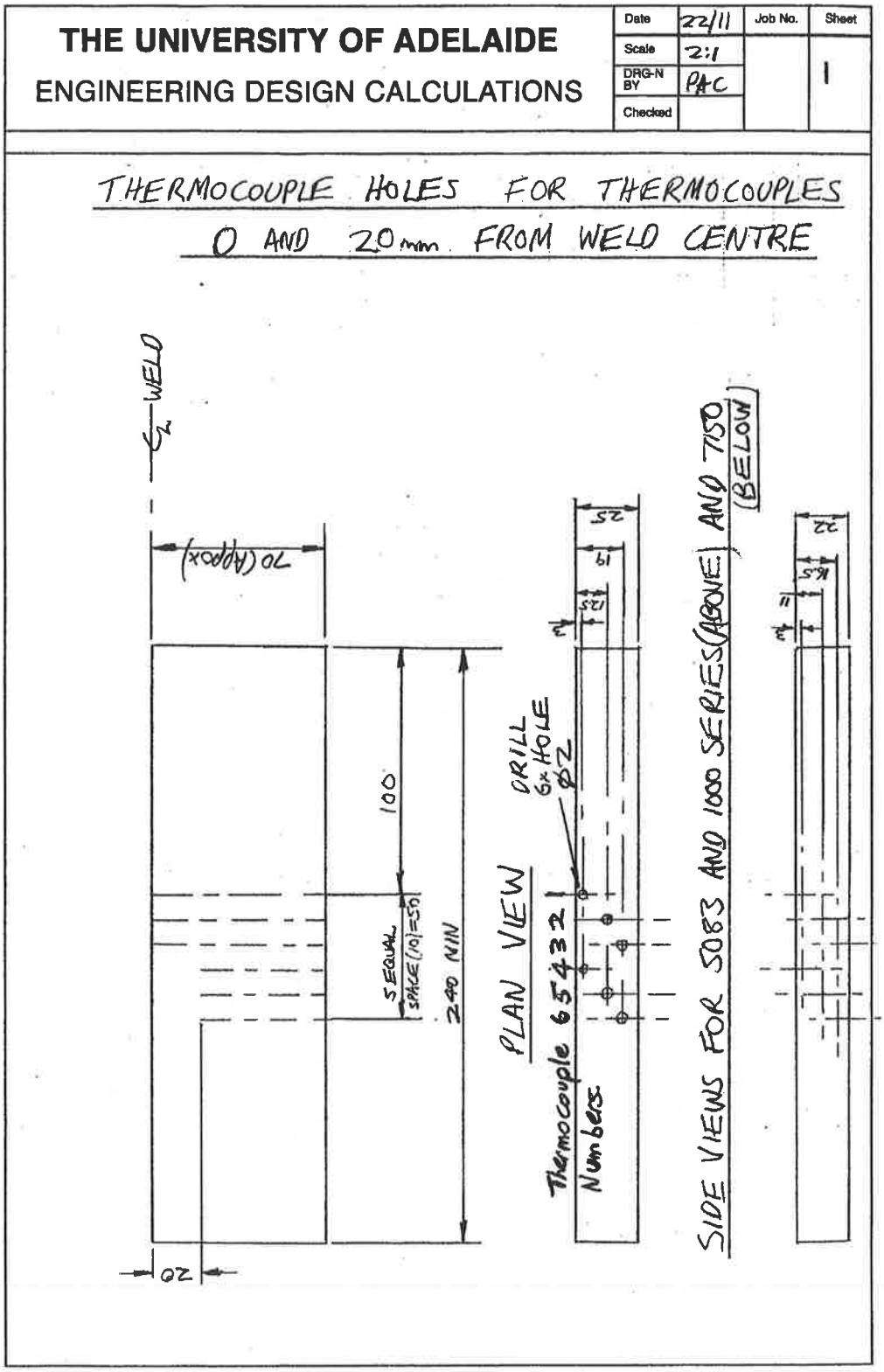

THE UNIVERSITY OF ADELAIDE
ENGINEERING DESIGN CALCULATIONS

Date	22/11	Job No.	Sheet
Scale	2:1		2
DRG-N BY	PAC		
Checked			

THERMOCOUPLE HOLES FOR THERMOCOUPLES
35 MM FROM WELD CENTRE